Search for dark matter and unparticles produced in association with a Z boson in pp collisions at $\sqrt{s} = 8\,\mathrm{TeV}$ at CMS

Von der Fakultät für Mathematik, Informatik und Naturwissenschaften der RWTH Aachen University zur Erlangung des akademischen Grades eines Doktors der Naturwissenschaften genehmigte Dissertation

vorgelegt von

M.Sc. RWTH Aachen

Michael Brodski

aus Moskau, Russland

Berichter: Universitätsprofessor Dr. Thomas Hebbeker

Universitätsprofessor Dr. Christopher Wiebusch

Tag der mündlichen Prüfung: 26.01.2017

Zusammenfassung

Der Large Hadron Collider (LHC) ist die größte Teilchenkollisionsmaschine, die je gebaut und in Betrieb genommen wurde. Seit dem Jahr 2008 ist sie aktiv und lieferte bereits große Datensätze, deren Auswertung viele neue Erkenntnisse mit sich brachte. Bei der Analyse der Protonenkollisionen am LHC ist es den Wissenschaftlern der CMS und ATLAS Kollaborationen im Jahr 2012 gelungen, das seit langem gesuchte Higgs-Boson zu entdecken. Obwohl das Standardmodell der Teilchenphysik in den vergangenen 60 Jahren durch viele Experimente mit hoher Genauigkeit überprüft und bestätigt werden konnte, gibt es inzwischen viele Beobachtungen, die auf die Existenz weiterer Phänomene hindeuten. In den kommenden 20 Jahren des Betriebes des LHC fällt daher der Fokus der Untersuchungen auf die Neue Physik, von der die Forscher eine Erklärung der bisher nicht erklärten Messergebnisse erwarten.

In der vorliegenden Arbeit wird der Datensatz, der im Jahr 2012 von dem Compact Muon Solenoid (CMS) Detektor am LHC aufgezeichnet wurde und eine integrierte Luminosität von 19.7 fb^{-1} aufweist, im Hinblick auf Signaturen von Dunkler Materie und Unparticles untersucht. Mit dem Ansatz einer effektiven Feldtheorie stellt man dabei die Hypothese auf, dass bei der Produktion eines Z-Bosons am LHC ebenfalls zwei Teilchen χ und $\bar{\chi}$ der Dunklen Materie entstehen können, die den Detektor unbemerkt verlassen und somit zur fehlenden Transversalenergie ($E_{\text{T}}^{\text{miss}}$) im Detektor führen, wobei das Z-Boson in zwei geladene Leptonen zerfällt. In gleicher Signatur könnte ebenfalls die Produktion von sogenannten Unparticles erfolgen. Nachdem in den ersten Kapiteln ein Einblick in das Standardmodell der Teilchenphysik und den Aufbau des Detektors erfolgt, wird die Ereignisselektion vorgestellt und anschließend die Hintergrundvorhersage für den Endzustand mit zwei Leptonen und fehlender Transversalenergie mit aufgezeichneten Daten verglichen und diskutiert. Kein Datenüberschuss ist verzeichnet und daher werden Ausschlussgrenzen auf den Produktionswirkungsquerschnitt von Teilchen χ der Dunklen Materie sowie der Unparticles abgeleitet. Im Fall von Unparticles werden die bis dato stärksten Ausschlussgrenzen gesetzt. Die Ergebnisse der vorliegenden Arbeit wurden in der Physics Analysis Summary CMS-EXO-12-054 und einem Paper in Physics Review D veröffentlicht [1].

Abstract

The Large Hadron Collider (LHC) is the biggest and the most powerful particle collider machine to be built and operated in the history of humankind. The operation of the LHC machine started in 2008 and to date a big dataset was recorded allowing for a great number of data analyses to be performed. Analyzing the proton-proton collisions, the scientists of the CMS and ATLAS collaborations were able to discover the long sought Higgs boson. Even though the Standard Model of particle physics has been very successful in the past 60 years, being tested with high precision, there still exist observations presenting strong evidence for phenomena the Standard Model can not explain. Therefore, the search for New Physics which is expected to supply the missing explanations will be gaining more and more attention in the next 20 years of the LHC operation.

The present thesis analyzes the dataset corresponding to an integrated luminosity of 19.7 fb^{-1} which was recorded by the CMS detector in 2012 in terms of dark matter and unparticle signatures. Employing an effective field theory approach, one proposes the hypothesis of dark matter particles χ and $\bar{\chi}$ production along a Z boson during a collision at the LHC, whereby dark matter leaves CMS undetected and the Z boson subsequently decays into two charged leptons. The so called unparticles could also lead to the same final state. After the introduction of the standard model of particle physics followed by the CMS setup description in the first chapters of the present thesis, the aspects of event selection and background prediction for the final state with two leptons along missing transverse energy ($E_{\text{T}}^{\text{miss}}$) are discussed and compared to the CMS measurement. No excess of data events is observed in the signal region and exclusion limits for the dark matter production are therefore set. For the unparticle scenario, the world's best exclusion limits are obtained as the result of this analysis. The results of the present analysis are published in the Physics Analysis Summary CMS-EXO-12-054 and in the Physics Review D journal [1].

Contents

1 Introduction 1
1.1 Notations and Conventions . . . 3

2 Standard Model of Particle Physics 7
2.1 The Particles of the Standard Model . . . 7
2.2 Quantum Electrodynamics . . . 10
2.3 Quantum Flavordynamics . . . 11
2.4 Quantum Chromodynamics . . . 12
2.5 Challenges to the Standard Model . . . 12
2.5.1 Fine tuning . . . 13
2.5.2 Gravity and the hierarchy problem . . . 13
2.5.3 The strong CP Problem . . . 13
2.5.4 Neutrino Masses . . . 14

3 Physics Beyond the Standard Model and Dark Matter 17
3.1 Supersymmetry . . . 17
3.1.1 Searches for Supersymmetry . . . 18
3.2 Large Extra Dimensions in the ADD approach . . . 20
3.3 Unparticles . . . 20
3.3.1 Unparticle Mass . . . 21
3.3.2 Phase space . . . 21
3.3.3 Unparticle propagator . . . 22
3.3.4 Unparticle spin . . . 23
3.3.5 Unparticle Interactions . . . 24
3.3.6 Matrix Element . . . 25
3.4 Dark Matter . . . 26
3.4.1 Axions . . . 26
3.4.2 Weakly interacting particles . . . 27
3.4.3 Neutrinos . . . 27
3.4.4 Collider searches for dark matter . . . 28
3.4.5 Non-collider searches for dark matter . . . 33

4 Large Hadron Collider and Compact Muon Solenoid Detector 37
4.1 General remarks . . . 37
4.2 The Large Hadron Collider . . . 38
4.2.1 Remarks about the LHC . . . 40
4.3 The Compact Muon Solenoid Detector . . . 41
4.3.1 The Superconducting Solenoid Magnet . . . 42
4.3.2 The Pixel Tracker . . . 42
4.3.3 The Silicon Tracker . . . 43
4.3.4 Electromagnetic calorimeter . . . 44
4.3.5 Hadron calorimeter . . . 46
4.3.6 The muon system . . . 48
4.3.7 Event Triggering . . . 54
4.4 Computing . . . 56

5 Software Framework 57
5.1 CMSSW and ROOT . . . 57
5.2 Physics Generators . . . 58
5.3 Detector Simulation . . . 58
5.4 Statistical Interpretation . . . 59

6 Physics Object Reconstruction and Event Selection 61
6.1 Electrons . . . 61
6.1.1 Electron energy clustering in the ECAL . . . 61
6.1.2 Electron track reconstruction . . . 62
6.1.3 Association of track and cluster . . . 64
6.1.4 Electron selection requirements . . . 64
6.1.5 Electron isolation requirement . . . 64
6.2 Muons . . . 65
6.2.1 Muon reconstruction in the tracker and the muon spectrometer . . . 65
6.2.2 Global muon track reconstruction . . . 66
6.2.3 Muon selection requirements . . . 67
6.2.4 Muon isolation . . . 68
6.2.5 Muon momentum scale and resolution . . . 68
6.3 Hadronic Jets . . . 68
6.3.1 Anti-k$_t$ algorithm . . . 68
6.3.2 Jet selection requirements . . . 69
6.3.3 B tagged jets . . . 69
6.4 Particle Flow . . . 71
6.4.1 Linking algorithm . . . 72
6.4.2 Particle reconstruction . . . 72
6.5 Missing transverse energy . . . 73
6.5.1 $E_{\mathrm{T}}^{\mathrm{miss}}$ corrections and filters . . . 73

7 Analysis Strategy 75
7.1 Datasets . . . 75
7.1.1 Signal samples for dark matter and unparticles . . . 76
7.1.2 Background samples . . . 79
7.1.3 CMS data . . . 79
7.2 Triggering . . . 81
7.3 Event Selection . . . 81
7.3.1 Invariant mass of the lepton pair . . . 82
7.3.2 Response requirement . . . 84
7.3.3 Balance requirement . . . 85
7.3.4 ϕ requirement and dilepton transverse momentum . . . 85
7.3.5 Selection summary . . . 87
7.4 Background Estimation . . . 87
7.4.1 Drell-Yan Process . . . 89
7.4.2 Non-resonant background processes . . . 91
7.4.3 WZ and ZZ background contributions . . . 93
7.4.4 Pileup reweighting . . . 93
7.4.5 W+jets background . . . 93
7.5 Systematic Uncertainties . . . 96
7.5.1 Jet energy resolution . . . 96
7.5.2 Jet energy scale . . . 97
7.5.3 Muon scale and resolution . . . 97
7.5.4 Unclustered $E_{\mathrm{T}}^{\mathrm{miss}}$ . . . 98
7.5.5 Lepton trigger, reconstruction and efficiency . . . 98
7.5.6 Parton distribution function uncertainties . . . 98
7.5.7 Pileup . . . 99
7.5.8 Luminosity . . . 99
7.5.9 Drell-Yan and non-resonant backgrounds . . . 101
7.5.10 ZZ background . . . 101
7.5.11 QCD scale uncertainty . . . 101
7.5.12 Summary . . . 101

8 Results and Limits 105
8.1 Dark Matter interpretation . . . 105
8.2 Unparticle interpretation and model-independent limits . . . 110
8.3 Updated preliminary result from CMS . . . 114

9 Conclusion and Outlook 119

10 Acknowledgements 137

Bibliography 139

CHAPTER 1

Introduction

The launch of the Large Hadron Collider (LHC) in 2007 in an underground tunnel with a circumference of almost 27 km opened a new page in the history of particle physics. Being designed for center of mass energies $\sqrt{s}$ of up to 14 TeV, the LHC provides a great opportunity for studying particle interactions at energies which remained unreached before. In each of four huge caverns located approximately 100 meters underground, a particle detector is installed. The main purpose of the LHC is the search for the Higgs boson along the search for New Physics – the theory which is expected to complement or supersede the standard model of particle physics. The postulate of the existence of New Physics is based on observations made at colliders and particle observatories all around the world which prove the imperfection of our understanding of the quantum world today. Furthermore, there are many mathematical and even philosophical considerations which support the hypothesis of New Physics. These considerations will be discussed further in chapter 2 and are the main motivation for the present work. The discovery of the Higgs boson once more proved the sustainability of the LHC and the great vision for the future which was guiding the scientists who constructed this machine. As of today, the LHC has reached the record center of mass energy $\sqrt{s} = 13$ TeV after being operated at $\sqrt{s} = 7$ TeV in 2011 and at $\sqrt{s} = 8$ TeV in 2012. The present work concentrates on the dataset collected in the latter setting. The Compact Muon Detector (CMS) is one of the two multipurpose detectors installed at the LHC. Being 21 meters long, over 15 meters high and having a weight of over 14000 tonnes, CMS is mainly dedicated to searches for Higgs boson as well as New Physics. The construction and performance parameters of CMS and LHC are discussed in chapter 4.

The observations of the dynamics of galaxies around us indicate that there is much more gravitational interaction than one can attribute to the visible matter only [2–4]. If one considers the rotation velocity of stars in a galaxy as a function of the distance of the star to the center of the galaxy only relying on Kepler's laws of motion, it is expected that the velocity drops after reaching a certain maximum. However, many observations show that the velocity stays at a plateau. The rotation velocity of stars near the NGC 6503 galaxy is shown in Fig. 1.1 as an example. These observations are

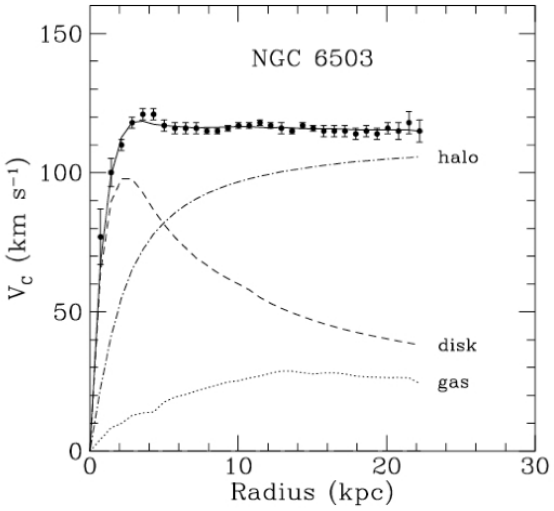

Figure 1.1: The measured rotation velocity of the spiral galaxy NGC 6503. The dashed and dotted lines represent the contribution by the visible matter and gas. The contribution of "halo" is attributed to the dark matter and is an assumption which can be used for explaining the observed curve [5].

the motivation for postulating dark matter (DM) [1]. In the past, many direct searches for dark matter have been conducted [6–13] as well as indirect [14, 15] and collider searches [16–28]. The present collider search relies on the effective field theory (EFT) proposal made in [29] where it is suggested that a Z boson produced in a proton-proton collision recoils against two dark matter particles χ and $\bar{\chi}$ and subsequently decays into two electrons or two muons. A similar search with a W boson was conducted by a group from RWTH Aachen University in [20] and by further colleagues in [30]. A detailed discussion of theory aspects for the chosen approach along the introduction of selected New Physics scenarios is given in chapter 3.

Analysis of huge amounts of data which are recorded by CMS as well as performing background and signal simulations require a well-structured distributing network with huge computing resources. Various sophisticated software frameworks are needed for performing efficient and reliable calculations. In chapter 5, the computing structure and software used in the present analysis are introduced.

The selection of collision events at CMS requires careful expertise. Depending on the particular details of the performed analysis, reasonable working points for selection requirements must be chosen by the analyst. Furthermore, the best possible signal extraction strategy is to be developed and applied. This is achieved by considering distributions of different kinematic variables and deriving further selection choices which aim for background suppression. A very careful examination of systematic uncertainties has to be performed including studies of the uncertainties arising from object selection in data and simulation, resolution and momentum scale studies as well as an investigation of theoretical uncertainties. Chapters 6 and 7 deal with those aspects.

[1] The author of the present thesis, however, privately prefers the name "transparent matter" due to the fact that dark matter does not have any color and simply does not interact with light at all.

In chapter 8, the results of the analysis are shown and discussed. After presenting the obtained distributions of $E_{\mathrm{T}}^{\mathrm{miss}}$ and transverse mass, a statistical interpretation of the results is presented. Recent CMS results are shown and discussed in this chapter.

A conclusion and an outlook in terms of proton-proton collisions at $\sqrt{s} = 13$ TeV which were performed at LHC in 2015 are given in chapter 9. The obtained results are compared to different experiments and an outlook for searches for dark matter in the future is given.

1.1 Notations and Conventions

The present thesis uses a set of conventions and variables which are common in high energy physics. Notably,

$$\hbar = c = 1, \tag{1.1}$$

where $\hbar$ denotes Planck's constant divided by 2π and c is the speed of light. As a consequence, the unit of mass $\frac{\mathrm{eV{\cdot}s^2}}{\mathrm{m^2}}$ and the unit of momentum $\frac{\mathrm{eV{\cdot}s}}{\mathrm{m}}$ are both reduced to the unit of energy eV. If not stated otherwise, i denotes the imaginary unit which satisfies $i^2 = -1$.

A four-vector p is defined by

$$p \equiv \begin{pmatrix} p_0 \\ p_1 \\ p_2 \\ p_3 \end{pmatrix} = \begin{pmatrix} E \\ \vec{p} \end{pmatrix} \tag{1.2}$$

where E denotes the total energy of a particle and $\vec{p}$ denotes its momentum vector in three dimensions. A scalar product of a four-vector p is defined via:

$$p \cdot p = p^2 \equiv p_0^2 - (p_1^2 + p_2^2 + p_3^2) = E^2 - \vec{p}^2 \tag{1.3}$$

relying on the Minkowski metric tensor $g^{\mu\nu}$ defined by

$$g = \begin{pmatrix} 1 & 0 & 0 & 0 \\ 0 & -1 & 0 & 0 \\ 0 & 0 & -1 & 0 \\ 0 & 0 & 0 & -1 \end{pmatrix}. \tag{1.4}$$

Applying the relation of energy and momentum to Eq. 1.3 yields

$$E^2 = m^2 + \vec{p}^2. \tag{1.5}$$

Now, Eq. 1.3 evolves into

$$p^2 = m^2. \tag{1.6}$$

One defines the transverse momentum $\vec{p}_{\mathrm{T}}$ by

$$\vec{p}_{\mathrm{T}} \equiv \begin{pmatrix} p_x \\ p_y \end{pmatrix} \tag{1.7}$$

whereby x and y are the coordinates of the plane which is perpendicular to the beam axis z. p_{T} denotes the magnitude of $\vec{p}_{\mathrm{T}}$. If not stated otherwise, the unit of p_{T} is always GeV.

When considering interactions of two particles ($2 \to 2$ processes with corresponding indices $i = 1,\ldots,4$) with the corresponding four-momenta $p_{1,\ldots,4}$, it is handy to use the Mandelstam variables. They are defined as follows:

$$s = (p_1 + p_2)^2 = (p_3 + p_4)^2 \tag{1.8}$$

$$t = (p_1 - p_3)^2 = (p_2 - p_4)^2 \tag{1.9}$$

$$u = (p_1 - p_4)^2 = (p_2 - p_3)^2. \tag{1.10}$$

Hereby, the Mandelstam variable s is also the square of the center-of-mass energy – the quantity $\sqrt{s}$ is a key property of collider machines describing the energy which is available for creation of new particles at the interaction point. For hadron colliders, where composite particles are brought to collision, $\sqrt{s}$ denotes the total center-of-mass energy of the interacting hadron pair, whereby the effective energy of the interaction, in which the substituents of the hadrons participate, is denoted by $\sqrt{\hat{s}}$. Generally, $\sqrt{\hat{s}}$ remains unknown.

Since the many particles considered in this work are moving with very high velocities ($v \approx c$), presenting with an unknown boost along the z axis, and are thus *ultrarelativistic* ($E \gg m$ and therefore $E \approx p$), one prefers Lorentz-invariant quantities. One defines the pseudorapidity η by:

$$\eta \equiv -\ln\left[\tan\left(\frac{\theta}{2}\right)\right] \tag{1.11}$$

where θ is the angle to the beam axis z in the $r-z$ plane. Using η has a great advantage due to the fact that differences of pseudorapidities $\Delta\eta = \eta_1 - \eta_2$ of two particles are Lorentz-invariant. The angle in the $x-y$ plane, sometimes also referred to as the $r-\phi$ plane, which is orthogonal to the beam axis, is measured using the angle ϕ. One additional handy quantity is

$$\Delta R = \sqrt{\Delta\phi^2 + \Delta\eta^2} \tag{1.12}$$

which is used as a measure for isolation of particles.

One further convention used in the present thesis is the Einstein summation convention. It implies that whenever a mathematical expression with indices in the upper and lower index appear, a summation over the indices is performed:

$$a^\mu b_\mu = \sum_{\mu=0}^{n} a_\mu b_\mu, \tag{1.13}$$

whereby n denotes the dimension of the space in which a, b are defined (e.g. $n = 3$ and $\mu = 0,\ldots,3$ in Eq. 1.3 for the four-dimensional case).

The slash notation, introduced by Richard Feynman, is used in the present thesis. First, one defines

the γ matrices (here in Dirac representation) via

$$\gamma^0 = \begin{pmatrix} 1 & 0 & 0 & 0 \\ 0 & 1 & 0 & 0 \\ 0 & 0 & -1 & 0 \\ 0 & 0 & 0 & -1 \end{pmatrix}; \qquad \gamma^1 = \begin{pmatrix} 0 & 0 & 0 & 1 \\ 0 & 0 & 1 & 0 \\ 0 & -1 & 0 & 0 \\ -1 & 0 & 0 & 0 \end{pmatrix} \tag{1.14}$$

$$\gamma^2 = \begin{pmatrix} 0 & 0 & 0 & -i \\ 0 & 0 & i & 0 \\ 0 & i & 0 & 0 \\ -i & 0 & 0 & 0 \end{pmatrix}; \qquad \gamma^3 = \begin{pmatrix} 0 & 0 & 1 & 0 \\ 0 & 0 & 0 & -1 \\ -1 & 0 & 0 & 0 \\ 0 & 1 & 0 & 0 \end{pmatrix} \tag{1.15}$$

$$\gamma^5 = i\gamma^0\gamma^1\gamma^2\gamma^3 = \begin{pmatrix} 0 & 0 & 1 & 0 \\ 0 & 0 & 0 & 1 \\ 1 & 0 & 0 & 0 \\ 0 & 1 & 0 & 0 \end{pmatrix} \tag{1.16}$$

In addition, one can define the tensor $\sigma^{\mu\nu}$ via

$$\frac{i}{4}\left[\gamma^\mu, \gamma^\nu\right] = \begin{pmatrix} \sigma^{\mu\nu} & 0 \\ 0 & \bar{\sigma}^{\mu\nu} \end{pmatrix}, \tag{1.17}$$

where $[a, b] = ab - ba$ is the commutator of the operators a and b. Using the γ matrices, one can simplify the representation of four-vectors multiplied by those defining the following notation, arriving at the slash notation:

$$\not{p} = \gamma^\mu p_\mu, \tag{1.18}$$

where the Einstein summation convention is applied as described above.

The transverse mass m_T of a dilepton pair $\ell\ell$ and $E_\mathrm{T}^\mathrm{miss}$ is chosen to be the variable of interest for the final event selection in the present thesis. It is defined by

$$m_\mathrm{T} = \sqrt{2 p_\mathrm{T}^{\ell\ell} E_\mathrm{T}^\mathrm{miss} (1 - \cos\Delta\phi_{\ell\ell,\vec{p}_\mathrm{T}^\mathrm{miss}})}. \tag{1.19}$$

For a particle, the helicity is defined as the sign of the spin projection on the particle's momentum axis. One speaks of a right-handed particle if its helicity is positive (the momentum has the same direction as the spin), and one speaks of a left-handed particle in case of a negative helicity.

A collision event is referred to as "event" for simplicity. For simulation of collision events, Monte Carlo (MC) simulation is used if not stated otherwise [31].

The dark matter particle is called the χ particle if not stated otherwise. The corresponding mass is denoted by m_χ. The literature value for the mass of the Z boson is $m_\mathrm{Z} = 91.2$ GeV [32].

CHAPTER 2

Standard Model of Particle Physics

The standard model of physics provides a theoretical framework for the description of particle interactions. The standard model is a quantum field theory and describes three kinds of interactions out of four known today – the electromagnetic, the weak and the strong force. Over a great region of interaction energies up to several TeV, the standard model delivers very precise predictions for various interactions, such as Z boson production, W boson production, top quark pair production at hadron and lepton colliders. Based on a perturbative approach, the interactions between elementary particles are assumed to be a "disturbance" to the freely existing particles. One can then use a perturbative series (expansion) for describing the interaction. In 1948, Richard Feynman proposed an elegant and very suitable way to calculate and present an interaction – the Feynman diagram[1]. One example is given in Fig. 2.1 whereby one has to note that due to the perturbative nature of the approach there is an infinite number of Feynman diagrams for every given process in a quantum field theory. One speaks of leading order (LO), next-to-leading order (NLO), next-to-next-to-leading order (NNLO) and so on diagrams in terms of the expansion order for the process. A diagram not containing any loops of particles is also often called a tree-level diagram. The following sections will give a description of selected aspects of the standard model and also discuss the theoretical concerns which exist about the standard model. The discussions are based on the common literature and lectures [33–36].

2.1 The Particles of the Standard Model

The set of particles which are considered within the standard model is sometimes referred to as the Particle Zoo (cf. Fig. 2.2). The standard model describes all matter interactions in terms of elementary spin 1/2 particles (*fermions*) and integer spin particles (*bosons*). The fermions are divided into three generations of leptons and quarks and interact with each other via an exchange of bosons, whereby Fermions obey the Dirac-Fermi statistics and the bosons obey the Bose-Einstein statistics model. The lepton generations (which are also sometimes referred to as "families") each consist of a negatively charged fermion – the electron e with a mass of $m = 511$ keV, the muon μ with a

[1] Sometimes the diagrams are also called Feynman-Dyson or Stueckelberg diagrams.

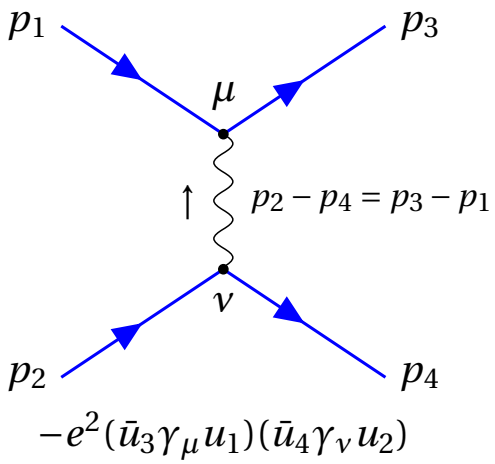

Figure 2.1: Electron-electron scattering described by the Feynman diagrams in leading order. The incoming electrons have the momenta p_1 and p_2 and interact an the vertices μ and ν exchanging a photon propagator. After the interaction, the exiting momenta are p_3 and p_4. At all vertices, the four-dimensional momentum is conserved.

mass of 105 MeV and the τ with the largest mass of $m = 1.78$ GeV. Due to its high mass, the τ is often granted a special interest in modern physics analyses and searches since some models of New Physics suggest an enhanced coupling to the τ or the third generation in general (cf. [38, 39]). Each charged lepton has a neutral partner – there is an electron-, a μ- and a τ-neutrino. Following a similar scheme, there are three generation of quarks. The first generations consists of an up quark with a charge of $2/3$ and a down quark with a charge of $-1/3$. The second generation consists of a charm and a strange quark with the same charges correspondingly, and, finally, there is the third quark generation consisting of a top quark and a bottom quark. The top quark is of particular interest due to the fact that it is the heaviest elementary particle known so far. The quarks with the charge $q = 2/3$ are also sometimes referred to as up-type quarks, the quarks with $q = -1/3$ are referred to as down-type quarks. There is an antiparticle to each fermion in the standard model. The antiparticles possess the same mass as their "ordinary" partners, but all other quantum numbers are inverted. In case of leptons, it is common not to stress the antimatter nature of the considered lepton but refer to its charge instead.

There are three kinds of interactions described by the standard model – the electromagnetic force, the weak force and the strong force – and each of them has at least one boson. The most prominent boson is the photon, which is also sometimes called the γ-particle. The photon is the mediator of the electromagnetic interaction and is massless. The electromagnetic interaction quantum property is the charge – all charged particles can interact with each other exchanging a photon, which is not charged itself. The weak interaction has three boson mediators: $W^\pm$ and the Z whereby $W^\pm$ are each other's antiparticles. The three weak bosons possess rather high masses with $m_Z = 91.2$ GeV and $m_{W^\pm} = 80.4$ GeV which are of a special importance for the standard model as one will see later. The weak interaction quantum property is the weak isospin – all particles carrying a weak isospin couple to the weak bosons. Both, the γ and the Z do not have an antiparticle. Finally, the strong force being responsible for the quark interaction is mediated via gluons. Each quark carries a so-called color

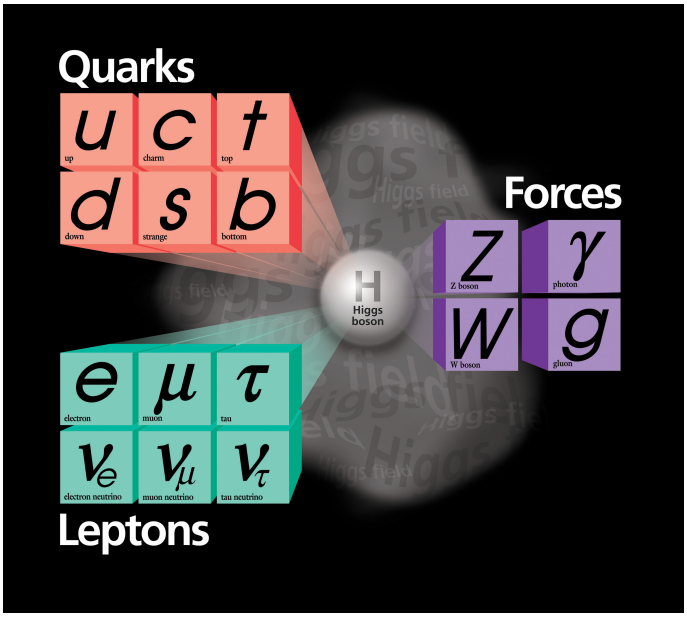

Figure 2.2: The standard model particles. Three generation of leptons and quarks can interact with each other via the bosons which are the carriers of the interaction forces. The Higgs boson is responsible for granting mass to the Z and W bosons, as well as quarks and leptons with the exception of neutrinos [37].

charge – green, red and blue (antigreen, antired and antiblue for antiquarks). The gluons carry both one color and one anticolor – resulting in eight possible independent color-anticolor states. Hence, while one generally speaks of one gluon as the mediator of the strong force, it is technically correct to distinguish eight gluons. All gluons are massless.

The Higgs boson is a particle which subsequently joined the standard model in 1964 in an attempt to explain the mass of the particles in the standard model since it was known from various experiments that the Z and W bosons as well as all quarks and charged leptons posses mass. Only in 2012, the existence of the Higgs boson was confirmed by the experiment. Particles gain mass through the interaction with the associated Higgs field – one can therefore speak of an additional Higgs "force" within the scope of the standard model. The coupling of weak gauge bosons to the Higgs field is referred to as the *Higgs mechanism*. However, in the time between 1964 and the discovery of the Higgs boson in 2012, it was experimentally confirmed that the neutral leptons – the neutrinos – also possess mass which can not be granted via the Higgs mechanism in the standard model (see section 2.5.4). The Higgs boson is also not to be confused with the hypothetical mediator of gravitational force – the graviton – since gravitation is not (yet) included in the standard model. This is considered to be one of the challenges to the standard model and is further discussed in sections 2.5 and 2.5.2.

The structure of the standard model as a theoretical foundation for the electromagnetic, the weak, the strong forces as well as the Higgs mechanism is discussed in the following sections.

2.2 Quantum Electrodynamics

Quantum Electrodynamics (QED) is the part of the standard model which deals with the electromagnetic interaction. In some way, the roots of QED go back to the 19th century, when the experiments with electrical currents showed evidence for the existence of a charged particle – the electron. Maxwell's equations, published in early 1860s, mark an important step in the understanding of the electromagnetic interactions. However, many years passed before in 1909 Milikan and Fletcher performed an experiment in which the elementary charge, the charge of the electron was measured. A quantum field theory which deals with the interactions of single charged elementary particles with each other as a perturbation theory was established in 1920s. Due to the fact that next-to-leading order corrections appear to be divergent, it took several years to develop the proper mathematical tools to deal with those accordingly. Today, it is known that all divergences which arise in the next-to-leading order calculations in QED can be renormalized. The need for such a procedure, however, makes many theorists doubt the perturbative approach of the standard model in general.

Within QED, one can define particles with a mass m and a charge q interacting via massless photons. QED is an abelian gauge theory with the symmetry $U(1)$. A free electron obeys the Dirac equation given by:

$$\left(i\gamma^{\mu}\partial_{\mu} - m\right)\Psi = 0. \tag{2.1}$$

Hereby, the derivative operator ∂_{μ} is defined by:

$$\partial_{\mu} = \left(\frac{\partial}{\partial t}, -\frac{\partial}{\partial x}, -\frac{\partial}{\partial y}, -\frac{\partial}{\partial z}\right) \tag{2.2}$$

The Lagrangian $\mathcal{L}$ of a free electron and a free photon then reads:

$$\mathcal{L} = \bar{\Psi}\left(i\gamma^{\mu}\partial_{\mu} - m\right)\Psi - \frac{1}{4}F_{\mu\nu}F^{\mu\nu}, \tag{2.3}$$

whereby the indices ν, μ run through values $1, \ldots, 4$ and Ψ represents the wave function of the electron. The tensor $F_{\mu\nu}$ is the field strength tensor given by:

$$F^{\mu\nu} = \partial^{\mu}A^{\nu} - \partial^{\nu}A^{\mu} \tag{2.4}$$

$$\tilde{F}^{\mu\nu} = \frac{1}{2}\epsilon^{\mu\nu\alpha\beta}F_{\alpha\beta} \tag{2.5}$$

where $\epsilon^{\mu\nu\alpha\beta}$ is the four-dimensional Levi-Civita symbol and A is a four-dimensional potential representing the photon field which is given by

$$A = A^{\mu} = \left(\phi, \vec{A}\right). \tag{2.6}$$

This notation is particularly elegant when formulating the classical Maxwell equations, which now read:

$$\partial_{\mu}F^{\mu\nu} = 0 \tag{2.7}$$

$$\partial_{\mu}\tilde{F}^{\mu\nu} = J \tag{2.8}$$

with the four-dimensional current $J = (\rho, \vec{j})$. A crucial step for the development of QED (and therefore the standard model) is the postulate of the *local gauge invariance*. So, one argues that the Lagrangian $\mathcal{L}$ must stay invariant under a gauge transformation of the form:

$$\begin{aligned} \Psi \rightarrow \Psi' &= U\Psi \\ \text{where } U &= \mathrm{e}^{i\alpha} \end{aligned} \tag{2.9}$$

with a parameter α at which one has to look closely in the following. It is important to mention that there is no fundamental argument which motivates the necessity of the local gauge invariance of the Lagrangian. The main argument arises from experiments which substantiate such an approach. The absence of a fundamental theoretical justification for the postulate, however, can be considered as a problem of the standard model. Returning to the parameter α, one has now to consider two possibilities. In the first case, α is just a constant parameter and if one applies the transformation U to the wave function, the Lagrangian $\mathcal{L}$ does not change. This case represents the global gauge invariance of the Lagrangian. Considering the second case, the parameter α can depend on spacetime, $\alpha = \alpha(x)$, which has consequences for the Lagrangian. If one applies the transformation U now, an additional term of the form

$$i\gamma^\mu \partial_\mu \left(\mathrm{e}^{i\alpha(x)}\Psi\right) = i\gamma^\mu \partial_\mu \alpha(x) + \ldots \tag{2.10}$$

is obtained. The Lagrangian and the derivative now have to be modified in order to stay invariant under such a transformation. One introduces the following modifications to the differential operator ∂^μ and the four-dimensional potential A_μ by:

$$\partial^\mu \rightarrow \mathrm{D}^\mu = \partial^\mu - i\,q\,A^\mu \tag{2.11}$$

$$A_\mu \rightarrow A'_\mu = A_\mu + \frac{1}{q}\partial_\mu \alpha(x) \tag{2.12}$$

with the charge q. The resulting Lagrangian is now gauge invariant and contains one further contribution

$$\mathcal{L} = \bar{\Psi}\left(i\gamma^\mu \partial_\mu - m\right)\Psi + Q\bar{\Psi}\gamma^\mu \Psi A_\mu - \frac{1}{4}F_{\mu\nu}F^{\mu\nu} \tag{2.13}$$

with the interaction term $Q\bar{\Psi}\gamma^\mu \Psi A_\mu$ representing the coupling of the electron to the photon field. The approach of requiring local gauge invariance is fundamental for the standard model and also justifies the practice to call the interaction carriers *gauge* bosons.

2.3 Quantum Flavordynamics

The theory of Quantum Flavordynamics (QFD) deals with the weak interaction. One representative of the weak interaction is the beta decay which was discovered by Rutherford in the end of the 19th century:

$$\mathrm{n} \rightarrow \mathrm{p}\mathrm{e}^- \bar{\nu}. \tag{2.14}$$

Back in the 1920s, the β-decay was a great challenge for physics, since the neutrino ν was not known. Therefore, the continuous momentum distribution of the electron could not be understood – if one assumes the β-decay to be a two-body process, the momentum of the electron should have a distinct peak at a certain value. As an "emergency" solution, Pauli proposed a new particle, which barely interacts with matter, in his famous letter "Liebe Radioaktive Damen und Herren" – "Dear radioactive ladies and gentlemen". The neutrino was discovered in 1956 by Clyde Cowan and Frederick Reines [40].

Today, we know that at least three kinds of neutrinos exist and that they couple to the weak interaction bosons described in a quantum field theory. QFD is a $SU(2)$ which means that it has three (instead of only one for $U(1)$) gauge bosons. One can go a further step, unifying the weak and the electromagnetic interaction into the electroweak $SU(2) \times U(1)_Y$ theory with four gauge bosons B, W^0, W^1, W^2. Hereby, the index Y denotes the electroweak hypercharge which is defined by $Y = 2(q - T_3)$ via the electromagnetic charge q and the third component of the weak isospin T. All four electroweak gauge bosons are massless and later obtain their mass through the Higgs mechanism.

2.4 Quantum Chromodynamics

The quantum field theory of strong interactions is called Quantum Chromodynamics (QCD). In 1935, H.Yukawa described a scattering interaction of a neutron and a proton via an exchange of a spinless particle. Almost 30 years later, Gell-Mann and Zweig independently introduced the quark – the constituent of hadrons. QCD is described by a $SU(3)$-group and has eight generators which correspond to the strong force carriers – the gluons. Each gluon carries a strong color and a strong anticolor and is massless. The strong coupling (as in fact all couplings) is a function of the momentum exchange q^2. While for the electroweak interaction, the coupling strength increases with q^2, QCD presents with opposite behavior. QCD is the strongest known interaction, which, due to the large coupling constant α_S, results in the non-applicability of a perturbative approach for low interaction energies. This is far-reaching consequences for particle physics experiments performed at colliders, such as the one considered in the present thesis. This behavior of QCD leads to the fact that the soft hadron-hadron interactions which occur during bunch crossings in addition to the hard interaction, which is of interest, can not be described by the common Monte Carlo generators which use a perturbative approach.

2.5 Challenges to the Standard Model

As one could see in the previous sections of this work, the standard model faces difficulties in describing certain aspects of particle interactions which have been observed in various experiments. An overview over those issues is given in the following subsections. As a consequence of this section, models beyond the standard model (BSM) and theoretical considerations about dark matter matter are discussed in chapter 3.

2.5.1 Fine tuning

While the standard model provides impressively accurate descriptions of particle interactions, there are still theoretical concerns about its structure. One particular aspect is the fact that large loop corrections (of the order of magnitude of the Planck Scale $\approx 10^{19}$GeV) to the electroweak scale arise in the standard model. This leads to the necessity of the so called *fine-tuning*, an adaption of the theory parameters to experimental results. Without the fine-tuning, the loop corrections to the self energy of the Higgs boson become huge which is obviously unnatural for a theoretical prediction. While performing the fine-tuning is not categorically considered wrong by the physics community, the argument is made that a theory of interactions shall not be bound to such restrictions and that all parameters of such a theory shall be deducible from a small set of fundamental postulates without any input from experimental data.

2.5.2 Gravity and the hierarchy problem

Some theoretical physicists consider the failure of the standard model to describe gravitational interactions to be the most important reason to look for New Physics [41, 42]. The gravitational force is much weaker than all other interactions (a factor $\approx \mathcal{O}(10^{-36})$ weaker than electromagnetic interaction – a gigantic difference which as well is not yet understood) and therefore the production of the hypothetical gravitation mediator particle, the graviton, would require a collider with a yet unachievable center of mass energy $\mathcal{O}(\sqrt{s}) \approx 10^{19}$ GeV. The fact that there is such a huge difference between the Planck scale and the mass of the Higgs boson, which stays small ($\approx$ 100 GeV) despite large corrections (cf. Sec. 2.5.1), is referred to as the *hierarchy problem*. Theories have been proposed which attempt to explain the weakness of the gravity (cf. Sec. 3.2 and further [43–45]).

A lot of theoretical effort is being put into creating a Great Unified Theory (GUT) which is expected to unify the three interactions of the standard model at high energies [46–48]. Along the GUTs, the attempts to incorporate gravity in the standard model have not been successful so far [49].

2.5.3 The strong CP Problem

It is now established that in order for the universe to consist of regular matter, there has to be a violation of the Charge-Parity (CP) symmetry. Andrej Sakharov was the first to point this out [50]. One introduces a transformation which switches the charge of a particle, turning it into an antiparticle, and produces a mirror image of the spatial system. If an interaction is symmetrical under such a transformation, it means that matter and antimatter are treated equally. If this was the case for all interactions, the universe would not evolve into the universe we observe now – most particles produced in the Big Bang would annihilate with the corresponding antiparticles. Today, it is known that the weak interaction violates the CP symmetry. The experiments performed by Wu (1956) [51] and Goldhaber (1957) [52] showed that only left-handed particles and right-handed antiparticles couple to the weak bosons – showing that the weak interaction separately violates the parity and the charge symmetries. In 1964, Christenson, Cronin, Fitch and Turlay studied the decay of long-living kaons and discovered that approximately 2‰ of the observed weak decays violate the CP symmetry [53].

Based on these considerations, it is expected that the interactions described by QCD also present with a CP violating mixing angle – with the order of magnitude $\mathcal{O}(\theta) \approx 1$ [54]. Contrary to this expectation, experimental results provide limits which imply $\mathcal{O}(\theta) < 10^{-10}$ [55]. The fact that no CP violating strong decays have been observed so far is referred to as the strong CP problem [56].

2.5.4 Neutrino Masses

The existence of the Higgs boson is needed for the theoretical explanation of the gauge boson masses in the standard model. In the standard model, the coupling to the Higgs field can generate the masses of the electroweak bosons, charged leptons and quarks which have been measured very precisely in the past decades [57]. Neutrinos, however, do not couple to the Higgs field and can not obtain their mass via the Higgs field within the Standard Model.

The key to the neutrino mass measurement is the neutrino flavor oscillation which can provide bounds on the square of the mass difference Δm^2 between neutrino generations. Suppose, an experiment produces a beam which consists of ν_α – neutrinos of a flavor α. Assuming two families of neutrinos, for simplicity, one can introduce a mixing angle θ_m between the flavors α and a further neutrino flavor β and the mass eigenstates $\nu_{1,2}$:

$$\begin{pmatrix} \nu_\alpha \\ \nu_\beta \end{pmatrix} = \begin{pmatrix} \cos\theta_m & \sin\theta_m \\ -\sin\theta_m & \cos\theta_m \end{pmatrix} \begin{pmatrix} \nu_1 \\ \nu_2 \end{pmatrix}. \tag{2.15}$$

One shall note that the states $\nu_{1,2}$ are not directly observable due to the fact that neutrinos only couple via the weak force and therefore only the flavor can be accessible to the experiment. Considering the beam of either flavor $\nu_{i=1,2}$ as a plain wave, one can then describe the time evolution at time t by

$$|\nu_i(t)\rangle = |\nu_i(0)\rangle \exp[-i(Et - px)], \tag{2.16}$$

whereby E is the energy, p is the momentum and x is the space coordinate. In the ultra-relativistic limit ($v \approx c \approx 1$), one can then express the flavor state as a function of the distance $x = L$ using Eq. 2.15 by:

$$|\nu_\alpha(L)\rangle = \cos\theta_m |\nu_1(0)\rangle \exp\left[-i\frac{m_1^2 L}{2E}\right] + \sin\theta_m |\nu_2(0)\rangle \exp\left[-i\frac{m_2^2}{2E}\right] \tag{2.17}$$

$$|\nu_\beta(L)\rangle = -\sin\theta_m |\nu_1(0)\rangle \exp\left[-i\frac{m_1^2 L}{2E}\right] + \cos\theta_m |\nu_2(0)\rangle \exp\left[-i\frac{m_2^2}{2E}\right]. \tag{2.18}$$

Using this expression, one can now calculate the probability P for the flavor eigenstate α to be measured as the eigenstate β at a distance L:

$$P(\nu_\alpha \to \nu_\beta) = |\langle \nu_\beta(0)||\nu_\alpha(L)\rangle|^2 \approx \sin^2\left(\frac{\Delta m^2 L}{4E}\right)\sin^2(2\theta_m) \tag{2.19}$$

whereby the Δm^2 is the difference of squared masses of the mass eigenstates of the neutrinos. Hence, observing neutrino oscillations delivers experimental evidence for at least one out of two (two out of three) neutrino flavors not to be massless. Even further, different measurements of neutrino flavor oscillations can be used for setting limits on neutrino masses as performed, for example, in [58, 59].

Within the standard model, a coupling of the neutrino to the Higgs field would result in a mixing of the left-handed and right-handed neutrinos. This introduces a further challenge to the Standard Model – only left-handed neutrinos have been observed so far as only left-handed particles (corresponding to right-handed antiparticles) couple to the weak bosons. If one tries to introduce mass to the neutrinos using the Majorana mass mechanism (this could imply that neutrinoless double beta decays exist, which have not been observed so far), the question remains, why the masses of the neutrinos are so much (about 500.000 times) smaller than the masses of other standard model particles [60].

CHAPTER 3

Physics Beyond the Standard Model and Dark Matter

In the present chapter, selected models beyond the standard model (BSM) will be discussed. The main focus is set on dark matter and unparticle physics, the subject of the present thesis.

3.1 Supersymmetry

The class of supersymmetric BSM theories proposes far-reaching symmetries as a supplement to the standard model. In supersymmetry (SUSY), every SM fermion receives a bosonic partner and each SM boson receives a fermionic partner. This introduction of a new degree of symmetry, which is explicitly broken, seems to complicate things at first sight – however, it relies on the past experience where introduction of new symmetries provided pioneering results (e.g. the local gauge invariance) [61, 62]. The new bosonic partners of SM particles obtain an "s" in front of their names – squarks, sleptons etc., whilst the fermionic supersymmetric partners obtain the ending "ino" – gluino, higgsino. The introduction of supersymmetry can provide a solution the hierarchy problem. The newly introduced particles contribute to the self energy of the Higgs boson with an inverted sign and therefore the large contributions which arise in the standard model are canceled. Supersymmetric theories can provide a dark matter candidate – the so called Lightest Supersymmetric Particle (LSP) [63–65]. Within the scope of supersymmetry, it is often assumed that the so called R-parity is a conserved quantity [66–68]. The R-parity is defined by

$$P_R = (-1)^{(3B+L+2s)}, \tag{3.1}$$

whereby B is the baryon number, L the lepton number and s the spin of the considered particle. All standard model particles have a positive R-parity $P_R = +1$, whereas supersymmetric particles are assumed to have a negative value $P_R = -1$. As a consequence, there has to be a stable supersymmetric particle – the R-parity conservation prevents it from a further decay. This particle is the LSP, a dark matter candidate often studied in theories beyond the standard model which are considered in collider searches [69–71].

Names		spin 0	spin 1/2	$SU(3)_C, SU(2)_L, U(1)_Y$
squarks, quarks	Q	$(\widetilde{u}_L \ \widetilde{d}_L)$	$(u_L \ d_L)$	$(\mathbf{3}, \mathbf{2}, \frac{1}{6})$
(×3 families)	$\overline{u}$	$\widetilde{u}_R^*$	$u_R^\dagger$	$(3, \mathbf{1}, -\frac{2}{3})$
	$\overline{d}$	$\widetilde{d}_R^*$	$d_R^\dagger$	$(3, \mathbf{1}, \frac{1}{3})$
sleptons, leptons	L	$(\widetilde{\nu} \ \widetilde{e}_L)$	$(\nu \ e_L)$	$(\mathbf{1}, \mathbf{2}, -\frac{1}{2})$
(×3 families)	$\overline{e}$	$\widetilde{e}_R^*$	$e_R^\dagger$	$(\mathbf{1}, \mathbf{1}, 1)$
Higgs, higgsinos	H_u	$(H_u^+ \ H_u^0)$	$(\widetilde{H}_u^+ \ \widetilde{H}_u^0)$	$(\mathbf{1}, \mathbf{2}, +\frac{1}{2})$
	H_d	$(H_d^0 \ H_d^-)$	$(\widetilde{H}_d^0 \ \widetilde{H}_d^-)$	$(\mathbf{1}, \mathbf{2}, -\frac{1}{2})$

Table 3.1: Squarks, sleptons and higgsinos in the Minimal supersymmetric standard model. The spin-0 fields are complex scalars, and the spin-1/2 fields are left-handed two-component Weyl fermions [61].

Names	spin 1/2	spin 1	$SU(3)_C, SU(2)_L, U(1)_Y$
gluino, gluon	$\widetilde{g}$	g	$(\mathbf{8}, \mathbf{1}, 0)$
winos, W bosons	$\widetilde{W}^\pm \ \widetilde{W}^0$	$W^\pm \ W^0$	$(\mathbf{1}, \mathbf{3}, 0)$
bino, B boson	$\widetilde{B}^0$	B^0	$(\mathbf{1}, \mathbf{1}, 0)$

Table 3.2: Gluino, winos and bino in the Minimal Supersymmetric standard model [61].

One further possible consequence of supersymmetry is gauge coupling unification. This approach aims to unify the electroweak and the QCD interaction into one at a certain high energy scale and is therefore of great interest for particle theory [72, 73]. An overview of the particles in a minimal supersymmetric standard model is given in Tab. 3.1 and Tab. 3.2. As of today, no evidence for supersymmetric particles has been observed [74–76].

3.1.1 Searches for Supersymmetry

In the minimal supersymmetric standard model (MSSM), an approach is made to introduce the minimal number of supersymmetric partners. Once one also assumes the R-parity to be conserved, the MSSM models provide a dark matter candidate while simultaneously solving further challenges of the standard model (cf. Sec. 3.1 and cf. Fig. 3.7). In this approach, the lightest neutralino serves as the LSP which is produced in along further detectable particles – e.g. in this case a chargino could serve as a mediator particle [77]. The corresponding production diagram is shown in Fig. 3.1.

Many searches for supersymmetric particles are performed today – as a results, the LSP is one of the most studied dark matter candidates. An overview over searches for Supersymmetry with dark matter interpretation is given in [78]. This study reviews the status of the supersymmetric dark matter searches, proposing several regions in the plane of the nucleon scattering cross section σ_p vs. the dark matter mass m_χ which are favored by the MSSM scenario (cf. Fig. 3.2). Further recent searches and data reinterpretations of CMS and ATLAS are discussed in [79, 80]. It should be noted that various non-collider dark matter detection experiments (cf. Sec. 3.4.5) perform searches for dark matter particles in terms of supersymmetric theories.

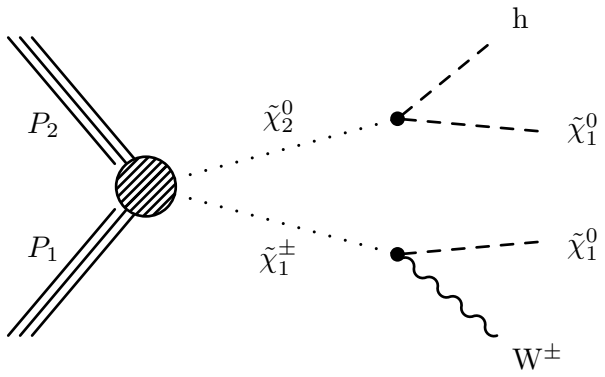

Figure 3.1: Event diagram for the production of the LSP in a MSSM scenario at the LHC. The pair of colliding protons produces a chargino $\tilde{\chi}_1^\pm$ and a neutralino $\tilde{\chi}_2^0$ which both decay into a detectable particle (the Higgs boson and the W boson) and the lightest neutralino, the LSP [77].

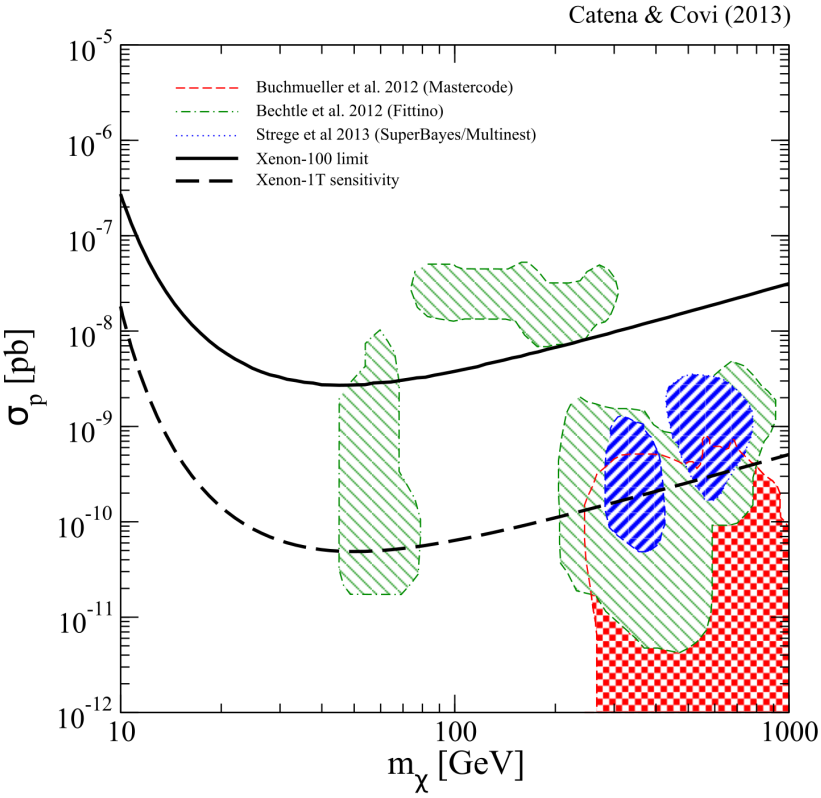

Figure 3.2: Regions in the plane of the dark matter mass m_χ vs. the spin-independent dark matter nucleon scattering cross section σ_p which are found to be favored by independent global fits of the MSSM to variety of observations including LHC, cosmological limits, low energy observables and dark matter searches. The favored regions of the phase space are shown in hatched colors. Exclusion limits by the Xenon experiment as well as the estimated sensitivity of Xenon-1T experiment after one year data taking are shown for comparison [78].

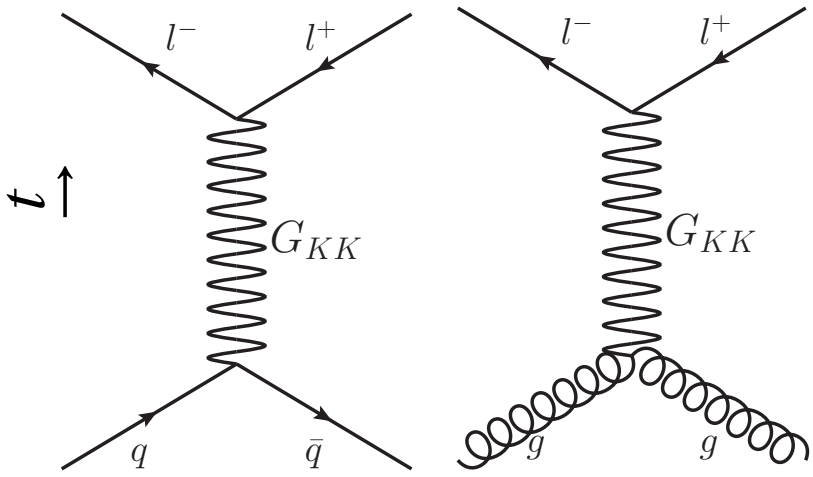

Figure 3.3: Virtual exchange of a Kaluza-Klein graviton G_{KK} at the LHC in the ADD theory with the subsequent decay into a lepton pair.

3.2 Large Extra Dimensions in the ADD approach

As stated earlier, the fact that the gravitational interaction is very much weaker than other interactions, is not yet well understood. There are theories beyond the standard model which propose explanations for such a behavior of gravity. One of them is the elegant ADD theory proposed by Arkani-Hamed, Dvali and Dimopoulos [81], which is also studied at the III. Physikalisches Institut A in Aachen, having an experimental signature similar to the one considered in the present work [82–85]. In this approach, gravity has the capability of reaching into large extra dimensions which explains the weakness of this interaction. The coupling of a hypothetical Kaluza-Klein (KK) graviton to the Standard model energy-momentum tensor leads to an enhanced non-resonant production of lepton pairs (cf. Fig. 3.3). The KK graviton was proposed by Kaluza and Klein in the 1920s in an approach unifying the electromagnetism and gravity in a five-dimensional theory [86–88]. As a results of the coupling of the KK graviton to the standard model within the ADD theory, one expects an excess of events in the invariant mass distribution of lepton pairs at CMS. Unfortunately, no experimental evidence for the validity of the ADD theory has been found so far [83, 89–91].

3.3 Unparticles

The idea of unparticles was first proposed by Howard Georgi and subsequently studied by further authors [92–95]. The main hypothesis is the existence of a scale-invariant field in a hidden sector at high energies – an idea which is favored in many BSM scenarios [96–98]. In this sector, the scale-invariant field – called the Banks-Zaks field ($\mathcal{BZ}$) – can interact with the standard model particles via the exchange of a heavy particle with the mass $M_{\mathcal{U}}$. Below the mass scale of $M_{\mathcal{U}}$, the interaction is suppressed by its powers and the interaction Lagrangian density $\mathcal{L}_{\text{int}}$ reads [92]

$$\mathcal{L}_{\text{int}} = \frac{\mathcal{O}_{\text{SM}}\mathcal{O}_{\mathcal{BZ}}}{M_{\mathcal{U}}^k}, \tag{3.2}$$

whereby $\mathcal{O}_{\mathrm{SM}}$ is the standard model operator, $\mathcal{O}_{\mathcal{BZ}}$ is the $\mathcal{BZ}$ field operator with a scaling dimension $d_{\mathcal{BZ}}$ and k is a parameter with $k = d_{\mathrm{SM}} - d_{\mathcal{BZ}} - 4 > 0$. At the energy scale $\Lambda_{\mathcal{U}}$, the renormalization coupling generates dimensional transmutation which leads to the effective interaction Lagrangian given by

$$\mathcal{L}_{\mathrm{int}}^{\mathrm{eff}} = C_{\mathcal{U}} \frac{\Lambda_{\mathcal{U}}^{d_{\mathcal{BZ}}-d_{\mathcal{U}}}}{M_{\mathcal{U}}^{k}} \mathcal{O}_{\mathrm{SM}} \mathcal{O}_{\mathcal{U}} = \frac{\lambda}{\Lambda_{\mathcal{U}}^{d_{\mathcal{U}}}} \mathcal{O}_{\mathrm{SM}} \mathcal{O}_{\mathcal{U}}. \tag{3.3}$$

In this equation, $C_{\mathcal{U}}$ denotes the normalization factor which is fixed by the matching, $d_{\mathcal{U}}$ is the scaling dimension of the unparticle operator $\mathcal{O}_{\mathcal{U}}$ and λ represents the coupling strength between unparticles and the standard model particles. It should be stressed that there is no formal requirement for $d_{\mathcal{U}}$ to be an integer parameter. Therefore, hereinafter $d_{\mathcal{U}}$ is assumed to be a non-integer parameter denoting the scale dimension of the unparticle. Since an unparticle is a part of the scaling-invariant field, it can not have a fixed mass, as is shown in the next subsection. It should be noted that in his original letter, Georgi only speaks about unparticle "stuff" which is the more precise description of his proposal for various reasons. However, the name "unparticle", as opposed to the usually used particle, is now well established in the physics community. Several searches for unparticles have been performed at the III. Physikalisches Institut A in Aachen [99–101]. Previously performed searches include reinterpretations of the data collected by the LEP collider in [102] and the Tevatron in [103].

3.3.1 Unparticle Mass

The scale invariance of the unparticles has very curious consequences. If one considers a dilatation generator D, which performs a scale transformation, and looks at its commutation relations with the spacetime translation generators P_μ, one finds [95]:

$$[D, P_\mu] = -iP_\mu\,. \tag{3.4}$$

From this, one can follow for a scale transformation employing a real parameter s

$$\exp(+isD)P^2\exp(-isD) = \exp(2s)P^2\,. \tag{3.5}$$

The translation generator P_μ is essentially the momentum four-vector and therefore its square is the square mass of the corresponding particle. The above equation shows that there can be no scale invariant unparticle with a definite mass – the mass is not invariant under a scale transformation since an additional factor $\exp(2s) \neq 1$ appears after a scale transformation. The unparticle would have a *continuous* mass spectrum.

3.3.2 Phase space

One can consider the two-point function for the scalar unparticle operator $O_{\mathcal{U}}$ [95]:

$$\begin{aligned}
\langle 0|O_{\mathcal{U}}(x)O_{\mathcal{U}}^{\dagger}(0)|0\rangle &= \langle 0|e^{i\hat{P}\cdot x}O_{\mathcal{U}}(0)e^{-i\hat{P}\cdot x}O_{\mathcal{U}}^{\dagger}(0)|0\rangle \\
&= \int d\lambda \int d\lambda' \langle 0|O_{\mathcal{U}}(0)|\lambda'\rangle\langle\lambda'|e^{-i\hat{P}\cdot x}|\lambda\rangle\langle\lambda|O_{\mathcal{U}}^{\dagger}(0)|0\rangle \\
&= \int \frac{d^4P}{(2\pi)^4}\, e^{-iP\cdot x}\,\rho_{\mathcal{U}}(P^2)\,,
\end{aligned} \tag{3.6}$$

where P^2 equals the square of the invariant mass of the unparticle, the spectral density $\rho_{\mathcal{U}}(P^2)$ is given by

$$\rho_{\mathcal{U}}(P^2) \quad = \quad A_{d_{\mathcal{U}}}\, \theta(P^0)\, \theta(P^2)\, (P^2)^{\alpha}\,. \tag{3.7}$$

Hereby, the Heaviside function Θ ensures that the energy and the unparticle mass are positive. The parameter α is derived from the scale invariance requirement and $A_{d_{\mathcal{U}}}$ is a normalization factor. One can now perform a scale transformation by putting $x \to sx$ and $O_{\mathcal{U}}(sx) \to s^{-d_{\mathcal{U}}} O_{\mathcal{U}}(x)$. It can be shown that requiring scale invariance leads to $\alpha = d_{\mathcal{U}} - 2$ [95]. Now, the Eq. 3.7 becomes

$$\rho_{\mathcal{U}}(P^2) = A_{d_{\mathcal{U}}}\, \theta(P^0)\, \theta(P^2)\, (P^2)^{d_{\mathcal{U}}-2} \geq 0\,. \tag{3.8}$$

For the determination of $A_{d_{\mathcal{U}}}$, one recalls the phase space for n massless particles with momenta $(p_1 + p_2 + p_3 + \cdots + p_n)^2 = s^2$ and $p_1^2 = p_2^2 = \cdots = p_n^2 = 0$. In this case, A_n is given by

$$A_n = \frac{16\pi^2\sqrt{\pi}}{(2\pi)^n} \cdot \frac{\Gamma\left(n+\frac{1}{2}\right)}{\Gamma\,(n-1)\,\Gamma(2n)}. \tag{3.9}$$

Now, one can identify the spectral density of unparticles with the phase space of $d_{\mathcal{U}}$-body massless particle. The above equation for the normalization factor $A_{\mathcal{U}}$ finally becomes

$$A_{d_{\mathcal{U}}} = \frac{16\pi^{5/2}}{(2\pi)^{2d_{\mathcal{U}}}} \cdot \frac{\Gamma\left(d_{\mathcal{U}}+\frac{1}{2}\right)}{\Gamma(d_{\mathcal{U}}-1)\,\Gamma(2d_{\mathcal{U}})}. \tag{3.10}$$

From this equation and the argumentation above, it is visible that the unparticle would appear as $d_{\mathcal{U}}$ number of massless particles – the integer parameter n normally denoting the number of particles has now transformed to $d_{\mathcal{U}}$. Since $d_{\mathcal{U}}$ is a continuous parameter, as stated above, and is not necessarily bound to integer values, unparticles would appear as fractional particles. One can reverse this argument – the massive particles known so far are not invariant under a scale transformation – independent of their momentum they always keep their fixed mass. Therefore, these particles of the standard model can only appear in integer numbers. The requirement of the scale invariance leads to the disappearance of this argument. In a scale invariant theory, the quantity known to us as the number of particles becomes a non-integer parameter leading to a more general definition of particles – this is what Georgi refers to as unparticle *stuff* in his original paper. As shown above, it is indeed a better designation since "stuff" is commonly not assumed to be countable. Once again, is becomes obvious that unparticles – the unparticle stuff – are something completely different to anything known in physics today. A hint to the existence of unparticles observed at the LHC would therefore mean a discovery of a yet unapprehended underlying theory of interactions with new symmetries which behave counterintuitively to the today's understanding of particle physics.

3.3.3 Unparticle propagator

The unparticle propagator can be derived from the formal approach used in Eq.7.6 of [36], which is called the Källén-Lehmann spectral representation

$$\Delta_F(P^2) \quad = \quad \frac{1}{2\pi} \int_0^{\infty} \frac{R(M^2)\mathrm{d}M^2}{P^2 - M^2 + i\epsilon}. \tag{3.11}$$

Hereby, the density $R(M^2) = A_{d_\mathcal{U}}(M^2)^{d_\mathcal{U}-2}$ is the spectral density defined in Eq. 3.7 and ensures the normalization, P^2 is the square of the unparticles momentum and the integration is performed over the mass square M^2. The function $\Delta_F(P^2)$ has to be scale invariant. The form $\Delta_F(P^2) = Z_{d_\mathcal{U}}(-P^2)^{d_\mathcal{U}-2}$ ensures the scale invariance, whereby the factor $Z_{d_\mathcal{U}}$ is to be determined later on. In order to ensure that propagator is real, the choice of $(-P^2)^{d_\mathcal{U}-2}$ is made [95]:

$$(-P^2)^{d_\mathcal{U}-2} = \begin{cases} |P^2|^{d_\mathcal{U}-2} & \text{if } P^2 \text{ is negative and real,} \\ |P^2|^{d_\mathcal{U}-2} e^{-i d_\mathcal{U} \pi} & \text{if } P^2 \text{ is positive with an infinitesimal } i0^+. \end{cases} \tag{3.12}$$

One can now rewrite equation 3.11 in a scale invariant form

$$\Delta_F(P^2) = Z_{d_\mathcal{U}}(-P^2_\mathcal{U})^{d_\mathcal{U}-2} \tag{3.13}$$

and use the imaginary part of the equation in order to determine the normalization parameter $Z_{d_\mathcal{U}}$ assuming that $P^2 > 0$ [95]:

$$\mathcal{I}\mathrm{m}\Delta_F(P^2) = -Z_{d_\mathcal{U}} \sin(d_\mathcal{U}\pi)(P^2)^{d_\mathcal{U}-2} = -\frac{1}{2} A_{d_\mathcal{U}}(P^2)^{d_\mathcal{U}-2}. \tag{3.14}$$

From this, one deduces the unparticle propagator to be

$$\Delta_F(P^2) = \frac{A_{d_\mathcal{U}}}{2\sin(d_\mathcal{U}\pi)}(-P^2)^{d_\mathcal{U}-2}\,. \tag{3.15}$$

For an s-channel process, $(-P^2)$ is negative and the propagator obtains a complex phase. This leads to interference effects between the unparticle and the standard model particles. It is easy to see that

$$\lim_{d_\mathcal{U}\to 1^+} \Delta_F(P^2) = \frac{1}{P^2}, \tag{3.16}$$

which is the photon propagator in the standard model. In the Drell-Yan process, the unparticle propagator interferes with the photon and both the real and imaginary parts of the propagator of the Z boson. Thus, the presence of unparticles can be tested when studying the decays of the Z boson similar to [82, 83, 89], where one looks for a non-resonant excess of events in the invariant mass $m^{\ell\ell}_{\text{inv}}$ distribution of lepton pairs. The $m^{\ell\ell}_{\text{inv}}$ distribution for different unparticle scenarios as expected at the Tevatron collider is shown in Fig. 3.4. It is important to note that virtual unparticle production has a negligible impact around the Z mass peak, as visible in the figure. As discussed in Sec. 7.3, the lepton pairs considered in the present thesis are required to be compatible with a real Z boson decay and the agreement between standard model prediction and the measurement around the Z boson mass peak can be used as a check for the accuracy of the performed lepton pair selection. Due to many technical similarities between the ADD theory and unparticles (cf. [104, 105]), the implementation of the virtual exchange of an ADD graviton and an unparticle in a physics generator is shared between ADD and unparticles.

3.3.4 Unparticle spin

Several spin scenarios for the unparticle are allowed in the theory. Depending on the spin choice (scalar, vector or tensor), a bound on $d_\mathcal{U}$ can be deduced from unitarity conditions [106]. It has been shown in [95, 107] that the virtual unparticle propagator diverges in case $d_\mathcal{U} \to 2$ (this has

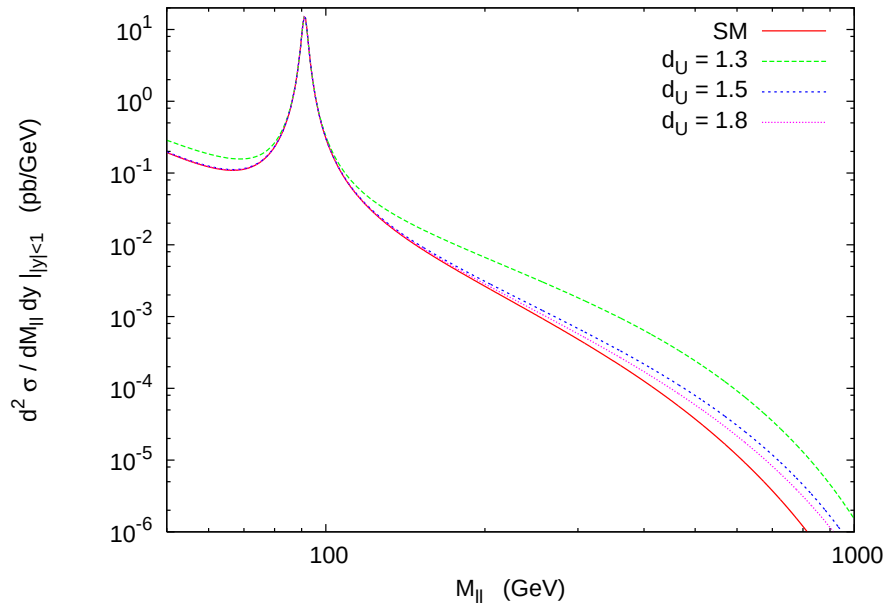

Figure 3.4: Simulated distribution of the invariant mass of a lepton pairs produced in $p\bar{p}$ collisions at the Tevatron collider ($\sqrt{s} = 1.96$ TeV) with possible scenarios of virtual unparticle production. The standard model contribution (Drell-Yan process) is shown in red. Scenarios of enhancement through the virtual unparticle exchange with $d_{\mathcal{U}} = 1.3; 1.5; 1.8$ are shown for comparison. It is visible that a non-resonant excess of events in the tail of the distribution (high values of $m_{\text{inv}}^{\ell\ell}$) can be interpreted as a hint for the existence of unparticles [95].

been also studied in [108]). Even though for the real emission of unparticles finite values are obtained even for $d_{\mathcal{U}} > 2$, it is pointed out that the interpretation of processes with $d_{\mathcal{U}} > 2$ is to be performed carefully [105]. Therefore, only values $1.01 < d_{\mathcal{U}} < 2.2$ are considered in the present thesis, whereby $d_{\mathcal{U}} = 2.2$ is the only considered value which lies over this threshold. For $\Lambda_{\mathcal{U}} = 1$ TeV, the largest parameter space is available for scalar unparticles (spin 0), reaching cross sections of up to $\sigma = 96.9$ pb. For spin 1/2, this cross section drops drastically to 1.8 pb. If one is to consider higher spins 1 or 2, the corresponding cross sections are too tiny to be detectable in collisions of today's colliders – below 10^{-4} pb. Therefore, the spin 0 scalar unparticle is chosen for the analysis in the present thesis.

3.3.5 Unparticle Interactions

Using the equation 3.3, one can now deduce the interactions of the unparticle field $O_{\mathcal{U}}$ with the particles of the standard model. As stated above, three kinds of unparticle operators are possible – scalar, vector and tensor operators which are denoted by $O_{\mathcal{U}}, O^{\mu}_{\mathcal{U}}$ and $O^{\mu\nu}_{\mathcal{U}}$ correspondingly. The following vertices for couplings of a scalar unparticle to fermions exist

$$\lambda \frac{1}{\Lambda_{\mathcal{U}}^{d_{\mathcal{U}}-1}} \bar{f} f O_{\mathcal{U}}, \qquad \lambda \frac{1}{\Lambda_{\mathcal{U}}^{d_{\mathcal{U}}-1}} \bar{f} i\gamma^5 f O_{\mathcal{U}}, \qquad \lambda \frac{1}{\Lambda_{\mathcal{U}}^{d_{\mathcal{U}}-1}} \bar{f} \gamma^{\mu} f (\partial_{\mu} O_{\mathcal{U}}). \tag{3.17}$$

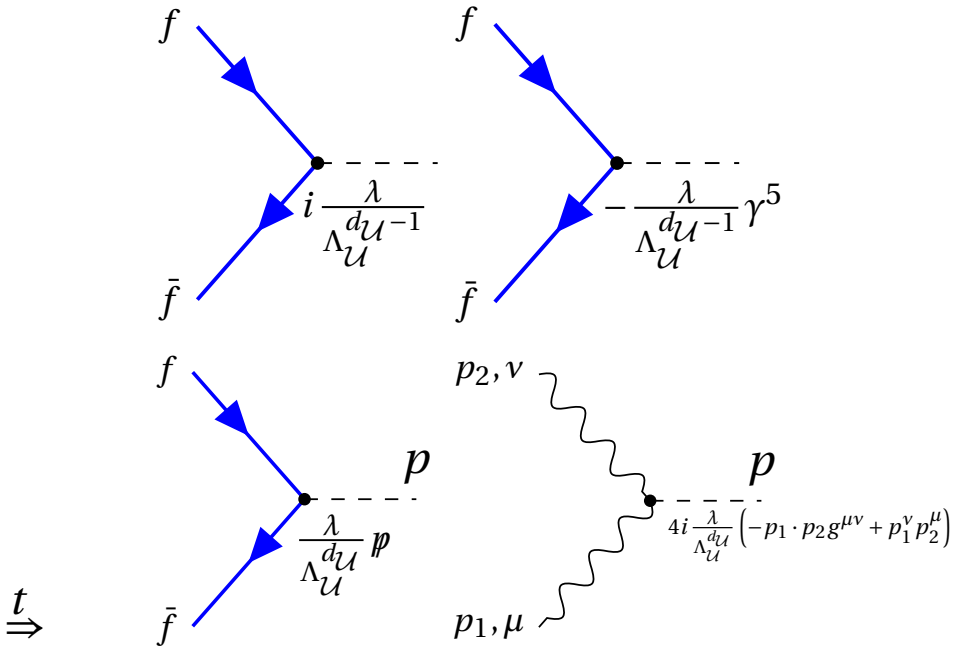

Figure 3.5: Vertices for the interactions of a scalar unparticle with the SM particles. The unparticle is indicated by a dashed line. A pair of fermions, a quark and an anti-quark for instance, couple to an unparticle (real emission) in the top diagrams and the bottom left diagram – this scenario is also considered in the present thesis. A gauge boson emits an unparticle in the scenario shown in the bottom right diagram.

These interaction vertices correspond to the top diagrams and the bottom left diagram shown in Fig. 3.5. The coupling of a scalar unparticle to a gauge field has the following form

$$\frac{\lambda}{\Lambda_{\mathcal{U}}^{d_{\mathcal{U}}-1}} G_{\alpha\beta} G^{\alpha\beta} O_{\mathcal{U}}, \tag{3.18}$$

with a general gauge field $G_{\alpha\beta}$ (cf. bottom right hand side of Fig. 3.5). It has to be stressed that the coupling strength λ can be different for each interaction. Here, the value of λ in each interaction scenario is assumed to be equal for simplicity.

The final state considered in the present thesis consists of an unparticle which couples to a pair of quarks, whereby the latter produce a Z boson. The Z boson is assumed to decay in either a pair of electrons or muons.

3.3.6 Matrix Element

The differential cross section for the production of an unparticle along a Z boson in a fermion-antifermion interaction ($f\bar{f} \to Z + \mathcal{U}$) at the LHC is given by [104]:

$$\frac{\mathrm{d}^2\sigma}{\mathrm{d}P_{\mathcal{U}}^2 \mathrm{d}t} = \frac{|\bar{M}|^2}{16\pi\hat{s}^2} \frac{A_{d_{\mathcal{U}}}}{2\pi\Lambda_{\mathcal{U}}^2} \left(\frac{dP_{\mathcal{U}}^2}{\Lambda_{\mathcal{U}}^2}\right)^{d_{\mathcal{U}}-2}, \tag{3.19}$$

whereby $|\bar{M}|$ denotes the matrix element which is averaged over the color and spin, $P^2_{\mathcal{U}}$ is the invariant mass of the unparticle. The matrix element $|\bar{M}|$ is given by [105]:

$$|\bar{M}|^2 = \frac{1}{N_{\mathrm{C}}}\left(\frac{1}{\sin^2\Theta_W \cos^2\Theta_W}\right)\cdot(g^2_{\mathrm{L,q}} + g^2_{\mathrm{R,q}})|A|^2, \tag{3.20}$$

where the $g^2_{\mathrm{L,q}}$ and $g^2_{\mathrm{R,q}}$ are electroweak couplings and N_C is the color factor. $|A|^2$ contains the kinematics:

$$|A|^2 = 4\left[-\frac{s}{t} - \left(1-\frac{m_Z^2}{t}\right)\left(1-\frac{P^2_{\mathcal{U}}}{t}\right) - \frac{s}{u} - \left(1-\frac{m_Z^2}{u}\right)\left(1-\frac{P^2_{\mathcal{U}}}{u}\right) + 2\left(1-\frac{P^2_{\mathcal{U}}}{t}\right)\left(1-\frac{P^2_{\mathcal{U}}}{u}\right)\right]. \tag{3.21}$$

Note that the boundaries $0 \leq P^2_{\mathcal{U}} < (\sqrt{s} - m_Z)^2$ exist for the unparticle. Given the very high energy available at the LHC $\mathcal{O}(\sqrt{\hat{s}}) \approx$ TeV, a large spectrum of possible unparticle signatures (corresponding to values of $d_{\mathcal{U}}$) can be studied.

3.4 Dark Matter

As briefly discussed in the introduction of the present thesis, the evidence for the existence of dark matter is based on astronomic measurements. The only definite property of dark matter is its capability to interact via the gravitational force. As of today, only the neutrino is a candidate for (hot – relativistic) dark matter within the standard model. However, measurements suggest that only $\approx 0.5\%$ of dark matter can be hot [109]. Many theories studying the nature of dark matter along a corresponding dark matter particle candidate have been proposed. The approach typically employs cosmological arguments considering the production mechanism of dark matter shortly after the Big Bang. Subsequently, the interaction properties of the dark matter candidates propagated in time to today in order to be comparable with today's observations. A selection of theories will be briefly discussed in the following.

3.4.1 Axions

Axions are hypothetical particles which were postulated in 1977 by Roberto Daniele Peccei and Helen Quinn in order to explain the fact that strong interactions do not break the CP-symmetry whereas weak interactions do (cf. 2.5.3) [110]. The CP violating strong mixing angle θ which is found to be small by observations is "protected" by the so called Peccei-Quinn symmetry in this approach. This is a $U(1)$ symmetry and the axion is the corresponding Goldstone boson. The Peccei-Quinn symmetry is broken by non-trivial QCD interactions which lend the axion its (small) mass. It is assumed that cold (nonrelativistic) axion have their origin in the vacuum realignment and string and wall decay [111]. There are several scenarios of how the Peccei-Quinn mechanism might have served in the early stages of the universe – those scenarios depend on various assumptions about the Big Bang. As of today, the axions are considered to be a valid dark matter candidate [111–113]. The discovery of axions could kill two birds with one stone – one could elegantly explain the absence of CP violation in strong interactions and also the solve the dark matter problem.

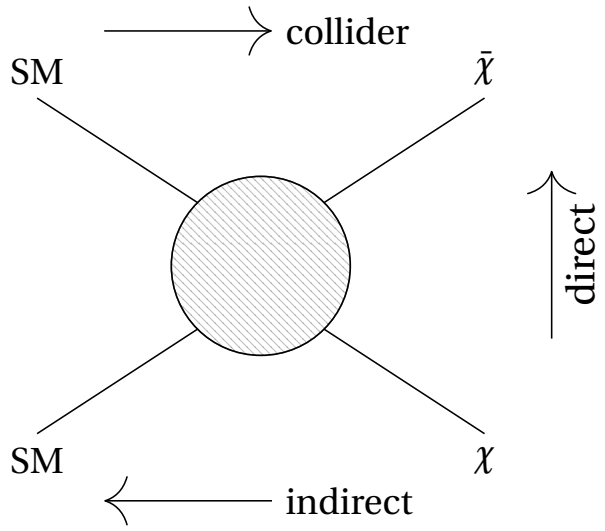

Figure 3.6: Three possible ways of detecting dark matter. Interaction of two standard model (SM) particles producing two dark matter particles is used in collider searches, whereby an additional standard model particle is needed (via initial or final state radiation) for observing (tagging) the interaction. Indirect detection relies on the annihilation of two dark matter particles producing two standard model particles which can be observed. Direct detection relies on the interaction of a dark matter particle with a standard model particle leading to a standard model particle which can be observed and a dark matter particle which escapes undetected.

3.4.2 Weakly interacting particles

One of the most prominent candidates for dark matter is the so called weakly interacting massive particle (WIMP). The WIMP is assumed to be massive and have a cross section comparable to the weak interaction [32]. There is one strong cosmological argument to support the WIMP hypothesis. Shortly after the Big Bang, the temperature and therewith the average interaction energy of particles were decreasing. As the average interaction energy fell below a certain threshold which depends on the mass of the particle and its annihilation cross section, the production and interactions of the corresponding particles stopped, leaving the particles produced until this moment free in the space. This is referred to as freeze-out [114]. If one assumes that the dark matter consists of light WIMPs ($\mathcal{O}(m_\chi) \approx$ 1–1 TeV), the corresponding freeze-out density is consistent with the modern observations of the dark matter relic density [32].

3.4.3 Neutrinos

The neutrino which is known to have mass observed in the neutrino mixing (cf. 2.5.4) was considered to be a valid dark matter candidate in the past. There are, however, indications that hot dark (ultrarelativistic) matter can not account for the total yield of observed dark matter [115, 116]. Therefore, ultrarelativistic neutrinos can not serve as the only dark matter candidate – they remain a valid candidate as long as they are accompanied by a further dark matter particle.

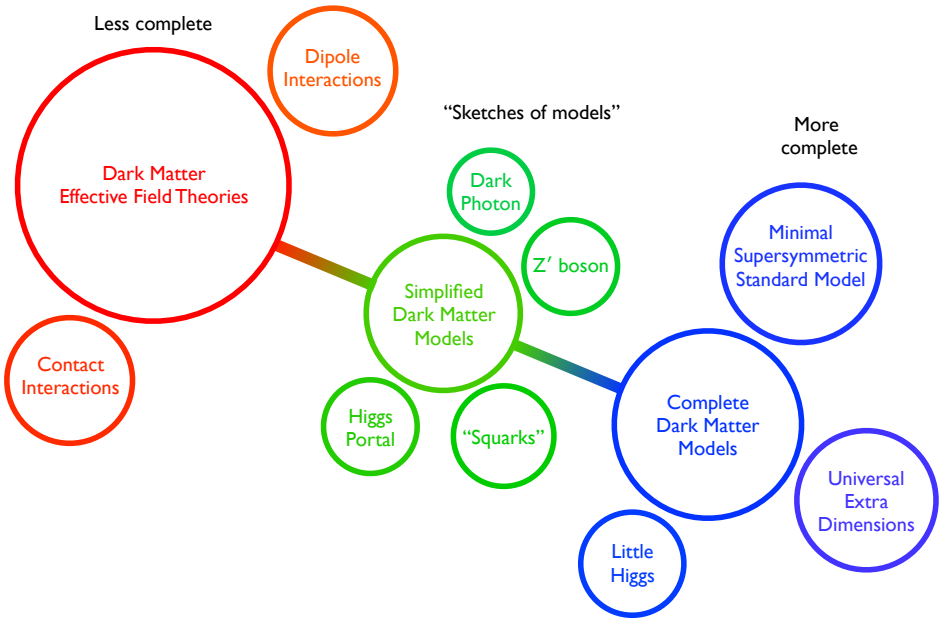

Figure 3.7: An artistic view of dark matter theories studied at particle colliders. The effective field theories (left) aim to explain the experimental effects of dark matter, whereas simplified models (middle) provide a more robust construct for the implementation of dark matter into theory. Theories like minimal supersymmetric SM (right) provide the most sophisticated explanation for dark matter from the theoretical point of view embedding it into a larger theory construction [117].

3.4.4 Collider searches for dark matter

There are three ways to create or observe interactions of dark matter with standard model particles – direct, indirect and collider, which are shown in Fig. 3.6. While this and the following subsections concentrate on the collider signature, subsection 3.4.5 briefly summarizes the non-collider searches for dark matter.

Several theories beyond the standard model naturally propose a dark matter candidate which would be visible at colliders (cf. Fig.3.7 and Sec. 3.1). The challenge of the LSP approach which was discussed above from the experimental point of view is that many assumptions about the supersymmetric parameters have to be made. Hence, one is interested in a pragmatic way of introducing dark matter into the standard model. In the following, two approaches are presented – the effective field theory (EFT) approach and the simplified model approach.

3.4.4.1 Effective field theory of dark matter

An effective field theory is an approximation which is performed when the underlying theory of the studied interaction is not known [118]. One introduces an interaction vertex at which a heavy mediator is exchanged. This vertex is characterized by the parameter Λ that parametrizes the effective cutoff scale. The effective theory is an approximation performing an operator product expansion in terms of $1/\Lambda$ providing a low energy approximation for the interaction at energies below Λ. For dark matter production considered in the present thesis, one assumes that a pair of dark

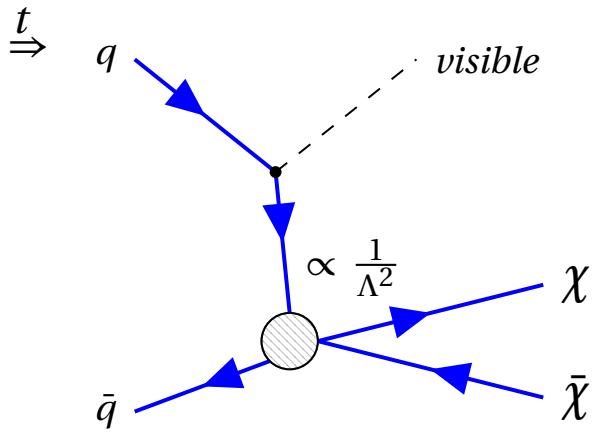

Figure 3.8: Collider production of dark matter in an effective field theory. The approximated vertex is indicated by a hatched circle. In this approach, dark matter particles χ and $\bar{\chi}$ couple to a pair of quarks exchanging a heavy mediator in the approximated vertex along the production of a visible particle (e.g. Z boson). Two parameters are of interest – the mass of the dark matter particle m_χ along the coupling strength of dark matter to quarks which is parametrized in terms of the cutoff scale Λ.

matter WIMPs χ and $\bar{\chi}$ can be produced along a Z boson as shown in Fig. 3.8 in such an effective field theory vertex. Within the scope of this thesis, the Z boson is assumed to decay in either a pair of electrons or muons. This approach was proposed in [119]. Similar approaches are also discussed in [120–122].

Generally, one can think of many different ways dark matter could couple to standard model particles in terms of an effective field theory. One of the easiest ways is to propose an interaction vertex via a scalar (S) coupling

$$\mathcal{L}_{\text{int}} = \frac{1}{\Lambda^2}\chi\bar{\chi}f\bar{f} \tag{3.22}$$

whereby f and $\bar{f}$ represent a standard model fermion and antifermion. Further coupling types one may propose are pseudoscalar (P), vector (V), axial-vector (AV), or tensor (T) which are represented by

$$\text{(P)} \qquad \mathcal{L}_{\text{int}} = \frac{1}{\Lambda^2}\chi\gamma^5\bar{\chi}f\gamma_5\bar{f} \tag{3.23}$$

$$\text{(V)} \qquad \mathcal{L}_{\text{int}} = \frac{1}{\Lambda^2}\chi\gamma^\mu\bar{\chi}f\gamma_\mu\bar{f} \tag{3.24}$$

$$\text{(AV)} \qquad \mathcal{L}_{\text{int}} = \frac{1}{\Lambda^2}\chi\gamma^5\gamma^\mu\bar{\chi}f\gamma_5\gamma_\mu\bar{f} \tag{3.25}$$

$$\text{(T)} \qquad \mathcal{L}_{\text{int}} = \frac{1}{\Lambda^2}\chi\sigma^{\mu\nu}\bar{\chi}f\sigma_{\mu\nu}\bar{f}. \tag{3.26}$$

Historically, the hypothetical interaction of dark matter with the standard model particles is sorted into two categories – spin-dependent and spin-independent. Furthermore, different operator names such as for example D5 or D9 are used in different publications [29, 119].

One considerable advantage of the effective field theory of dark matter approach is its simplicity. The cutoff scale Λ along the mass m_χ of the proposed dark matter particle are the only two free

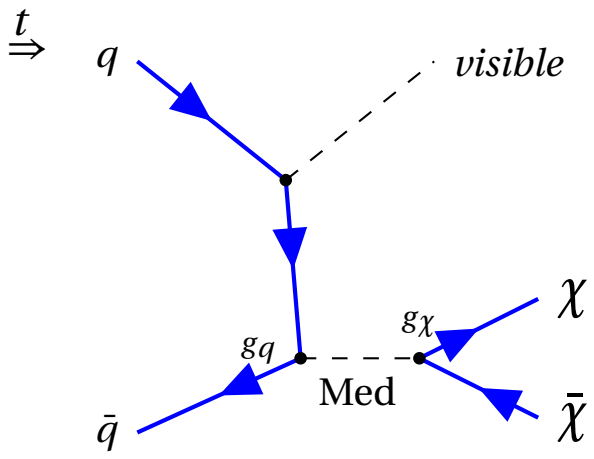

Figure 3.9: Collider production of dark matter in terms of a simplified model approach. Here, a pair quarks produces a particle which is detectable (marked by "visible" in the figure, e.g. Z boson) and also a heavy mediator, which is denoted by "Med". The mediator then decays into two dark matter particles χ and $\bar{\chi}$. The coupling strength of dark matter to the mediator particle is denoted by g_χ, the coupling strength of the mediator particle to the quarks is denoted by g_q. Further parameters are the mass of the mediator particle (typically denoted by m_{Med}) and the mass of the dark matter particle m_χ.

parameters which contribute. This also allows for a rather general analysis strategy which does not have to focus on the details of the considered scenario leading to the fact that model independent searches and respective reinterpretations can also be performed. On the other hand, the modeling of the kinematics of the dark matter production is approximate in an effective field theory approach which leads to discrepancies between the prediction of the effective field theory approach compared to simplified models (cf. Sec. 3.4.4.2).

3.4.4.2 Simplified models

Another approach is the introduction of a mediator particle which acts as a propagator between the standard model particles and dark matter [123–127]. Albeit this approach is somewhat more complex than the EFT approach and relies on a larger number of assumptions, it is referred to as "simplified models". This denotation is supposed to stress the fact that the mediator approach still aims at a description of dark matter which is not necessarily embedded in a larger complex inside the standard model – therefore, not being able to solve more than the dark matter problem at once. An example diagram is shown in Fig. 3.9.

The simplified models of dark matter typically possess four parameters – the mass of the dark matter particle χ denoted by m_χ, the mass of the mediator particle m_{med}[1], and the two couplings of the mediator – the coupling to quarks g_q and the coupling to the dark matter particles g_χ. Different kinds of couplings are considered – vector-couplings, axial-vector couplings, scalars. This leads to a four-dimensional space of parameters for each coupling type which is considered for comparing the results of searches for simplified-model dark matter at colliders. The successor analysis performed

[1] Different names for the mediator particle are found in the literature. In the present thesis, the name Med is chosen.

in LHC Run II uses the simplified model approach [128].

3.4.4.3 Comparison of EFT vs. Simplified Models

Due to a more complete approach, the simplified models are considered somewhat more reliable for collider searches than the EFT in the current literature [129–131]. This section briefly discusses the differences between the EFT and simplified models.

Going from the effective field theory to the simplified model, one resolves the hatched interaction vertex (cf. Fig. 3.8) while introducing the mediator particles and the respective couplings (cf. Fig. 3.9). One can think of a Z′ spin-one boson which is exchanged in the s-channel [132, 133]. In this case, the Lagrangian with the Z′ reads:

$$\begin{aligned}\mathcal{L} = &-\frac{1}{4} Z'_{\mu\nu} Z'^{\mu\nu} + \frac{1}{2} m^2_{\text{med}} Z'^{\mu} Z'_{\mu} + i\bar{\chi}\gamma^{\mu}\partial_{\mu}\chi - m_{\text{DM}}\bar{\chi}\chi \\ &+ Z'_{\mu}\bar{\chi}\gamma^{\mu}(g_{\chi V} - g_{\chi A}\gamma^5)\chi + Z'_{\mu}\sum_q \bar{q}\gamma^{\mu}(g_{qV} - g_{qA}\gamma^5)q\,,\end{aligned} \tag{3.27}$$

whereby $g_{\chi V}$ ($g_{\chi A}$) denote the vector (axial-vector) coupling strengths. The sum runs over all quarks and it assumed that $g_{\chi V}$ and $g_{\chi A}$ couple to all quark flavors equally. If one considers the axial-vector coupling case and therefore sets $g_{\chi V} = 0$, one can compare the result to Eq. 3.25 in the effective field theory approach after integrating over the heavy mediator Z′

$$\Lambda \equiv \frac{m_{\text{med}}}{\sqrt{g_q g_\chi}}. \tag{3.28}$$

This is a very intuitive equation. One can easily see that the approach of the effective field theory unites the mass of the (possibly existing) heavy mediator and its couplings to the quarks and the dark matter particles to one single parameter Λ. One can now perform cross checks of the predictions which one obtains from the EFT and the simplified models. One particular comparison for a monojet final state is shown in Fig. 3.10. In this calculation, the couplings are set to $g_q = g_\chi = 1$, so $\Lambda = m_{\text{med}}$ and a requirement on $p_{\text{T}} > 110$GeV of the jet is set. Hereby, the width of an axial-vector mediator particle with a generic coupling to fermions g_f (= g_q) is [131]

$$\frac{\Gamma}{m_{\text{med}}} = \frac{N_C\, g_f^2}{12\pi}\left(1 - \frac{4m_f^2}{m_{\text{med}}^2}\right)^{3/2} \tag{3.29}$$

with $N_C = 1$ for particles with a color charge and $N_C = 1$ otherwise. If one changes the coupling, the boundaries of the regions defined in the Figure can vary by ≈ 10% leading to a tolerably similar picture. The Figure 3.10 is subdivided into three regions. Region 1 corresponds to a large mediator mass $m_{\text{med}} > 2.5$ TeV and a relatively small dark matter mass $m_\chi < 100$ GeV. In region 1, the cross section predictions of the effective theory approach and of the simplified model approach agree within the assumed uncertainties of 20%. This can be seen from the expansion of the dark matter propagator in powers of the momentum transfer Q^2 over m^2_{med} [131]:

$$\frac{g_q\, g_\chi}{Q^2 - m^2_{\text{med}}} \approx -\frac{g_q\, g_\chi}{m^2_{\text{med}}}\left(1 + \frac{Q^2}{m^2_{\text{med}}} + \mathcal{O}\left(\frac{Q^4}{m^4_{\text{med}}}\right)\right). \tag{3.30}$$

The first factor in front of the brackets is the inverse square of EFT parameter $\frac{1}{\Lambda^2} = \frac{g_\chi g_q}{m^2_{\text{med}}}$. As long as the correcting term $\frac{Q^2}{m^2_{\text{med}}}$ is small, its effect is negligible and the effective field theory delivers a

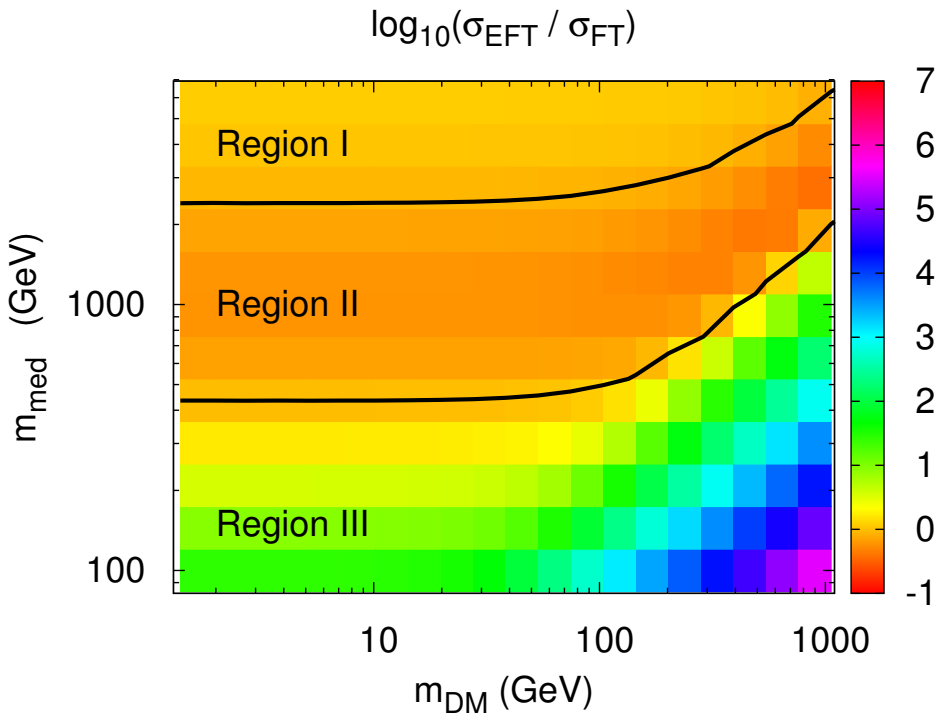

Figure 3.10: Ratio of the cross sections for a monojet final state computed with EFT and the simplified model approach (FT for Full Theory) as a function of m_{med} and m_{χ}. Couplings are assumed to be $g_q = g_{\chi} = 1$ and the requirement $p_{\text{T}} > 110$GeV for the jet is introduced [131].

satisfying prediction. Simulations performed in [129] for the 8 TeV Run of the LHC suggest that $\langle Q^2 \rangle^{1/2}$ is always larger than ≈ 500 GeV, therefore concluding that the value of m_{med} must be at least ≈ 2.5 TeV in order for the correction term $\frac{Q^2}{m_{\text{med}}^2}$ to be smaller than 20%.

In region 2, the cross section of the effective field theory is smaller compared to the simplified model approach. This happens due to resonant enhancement of the mediator on-shell production. Here, the effective field theory approach underestimates the process cross section leading to more conservative limits from the experiments. Finally, in region 3 the cross section of the effective field theory approach is overestimated compared to the simplified model approach due to the fact that the approximation $m_{\text{med}} \gg Q$ is no longer applicable.

Following the arguments presented above, a *truncation* procedure is introduced in order to estimate the impact of the effective field theory approximation and exclude unreliable signal events from further consideration. The procedure is described in the following subsection.

3.4.4.4 Truncation

It has been stressed in the past that the EFT approach, the approach considered in the present thesis, is not valid over the full range of phase space available at the LHC [29, 134–136]. One introduces the condition on the coupling strength $\sqrt{g_q g_{\chi}} < 4\pi$ which keeps the perturbative calculation stable and furthermore the mass requirement for the heavy mediator $m_{\text{Med}} > 2m_{\chi}$ which leads to a lower bound for the region of validity $\Lambda > {}^{m_{\chi}}/_{2\pi}$. Below this limit, one does not expect the effective field theory

approach to deliver solid predictions. However, in the literature the point has been made that this lower bound is not sufficient [124, 134, 136–139]. Using Eq. 3.28, one introduces a further condition $Q < m_{\mathrm{Med}} \sim \sqrt{g_q g_\chi}\Lambda$ which shall denote the border beyond which the effective field theory does not deliver reliable prediction. Now, the ratio of events R_Λ satisfying the requirement in relation to the total number of events can now be defined via

$$R_\Lambda = \frac{\int_{p_{\mathrm{T}}^{\mathrm{min}}}^{p_{\mathrm{T}}^{\mathrm{max}}} \mathrm{d}p_{\mathrm{T}} \int_{\eta^{\mathrm{min}}}^{\eta^{\mathrm{max}}} \mathrm{d}\eta \frac{\mathrm{d}^2\sigma_{\mathrm{eff}}}{\mathrm{d}p_{\mathrm{T}}\mathrm{d}\eta}\Big|_{Q_{\mathrm{tr}}<\sqrt{g_q g_\chi}\Lambda}}{\int_{p_{\mathrm{T}}^{\mathrm{min}}}^{p_{\mathrm{T}}^{\mathrm{max}}} \mathrm{d}p_{\mathrm{T}} \int_{\eta^{\mathrm{min}}}^{\eta^{\mathrm{max}}} \mathrm{d}\eta \frac{\mathrm{d}^2\sigma_{\mathrm{eff}}}{\mathrm{d}p_{\mathrm{T}}\mathrm{d}\eta}}, \tag{3.31}$$

whereby an integration is performed over the transverse momentum p_{T} and the pseudorapidity η phase space. The ratio R_Λ is used for the indication of the truncation approach (along the couplings g_q and g_χ) and has to be chosen manually. The choice of the value of the limiting parameter R_Λ is somewhat arbitrary and has to be agreed on by the different experiments which publish their results in order to make a comparison possible. As an alternative, one can also remove the dark matter signal events with $Q_{\mathrm{tr}} > \sqrt{g_q g_\chi}\Lambda$ by hand on the generator level of the considered Monte Carlo sample. A choice of the product $\sqrt{g_q g_\chi}$ has then to be made. In the results presented in this thesis, the choice of those parameters is always specified in the corresponding display. It should be stressed that comparing "truncated" results (often in terms of exclusion limits) is meaningful only if the applied truncation procedures are identical.

3.4.5 Non-collider searches for dark matter

Instead of producing dark matter at colliders, one can also build a detector aiming to observe the products of dark matter particle annihilation or the interaction of a dark matter particle with the active material (direct and indirect searches for dark matter following the structure in Fig. 3.6). In the following, a (non-exhaustive) representative overview over non-collider searches for dark matter is given.

3.4.5.1 IceCube

The IceCube neutrino observatory is a telescope which uses Antarctic ice as the active medium. The IceCube detector is located at the Amundsen-Scott South Pole Station in Antarctica [140–142]. In the ice, 5160 digital optical modules (DOMs) are located, each of them being equipped with a ten-inch photomultiplier tube and the corresponding electronics structure. The DOMs are located on vertical "strings" which are frozen into 86 boreholes, whereby each string holds 60 DOMs. The boreholes are located over a cubic kilometer from 1450 to 2450 meters depth forming a hexagonal grid with 125 meters spacing. Additionally, the IceTop detector consisting of 81 stations above the footprint. With this equipment, IceCube can measure particle interactions which occur in the ice, typically neutrino interactions producing muons. These muons are ultrarelativistic, traveling with a higher speed than the speed of light in the ice, therefore radiating Cherenkov light which is captured by the photomultipliers of IceCube.

IceCube can detect neutrinos which arise from hypothetical dark matter annihilations in the Sun, following the principle discussed in [143]. Hereby, the process $\chi\bar{\chi} \rightarrow f\bar{f} \rightarrow \nu_i\bar{\nu}_i + X$, whereby

i stands for any of the three possible neutrino flavors, is considered. The neutrinos produced in such a scenario can be detected using the IceCube apparatus – in such an analysis, backgrounds consisting of muons and neutrinos created in the Earth's atmosphere also have to be considered [144]. Comparing the background prediction to the number of expected signal events for different scenarios of dark matter annihilation rate inside the sun μ_s, either evidence for dark matter annihilation inside the sun can be found or exclusion limits on the dark matter nucleon cross section can be set. The most recent results of searches for dark matter with IceCube can be found in [145]. Exclusion limits for effective couplings based on spin-dependent scattering cross sections can be found in [146]. Another analysis of IceCube exclusion limits along the LHC mono-jet searches can be found in [147].

3.4.5.2 Large Underground Xenon Experiment

The Large Underground Xenon experiment (LUX) is a detector apparatus which is operated in the Sanford Underground Laboratory, South Dakota, USA. LUX employs 368 kilograms of ultra-pure xenon which serves as a scintillator producing light proportional to the amount of energy deposited in it [148]. The light is then collected by arrays of light detectors, whereby many measures are taken in order to reduce the background noise, which arises from natural radioactivity of the employed materials. The experiment targets to observe recoils between a WIMP and a target (xenon) nucleus, whereby the recoil energy is deposited in the detector in three channels – scintillation (production of photons), ionization (production of electrical charges) and heat (production of phonons – excitations in the detector material). The most recent results by the LUX collaboration can be found in [149]. As of today, no evidence for WIMP dark matter has been observed.

3.4.5.3 The XENON dark matter experiment

The XENON dark matter experiment, located in an underground cavern at the Gran Sasso Laboratory (Italy), is another experiment employing liquid xenon for dark matter detection [150]. It is the successor of the XENON10 experiment [151], whereby the amount of liquid xenon has been significantly increased and the background rate is expected to be reduced by a factor of 100. The XENON apparatus employs an array of position-sensitive liquid xenon time projection chambers with overall 100kg of sensitive liquid xenon which is surrounded by two arrays of total 178 photomultiplier tubes. In this manner, the primary scintillation signal of an interaction can be detected along the detection of the ionization signal via the proportional scintillation mechanism. The active xenon target is placed in a PTFE cylinder which has a radius of 15 cm and a height of 30 cm. The PTFE cylinder reflects the scintillation light while also optically separating the liquid xenon target from the surrounding liquid xenon which is used for the separation of the active material. The active xenon target is put into an electric field which is necessary for drawing the free electrons to the anode at the top of the tank.

A particle interaction with the liquid xenon results in a light flash, which is detected by photomultipliers, and a release of free electrons, producing a secondary light flash due to the introduced electric field. The relative brightness of the flashes can be used for identification of the particle type and thus for the background reduction. The most recent results obtained by the XENON100 collaboration can be found in [152], whereby no evidence for dark matter has been observed. The XENON100 experiment will be succeeded by the XENON1T experiment [153, 154], which is in the final phase of

construction and is being commissioned as of today.

3.4.5.4 Super Cryogenic Dark Matter Search

Super Cryogenic Dark Matter Search (SCDMS) is an experiment which is located in the Soudan Underground Laboratory and employs 15 interleaved Z-sensitive Ionization Phonon (iZIP) detectors for the search of WIMP dark matter [155]. iZIP detectors, consisting of a 0.6 kg germanium crystal each, are arranged in five towers of three. The SCDMS apparatus targets to measure the energy of the recoil which is caused by a WIMP-nucleon interaction inside the active germanium material producing a distinguished phonon signature in the germanium crystal of SCDMS. Sensitive phonon detection techniques are employed for this purpose which trigger the event recording on phonon signals with $\gtrsim 2$ keV corresponding to a WIMP mass sensitivity down to 10 GeV [155, 156]. The apparatus is cooled to temperatures as low as 10 mK, since sensitivities to keV signals can only be reached by suppressing thermal backgrounds. No evidence for dark matter has been observed by SCDMS so far, whereby the most recent publication can be viewed in [157].

3.4.5.5 Alpha Magnetic Spectrometer

The results obtained by the Alpha Magnetic Spectrometer (AMS) experiment, which is located on the International Space station, can be interpreted in terms of dark matter detection [158, 159]. Data results obtained by the AMS collaboration and presented by Samuel Ting in a seminar at CERN on the 3rd of April 2013, show an excess of positrons compared to the expected flow rate (positron excesses have also been reported before [160, 161]). Studies considering the scenario of $\chi\bar{\chi} \rightarrow e^+e^-, \mu^+\mu^-, \tau^+, \tau^-$ while adopting a number of assumptions including electroweak interactions connecting all standard model particles, show that the excess of positrons can be interpreted as a hint for dark matter particles with $m_\chi \approx 1$ TeV [162]. No further results have been presented by AMS since then.

CHAPTER 4

Large Hadron Collider and Compact Muon Solenoid Detector

4.1 General remarks

The idea of accelerating particles and "smashing" them together is nearly 100 years old as of today. Back in the beginning era of particle physics, the scientists studied the particles which are produced naturally – when high-energetic particles from the Universe rain on the atmosphere, collide with the air and produce further particles one can detect using detectors installed on the surface on the Earth. Over the years, the physicists developed machines which are capable of producing, storing and colliding large amounts of different kinds of particles. One of the fundamental ideas behind this approach is the recreation of the circumstances which existed very shortly (small fractions of a second) after the Big Bang and studying the particle interactions [163, 164]. Once one has gathered knowledge about the production and annihilation rates of different particles, one can propagate this knowledge when studying the formation of the Universe, the galaxies and eventually the Earth itself.

There are two general approaches to particle collisions. One is to build a fixed target and to irradiate it with a particle beam. This approach is widely used in medicine and also in physics research at (relatively) low energies. If one, however, wants to increase the energy available for particle production – the center-of-mass energy $\sqrt{s}$, this approach is disadvantageous. Due to the high difference in the momentum of the incoming beam to the resting fixed target, the main energy of the incoming beam is transferred into the momentum of exiting particles, not into their production. This is why one uses beams circulating in opposite directions for high energy research. If both particle beams contain particles with opposite momentum, the total momentum at the interaction point is 0 and therefore all energy can be used for production of new particles. Therefore, the center-of-mass energy $\sqrt{s}$ for circular particle colliders with two beams with the same momentum is given by

$$\sqrt{s} = 2E_{\text{beam}}. \tag{4.1}$$

For hadron colliders, one has to further note that the energy E from the equation above is the total energy of a hadron. Since hadrons are not pointlike and contain a number of constituents, the energy

E is distributed among the constituents leading to the fact that the effective center-of-mass energy $\sqrt{\hat{s}}$ remains unknown.

One of the key properties of a particle collider is its instantaneous luminosity $\mathcal{L}$. This quantity is a measure for the data amount per time produced by the machine. The better the ability of the machine to align the beams and bring them to collision effectively, the higher is the luminosity. The luminosity is approximately given by [34]:

$$\mathcal{L} = \frac{nN^2 f}{4\pi\sigma_x\sigma_y} \tag{4.2}$$

whereby $\sigma_{x,y}$ are the beam cross sections on the corresponding axes, f is the rotation frequency, n is the number of particle bunches stored in the machine with N particles in each bunch. The rate of interactions $\dot{N}$ for a process with a cross section σ is then given via

$$\dot{N} = \mathcal{L} \cdot \sigma. \tag{4.3}$$

Integrating the above expression over time (whereby one has to keep in mind the d$\mathcal{L}$ is generally time dependent), one obtains the total number N of events arising from a process with the cross section σ

$$N = \mathcal{L}_{\text{int}}\,\sigma. \tag{4.4}$$

For this reason, the size of the dataset produced by a collider is often given in terms of $\mathcal{L}_{\text{int}}$. Since the cross sections are given using the unit "barn":

$$1\text{b} = 10^{-28}\text{m}^2, \tag{4.5}$$

the integrated luminosity $\mathcal{L}_{\text{int}}$ has the dimension inverse barn. Typical values of $\mathcal{L}_{\text{int}}$ for modern colliders are inverse femtobarn – fb^{-1}.

The data considered in the present thesis were recorded in the year 2012 by the Compact Muon Solenoid (CMS) detector which is located in an underground cavern at the Large Hadron Collider (LHC). In the following sections, an overview over the collider machine and the CMS detector will be given [165, 166]. Since the focus of the present thesis lies in the proton-proton collisions, the properties of LHC concerning lead ion collisions will not be discussed circumstantially.

4.2 The Large Hadron Collider

The LHC is an underground machine which accelerates protons to energies of up to 6.5 TeV (design value is 7 TeV) and lead ions bringing them to collision in four interaction points where the detectors are located (cf. Figure 4.1). The four detectors are located in the underground caverns and pursue different physical interests. The ATLAS detector located at Point 1 [168] is a multipurpose detector which is well suited for Higgs Boson measurements as well as searches for Physics Beyond the Standard Model. The ALICE detector is located in the underground cavern of Point 2 [169]. The ALICE detector is designed to observe collisions of lead ions and to study the quark-gluon plasma. LHCb (whereby b stands for the b quark) detector located at Point 8 is dedicated to b physics [170].

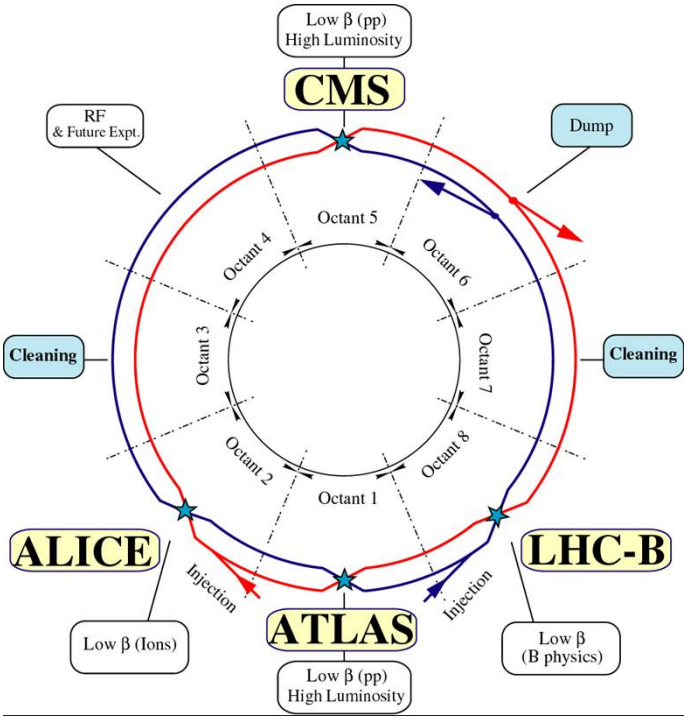

Figure 4.1: A schematic drawing of the LHC accelerator ring. Two accelerator vacuum tubes are shown as well as the four interaction points at which the detectors are located. The centers of the octants are often referred to as points – e.g. Point 5, for the CMS underground cavern [167].

The cross section of b quark production is large for high absolute values of η and therefore the detector is built asymmetrically. The collision at Point 8 happens outside the LHCb detector and the b quark hadrons are measured inside at high $|\eta|$. The CMS detector which recorded all particle collisions considered in the presented thesis is discussed in a separate section 4.3.

The underground tunnel which hosts the LHC has a circumference of almost 27 km. It is the same tunnel which was used for the previous collider machine operated by CERN – the Large Electron Positron Collider (LEP) [171]. The energy loss of a charged particle with the mass m which is subject to acceleration in a ring of a radius R at ultrarelativistic velocities at the energy E is proportional to the ratio $\frac{E^4}{R \cdot m^4}$ [34]. This energy loss is due to synchrotron radiation. The LEP collider was operated at center-of-mass energies of up to 209 GeV using electron and positron bunches. The top center-of-mass energy of LEP was therefore limited by the synchrotron radiation. Since the mass of protons (and lead ions) which are accelerated in the LHC is at least 1800 times larger, the effect of the synchrotron radiation is reduced by many orders of magnitude allowing to increase the center-of-mass energy of hadron collisions significantly without building a new tunnel with a larger radius of curvature R. The maximal center-of-mass energy at the LHC is limited by the highest achievable magnetic field which is used for keeping the hadrons on their circular paths.

The LHC is designed to store up to 2808 bunches of protons in each circulating direction whereby each bunch can contain up to $1.1 \cdot 10^{11}$ protons. The design spacing between the bunches is 25 ns leading to a bunch collision rate of $\approx 40 \cdot 10^6$ Hz. This collision rate is necessary in order to achieve the high luminosity (cf. Eq. 4.2) which is needed for studying rare particle interactions like top quark or Higgs boson production. Storing one collision event requires approximately one megabyte of disk

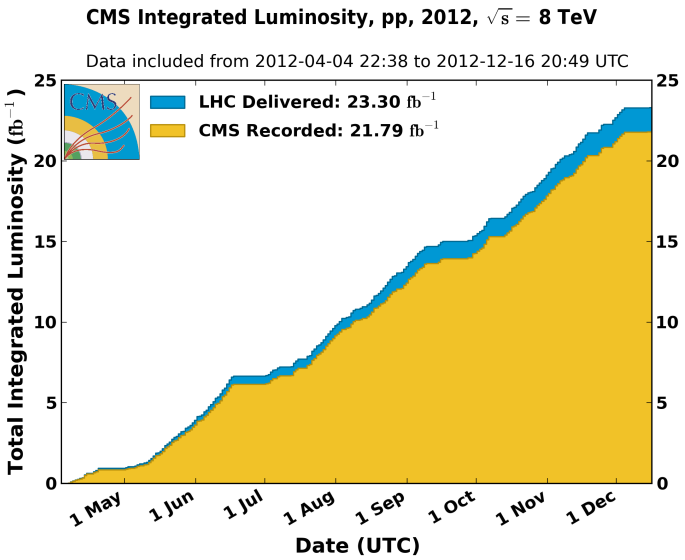

Figure 4.2: Total integrated luminosity delivered by the LHC and recorded by the CMS detector as a function of date in 2012 [172].

space and therefore recording all these events is not possible since there is no available computing system capable of recording 40 terabyte of data each second. A sophisticated system of triggers is therefore employed by each detector. For CMS, the final rate of recorded events varies around 1 KHz (cf. Sec. 4.3.7). Powerful computer centers installed all over the world are then used for offline reconstruction of particles measured by CMS (cf. Sec. 4.4).

In 2012, LHC delivered an outstanding integrated luminosity of over 23 fb^{-1} (cf. Fig. 4.2). In the future, the LHC will be upgraded in order to achieve an even higher integrated luminosity. In one of the proposed LHC development scenarios [173], the targeted dataset size for the next years of LHC operation is 3000 fb^{-1}.

4.2.1 Remarks about the LHC

At a hadron collider, production of hadrons – particles consisting of quarks – is the dominant process. Due to color confinement, quarks and gluons produced in proton-proton collisions can not exist individually thus creating a "cloud" of further quarks and gluons around them. This process is called hadronization and its understanding at a hadron collider is crucial. It should be further noted that hadronization is a QCD process (cf. Sec. 2.4) which can not be accurately described by MC simulation as of today, requiring further background estimation techniques. Another challenge is the understanding of the proton content, since in contrary to lepton collides (e.g. LEP), protons which are brought to collision at LHC are composite particles consisting of partons. The parametrization of the proton content is performed using parton distribution functions (PDF) [174], whereby the parameters of the collider machine play a major role. Several approaches to the PDF estimation are performed by different groups. This is further discussed in Sec. 7.5.6. Finally, due to high instantaneous luminosity a number (≈ 20) of soft interactions between proton pairs occur during a bunch crossing – an effect which is referred to as underlying event or pileup. Therefore, when

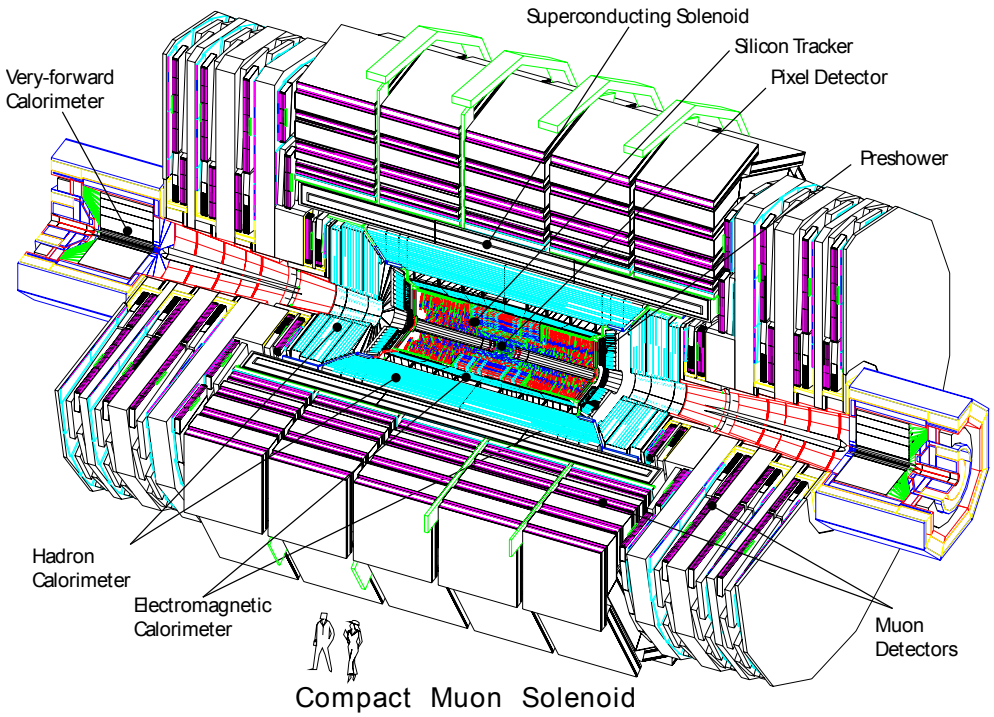

Figure 4.3: The CMS detector at CERN. The "onion"-like structure is shown and all subdetectors are indicated [166].

simulating interactions at a hadron collider one needs to assume a certain pileup scenario and take the effects of a possible disagreement to the measurement into account. Special techniques like pileup reweighting have been developed for this purpose. The effect of pileup depends on the particular analysis and its selection requirements (e.g. the analysis performed in [90] is considered not to be affected by pileup). The pileup impact on the present analysis is discussed in Sec. 7.4.4.

4.3 The Compact Muon Solenoid Detector

The Compact Muon Solenoid detector is a general-purpose detector which is installed in the underground cavern at Point 5 of the LHC tunnel near the french town Cessy. CMS is designed for Higgs boson searches as well as searches for New Physics. Over a large range of possible Higgs boson masses (the mass of the Higgs boson was of course unknown when CMS was designed), the decay into two Z bosons with a subsequent decay into 4 muons remains one of the channels best suited for detection. The inclusion of the word "muon" into the name of the detector strengthens this statement. Furthermore, CMS possesses an excellent tracking apparatus which is responsible for measuring the trajectories of charged particles.

The general characteristics of CMS are

- Good dimuon mass resolution of about 1% for muon pairs originating from Z boson decays as well muon charge identification for muon with momenta $|\vec{p}| < 1$ TeV
- Good energy reconstruction of electromagnetically interacting particles (below 1% for electrons with an energy of 120 GeV). Since the Higgs boson is expected to decay into photons,

this requirement is crucial for measuring a hypothetical Higgs signal in a further channel

- Good resolution of missing transverse energy. Many scenarios of physics Beyond the Standard Model, e.g. the supersymmetric models, involve particles which do not interact with the detector material. Therefore, a good understanding of all subsystems of CMS is crucial in order to achieve good sensitivity towards missing transverse energy $E_{\mathrm{T}}^{\mathrm{miss}}$ and subsequently many New Physics scenarios.

In the following, all subdetectors of CMS are described based on CMS design report [166].

4.3.1 The Superconducting Solenoid Magnet

The letter "S" in the name of the detector stands for solenoid which is one of the largest magnets of its kind ever built. The magnet consists of niobium-titanium fibers which, once cooled to 1.9 K, are superconductive and can deliver a magnetic field of up to 4 T at the full length of the barrel. A sophisticated fluid helium cooling is employed. The current inside the solenoid can reach values of up to 19.14 kA and the total energy stored in the magnet adds up to the colossal 2.6 GJ, whereby typically the solenoid is operated with ≈ 18 kA delivering a magnetic field of $B = 3.8$ T. Outside the solenoid in the barrel part, as well as in the endcaps, an iron return yoke is installed. The yoke consists of 11 elements – five in the barrel "wheels" and six endcap disks. The purpose of the magnet is to deflect charged particles via the Lorentz force, so one can reconstruct their momentum using the relation

$$p_{\mathrm{T}} = q \times R \times B, \tag{4.6}$$

where q is the charge of the considered particle, R is the curvature radius of the muon path and B is the magnetic field. Using the sagitta variable s and the arc length l one arrives at [175]:

$$R = \frac{l^2}{8s}. \tag{4.7}$$

The total weight of the yoke is 12500 t – the largest portion of the 14000 t total weight of CMS. The high currents to which the magnet is exposed also require for an effective magnet safety system which can "dump" the current in case the solenoid (or one part of it) looses the superconductive property due to, e.g., a cooling problem – a problem often referred to as a "quench". There are two redundant safety systems, each employing 5 detectors, which monitor the state of the magnet at all times.

4.3.2 The Pixel Tracker

A schematic cross section of the tracker is shown in Fig. 4.4. CMS has a pixel tracker with 66 Mio. pixels which are accumulated in 1440 modules arranged in three cylindrical layers starting at a distance of 4.4, 7.3 and 10.2 cm to the interaction point in the x-y plane. Two disks of pixel modules are additionally installed on each side. In total, the pixel tracker covers an area of ≈ 1 m^2 around the interaction point. The pixel structure at distances of a few cm to the interaction point is chosen with respect to the occupancy of a measuring unit during a bunch crossing which should be kept around

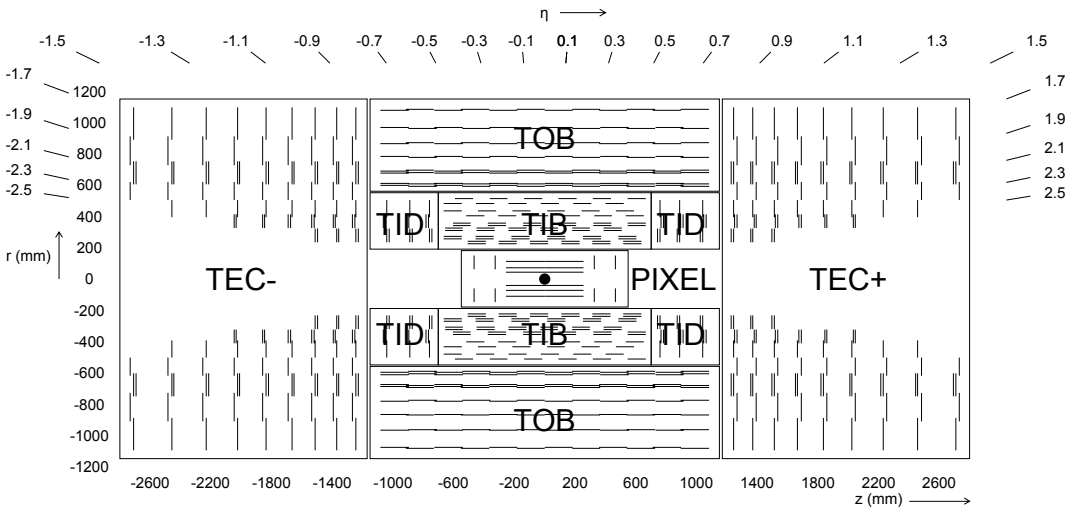

Figure 4.4: A schematic cross section of the CMS inner tracker system. TIB stands for Tracker Inner Barrel and TID stands Tracker Inner disks. TOB corresponds to Tracker Outer Barrel and TEC stands for Tracker EndCaps [166].

1% for achieving a good resolution. The pixels have a size of $100 \times 150\ \mu\text{m}^2$ in the $r-\phi$ and z plane leading to an occupancy of 10^{-4} per bunch crossing. The pixel tracker covers a pseudorapidity range of $|\eta| < 2.5$.

4.3.3 The Silicon Tracker

The barrel silicon tracker surrounds the pixel detector and has 10 layers, which reach up to distances of up to 1.1 m from the interaction point in the x-y plane, consisting of 15148 modules. In the endcaps, 12 silicon strip disks are installed. For distances of 20 cm $< r <$ 55 cm, silicon micro-strip modules are employed with a typical cell size of 10 cm $\times$ 80 μm and a thickness of 320 μm leading to an occupancy of $2-3\%$ for a strip per bunch crossing. For distances 55 cm $< r <$ 110 cm to the interaction point, the strip size is increased to 25 cm $\times$ 180μm whereby the thickness of the modules rises to 500 μm in order to maintain a signal-to-noise ratio > 10. The occupancy of this outer region is about 1%. The overall active area of the silicon tracking detector adds up to over 200 m^2 – a value which holds the world's record for the biggest silicon tracker to be ever constructed.

Since the tracker is very close to the interaction point, the effects of radiation played a major role during its design. Three effects are to be considered. First of all, the passage of ionizing particles creates positively charged holes in the surface of the tracker material. The damage and the number of damaged cells scale linearly with the radiation dose. As a consequence, the n-doped parts of the semiconductor turn into p-doped ones resulting in a change of the depletion voltage by up to hundreds of volts. Furthermore, additional trapping centers are created leading to an expected reduction of the tracker signal by some 10% over 10 years of the LHC operation. Transient phenomena arising from charge generation in electric circuits of the tracker will affect or even destroy the memory cells of the tracker compromising its read-out.

The detector leakage current can lead to the heating of the detector and since the leakage current depends on the temperature exponentially, a so-called thermal runaway can occur. Therefore, the

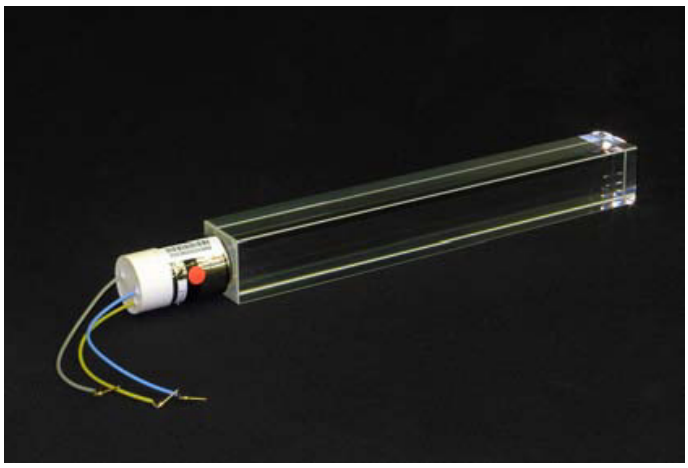

Figure 4.5: A picture of a ECAL scintillating $PbWO_4$ crystal from the endcap region [166].

tracker is cooled to ≈ −10°C. As the detector leakage current is expected to rise during the operation due to radiation effects described above, the cooling temperature is to be decreased to an expected value of ≈ −27°C after 10 years of LHC operation.

4.3.4 Electromagnetic calorimeter

After passing through the pixel and the silicon tracker systems, the particles arrive at the electromagnetic calorimeter (ECAL). The purpose of the ECAL is to produce and absorb an electromagnetic avalanche (also commonly referred to as a "shower") which is triggered by an entering electromagnetically interacting particle. The ECAL employs lead tungstate ($PbWO_4$) crystals which serve as scintillators. When a high-energy electron or photon enters the ECAL material, it collides with the heavy nuclei in it producing a shower of electrons, positrons and photons. These particles excite the electrons in the atoms of the ECAL which then relax, emitting the deposited energy in form of light. The light produced by $PbWO_4$ crystals has blue-green color with a broad maximum at 420 − 430 nm. The amount of light corresponds to the energy of the original particle, whereby about 4.5 photoelectrons per MeV are collected at 18° C. The scintillation time is in the order of magnitude of the LHC design bunch crossing time with about 80% of the light being emitted in 25 ns. Avalanche phototriodes (APD) and vacuum photodriodes (VPTs) are used for collecting and amplifying the signal. APDs are semiconductor detectors, employing silicon in an electric field. Once a scintillation photon arrives at the silicon in the APD, it "kicks" out an electron from an atom – the electron is then accelerated by an electric field, releasing further electrons which are also accelerated leading to an avalanche which is measured. The quantum efficiency of APDs for 430 nm light is 75% at 18° C. The VPTs are photomultipliers with one gain stage. The anodes of VPTs are made of very fine copper mesh (10 μm pitch) which allows for an operation in the 4 T magnetic field of CMS. The mean quantum efficiency of VPTs at 0 T field is 22% at 430 nm whereby the typical response in the 4T magnetic field varies around > 90% of that without magnetic field.

The barrel region of the ECAL consists of 61200 crystals whereby the endcap region holds 14648 additional units. Lead tungstate has a high density of 8.28 g/cm^3, a short radiation length of 0.89 cm and a small Molière radius of only 2.2 cm. The light detection is performed by APDs in the barrel

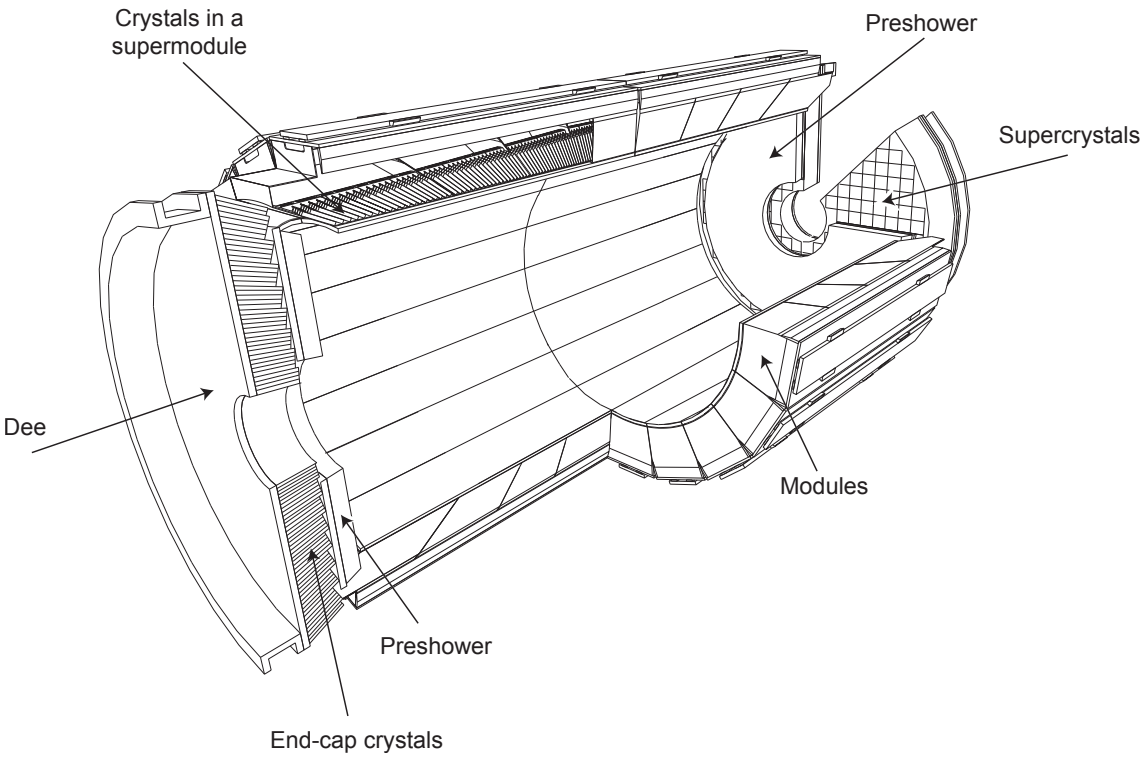

Figure 4.6: A schematic drawing of the electromagnetic calorimeter of CMS [166].

region and VPTs in the endcap region. The full scale signals which are delivered by the APDs (VPTs) are 60 pC (12.8 pC) corresponding to ≈ 1.5 TeV (1.6-3.1 TeV) for the barrel (endcap) region.

The barrel region of the ECAL covers pseudorapidities of $|\eta| < 1.479$. Here, crystals are installed in the ϕ plane with a 360° granularity, whereby in the η direction crystals are installed in a $2 \cdot 85$ manner. In order to avoid borders of crystals aligning with the trajectories of the particles, the crystals are installed at an angle of 3° in ϕ as well as the η projection to the radial vector directed at the interaction point. The front cross section of each crystal is 22×22 mm^2 which grows towards the back of the crystal reaching 26×26 mm^2. The length of the crystals is 230 mm which corresponds to 25.8 interaction lengths. The total volume of the crystals installed in the barrel region adds up to 8.14 m^3 whereby the total weight is 67.4 t. The centers of the crystal's front side have a distance of 1.29 m to the interaction point. 400 or 500 crystals are assembled together in a module depending on the η position.

The endcap regions of the ECAL cover pseudorapidity regions of $1.479 < |\eta| < 3.0$. The crystals are grouped into supercrystals of 5×5 and installed at a distance of 315.4 cm to the interaction point. Each endcap consists of two halves (*Dees*) consisting of 3662 crystals. The front cross section of the crystals is 28.62×28.62 mm^2 increasing towards the back of the crystal to 30×30 mm^2 with a length of 220 mm. In front of the ECAL endcap region, a preshower detector is installed. Its main purpose is to identify neutral pions (which almost always decay into a pair of photons [32]) and to improve the discrimination of electrons against minimum ionizing particles. A schematic drawing of the ECAL apparatus is shown in Fig. 4.6.

For shower energies below 500 GeV, the energy resolution of the ECAL can be parametrized by the

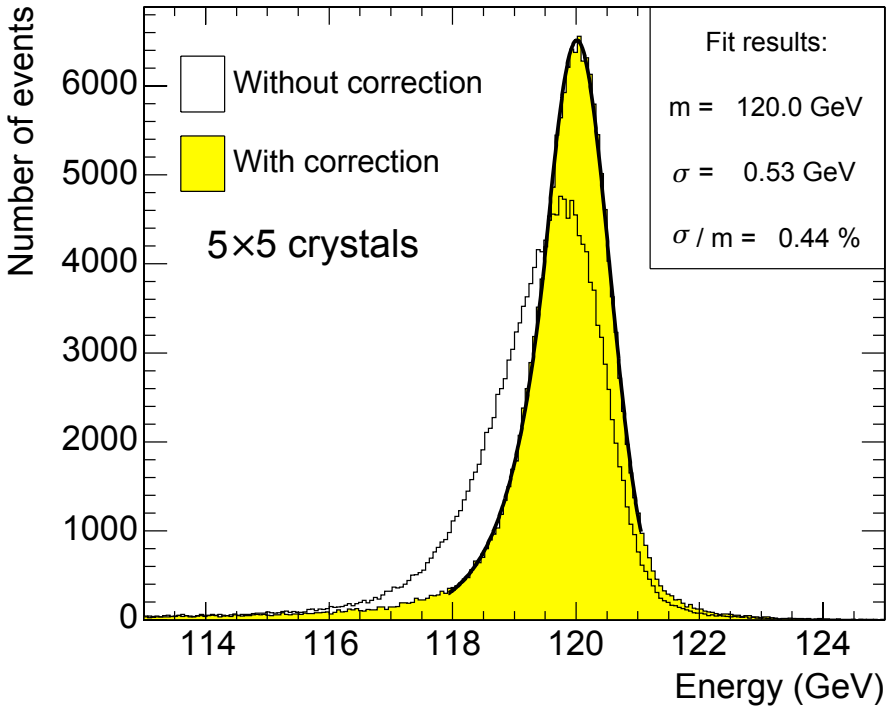

Figure 4.7: Distribution of energy reconstructed in a 5×5 $PbWO_4$ crystal arrangement radiated with 120 GeV electrons over a 20×20 mm^2, showing the results before and after correction for containment [166].

stochastic term S, the noise term N and the constant term C via [166]

$$\left(\frac{\sigma}{E}\right)^2 = \left(\frac{S}{\sqrt{E}}\right)^2 + \left(\frac{N}{E}\right)^2 + C^2. \tag{4.8}$$

Hereby, the stochastic term includes event-to-event fluctuation in the lateral shower containment, a photostatistics contribution of 2.1% and fluctuation in the energy deposited in the preshower absorber. The main contributions to the constant term C arise from non-uniformity of the longitudinal light collection, intercalibration errors and leakage of energy from the back of the ECAL crystal. Finally, the noise term N accounts for the electronis and digitization noise as well as for noise arising from pileup (underlying bunch-bunch interaction. Comissioning of the ECAL crystals on a test beam stand delivered a typical resolution of [166]

$$\left(\frac{\sigma}{E}\right)^2 = \left(\frac{2.8\%}{\sqrt{E}}\right)^2 + \left(\frac{0.12}{E}\right)^2 + (0.30\%)^2, \tag{4.9}$$

whereby E is given in GeV. For a 5×5 crystals arrangement radiated with 120 GeV electrons, an energy resolution of about 0.45 % has been measured (cf. Fig. 4.7), whereby a containment correction has been applied as a function of the incident point in order to account for the amount of energy contained in the crystal matrix.

4.3.5 Hadron calorimeter

The measurement of hadrons and gluons – particles which hadronize and produce a jet signature – plays an important role in the operation of CMS since many of hadrons are expected to be produced during the collisions. An schematic drawing of the hadron calorimeter is presented in Fig. 4.8.

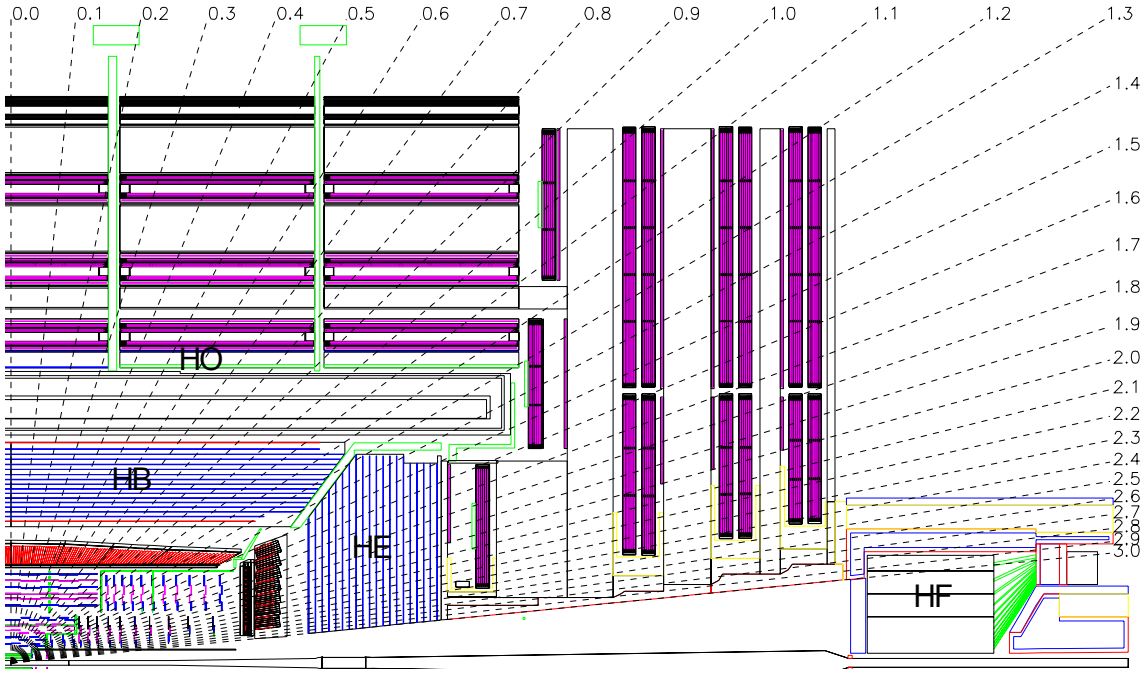

Figure 4.8: A schematic drawing of the hadron calorimeter of CMS – HB stands for the hadron barrel region, HE denotes the hadron endcap region, hadron outer detector is labeled by HO and finally HF marks the hadron forward calorimeter. The dashed lines denote fixed pseudorapidity values. Also the muon detection system is visible [166].

In the barrel region of CMS, the hadron calorimeter (HCAL) is placed between the ECAL and the solenoid magnet, starting at the distance $R = 1.77$ m and extending to $R = 2.95$ m. This part of the HCAL is referred to as HB (hadron barrel) and covers pseudorapidities of $|\eta| < 1.3$. The HB consists of 36 identical azimuthal wedges which are installed on both sides of the interaction point (HB+ and HB- respectively). Each wedge contains four sectors covering the ϕ space. The absorber of the HCAL consists of a front steel plate with a thickness of 40 mm, six brass plates with a thickness of 56.6 mm and a 75 mm-thick steel back plate. The HCAL brass absorber material is C26000 cartridge brass and consists of 70% copper and 30% zinc which results in an interaction length of $\lambda_1 = 16.42$ cm. In total, 5.82 interaction lengths are available at $\eta = 0$ – a value which increases with the opening polar angle reaching up to 10.6 at $|\eta| = 1.3$. The HCAL consists of about 70000 tiles which are grouped into a mechanical scintillator tray unit based on the corresponding ϕ layer. The active medium is a Kuraray SCSN81 plastic scintillator, which has a thickness of 3.7 mm in the HB region. From each tray, the light is collected using a wavelength-shifting fiber.

The stopping power of the HCAL in the barrel region is not sufficient – for $\eta = 0$, only 5.82 interaction lengths (λ_s) are available. Therefore, a special hadron outer (HO) calorimeter is placed outside the solenoid magnet in order to ensure a suitable sampling depth (cf. Fig. 4.8). The sensitive layers of HO are installed in each of the return yoke rings. Since at $\eta = 0$, the value of absorber depth is minimal, two layers of HO scintillators are installed on the central ring being placed on each side of the 19.5 cm iron piece, at radial distances of 3.82 m and 4.07 m respectively. Therefore, the total depth of the HCAL system increases to at least $11.8\lambda_1$ with the exception of the barrel-to-endcap transition region.

The hadron calorimeter installed in the endcap is referred to as HE and covers a pseudorapidity range of $1.3 < |\eta| < 3$. About 34% of particles produced at the LHC are expected in this geometrical subspace. The HE is installed inside the ends of the solenoid magnet. The absorber plates have a thickness of 79 mm and are installed with gaps of 9 mm which are used for scintillators. The total absorption depth adds up to $10\lambda_1$. For very high η values, a dedicated part is added to the HCAL – the hadron forward (HF) subdetector. According to the CMS design report, about 760 GeV are expected to be deposited on average in this region in LHC proton-proton interaction event whereby only 100 GeV are expected in the rest of the detector. The HF covers remaining pseudorapidity regions of up to $|\eta| < 5$. The HF consists of steel absorbers which are arranged in 5 mm thick grooves. The HF has an important impact on the present thesis since it is also employed for the luminosity measurement of CMS.

The performance of the HCAL has been evaluated in various studies – both before and after the construction of CMS [176–178]. The studies are based on different reconstruction algorithms – employing the HCAL only, employing jets matched to a track in the tracker system (JPT jets), or particle flow (PF) jets (cf. Sec. 6.4).

The study performed in [177] analyzed jets selected with the loose Jet ID (cf. Sec. 6.3.2) and employed the Dijet Asymmetry Method and the Photon Plus Jet Balance Method for evaluating the jet p_T resolution in data and MC simulation. A fit has been performed to the standard calorimeter-based resolution formula

$$\frac{\sigma(p_T)}{p_T} = \sqrt{\mathrm{sgn}(N) \cdot \left(\frac{N}{p_T}\right)^2 S^2 \cdot p_T^{(M-1)} + C^2}, \tag{4.10}$$

whereby N describes the noise fluctuations, S describes the sampling and showering fluctuations and detector imperfections at high energies are described by the constant term C [179]. The additional parameter M is introduced in order to improve the fits to the jet resolution for jets which use the tracking information. A systematically higher resolution is observed in data compared to MC simulation which is accounted for by an extra constant term, which is added in quadrature. The resolution for different $|\eta|$ regions is shown in Fig. 4.9. Over all, the jet p_T resolution for PF jets varies around 10% depending on the η and p_T of the considered jet.

4.3.6 The muon system

Muon detection is the key property of CMS. There is an anecdote circulating in the CMS collaboration stating that in the early stages of the CMS proposal, suggestions were made that CMS should only detect muons and no other particles. As one could already see above, those suggestions were not implemented – however the muon detection is still very important for CMS and also for the present thesis. The muon system is used for muon identification, the measurement of the muon momentum and event triggering.

Three types of gaseous muon detectors are installed in the muon system – drift tubes (DT), cathode strip chambers (CSC) and resistive plate chambers (RSC). In the barrel region, DTs are used since the expected muon rate is rather low. The cathode strip chambers are used in the endcap region of CMS since their fast response time suits the higher muon rate. Both DT and CSC are also used for

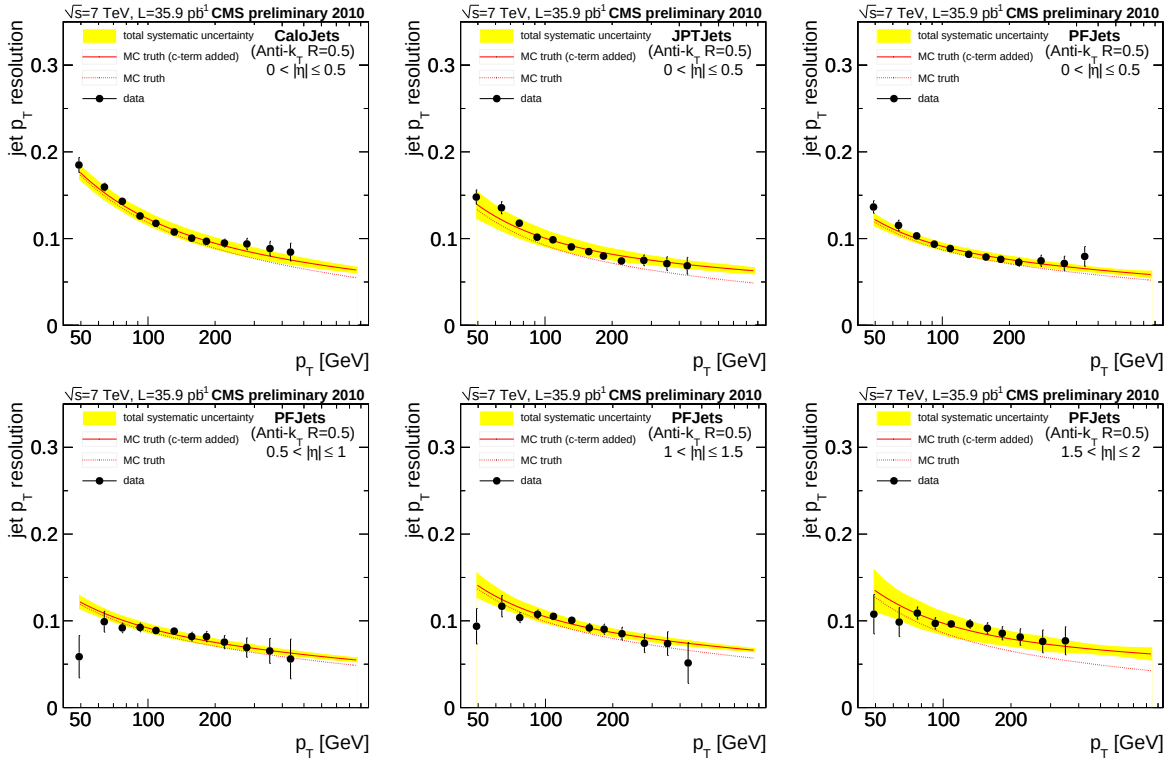

Figure 4.9: Top: Corrected jet p_{T} resolution in the $0 \leq |\eta| \leq 0.5$ region for MC simulation and data before and after correction for the observed discrepancy. It is visible that p_{T} resolution improves with increasing p_{T} of the jet, whereby the PF reconstruction algorithm delivers best values. Bottom: Corrected jet p_{T} resolution for MC simulation and data before and after correction for higher values of $|\eta|$ employing the PF algorithm [177].

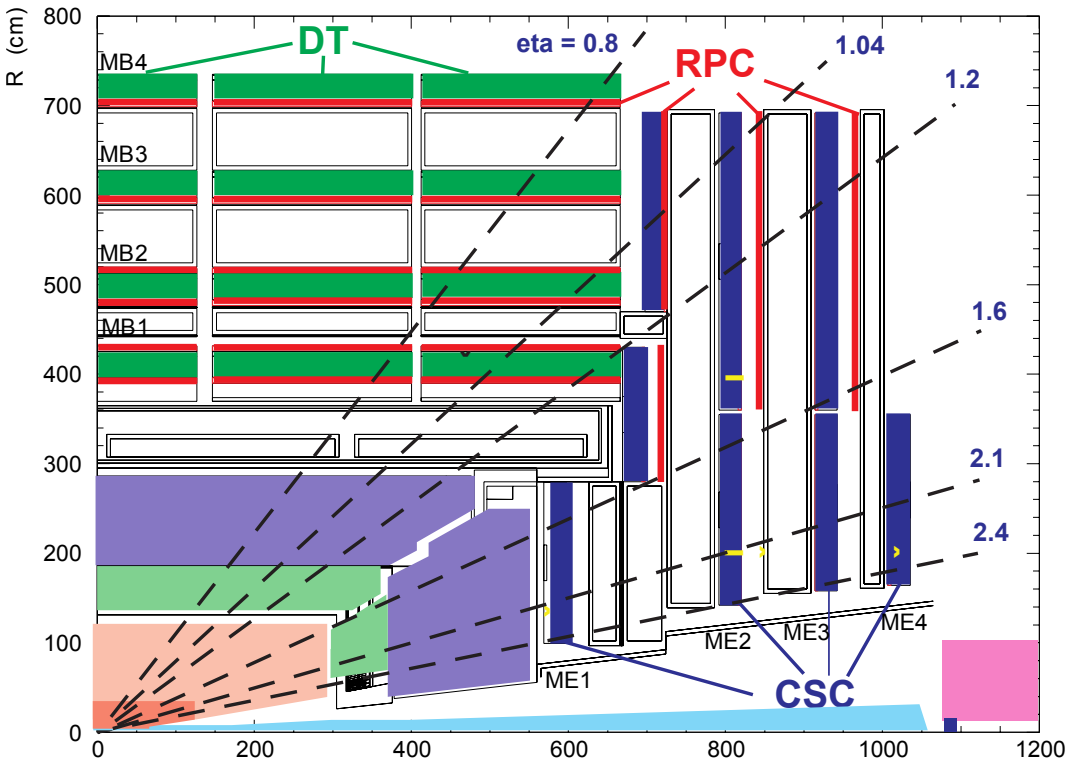

Figure 4.10: Muon detection system of CMS. The green detectors denote the drift tubes which are only installed in the barrel region, the resistive plate chambers in both the barrel and the endcap regions are presented in red, the cathode strip chambers in the endcap are plotted in blue [166].

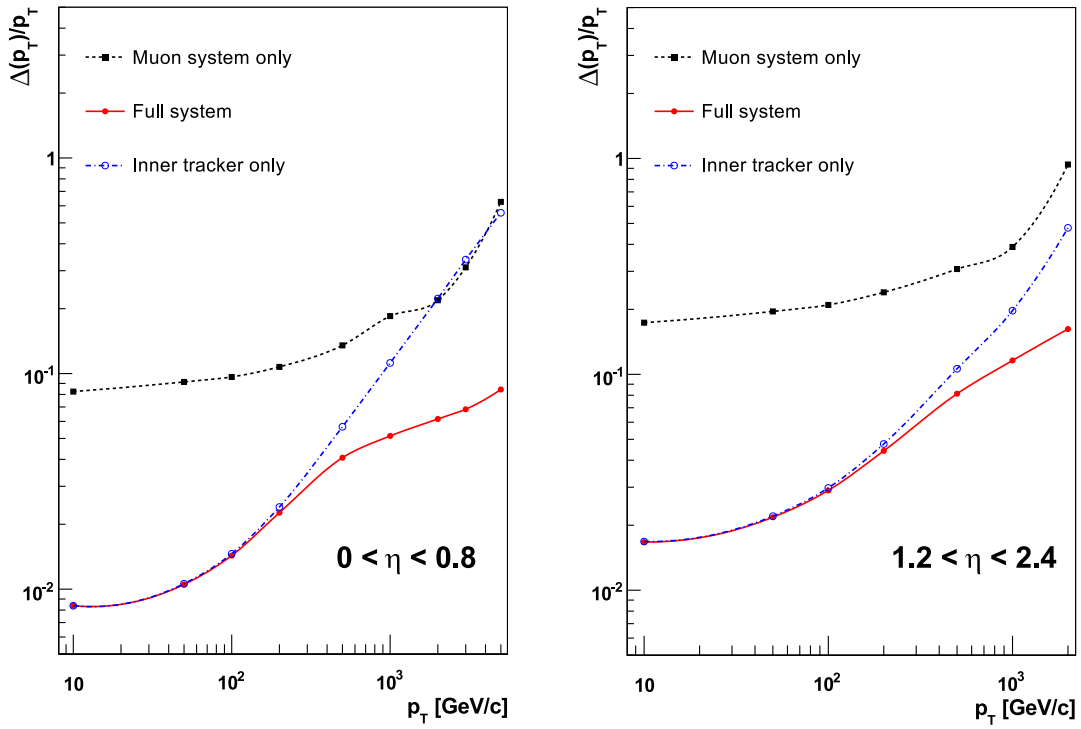

Figure 4.11: The relative muon momentum resolution as a function of muon p_T for two regions in $|\eta|$ measured by the muon system only, the inner tracking system only and employing both systems at once [166].

triggering. The RPC system serves as a complementary muon triggering system, having a capability of identifying muon events of interest in a much shorter time span than the 25 ns time gap between two bunch crossings (BX). Since muon identification and measurement is crucial for the present thesis, the different muon detecting systems are described in detail in the following. A schematic plot of the CMS muon system is shown in Fig. 4.10.

The offline standalone (without matching tracks to the tracker) muon momentum resolution is about 9% for small values of η and p for muons with p_T up to 200 GeV. For standalone muons at p_T = 1 TeV, the muon momentum resolution takes values between 15% and 40% depending on the $|\eta|$ of the considered muon. Once the inner tracker system is used for the muon momentum reconstruction, the momentum resolution improves significantly, especially for low momenta of the muon. At 1 TeV, the performance of the tracker with the muon system delivers a momentum resolution of about 5% (cf. Fig. 4.11).

4.3.6.1 Drift Tubes

Drift tubes are installed in the barrel region of CMS. An overview of the DT system is shown in Fig. 4.12. The DT system contains 4 layers (named MB1, MB2, MB3 and MB4), installed between the layers of the iron return yoke covering the pseudorapidity range of $|\eta| < 1.2$. A drift-tube chamber consists of 2 or 3 superlayers, each consisting of 4 layers of rectangular drift cells (cf. Fig. 4.12). In order to achieve the best possible measurement resolution, each cell layer is shifted by half a cell length. The superlayer is the smallest independent part of the DT system. In the two outer

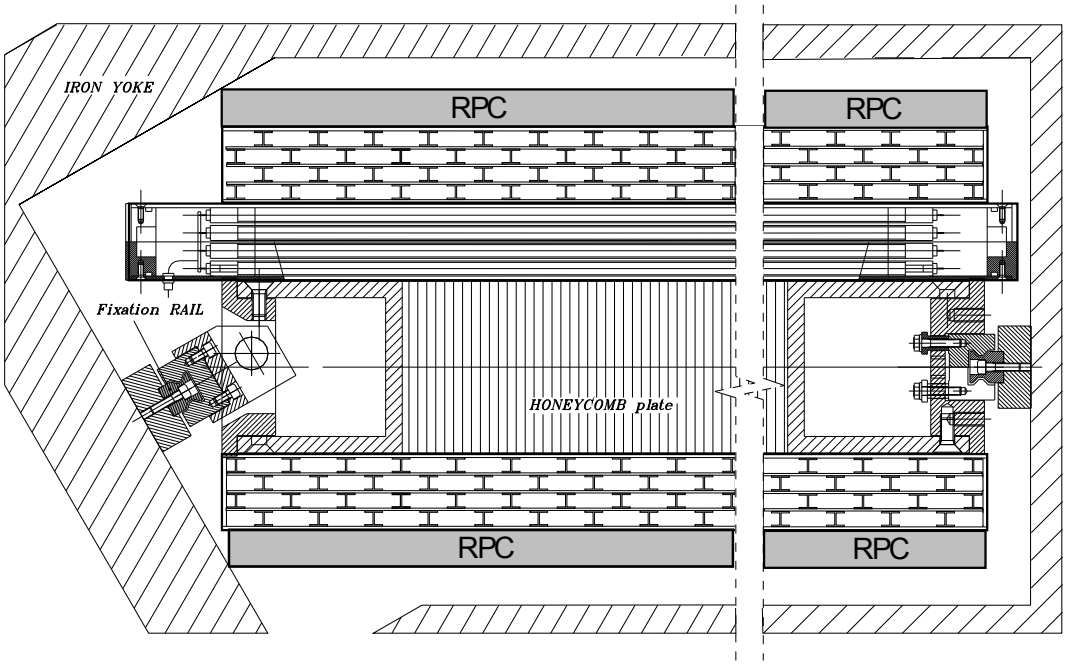

Figure 4.12: Drift tube chambers of CMS shown in the $r-\phi$ plane. The two superlayers are visible, each containing 4 layers of rectangular drift cells, which are shifted by half a cell length with respect to each other. The resistive plate chamber are only indicated, the structure is not shown [166].

superlayers, the wires are placed parallelly to the beam axis providing a track measurement in the magnetic bending plane – the $r-\phi$ plane. In the inner superlayers, the wires are placed orthogonally to the beam axis providing the measurement along the z axis. However, no inner superlayer is installed in the MB4 – only the ϕ coordinate of the muon can be measured there. Argon and CO_2 serve as the detection gas mixture and are mixed in proportions of 85% and 15% respectively. The transverse dimension of each cell is set to 21 mm which implies a drift time of 380 ns.

It should be noted that many of the fellow colleagues from the III Physikalisches Institut A made major contributions to the DT system, manufacturing the first inner ring of the DT system in Aachen, as well as the maintenance and service of this muon detection subsystem.

4.3.6.2 Cathode Strip Chambers

There are 468 cathode strip chambers installed in the endcap region of CMS, arranged in eight groups (cf. Fig. 4.13). The trapezoidal CSCs cover 10° or 20° in the ϕ coordinate and a muon going through the endcap with a pseudorapidity $1.2 < |\eta| < 2.4$ will cross at least 3 CSCs whereby a muon with $0.9 < |\eta| < 1.2$ will be registered by both the DT and CSC systems. The CSCs have 6 anode wire planes which are interlaced by 7 cathode panels whereby the wires are directed azimuthally(cf. Fig. 4.14). The CSC system covers an area of about 5000 m^2 with a gas volume of over 50 m^3. All in all, about 220000 cathode read-out channels and about 180000 anode read-out channels are employed with about 9000 high-voltage channels.

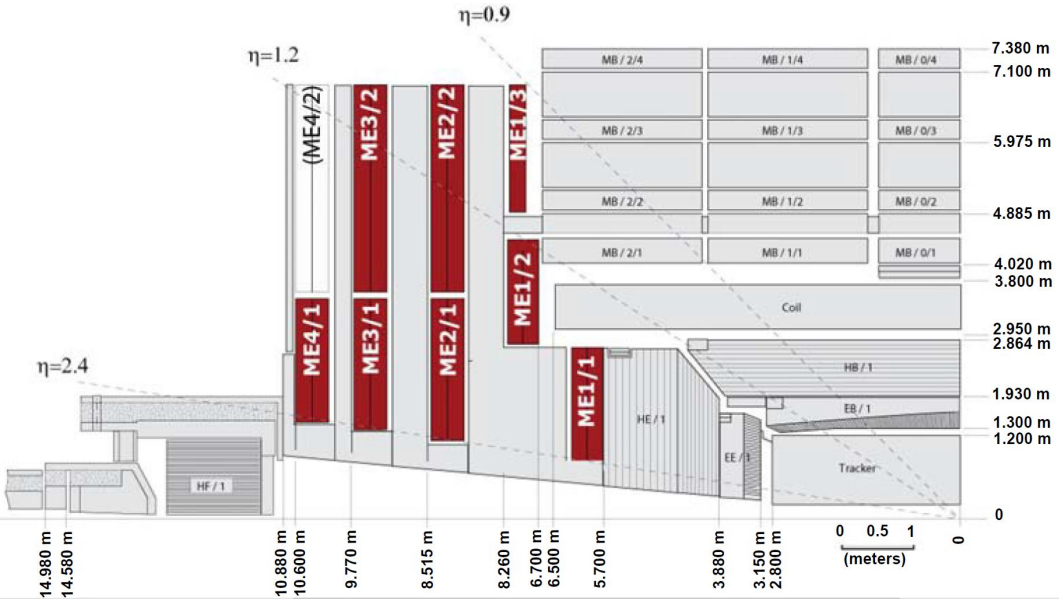

Figure 4.13: Cathode drift chambers of CMS shown in the $r-\phi$ plane. The different chambers are labeled by "ME X/Y" where X denotes the layer number in the z direction and Y stands for the layer number in r direction [166].

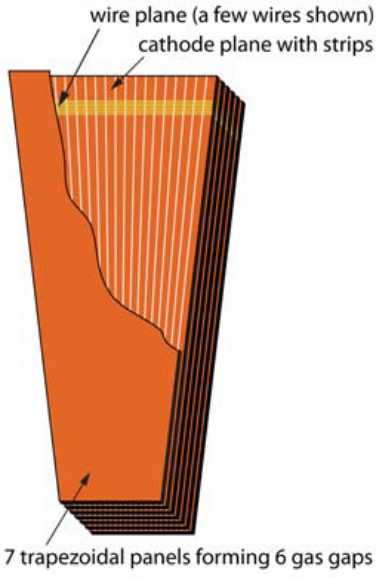

Figure 4.14: The structure of the cathode drift chambers of CMS. The strips are aligned radially. The largest chambers are 3.4 m long [166].

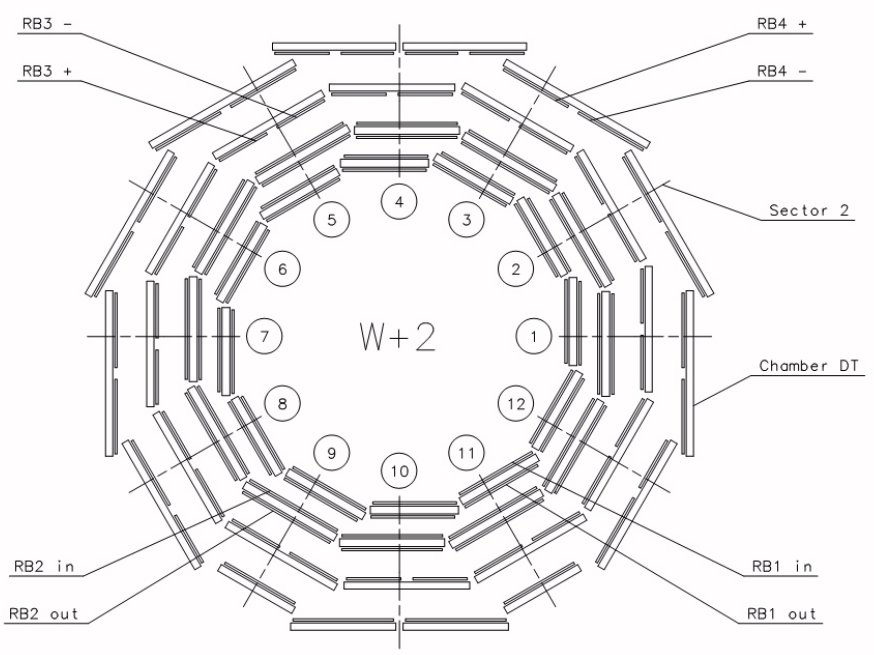

Figure 4.15: Cross section of a barrel Resistive Plate Chamber ring of CMS. The different wheels are numbered from $1,\ldots,12$, five rings (numbered $-2,\ldots,2$) are arranged in the barrel region [166].

4.3.6.3 Resistive Plate Chambers

Resistive Plate Chambers (RSC) round up the composition of the muon detection system. The RPCs are installed in both the barrel and the endcap regions of CMS. The RPCs provide an excellent time resolution which is far below the nominal time between bunch crossings of 25 ns (whereby the collisions of the dataset considered in this thesis were performed with a 50 ns bunch spacing). A resistive plate chamber has a double-gap module which is operated in the avalanche mode (cf. Fig.4.16). The RPCs are employed using a mixture of three gases – 96.2% of $C_2H_2F_4$, 3.5% of iC_4H_{10} and 0.3% SF_6. In order to avoid changes in the resistivity of the chambers, a relative humidity of $\approx 45\%$ has to be maintained. Therefore, an appropriate amount of water vapor is added to the gas compound.

In the barrel of CMS, RPCs are installed in 6 cylinders around the z-axis forming four stations in the transverse plane (cf. Fig. 4.15). All in all, there are 480 chambers installed in the barrel region. In the endcap region, the RPCs are installed together with the CSC system. In addition to the four layers of CSC, three layers of RPC are installed on the transverse disks of CMS endcaps with a small overlap in ϕ in order to avoid dead space between the chambers.

4.3.7 Event Triggering

The LHC is designed to deliver collisions every 25 ns, whereby in 2012 the bunch spacing was set to 50 ns. This implies very high event rates of up of 40 MHz at the design bunch spacing of 25 ns [166]. The storage of every CMS event requires around 1 MB and hence over 40 TB of CMS data is produced every second. This is a gigantic amount of data which of course can not be stored. CMS employs a two stage "gearbox" – the decision whether the event is to be stored is made in two steps.

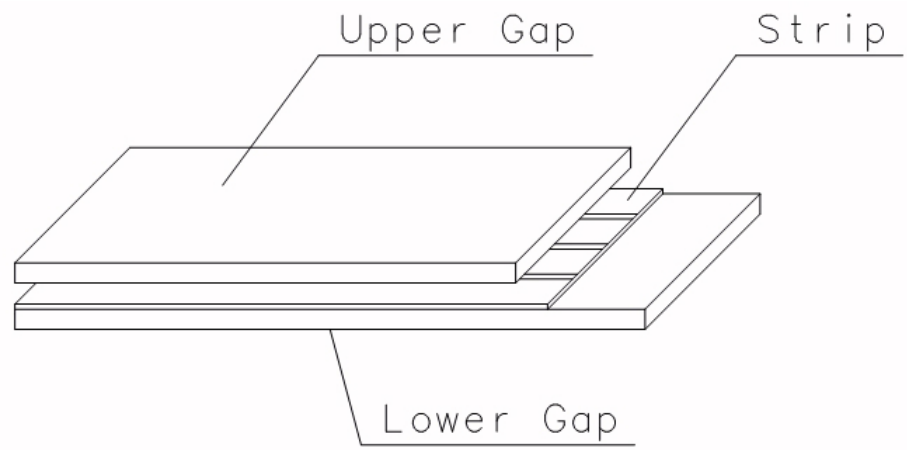

Figure 4.16: Structure of a two-gap RPC module installed in the muon system of CMS. The resistive plate in-between two gaps is visible [166].

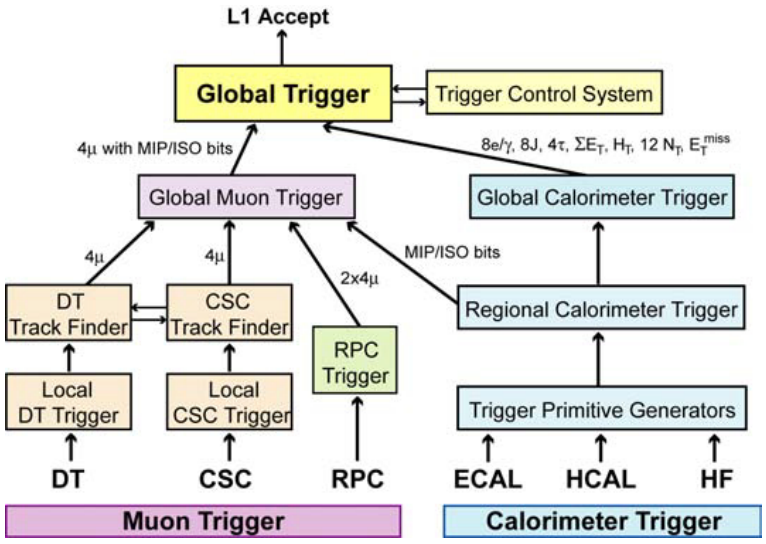

Figure 4.17: The structure of the level 1 trigger system of CMS. Information from calorimeters as well as from the muon system is employed for the decision making. [166].

The level 1 (L1) trigger system employs programmable electronic devices which are designed for very fast decision making. The L1 system uses coarsely segmented data for making the decision and the maximal output rate is typically around 30 kHz (a typical L1 trigger rate in the LHC RunII can reach values of up to 90 KHz). Calorimeters and the muon system are involved in the decision making by the L1 system. More details are shown in Fig. 4.17. The L1 trigger system consists of local, regional and global components. The local components consider the energy deposits in the calorimeter trigger towers as well as the patterns measured in the muon chambers. The regional components combine the information from the local components and determine particle candidates ranking them based on the determined momentum (or energy) and quality of reconstruction. The global components determine the objects which are ranked the highest within the corresponding lists and forwards those to the Global Trigger which represents the final stage of the L1 system. The Global Trigger makes the final decision, evaluating special algorithms and also considering the status of the Data Acquisition system (DAQ) and the state of the subdetectors. For the future, the upgraded tracker is also expected to be involved into the triggering [180].

A system of high level triggers (HLT) is employed as the second step. A high level trigger is a software program which in general has access to the complete read-out and can perform a deeper analysis of the collision events before finally accepting or rejecting additionally employing the information from the tracker [181]. Many different HLTs are requested by different analysis groups prior to the data taking and a special working group within CMS prepares the final set of all HLTs to be used. Since the rate of events falls as a function of any considered particle candidate's momentum, usually the HLTs present with a p_{T} threshold and a basic isolation requirement for the considered candidate which is also reflected in the name of the HLT – e.g. `IsoElectron13` stands for the requirement of $p_{\mathrm{T}} > 13$ GeV and a basic isolation for an electron candidate. The decision on the threshold is always a compromise between the expected data rate and the desire to study as many collisions as possible. In order to put the p_{T} threshold of recorded events even lower, some HLTs are prescaled – they only record a portion of the events satisfying their requirements. For example, an `IsoPhoton30` with a prescale of 100 would only record $1/100$ of all events satisfying its requirements.

The high level triggers are merged in streams based on the particle (physics objects) on which they trigger. This way, one has a muon stream, an electron stream, a dielectron, a dimuon stream and so on. This simplifies the data analysis for the user later on.

4.4 Computing

The large amount of data produced by CMS (and other experiments at the LHC) adding up to ≈ 30 PB = 30000000 GB is analyzed using the worldwide GRID [182]. It consists of over 170 computing centers which are installed in 42 countries. The total number of processor units varies as old computer blades are continuously being replaced by new ones – the order of magnitude is, however, stunning with hundreds of thousands CPUs installed. The GRID is also used for the production of simulation samples which are needed for the background estimation, searches for New Physics, as well as for the calibration and the commissioning of the detector.

CHAPTER 5

Software Framework

Evaluation of a large dataset puts very high requirements on the software which is used in the particular analysis. As one could see in the previous parts of the present thesis, one collision event needs about 1 MB of disk storage when it is recorded at CMS. This data includes all the information from the subdetectors of CMS. This information has to be analyzed in order to produce tracks of all measured particles – special software and algorithms are developed by CMS collaborators for this purpose. In the following, a brief overview is given.

5.1 CMSSW and ROOT

CMSSW – as CMS SoftWare – is the software framework employed at CMS for both data taking and data analysis [183]. This software consists of different modules which are used for recording and simulation of events, calibration and alignment of the detector and furthermore for the reconstruction of both data and simulation events. Configuration files have to be provided in order to specify which module is to be called and used – those configuration files are typically written using the Python programming language. CMSSW uses the Event Data Model (EDM) [184].

The information used by CMSSW can be stored in binary files in the ROOT format. ROOT is a very sophisticated data analysis software which was developed at CERN and is the main analysis tool in the present thesis [185]. ROOT offers the user a broad spectrum of different tools for storage, analysis and data presentation.

Technically, the present analysis is a set of different computer code files – the largest of them are written in C++ and use the ROOT libraries. In the first step, different algorithms are applied to the recorded and simulated data – those apply reconstruction algorithms for all information available in an event. This information is stored in different collections inside a ROOT file – e.g. there may be more than one τ lepton reconstruction algorithms which are applied (and the user can decide which one to use, or even use all) and the output of each algorithm is stored in a corresponding collection. This is performed centrally for all data and simulation samples – the procedure can be repeated for the same data and simulation samples when new algorithms are introduced. The result of these operations is stored in the Analysis Object Data (AOD) ROOT files for data samples and in simulation

Analysis Object Data (AODSIM) ROOT files for simulated data samples. In the next step, n-tuples are produced – this procedure is often referred to as skimming. A huge computer program - a.k.a. the Skimmer – has been written in the III. Physikalisches Institut A by many of my fellow colleagues. The Skimmer is a module which is plugged into CMSSW and can run on both AOD and AODSIM ROOT files. Depending on the number of data streams (cf. Sec. 4.3.7), and the size of the recorded data and simulation datasets, this procedure can take several days. The worldwide GRID is used for the analysis step and many thousands of processors can be used at once. In the next step, a user-specific code runs over the tuples. In this step, the largest part of the analysis is performed. The selection requirements on the set of the events are applied and the spectra of interest are saved.

For the LHC RunII, a modern software framework TAPAS (Three A Physics Analysis Software) has been developed at the III. Physikalisches Institut A, simplifying many analysis steps and providing a flexible and reliable software platform [186].

It should be noted that even though the software framework chapter is one of the shortest parts of the present thesis, the most effort of an analysis is put into the development and the fine tuning of the analysis code.

5.2 Physics Generators

The simulation of particle collisions at high energy is a very broad topic. In this section, a brief overview over the functionality of those generators is given. Usually, the Monte Carlo simulation approach is used [31]. As input, the basic parameters of the collider machine – the center of mass energy, particles type brought to collision – and some phase space requirements are used.

The main idea is to calculate the cross section of a standard model process or a BSM process and optionally simulate the kinematic parameters and observables of particles which participate. For the cross section calculation, different approaches exist [187, 188]. These generators can be used for calculation of the cross sections of different processes in LO, NLO and sometimes even NNLO (in QCD) and studies of observables, like p_{T} spectra. They, however, do not simulate the kinematics of every event. Another class of generators are the generators which do so.

There are a handful of generators which simulate the kinematic properties of all particles participating in the collision – good examples are `MadGraph`, `Powheg` and some further [189–193]. Those generators store the information about each event in a file with a special format. One prominent example is the Les Houches format [194]. In this format, the information about every event is written in a human readable text file with the extension ".lhe" – this is a very user friendly approach which allows for prompt analysis of the generator output with a very small computational effort. The so produced .lhe file can be used as input for detector simulation.

5.3 Detector Simulation

The output of physics generators discussed in the previous section is independent of the particular detector. After the interaction itself is simulated, the conditions of the experiment have to be "added". For this purpose, the `GEANT` software is used [195]. In `GEANT`, it is possible to produce a model of a corresponding detector and simulate the interactions of different particles whilst they traverse it as

well as the corresponding detector response. The CMS detector model in GEANT is fully implemented in CMSSW and different simulation settings are available depending on the interest of the user. The computation of the particle-detector interaction is expensive in terms of time – the simulation of one collision event takes about 90 sec.

5.4 Statistical Interpretation

The final step of the analysis is the statistical interpretation of the observed results. For this, the Higgs Combine Tool is employed in the present thesis [196] which uses the RooStats package [197]. The Higgs Combine Tool is capable of employing various approaches (Bayesian, Frequentist) for statistical evaluation of model parameters which are disfavored by the measurement (this is commonly called exclusion limit setting) or for the estimation of the significance of the potential hint for New Physics. In the present thesis, the modified frequentist CL_s method is employed [198–200] relying on asymptotic formulas [201, 202] in order to set exclusion limits on theory parameters for dark matter and unparticle production.

One starts with a test statistic t and two hypotheses – H_0 (the null hypothesis, e.g. absence of New Physics) and H_1 (the alternative hypothesis, e.g. existence of a New Physics signal). One then establishes a relation between two values t_1 and t_2 in a way that $t_2 \rhd t_1$ implies that t_2 favors the hypothesis H_0 less than t_1 does. Having observed a value for the test statistic t_{obs}, one defines the p-value [203] of H_0 with respect to the test statistic t as the probability:

$$\text{Probability}(t \rhd t_{\text{obs}} | H_0) \equiv p. \tag{5.1}$$

The lower the p-value, the more doubt exists for the validity of H_0. The CL_s method is based on p-value evaluating in terms of the underlying test statistic t. One can now define [83, 199]:

$$CL_s = \frac{p(t|H_1)}{1 - p(t|H_0)} = \frac{p\text{-value of } t \text{ under assumption of } H_1}{1 - p\text{-value of } t \text{ under assumption of } H_0}. \tag{5.2}$$

The requirement of a threshold α, so that $CL_s \leq \alpha$ is then used for defining a confidence interval for the hypothesis H_1 – all parameters with $CL_s < \alpha$ are then excluded at a confidence level (CL) of $1 - \alpha$. Typically, in high energy physics the value of α is set to 5%, whereby in the dark matter experiment community the value of $\alpha = 10\%$ is more common. The confidence level of all exclusion limits presented in this theses are always indicated in the corresponding figures.

In the present analysis, the number of background events and the number of signal events, whereas the latter are scaled by a signal strength modifier μ, are combined in a binned likelihood ratio (test statistic) for each bin of the distribution of the variable of interest, computing the exclusion limit for the concerned scenario of New Physics.

CHAPTER 6

Physics Object Reconstruction and Event Selection

In this chapter, the reconstruction of physics objects in CMS is explained. Both electrons and muons are considered in the selection along with hadronic jets and jets marked as b jets. The reconstruction procedures employed by CMS are discussed in the following sections.

6.1 Electrons

Electrons can be measured with great precision in CMS – an energy resolution of 0.45% has been achieved in commissioning tests as discussed above (cf. Sec. 4.3.4). In the next sections, the electron reconstruction procedure in CMS is described.

6.1.1 Electron energy clustering in the ECAL

The electron candidates are reconstructed in both the tracker and the ECAL – two algorithms are considered for this purpose [204, 205]. In the first step, a seed in the ECAL barrel with the largest energy deposit above a well defined threshold $E^{\text{min}}_{\text{T, seed}}$ is chosen and arrays of 5×1 crystals in the $\eta - \phi$ plane are added around it in a range of N_{steps} crystal if their energies exceed the threshold $E^{\text{min}}_{\text{array}}$. The arrays are then collected into clusters, whereby each cluster is required to have a seed array with an energy larger that $E^{\text{min}}_{\text{seed-array}}$. All clusters satisfying this requirement are stored in the final global supercluster (SC). The corresponding threshold values for the barrel region are summarized in Tab. 6.1.

In the endcap, the algorithm is somewhat different. There, seeds with a local maximum energy deposit with respect to the four direct neighbours are chosen if its transverse energy is larger than $E^{\text{min}}_{\text{T, EEseed}}$. The clusters around these seeds are then considered in 5×5 crystals starting with the crystal with the largest energy deposit. Hereby, the clusters can overlap. The clusters are grouped into superclusters within the range $\eta \pm \eta^{\text{range}}$ and $\phi \pm \phi^{\text{range}}$ if energy threshold requirement $E_{\text{T, cluster}} > E^{\text{min}}_{\text{T, cluster}}$ is met. The positions of the clusters is then weighted by the energy deposit and extrapolated to the preshower. Here, the most energetic cluster acts as a reference. The so matched energy deposit

Barrel		Endcaps	
Parameter	Value	Parameter	Value
$E^{\text{min}}_{\text{T, seed}}$	1GeV	$E^{\text{min}}_{\text{T, EEseed}}$	0.18GeV
$E^{\text{min}}_{\text{seed-array}}$	0.35GeV	$E^{\text{min}}_{\text{T, cluster}}$	1GeV
$E^{\text{min}}_{\text{array}}$	0.1GeV	η^{range}	0.07
N_{steps}	17 (≈0.3rad)	ϕ^{range}	0.3rad

Table 6.1: Threshold values of parameters used in the hybrid superclustering algorithm in the barrel, and in the 5×5 superclustering algorithm in the endcaps [204].

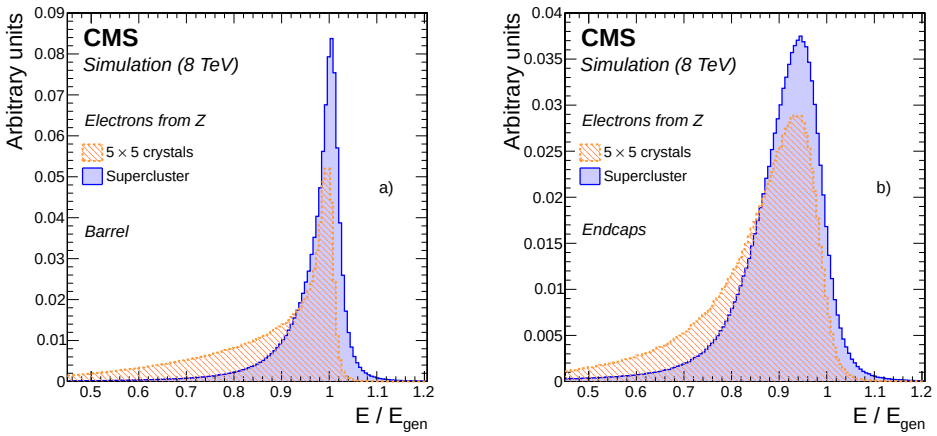

Figure 6.1: Distribution of the ratio of reconstructed and generated energy of a simulated electron arising from a $Z \rightarrow ee$ decay for the barrel (left hand side) and endcaps (right hand side). The performance of the 5×5 crystals versus the performance of superclusters is shown whereby no further corrections are applied. It is visible that the Supercluser approach performs better [204].

in the preshower is then added to the total energy of the SC. The threshold values for the endcap region are shown in Tab. 6.1.

The second algorithm also serves as a part of the particle flow (PF) algorithm (cf. Sec. 6.4). In this approach, all neighbour clusters around a seed are united if the energy deposit in them exceeds the noise by two standard deviations. Hereby, the energy of the seed has to be $E_{\text{seed}} < 230$ MeV in the barrel and $E_{\text{seed}} < 600$ MeV or $E_{\text{T,seed}} < 150$ MeV in the endcaps. Such clusters are referred to as PF clusters. The difference to the approach shown above is that several PF clusters can share the energy of one crystal.

The comparison of the generated and reconstructed energy for different clustering approaches is shown in Fig. 6.1. It is visible that the algorithm employing superclusters performs much better, reconstructing a more narrow distribution around the generated value.

6.1.2 Electron track reconstruction

The first and very important step of the electron track reconstruction is finding the two (or if possible three) first electron hits in the tracker – this selection step can greatly influence the reconstruction efficiency. Again, two algorithms are employed and their results are combined later on. The so

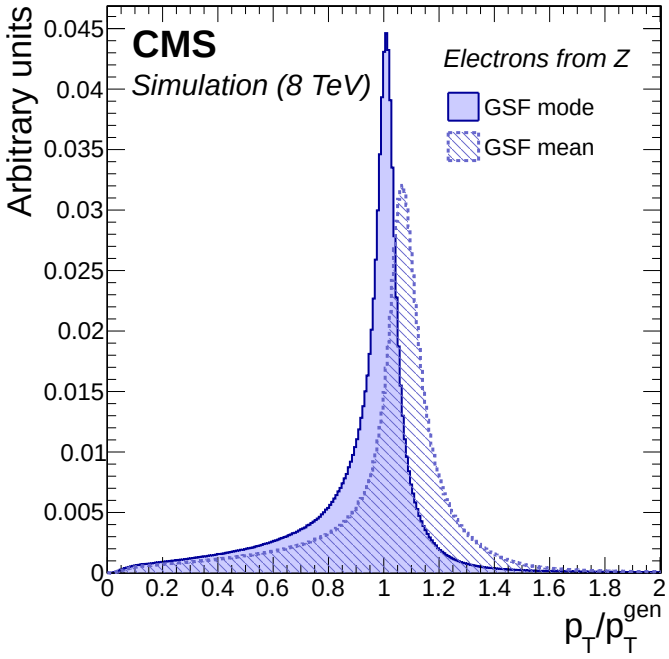

Figure 6.2: Ratio of reconstructed p_{T} of the electron and the generated p_{T} of the electron in simulation of $Z \rightarrow ee$ events. Two reconstruction modes are shown – one using the most probable value of the GSF track component in solid and the weighted mean of the GSF fit in dashed [204].

called ECAL-based seeding starts with a SC in the ECAL and extrapolates the trajectory back to the interaction vertex using the energy and the position of the SC. Hereby, both possibilities – a negative and a positive charge of the electron candidate – are considered. In addition to that, a veto on a hadronic energy deposit is introduced on the track candidate. In the second approach, pixel tracks are used to form tracker seeds. For every SC, a seed is chosen by comparing the hits of each tracker seed and the seed predicted in the SC within an optimized window in the ϕ and z directions. All in all, an efficiency of $\approx 92\%$ is achieved for an electron from a simulated Z boson decay.

The tracker-based seeding is a part of the PF algorithm. It starts with tracks reconstructed by the Kalman algorithm [206]. This procedure can be employed if the energy losses due to bremsstrahlung is negligible. In this case, the Kalman filter (KF) algorithm selects all hits from the tracker up to the ECAL. In case, the energy losses due to bremsstrahlung are not negligible, tracks reconstructed by the KF algorithm are refitted using a Gaussian sum filter (GSF) [207]. The GSF performance in simulation is shown in Fig. 6.2.

The electron seeds chosen as described above, are then used for the building of the electron track. The combinatorial KF method is employed – each electron seed is handled iteratively including each next tracker layer successively. Hereby, the energy loss of the electron is modeled using a Bethe-Heitler function, no more than one missing hit is allowed for a track candidate and a missing hit is reflected in the χ^2 of the track fit.

6.1.3 Association of track and cluster

After the successful reconstruction of the energy deposit in the ECAL and the track in the tracker, those two pieces of the electron reconstruction are matched. In case of ECAL-seeded electrons, the associated ECAL cluster is the one reconstructed using the multi 5×5 approach or the hybrid approach. If the electron is seeded using the tracker-based approach only, the electron PF cluster is associated. Special multivariate variables are defined in order to grade the quality of the track-cluster association. They are later used for grading of the reconstruction quality of the considered electron candidate.

6.1.4 Electron selection requirements

In the following, the selection requirements applied to electron candidates considered in the present thesis are summarized. It must be noted that the dielectron selection has been performed by the partner side at the Northeastern university and is shown here for completeness. The selected electron candidates have to satisfy a set of requirements in order to be considered in the final selection [208]. The transverse momentum of the considered electron has to satisfy $p_{\mathrm{T}} > 20$ GeV (which is set slightly over the trigger threshold of 17 GeV) and be reconstructed within $|\eta| < 2.5$, whereby the transition region $1.442 < |\eta| < 1.556$ is not considered. The $\Delta\eta$ between the track and the supercluster has to satisfy $\Delta\eta < 0.004$ in the barrel and $\Delta\eta < 0.007$ in the endcap region. For ϕ, the requirement is $\Delta\phi < 0.06$ for the barrel and $\Delta\phi < 0.03$ in the endcap. The jet–electron discriminating variable, the condition $\sigma_{i\eta i\eta} < 0.01$ in the barrel and $\sigma_{i\eta i\eta} < 0.03$ is set. The track distance to the primary vertex in the transverse plane has to be $d_0 < 0.02$ cm and the distance in the z direction has to satisfy $d_z < 0.1$ cm. In order to suppress electrons arising from interactions in the detector material, the ΔR with respect to muon candidates in the tracker has to be larger than 0.1. In order to minimize the contamination by hadronic jets, the ratio of the energy deposit of the associated track in the HCAL H compared to the energy deposit in the ECAL E has to be $H/E < 0.12$ in the barrel and $H/E < 0.1$ in the endcap. Since electrons are expected to be ultrarelativistic, a requirement is set on the difference of the inverse electron energy E and its inverse momentum p: $|\frac{1}{E} - \frac{1}{p}| < 0.05$ for both the barrel and endcap regions. In order to ensure that only well reconstructed electron tracks are considered, no electron candidates with more than one missing hit in the tracker are considered. Finally, in order to further suppress electrons originating from secondary vertices, the vertex fit probability has to satisfy $p > 10^{-6}$.

Any further electrons are used to veto on the selected event if they satisfy the veto ID. All selection requirements are summarized in Tab. 6.2.

6.1.5 Electron isolation requirement

The electrons considered in the final selection have to be isolated against other physics objects in CMS. For this, one defines an isolation variable $I^{\mathrm{e}}_{\mathrm{rel}}$. This variable is computed for particles within a cone of $\Delta R < 0.4$ of the considered electron candidate and takes into account the flux of neutral hadrons corrected for the multiple soft interactions during the bunch-bunch crossing (underlying

Requirement	Barrel $\lvert\eta\rvert < 1.4442$		Endcap $1.566 < \lvert\eta\rvert < 2.5$	
	Veto	Selection	Veto	Selection
$\Delta\eta$(track,SC)	< 0.007	< 0.004	< 0.01	< 0.007
$\Delta\phi$(track,SC)	< 0.8	< 0.06	< 0.7	< 0.03
$\sigma_{i\eta i\eta}$	< 0.01	< 0.01	< 0.03	< 0.03
H/E	< 0.15	< 0.12	-	< 0.1
d_0(vtx) (cm)	< 0.04	< 0.02	< 0.04	< 0.02
d_z(vtx) (cm)	< 0.2	< 0.1	< 0.2	< 0.1
ΔR from muon candidates	> 0.1		> 0.1	
$\lvert 1/E - 1/p\rvert$	-	<0.05	-	<0.05
Missing hits	-	≤ 1	-	≤ 1
Conversion vertex fit prob.	-	$>10^{-6}$	-	$>10^{-6}$

Table 6.2: Electron identification requirements used for both the selection and the veto of events. Only events containing exactly two electrons satisfying the selection requirement and no electrons satisfying the veto requirement are considered in the analysis [209].

event or pileup). The variable reads:

$$I^{\mathrm{e}}_{\mathrm{rel}} = \frac{1}{p_{\mathrm{T}}} \left[I_{\mathrm{ch}} + \max\left(I_{\mathrm{nh}} + I_{\mathrm{g}} - A_{\mathrm{eff}} \cdot \rho, 0 \right) \right]. \tag{6.1}$$

In this equation, I_{ch} and I_{nh} stand for charged and neutral hadron fraction respectively, I_{g} marks the photon contribution. ρ stands for the average energy deposit due to pileup in the effective detector area A_{eff}. The electron candidate is considered isolated when $I^{\mathrm{e}}_{\mathrm{rel}} < 0.15$.

6.2 Muons

The muons give the CMS detector its name and can be measured with high precision as outlined earlier. Special algorithms have been designed by the corresponding physics object group of CMS. On the following pages, the procedure of track reconstruction as well as quality requirements for the muon identification are discussed [210–212]. The following description is based on these sources.

6.2.1 Muon reconstruction in the tracker and the muon spectrometer

The muon track reconstruction in the tracker is performed in four steps. In the first step, the initial point of the track is determined based on the trajectory estimate. Two types of seeds are considered – the hit-based and the state-based seeds. In the second step, the trajectory is built. Starting at the position identified in the previous step, a combinatorial Kalman filter is applied for track finding and track fitting. Starting with track parameters $\tilde{p}_o$ and their covariance $C(\tilde{p}_i)$, the Kalman filter propagates those to the level $i+1$ using the known equation of motion. Hereby, the scattering effects are taken into account. Furthermore, the knowledge of the magnetic field and the effects of the

muon interaction with the detector material are taken into account. In the third step, ambiguities in possible trajectories are resolved whereby the maximal possible amount of track candidates is kept. In the last step, a backward fitting procedure is employed in order to smoothen the track candidates.

In the muon stations of CMS, the Kalman filter approach is also used for the muon reconstruction. Starting with the estimation of the seed state from the track segments, the track is iteratively built including more muon stations (DT, CSC and RPC are handled) in each iteration.

6.2.2 Global muon track reconstruction

The muon candidates considered in the present analysis have to be reconstructed in both the tracker and in the muon system. Such muons are colloquially called global muons as opposed to tracker- or muon-system-only muons. The latter are also often called stand-alone muons. The matching of the track from the tracker to the track in the muon system is performed in two steps. In the first step, a rectangular region of interest for the stand-alone muon track in the muon system is defined in the $\eta - \phi$ space and the corresponding tracker tracks are selected. Here, seven parameters are considered – the origin of the track, the spread from the origin in ΔZ and ΔR, the direction from the origin of the tracking region, the spread in $\Delta\phi$ and $\Delta\eta$ and finally the minimal p_{T} of the considered track (corresponding to the curvature of the track in the tracker). In the next step, an iteration is performed over those tracker tracks and the best combination of a tracker track and a stand-alone muon track based on the spatial and momentum matching criteria is selected. Five variables are used for the matching of the tracker track to the muon system track. For this, a common matching surface is selected. Based on the parameter space defined by $q/p, x, y, x', y'$, a set of five discriminating variables is employed:

1. The χ^2 of the similarity comparison using the covariance matrices C_i of the propagated tracks

$$\chi^2 = (\vec{p}_1 - \vec{p}_2)^T [C_1 + C_2]^{-1} (\vec{p}_1 - \vec{p}_2) \tag{6.2}$$

2. Comparison of the track positions on the plane in coordinates local to the plane

$$d = \sqrt{(x_1 - x_2)^2 + (y_1 + y_2)^2} \tag{6.3}$$

3. Comparison of the local position parameters by comparing χ^2 and considering the local covariance matrices C_{di} (hereby, $\vec{d} = \{x, y\}$)

$$\chi^2 = (\vec{d}_1 - \vec{d}_2)^T [C_{d1} + C_{d2}]^{-1} (\vec{d}_1 - \vec{d}_2) \tag{6.4}$$

4. Comparison of the track positions in the $\eta - \phi$ plane for the position vector at the surface

$$\Delta R = \sqrt{(\eta_1 - \eta_2)^2 - (\phi_1 - \phi_2)^2} \tag{6.5}$$

5. Comparison of the track directions in the same plane for the momentum vector at the primary vertex (also sometimes referred to as the impact parameter)

$$\Delta R_{\mathrm{IP}} = \sqrt{(\eta_1^{\mathrm{mom}} - \eta_2^{\mathrm{mom}})^2 + (\phi_1^{\mathrm{mom}} - \phi_2^{\mathrm{mom}})^2} \tag{6.6}$$

Subsequently, a global fit is performed for the selected tracker and muon tracks. This is performed for all pairs of tracks. In case, there are disambiguities, the global muon track with the lowest χ^2 is chosen.

There also exist algorithms which are especially suited for reconstruction of muon tracks with high p_T [213, 214]. Since the muons originating from a Z boson which recoils against undetectable particles are not expected to have a very hard p_T spectrum in the present scenario, this approach is not employed. For instance, this approach is used in [90].

6.2.3 Muon selection requirements

In order so ensure a good quality of the considered muon candidates, a set of requirements is introduced for each muon candidate considered in this thesis [215]. Each muon candidate has to satisfy the requirement $p_T > 20$ GeV (this requirement is set both for selecting muons with a p_T slightly higher than the trigger threshold as well as for synchronization purposes with the dielectron side). The muon candidate has to be reconstructed within the range $|\eta| < 2.4$. It must possess at least two muon chamber hits and two matched muon stations hit. Furthermore, it has to have at least one hit in the pixel tracker. At least six silicon tracker layers have to be present in the track. The impact parameter of the tracker track has to fulfill $d_{xy} < 0.2$ cm. The distance in the z direction has to be $d_z < 0.5$ cm. In addition to these criteria, the muon must be associated with a so called "good" vertex. A good vertex has at least four tracks associated with it and has to be reconstructed within a distance $d_z < 24$ cm in the z coordinate. This set of identification parameters is often referred to as "TightID". The requirements are summarized in Tab. 6.3. The identification efficiency of the "TightID" is found to be to be approximately 94% for both data and MC simulation. Data-to-MC scale factors are applied which depend on the p_T and $|\eta|$ of the considered muon candidate [216].

Variable	Selection	Veto
Global muon	true	
p_T	> 20 GeV	> 5 GeV
$\|\eta\|$	< 2.4	
Tracker layers	> 5	> 5
Muon chamber hits	> 1	
Matched muon station hits	> 1	
Pixel hits	> 0	
Pixel layers		>1
d_{xy}	<0.2 cm	< 3
d_z	<0.5 cm	< 30
χ^2/ndof (global)	< 10	
χ^2/ndof (inner)		< 1.8

Table 6.3: The requirements for the selection of muon candidates and the veto. Only events containing exactly two muons satisfying the selection requirement and no muons satisfying the veto requirement are considered in the analysis. The identification requirements are taken from [215], whereas the p_T requirement is introduced by the analyst.

6.2.4 Muon isolation

The selected muon candidates are required to be isolated against other physics objects in the considered event. The applied set of requirements corresponds to the so called combined relative particle flow isolation [215]. A special correction, the so called delta beta correction [217], is applied in order to correct for the effects caused by pileup. The muon isolation variable is computed for the considered muon candidate relative to all physics objects within a cone of$\Delta R < 0.4$ and is defined in a similar way to the electron isolation variable via:

$$I^{\mu}_{\text{rel}} = \frac{1}{p_{\text{T}}} \left[I_{\text{ch}} + \max\left(I_{\text{nh}} + I_{\text{g}-0.5\cdot I_{\text{chPU}}}, 0 \right) \right]. \tag{6.7}$$

Hereby, I_{ch} denotes the charged hadron transverse energy deposit, I_{nh} stands for the neutral, and I_{g} denotes the photon contribution. $0.5 \cdot I_{\text{chPU}}$ marks the pileup contribution which is subtracted in terms of the delta beta correction as stated above. Only muons with $I^{\mu}_{\text{rel}} < 0.2$ are considered in the selection.

6.2.5 Muon momentum scale and resolution

The muon momentum scale and resolution are studied using different techniques in different p_{T} ranges. For muons with $p_{\text{T}} \lesssim 100$ GeV, the resonant decays of J/ψ and Z boson are used for the determination of momentum scale and resolution. For studies of muon momentum scale and resolution at transverse momenta above 100 GeV, cosmic muons traversing the CMS detector are used.

6.3 Hadronic Jets

One important part of physics at hadron colliders is the reconstruction of hadronic jets (also simply referred to as jets). For dark matter signatures produced at the LHC, the cross section fraction with an additional hadronic jet in the final state is found to be of the same order of magnitude as the production without additional jets. Therefore, the reconstruction procedure of jets is discussed briefly in the next sections [218].

6.3.1 Anti-k$_t$ algorithm

The jet reconstruction in CMS uses the anti-k$_t$ algorithm which is an extension of the k$_t$ [219] and Cambridge/Aachen [220, 221] jet reconstruction algorithms [222]. One starts by defining the distances d_{ij} between the respective entities (which can be particles or pseudojets) i and j, and the distance d_{iB} of an entity i to the beam B. The clustering is performed by recognizing the smallest of all distances and in case it is between i and j, those are recombined; in case it is between i and B, i is recognized as a jet and removed from the list of entities. This procedure of recalculating distances is repeated until the entities list is empty. Here, the extension of both the k$_t$ and the Cambridge/Aachen

algorithms lies in the definition of the of the distance definition. One defines [222]:

$$d_{ij} = \min\left(k_{ti}^{2p}, k_{tj}^{2p}\right)\frac{\Delta_{ij}^2}{R^2}, \tag{6.8}$$

$$d_{iB} = k_{ti}^{2p}. \tag{6.9}$$

Here, $\Delta_{ij}^2 = (y_i - y_j)^2 + (\phi_i - \phi_j)^2$ is the distance in terms of the rapidity y and azimuth ϕ, and k_{ti} denotes the transverse momentum of particle i. The already known radius parameter R is joined by an additional parameter p. The value of $p = 1$ corresponds to the inclusive k_t algorithm, the $p = 0$ case covers the inclusive Cambridge/Aachen algorithm. The choice of $p = -1$ is called the anti-k_t algorithm. The resulting jet reconstructing algorithm is infrared and collinear safe and works faster than alternatives mentioned above. The procedure of track and calorimeter energy deposits reconstruction for jets is discussed in Sec. 6.4.

6.3.2 Jet selection requirements

Jet are selected following the official jet selection requirement of the CMS working groups. The jet selection in the current analysis follows the so called Loose selection [223]. The jets considered in the selection must have a transverse momentum $p_T > 30$ GeV and be reconstructed in the pseudorapidity range $|\eta| < 5.0$. The neutral hadron fraction has to satisfy < 0.99 and the neutral EM fraction < 0.99. The number of constituents has to be larger than 1. The jets in the barrel region have to have a hadron fraction > 0 and the charged multiplicity > 0 along with the charged EM fraction > 0.99. Only events with up to one jet satisfying the requirements summarized in this section are considered. All collision events with two or more jets satisfying these requirements are banned from the selection.

6.3.3 B tagged jets

Top quark decays will always produce b quark hadrons since the top quark dominantly decays in the chain $t \rightarrow bW$ [32]. B quark hadrons furthermore possess a lifetime which is long enough for traveling a measurable distance from the interaction point and therefore jets arising from or containing b hadrons can be registered using this property. Several algorithms have been developed in order to distinguish b jets from other hadron decays in CMS. These approaches employ the information about the impact parameter (IP) and the reconstruction of a secondary vertex. The following description of these methods is based on [224, 225].

The impact parameter of a track is defined as the closest distance from the primary vertex to the track. The distribution of the impact parameter values for the b quark has a different shape than for other quark flavor (cf. Fig. 6.3). Based on the significance of the impact parameter, a discriminator variable is introduced. In addition to that, the presence of a secondary vertex is evaluated. Within the jet, an adaptive vertex fitter is used [226]. The fitter delivers a set of vertices which are then cleaned based on the associated tracks - only candidates which share less than 65% of their tracks with the primary vertex survive this selection. In order to reject neutral kaons, the candidates with a radial distance from the primary vertex $d > 2.5$ cm are rejected if their mass is compatible with the kaon mass. The secondary vertex candidate has to be measured within a $\Delta R < 0.5$ of the original jet direction. Based on these considerations, three discriminator values are

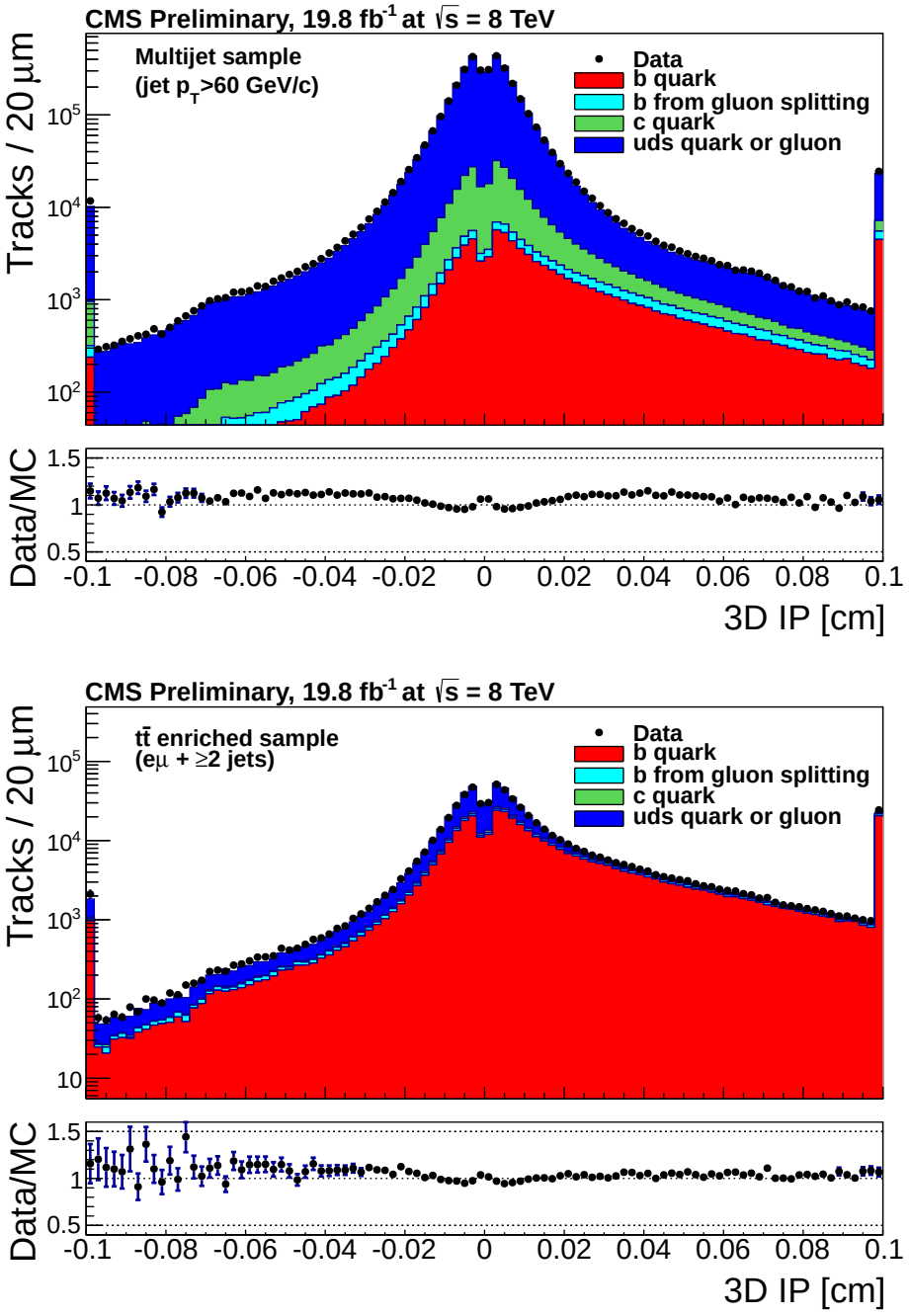

Figure 6.3: Distribution of the 3-dimensional impact parameter for a multijet (top) and $t\bar{t}$ enriched sample measured with CMS in 2012. On the right (bottom) of each distribution, the contribution is added in one overflow (underflow) bin [224].

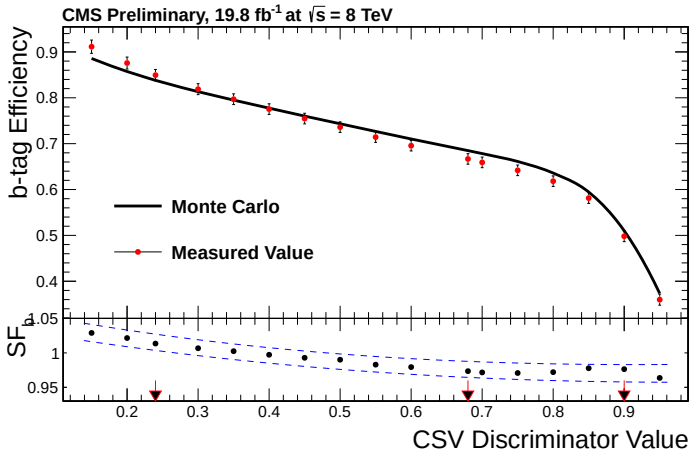

Figure 6.4: B tagging efficiency as function of the CSV discriminator variable shown for Monte Carlo simulation and data in $t\bar{t}$ events. The arrows on the x-axis indicate the three working points (from left to right) –"Loose", "Medium" and "Tight". The lower panel shows the scaling factor between data and simulation [224].

provided by the reconstruction algorithm. *Track Counting High Purity* discriminator is defined as the impact parameter significance of the track with the third highest impact parameter significance, *Jet Probability* is a likelihood that all associated tracks come from the primary vertex and the *Combined Secondary Vertex* (CSV) discriminator variable which is computed using secondary vertices and track-based lifetime information. The latter is used in the present analysis for the tagging of b jets since the events containing b jets are vetoed for background suppression purposes (leptonic decays of top quark pairs can lead to a dilepton+$E_{\mathrm{T}}^{\mathrm{miss}}$ signature). The distribution of the CSV discriminator variable is shown in Fig. 6.4.

The b jets considered in the present analysis have to be tagged as such by the CSV discriminator at the "Loose" working point. For b tagged jet candidates, the p_{T} threshold is lower – jets with $p_{\mathrm{T}} > 20$ GeV are selected (cf. to the $p_{\mathrm{T}} > 30$ GeV requirement in Sec. 6.3.2).

Studies of the efficiency of the b tagging algorithm have been performed in order to estimate the difference between tagging measured events and events from simulation. A scaling factor as a function of the p_{T} of the b tagged jet for the CSV algorithms has been derived in order to account for the different b tagging efficiency [227]:

$$\mathrm{SF} = \left(0.927563 + \left(\frac{1}{\mathrm{GeV}} \cdot 0.000015547 \cdot p_{\mathrm{T\,jet,btag}}\right) + \left(-\frac{1}{\mathrm{GeV}}(1.90666\mathrm{e}-07) \cdot p_{\mathrm{T\,jet,btag}}\right)^2\right). \quad (6.10)$$

The scale factor are applied to the resulting MC spectrum of the selection stages where the b tag veto is applied.

6.4 Particle Flow

Particles produced in collisions at CMS will propagate from the primary vertex to the outside of CMS. They are measured in respective subdetectors, often in two or even more at the same time. In order to increase the identification and reconstruction efficiencies of particles in CMS, a concept of Particle

Flow has been introduced [228, 229]. In the PF approach, the information from all subdetectors is included for the reconstruction of particle propagation through CMS. As a result, not only the reconstruction quality of a single particle candidate improves – the reconstruction performance of the collision event over all can be improved. This has a great impact on the present analysis since the physical quantity of interest $E_{\mathrm{T}}^{\mathrm{miss}}$ is influenced by the reconstruction efficiencies of *all* object present in the event. The reconstruction of separate physics objects has been described above. Here, the particle flow algorithm combining the information from previous reconstruction steps is to be described based on [228, 229].

6.4.1 Linking algorithm

Each particle in CMS is generally expected to produce more than one particle-flow element. For example, a hadronic jet, say a π^0, will produce photons and a number of further particles. In order to take this phenomenon into account, a linking algorithm is used. This algorithm is called for each pair of elements in an event and produces blocks of elements using the spacial distance between those elements for quantifying the grade of the link. In this matter, a track between a charged-particle track and a calorimeter cluster is linked as follows. In the first step, the track is extrapolated from the last tracker hit to the preshower and to the ECAL (HCAL), taking a typical depth of an electron (hadron) shower into account. If the extrapolated position of the track lies inside the cluster borders, the track is then linked to this cluster. Also, track tangents are extrapolated from the intersection points of the track and the tracker layers to the ECAL in order to take energy losses due to Bremsstrahlung into account. The link between an ECAL and an HCAL cluster or between ECAL and the preshower can be performed using the cluster borders in the calorimeter with the smaller granularity. The muon tracks are matched following the procedure described in 6.2.

6.4.2 Particle reconstruction

The particle flow algorithm iterates over the blocks produced in the previous step and then performs the following steps. First, every global muon (cf. Sec 6.2), triggers the creation of a particle-flow muon if the global muon momentum is compatible with the tracker only momentum within three standard deviations σ. The track associated with the global muon is then removed from the block also taking into account an estimate of the energy deposit in the ECAL and the HCAL. In the next step, the electrons reconstructed following the procedure described in Sec. 6.1 are used for creating particle-flow electrons. The respective tracks and ECAL clusters are then removed from the block. The remaining tracks experience tighter quality requirements. Here, the relative uncertainty of the measured p_{T} is to be smaller than the corresponding relative calorimeter resolution for charged hadrons. An important decision has to be made by the algorithm since the remaining tracks can be connected to both ECAL and HCAL clusters whilst also being fake tracks. The ECAL clusters linked to any of the remaining tracks are ordered corresponding to their distance to the closest track in the first step. Secondly, this list is scanned and is kept the way it is as long as the total calibrated calorimeter energy is smaller than the total momentum of the charged particle. All remaining tracks in the block are considered to be particle flow charged hadrons whereby the momentum is taken from the track under the hypothesis of the charged pion mass. In case the calorimeter energy is in

agreement with the track momentum within the uncertainties, a fit is performed and the momentum is taken from this fit. In case significantly more energy is found in the calorimeter, a particle flow photon is assumed. If the excess is larger than the total energy deposit in the ECAL, a particle-flow hadron for the remaining excess is created in addition. This is founded in the observation that photons are responsible for around 25% of total energy in jets and only 3% of the energy in the ECAL is deposited by neutral hadrons. The remaining unassigned ECAL (HCAL) clusters give rise to particle-flow photons (particle-flow neutral hadrons).

6.5 Missing transverse energy

The missing transverse energy $E_{\mathrm{T}}^{\mathrm{miss}}$ is the final physical quantity considered in the present thesis. It is defined by:

$$\vec{E}_{\mathrm{miss}}^{\mathrm{T}} = -\sum_{i}^{N_{\mathrm{PF}}} p_{i,\mathrm{T}}. \tag{6.11}$$

In this equation, an iteration is performed over N_{PF} reconstructed particle flow particle candidates [229]. The magnitude of $\vec{E}_{\mathrm{miss}}^{\mathrm{T}}$ is denoted by $E_{\mathrm{T}}^{\mathrm{miss}}$. The $E_{\mathrm{T}}^{\mathrm{miss}}$ of the event is reconstructed from all present particles therefore being subject to detector effects (e.g. electronic noise) and imperfect resolution of the detector. Studies have been performed aiming to estimate the performance of $E_{\mathrm{T}}^{\mathrm{miss}}$ reconstruction at CMS [230, 231]. As a result, corrections are applied to the measured $E_{\mathrm{T}}^{\mathrm{miss}}$ spectrum in order to take the known detector effects into account.

6.5.1 $E_{\mathrm{T}}^{\mathrm{miss}}$ corrections and filters

The most important correction to the $E_{\mathrm{T}}^{\mathrm{miss}}$ is the so called *Type-I* corrections. This correction propagates the effects of jet energy corrections (JEC) (cf. to Sec. 7.5) into the calculation of $E_{\mathrm{T}}^{\mathrm{miss}}$. One loops over all jets with a $p_{\mathrm{T}} > 10\mathrm{GeV}$ in an event and sums up the applied corrections. Thus, one defines the *Type-I* corrected missing energy via

$$\vec{E}_{\mathrm{miss,Corr.I}}^{\mathrm{T}} = \vec{E}_{\mathrm{miss,raw}}^{\mathrm{T}} - \vec{\Delta}_{\mathrm{JEC}}, \tag{6.12}$$

where $\vec{\Delta}_{\mathrm{JEC}}$ contains the vector sum of the corrections. One further correction is the $x-y$ correction where the $E_{\mathrm{T}}^{\mathrm{miss}}$ is corrected for the slight ϕ asymmetry arising from a detector misalignment, tracker asymmetry and the shift of the interaction points in the $x-y$ plane. This correction is performed for data and simulation and is based on the number of reconstructed vertices in the present event. The correction has a form of $c_i^0 + c_i^1 \cdot N_{\mathrm{vtx}}$ where $i = x, y$.

Furthermore, special filters have been developed in order to filter events with not reliable $E_{\mathrm{T}}^{\mathrm{miss}}$. Multiple effects can lead to an unreliable measurement of $E_{\mathrm{T}}^{\mathrm{miss}}$ and the corresponding filters are:

- CSC beam halo filter – the measurements in CSC are used in order to remove events from beam halo
- HBHE noise filter – the events with electronics noise from Hybrid Photo Diodes and the Readout box in HB and HE are removed

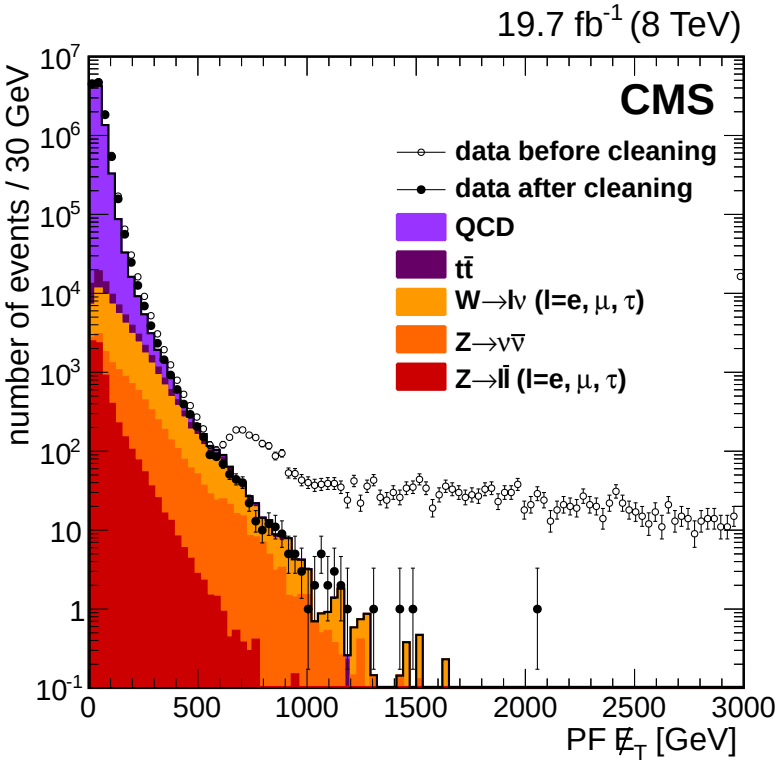

Figure 6.5: Distribution of particle flow $E_{\mathrm{T}}^{\mathrm{miss}}$ for a dijet selection. The data points with empty markers denote the selection before the employment of the $E_{\mathrm{T}}^{\mathrm{miss}}$ filters, the filled data points denote the selection after $E_{\mathrm{T}}^{\mathrm{miss}}$ filters have been applied [231].

- HCAL laser filter – events with the calibration laser firing into the HCAL with wrong timing are removed
- ECAL laser filter – events with the calibration laser firing into the ECAL with wrong timing are removed
- Tracking failure filter – events in which the tracking algorithm failed due to a large multiplicity of tracks are removed
- Bad EE Supercluster filter – events with large energy deposits in the ECAL
- Particle based noise rejection – events with large and trustless energy deposits in the ECAL and HCAL are removed.

Fig. 6.5 shows the distribution of $E_{\mathrm{T}}^{\mathrm{miss}}$ before and after the filter requirement.

CHAPTER 7

Analysis Strategy

In this chapter, the analysis is explained in detail. The two channels – $Z \to ee$ and $Z \to \mu\mu$ – were analyzed by two groups working close together and therefore synchronizing their selection requirements. The dielectron part of the analysis was performed by the Northeastern group whilst the dimuon decay channel analysis was performed in Aachen by the presenter of this thesis. Since the results of both groups are published in one paper [1] and the public result includes combined exclusion limits, both the electron (detailed description available for collaboration review in [209] and [232]) and the muon (detailed description available for collaboration review in [233]) side of the analysis are therefore discussed in the present thesis. For purposes of synchronized demonstration of results for both sides of the analysis, only one framework – the framework employed at the Northeastern university – was used for plotting the final figures. All input needed for these figures concerning the dimuon final state as well as the dimuon contribution to the combined exclusion limits (final yields, $E_{\mathrm{T}}^{\mathrm{miss}}$ and m_{T} distributions, datacards for statistical combination, the uncertainties etc.) was hereby provided by the presenter of this thesis.

In section 7.1, the background estimation, the signal prediction and the CMS dataset from 2012 are presented. In section 7.3, the summary of requirements is given for the best possible signal extraction – the different analysis stages are also discussed. In section 7.5, the systematic uncertainties considered in the final selection are discussed.

7.1 Datasets

Three kinds of datasets are to be considered in the present search for new physics. First, one has to estimate the contribution from the new physics signature one is interested in – this signature is also often called the signal. Once a theoretical prediction is published and discussed, one has to perform a full simulation of the signal samples, preferably for a set of different parameters of the considered theory. In this manner, one can study the special characteristics of the signal in the experimental environment. The second step is the estimation of the contributing backgrounds. As one will see in the following, the possible signatures of dark matter and unparticles could appear on top of many standard model processes. Therefore, a careful examination of all standard model contributions

to the final state in which the search for new physics is performed is crucial. After these steps are established and performed, the dataset delivered by the experiment is compared to the background estimation and the predicted signal contribution is considered in addition to the standard model backgrounds. In case the standard model expectations are not met, one can speak of a hint for new physics and has to statistically evaluate the significance of the found disagreement and whether it can be interpreted in terms of the studied signal scenario.

7.1.1 Signal samples for dark matter and unparticles

The signal samples considered in the present analysis have been generated using MC simulation. The dark matter scenario of an effective field theory has been implemented in `MadGraph` and corresponding samples have been produced for different values of m_χ and different coupling types, namely:

$$\begin{aligned}
&\text{Vector, spin independent (D5)}: && \frac{\bar{\chi}\gamma^\mu\chi\bar{q}\gamma_\mu q}{\Lambda^2};\\
&\text{Axial vector, spin dependent (D8)}: && \frac{\bar{\chi}\gamma^\mu\gamma^5\chi\bar{q}\gamma_\mu\gamma^5 q}{\Lambda^2};\\
&\text{Tensor, spin dependent (D9)}: && \frac{\bar{\chi}\sigma^{\mu\nu}\chi\bar{q}\sigma_{\mu\nu} q}{\Lambda^2};\\
&\text{Vector, spin independent (C3)}: && \frac{\chi^\dagger\overleftrightarrow{\partial_\mu}\chi\bar{q}\gamma^\mu q}{\Lambda^2}.
\end{aligned} \tag{7.1}$$

Hereby, interaction operators marked by "D" represent a Dirac fermion WIMP hypothesis whilst "C" denotes the complex scalar WIMP scenario. The choice of the WIMP scenario and the effective field theory operators aims to cover the broadest possible selection of particle and coupling types – vector, axial vector, tensor. For all particle and coupling scenarios, a set of samples with m_χ = 1, 10, 100, 200, 300, 500, 1000 GeV with 60000 events each has been generated in `MadGraph` and subsequently simulated in a full `GEANT4` CMS detector simulation. The hadronization was performed by `Pythia` 6.4.26 with the $Z2*$ parton showering tune. The corresponding parton distribution function set is CTEQ6L [234]. In the generation step, the Z boson is assumed to decay in either a pair of electrons or muons in the presence up to one jet – either initial or final state radiation. The effective cutoff scale is set to Λ = 1000 GeV. The corresponding Feynman diagrams are shown in Fig. 7.1. The graphic representation of the Feynman diagrams does not depend on the coupling type or the value of m_χ. The table of all samples along their normalization cross sections times the branching ratio into a lepton pair can be found in Tab. 7.1. Since the branching ratios (BR) of the Z boson decay into electrons and into muons are equal, the cross section portions for each channel are also equal.

Unparticle samples are produced using the `Pythia8` generator using the 4C tune [104]. The Z boson decay into electrons and muons are handled in separate datasets. The theory parameter of interest is $d_\mathcal{U}$, which runs over values between 1.01 and 2.2 with different granularity. The corresponding cross section times branching ratio is shown in Tab. 7.2. The energy scale is chosen to $\Lambda_\mathcal{U}$ = 15 TeV. The Feynman graphs for the unparticle production are shown in Fig. 7.2. The graphic representation of the Feynman diagrams does not depend on the value of $d_\mathcal{U}$ or $\Lambda_\mathcal{U}$.

Signal sample	m_χ(GeV)	Coupling	σ(fb)× BR
EFT_FermionWIMP_M1_D5	1	vector	0.749
EFT_FermionWIMP_M10_D5	10	vector	0.751
EFT_FermionWIMP_M100_D5	100	vector	0.716
EFT_FermionWIMP_M200_D5	200	vector	0.599
EFT_FermionWIMP_M300_D5	300	vector	0.463
EFT_FermionWIMP_M500_D5	500	vector	0.237
EFT_FermionWIMP_M1000_D5	1000	vector	0.0270
EFT_FermionWIMP_M1_D8	1	axial-vector	0.743
EFT_FermionWIMP_M10_D8	10	axial-vector	0.746
EFT_FermionWIMP_M100_D8	100	axial-vector	0.616
EFT_FermionWIMP_M200_D8	200	axial-vector	0.424
EFT_FermionWIMP_M300_D8	300	axial-vector	0.275
EFT_FermionWIMP_M500_D8	500	axial-vector	0.106
EFT_FermionWIMP_M1000_D8	1000	axial-vector	0.00689
EFT_FermionWIMP_M1_D9	1	Tensor Coupling	13.554
EFT_FermionWIMP_M10_D9	10	Tensor Coupling	13.621
EFT_FermionWIMP_M100_D9	100	Tensor Coupling	12.330
EFT_FermionWIMP_M200_D9	200	Tensor Coupling	9.8470
EFT_FermionWIMP_M300_D9	300	Tensor Coupling	7.3537
EFT_FermionWIMP_M500_D9	500	Tensor Coupling	3.5951
EFT_FermionWIMP_M1000_D9	1000	Tensor Coupling	0.36975
EFT_ScalarWIMP_M1_C3	1	vector (C3)	0.18701
EFT_ScalarWIMP_M10_C3	10	vector (C3)	0.18657
EFT_ScalarWIMP_M100_C3	100	vector (C3)	0.15401
EFT_ScalarWIMP_M200_C3	200	vector (C3)	0.10602
EFT_ScalarWIMP_M300_C3	300	vector (C3)	0.068642
EFT_ScalarWIMP_M500_C3	500	vector (C3)	0.026282
EFT_ScalarWIMP_M1000_C3	1000	vector (C3)	0.0017185

Table 7.1: List of all dark matter Mono-Z MC samples produced with `MadGraph` including up to one addition jet at a center of mass energy $\sqrt{s}$ = 8 TeV. The working point for all masses is set to Λ = 1000 GeV. The signal samples are simulated on tree level – no loop corrections are considered.

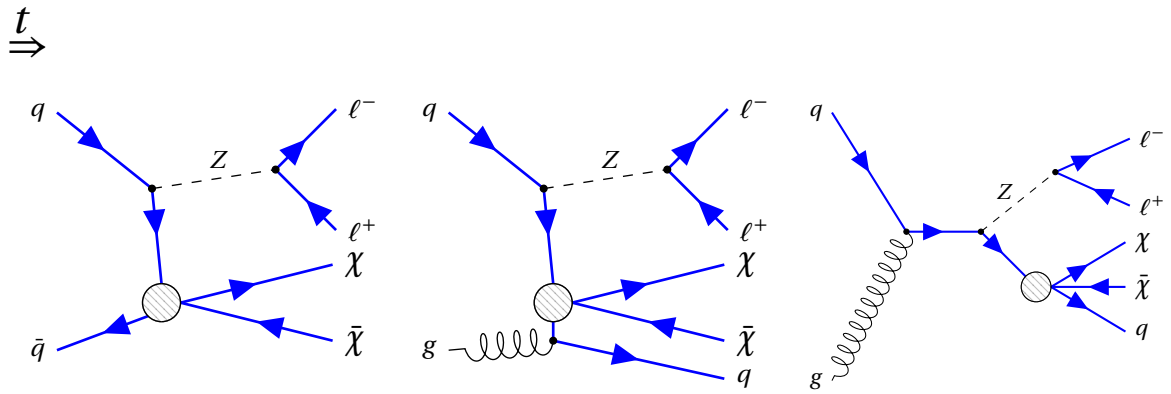

Figure 7.1: Dark matter signatures considered in the present thesis. The Z boson is produced in a proton-proton collision and recoils against two undetectable dark matter particles χ subsequently decaying into a pair of electrons or muons. Also scenarios with radiation of one jet are studied. The time axis is horizontal as indicated above the diagrams. The dashed circle represents the interaction modeled by the effective field theory.

Signal sample	$d_{\mathcal{U}}$	σ(pb)× BR
Unpart_ZToMuMu_SU-0_dU-2p20_LU-15	2.2	1.04×10^{-5}
Unpart_ZToMuMu_SU-0_dU-2p00_LU-15	2.0	1.43×10^{-4}
Unpart_ZToMuMu_SU-0_dU-1p90_LU-15	1.9	5.01×10^{-4}
Unpart_ZToMuMu_SU-0_dU-1p80_LU-15	1.8	0.002236
Unpart_ZToMuMu_SU-0_dU-1p70_LU-15	1.7	0.008583
Unpart_ZToMuMu_SU-0_dU-1p60_LU-15	1.6	0.03758
Unpart_ZToMuMu_SU-0_dU-1p50_LU-15	1.5	0.14
Unpart_ZToMuMu_SU-0_dU-1p40_LU-15	1.4	0.604
Unpart_ZToMuMu_SU-0_dU-1p30_LU-15	1.3	2.435
Unpart_ZToMuMu_SU-0_dU-1p20_LU-15	1.2	9.201
Unpart_ZToMuMu_SU-0_dU-1p10_LU-15	1.1	29.2
Unpart_ZToMuMu_SU-0_dU-1p09_LU-15	1.09	31.1
Unpart_ZToMuMu_SU-0_dU-1p06_LU-15	1.06	36.97
Unpart_ZToMuMu_SU-0_dU-1p04_LU-15	1.04	35.19
Unpart_ZToMuMu_SU-0_dU-1p02_LU-15	1.02	25.52
Unpart_ZToMuMu_SU-0_dU-1p01_LU-15	1.01	15.52

Table 7.2: List of unparticle samples along a $Z \to \mu\mu$ decay at a center of mass energy $\sqrt{s} = 8$ TeV with different values of $d_{\mathcal{U}}$ (denoted in the sample name by dU) and the corresponding normalization cross section times the branching ratio. $Z \to ee$ signal samples are generated in the same way possessing the same properties.

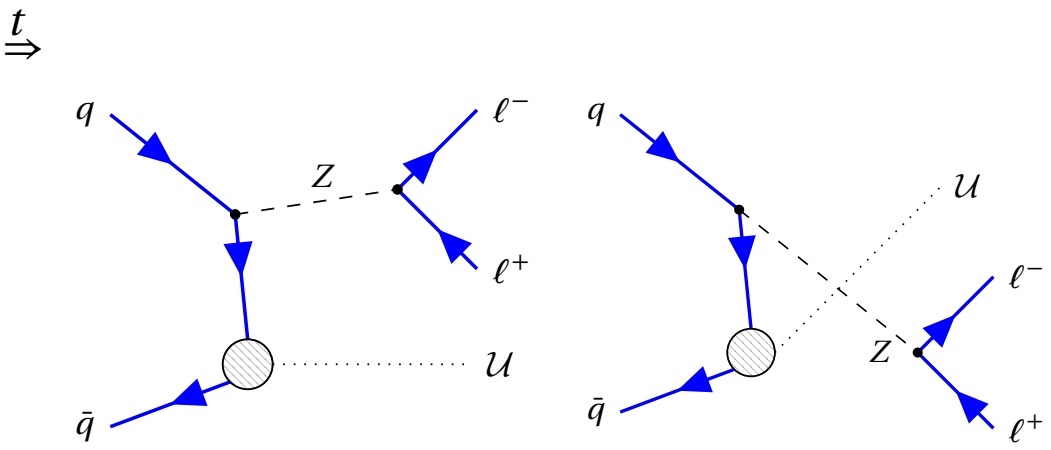

Figure 7.2: Feynman diagrams for unparticle $\mathcal{U}$ production in association with a Z boson which subsequent decays into a pair of electrons or muons. The time axis is horizontal as indicated above the diagrams. The hatched circles indicate the interaction modeled with an effective field theory.

Directly after the generation step, it is salutary to review the kinematic variable of interest on generation level. This brings several benefits – the general knowledge of the signal shape which is beneficiary for designing the selection requirements and the review of the selection efficiency after the detector simulation. Comparing the generation level and the reconstructed level of the signal can hence bring a lot of insight into the experimental challenges of hypothetical signal detection. The normalized distribution of different dark matter signal scenarios along the leading background $ZZ \to \ell\ell\nu\nu$ on generation level are shown on the left hand side of Fig. 7.3. The $E_{\mathrm{T}}^{\mathrm{miss}}$ at generation level of unparticles production along the leading background $ZZ \to \ell\ell\nu\nu$ is shown on the right hand side of Fig. 7.3. Further figures are available in the Appendix (cf.Fig. 9.1 and Fig. 9.2).

7.1.2 Background samples

The background samples include several processes of the standard model – the standard model production of Z boson via quark-antiquark annihilation (Drell-Yan process), the production of single top quark or top quark pairs and diboson processes – ZZ, WZ and WW. The backgrounds for the dimuon side are summarized in Tab. 7.3. The Parton Distribution Function set used for the production is also shown (cf. Sec. 7.5.6). Due to the fact, that Monte Carlo samples of standard model processes present with different kinematics and were produced with different generators and corresponding sets of settings, the background estimation based on each sample has to be carefully examined. This is done in Sec. 7.4.

7.1.3 CMS data

The dataset accumulated by CMS in 2012 corresponding to the integrated luminosity of $\int \mathcal{L}\,\mathrm{d}t = 19.7\ \mathrm{fb}^{-1}$ is analyzed in the present analysis [235]. The dataset consists of four different Runs (data taking sequences) which are listed in Tab. 7.4. The total amount of events entering the analysis for the dimuon side adds up to over 10^6 events.

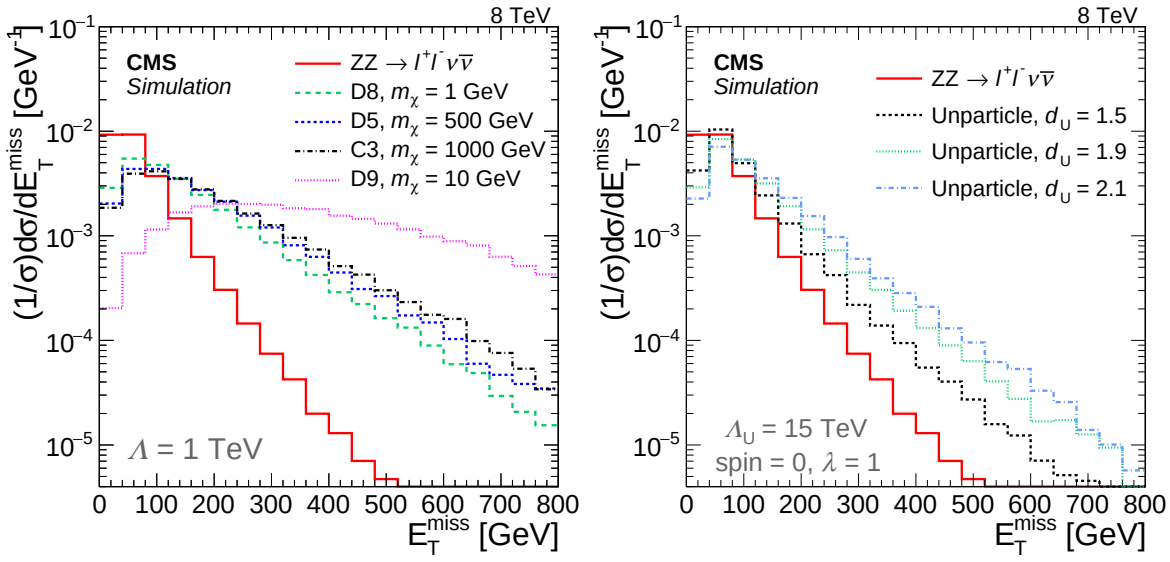

Figure 7.3: The normalized distribution in $E_{\mathrm{T}}^{\mathrm{miss}}$ at the generator level, for DM (left) and unparticle (right) scenarios. The DM curves are shown for different m_χ with vector (D5), axial-vector (D8), and tensor (D9) coupling for Dirac fermions, and vector (C3) coupling for complex scalar particles. The scaling dimension $d_{\mathcal{U}}$ ranges from 1.5 to 2.1. The SM background $ZZ \to \ell^-\ell^+\nu\nu$ is shown as a red solid curve [1].

Process	Generator	σ(pb)	PDF set
$WW \to 2\ell 2\nu$	MadGraph	5.995 (NLO)	CTEQ6L1
$ZZ \to 2\ell 2\nu$	MadGraph	0.38 (NLO)	CTEQ6L1
$WZ \to 3\ell 1\nu$	MadGraph	1.057 (NLO)	CTEQ6L1
$\bar{t}W$	Pythia	11.1 (NNLO)	CTEQ6L1
tW	Pythia	11.1 (NNLO)	CTEQ6L1
$t\bar{t}$	Powheg	245.8 (NNLO)	CT10
$W+$Jets	MadGraph	36257 (NNLO)	CTEQ6L1
$Z \to \mu\mu$	Madgraph	various (NNLO)	CT10

Table 7.3: Summary of MC background samples and the corresponding production generators. The $Z \to \mu\mu$ background sample is binned based on the number of jets (1…4). The cross section σ is given as the overall normalizing parameter of the MC sample.

Dataset	Run range
/DoubleMu/DoubleMu_Run2012A-22Jan2013-v1	190645–193621
/DoubleMu/DoubleMuParked_Run2012B-22Jan2013-v1	193834–196531
/DoubleMu/DoubleMuParked_Run2012C-22Jan2013-v1	198049–203709
/DoubleMu/DoubleMuParked_Run2012D-22Jan2013-v1	203777–206088

Table 7.4: Datasets and run ranges of the double muon triggered datasets in 2012. The integrated luminosity adds up to 19.7fb^{-1}.

Dataset	Trigger paths
$\mu\mu$	HLT_Mu17_TkMu8
$e\mu$	HLT_Mu8_Ele17_CaloIdT_CaloIsoVL_TrkIdVL_TrkIsoVL
	HLT_Mu17_Ele8_CaloIdT_CaloIsoVL_TrkIdVL_TrkIsoVL

Table 7.5: High level triggers employed for the selection of the present thesis. For the $e\mu$ case, a logical OR condition is set on the trigger signal, meaning that it is enough for one trigger to fire. This approach ensures the prevention double counting of events.

7.2 Triggering

The event selection is performed based on a dimuon triggers and cross triggers for $e\mu$ selection, whereby the $e\mu$ final state is used for the estimation of non-resonant backgrounds (cf. Sec. 7.4.2). The triggers are shown in Tab. 7.5. The efficiency of the dimuon trigger has been studied by the corresponding object reconstruction group within CMS and the efficiency difference in triggering simulated and data events was found to be negligible [236].

7.3 Event Selection

The selection of events begins with the requirement set on the physics objects. Those are elaborately discussed in Sec. 6. The next step is the consideration of special features of the studied signal – these features can be used for suppression of background processes and improving the sensitivity of the analysis towards a possible signal. The findings of these studies are summarized in the following section. Fig. 7.4 shows the expected distribution of missing transverse energy $E_{\mathrm{T}}^{\mathrm{miss}}$ after a basic muon pair selection, which only requires the identification and isolation of the muons. It is visible that the Drell-Yan process is dominant in the low $E_{\mathrm{T}}^{\mathrm{miss}}$ region ($E_{\mathrm{T}}^{\mathrm{miss}} < 100$ GeV) and that top quark processes and diboson production become important in the region with $E_{\mathrm{T}}^{\mathrm{miss}} > 100$ GeV. Two example signal contributions with D9 coupling at $m_\chi = 10$ GeV and D5 coupling at $m_\chi = 1$ GeV are shown. This display motivates the event selection discussed in this chapter. It is visible that the $E_{\mathrm{T}}^{\mathrm{miss}}$ contribution of dark matter production is expected to present with a rather broad $E_{\mathrm{T}}^{\mathrm{miss}}$ spectrum. Thus, reducing top and dibosonic contributions in the high $E_{\mathrm{T}}^{\mathrm{miss}}$ region is crucial for optimizing the sensitivity of the present analysis. The diboson $ZZ \to \ell\ell 2\nu$ background is irreducible due to the

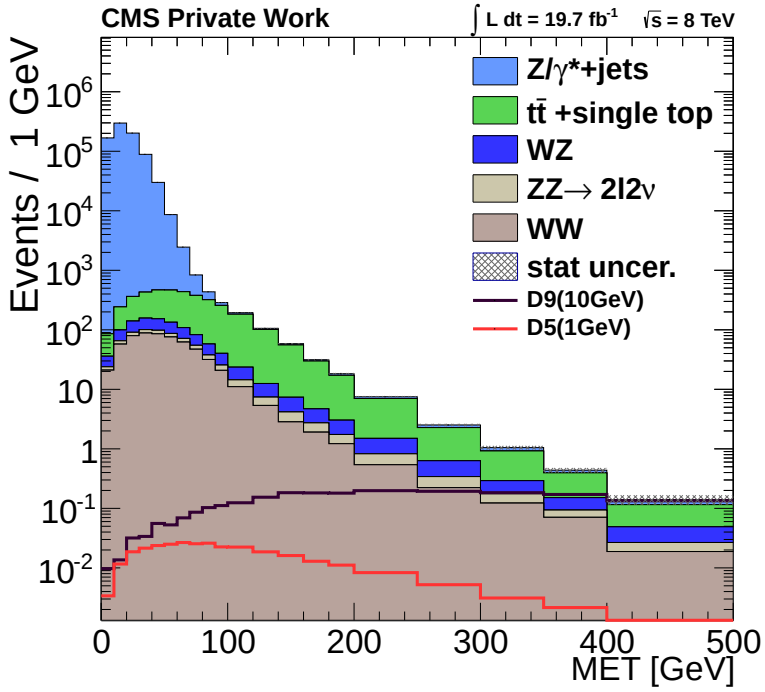

Figure 7.4: Simulated $E_{\mathrm{T}}^{\mathrm{miss}}$ distribution of background contributions for a basic dimuon selection. One can see that the Drell-Yan contribution leads in the low $E_{\mathrm{T}}^{\mathrm{miss}}$ region whilst top quark production is dominant in the high $E_{\mathrm{T}}^{\mathrm{miss}}$ region. One scenario for D9 coupling with $m_{\chi} = 10$ GeV and a scenario for D5 coupling with $m_{\chi} = 1$ GeV are shown. The value of Λ is set to 1000 GeV.

fact that its kinematics are very similar to those of the hypothetical signal (Z boson recoiling against a pair of undetectable particles). It should be further noted that the overall normalization of the plotted dark matter signal contribution scales as a function of the cutoff parameter Λ (cf. Eq 7.1) which is set to 1000 GeV in the analyzed signal samples. Therefore, the shape of the dark matter $E_{\mathrm{T}}^{\mathrm{miss}}$ spectrum plays a major role in the signal sensitivity optimization since the value of parameter Λ, in case of the existence of a dark matter signal, is unknown.

7.3.1 Invariant mass of the lepton pair

Dilepton pairs which accompany the pair of dark matter particles χ always arise from a Z boson decay in the considered scenario (cf. Fig. 7.1 and Fig. 7.2). Therefore, it is natural to expect that the only dilepton pairs with an invariant mass of the Z boson can contribute to the detection of dark matter. Fig. 7.5 shows the invariant mass spectrum of muon pairs after performing the basic selection of physics objects, whereby only the identification requirement is set.

One observes that the measured data is well described by the standard model prediction and that signal processes have a peak around the Z mass. It is visible that within ± 10 GeV with respect to the Z boson mass the expected contribution from signal processes drops significantly. As a consequence, no significant signal contributions are expected outside of this region. It is also apparent from Fig. 7.5 that all background processes involving the production of a Z boson (also sometimes referred to as "resonant" backgrounds) also have peak in the same area whereas background processes without a Z

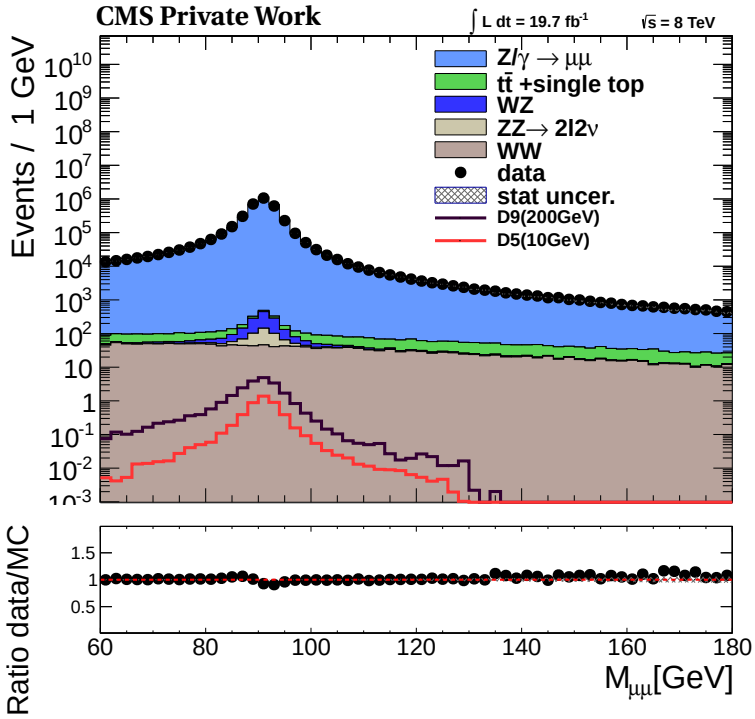

Figure 7.5: Invariant mass of dimuon pairs after the physics object selection requirement. Standard model prediction estimates from MC from different processes are shown stacked in different colors. Two signal hypotheses are plotted for clearness. Agreement between the prediction and measurement is observed. It is visible that both signal hypotheses have a clear peak around the Z mass. Only events with the invariant mass within $m_Z \pm 10$ GeV are considered for further analysis.

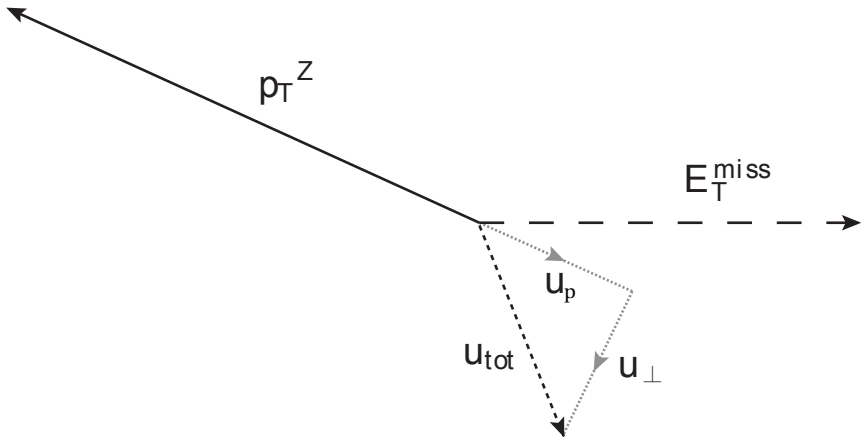

Figure 7.6: Geometrical construction of the response vector $\vec{u}_{\text{tot}}$. For processes in which the Z boson recoils against dark matter particles, one expects that the component u_p which is parallel to the axis of the p_T^Z be minimal due to the fact that the angle between the Z boson and missing energy $E_{\text{T}}^{\text{miss}}$ is 180° (back-to-back).

boson (sometimes referred to as "non-resonant" backgrounds) have a rather flat behavior. Therefore, only events where the mass of the dilepton pair is reconstructed to be within 10 GeV of the Z boson mass are admitted to further analysis. This selection requirement greatly suppresses non-resonant background contributions – e.g. the portion of top quark background processes passing this selection requirement is found to be about 4% whilst 83% of dark matter signal events assuming a scenario with a vector coupling and $m_\chi = 100$ GeV survive this selection step. The selection efficiency of this step for other dark matter and unparticles scenarios is found to be comparable.

7.3.2 Response requirement

The next kinematic quantity to be reviewed is the so called response. One can define the vector $\vec{u}_{\text{tot}}$ in the transverse plane via

$$\vec{u}_{\text{tot}} = -\vec{p}_T^{\,Z} - \vec{E}_T^{\text{miss}}, \tag{7.2}$$

whereby the transverse momentum of the Z boson is reconstructed from the muon pair. A geometrical sketch is shown in Fig. 7.6. Response is defined as the projection of the parallel component u_p onto the axis of the Z boson which is subsequently normalized to the p_{T} of the Z: $u = \frac{u_p}{|\vec{p}_T^{\,Z}|}$. The distribution of the response variable after a basic identification and isolation selection is shown in Fig. 7.7. It is found that the signal predictions peak around the value of $u = 0$ whereby top quark background processes and the Drell-Yan process peak around $u = -1$. The WZ and ZZ background contributions possess the same kinematic structure in terms of response as the signal hypotheses and therefore also peak around $u = 0$. They can not be suppressed by a response requirement. The requirement region is identified to be $-1 < u < 1$ due to a rather broad distribution of the signal.

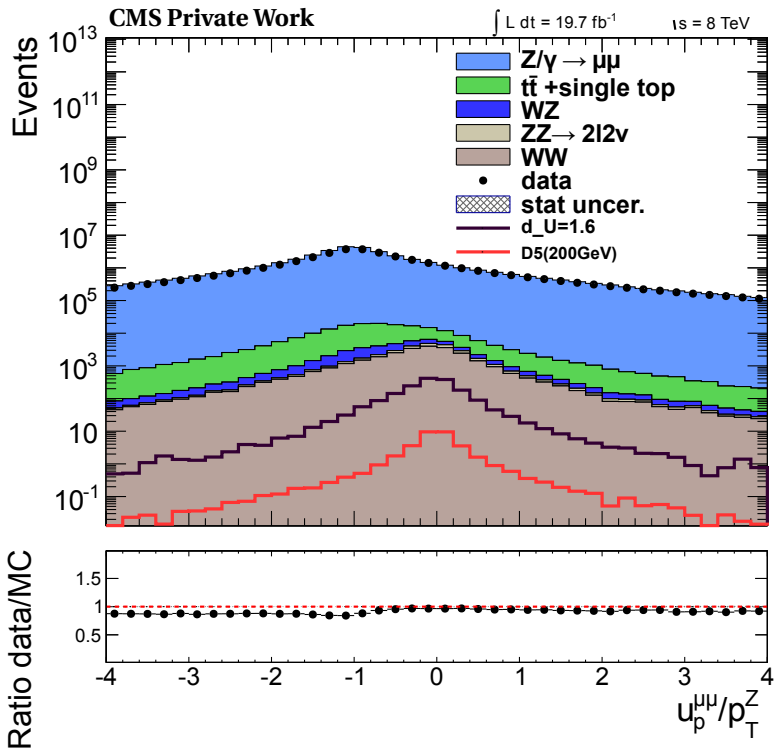

Figure 7.7: Distribution of the response variable u in the dimuon channel for the background samples and two signal hypotheses. It is visible that both signal assumptions peak around 0 whilst Z and top background peak around -1.

7.3.3 Balance requirement

Another requirement which is based on the same kinematic considerations is the requirement for the event to be balanced in the transverse plane. One defines the balance b of an event as the absolute value of the difference of p_T and E_T^{miss} normalized by the p_T of the reconstructed Z boson:

$$b = \frac{|p_T^Z - E_T^{miss}|}{p_T^Z}. \tag{7.3}$$

Due to the recoil of the Z boson against dark matter particles or an unparticle, one expects the balance of signal events to peak at zero. The distribution of the balance variable for a basic muon identification and isolation selection is shown in Fig. 7.8. One can see that Drell-Yan contribution has a different shape compared to signal hypotheses and can therefore be greatly suppressed. The requirement on the balance is set to $b < 0.2$.

7.3.4 ϕ requirement and dilepton transverse momentum

Two further conditions are introduced in order to suppress background contributions – both are based on the kinematic features discussed above. The angle between the Z boson and E_T^{miss} is expected to be π, and therefore no events with $\Delta\phi_{\ell\ell,\vec{p}_T^{miss}} < 2.7$ are accepted. Additionally, one introduces a loose requirement which aims to suppress Z bosons produced almost at rest with $p_T^Z > 50$ GeV. A summary of all selection requirements is given in Sec. 7.3.5.

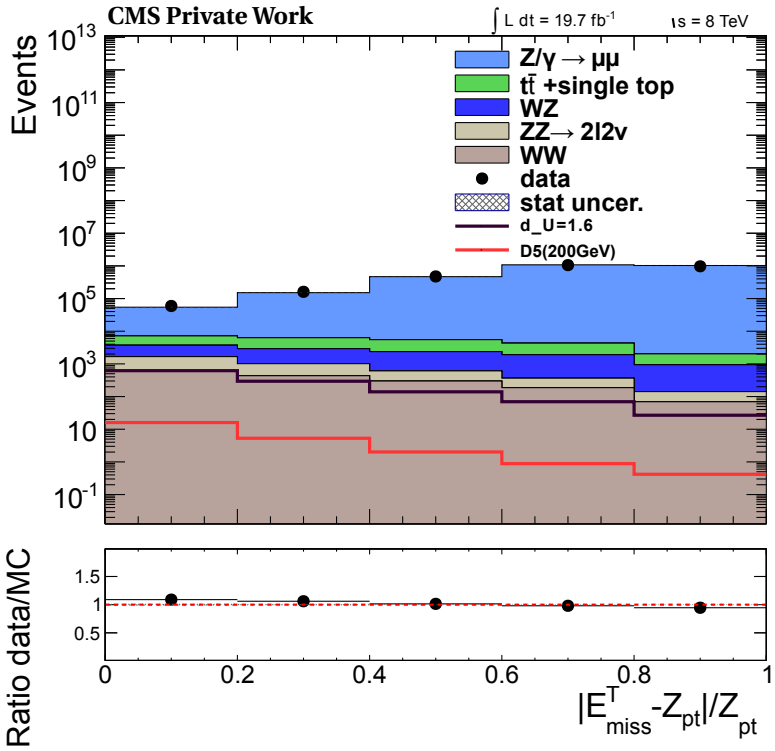

Figure 7.8: Distribution of the balance variable in the dimuon channel for the background samples and two signal hypotheses. The shape of the balance variable is different for the Drell-Yan background compared to signal hypotheses of dark matter and unparticle production allowing for an effective separation.

	Variable	Requirement
Preselection	p_{T}^{ℓ}	>20GeV
	opposite charge	true
	$\lvert m_{\ell\ell} - m_Z \rvert$	<10GeV
	Jet counting	≤1 jets with $p_{\mathrm{T}}^{\mathrm{j}} > 30$GeV
	$p_{\mathrm{T}}^{\ell\ell}(p_{\mathrm{T}}^{Z})$	>50GeV
	3rd-lepton veto	$p_{\mathrm{T}}^{\ell} > 10$GeV
	Top quark veto	veto on b jets and soft muon
Selection	$\lvert u_{\parallel} / p_{\mathrm{T}}^{\ell\ell} \rvert$	<1
	$E_{\mathrm{T}}^{\mathrm{miss}}$	>80GeV
	$\Delta\phi_{\ell\ell,\vec{p}_{\mathrm{T}}^{\mathrm{miss}}}$	>2.7 rad
	$b = \lvert E_{\mathrm{T}}^{\mathrm{miss}} - p_{\mathrm{T}}^{\ell\ell} \rvert / p_{\mathrm{T}}^{\ell\ell}$	<0.2

Table 7.6: Summary of selections used in the analysis for both the dark matter and unparticle interpretations. The preselection stage acts as a check before applying the final set of requirements. Identical criteria are applied to both muon and electron pairs. Further control plots are shown in the Appendix.

7.3.5 Selection summary

In order to suppress contributions from background processes, several selection requirements have been introduced above. Those are grouped in two selection stages. The preselection stage acts as a "sanity" check of the selection requirements and provides feedback about the general understanding of the background and data behavior. The final selection is the final step of data analysis which is evaluated in terms of an evidence for New Physics (cf. Tab. 7.6). This region is also referred to as the "signal region" in the following. The systematic uncertainties are only estimated for the final selection stage (cf. Sec 7.5).

7.4 Background Estimation

Different background processes from the standard model will contribute to the final state with a lepton pair and $E_{\mathrm{T}}^{\mathrm{miss}}$ even with the tight selection requirements introduced in the sections above (cf. Sec. 7.3). In general, it has been shown in the past that simulation can provide reliable predictions of background contributions [83,237–239]. Nevertheless, one should carefully consider the contribution of different background processes and perform crosschecks to evaluate their contribution to the final selection. Thereby, the preselection stage defined in the upper part of Tab. 7.6 aims to perform a "sanity" check of the selection steps on the way to the final stage. Fig. 7.9 shows the distribution of $E_{\mathrm{T}}^{\mathrm{miss}}$ for the dielectron and the dimuon final states. A good agreement between the data and standard model prediction is observed at this stage.

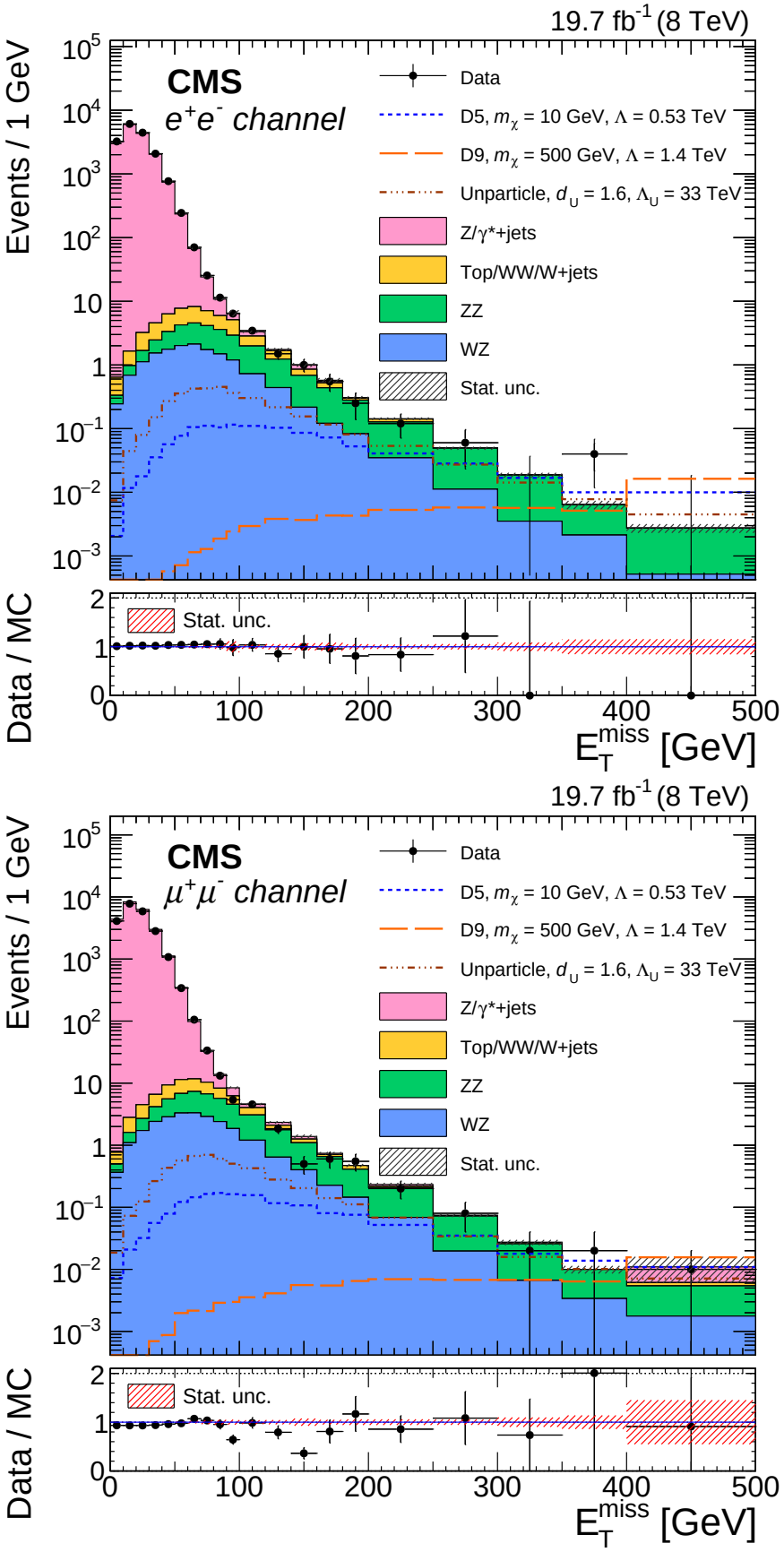

Figure 7.9: The distribution of $E_{\mathrm{T}}^{\mathrm{miss}}$ after preselection for the $Z \to ee$ (top, Northeastern) and $Z \to \mu\mu$ (bottom, this thesis) channels. Several signal scenarios are shown for comparison. The statistical uncertainty is indicated by hatched regions. No scale factor from data-driven background estimation have been applied as these are only determined for the final selection step. The last bin of each distribution is the overflow bin containing all contributions above. Agreement is observed between the measurement and prediction whereby an outlier is visible for the dimuon side ([1], based on input from the present analysis).

channel	control region	scale factor (± stat. error)	nominal scale factor
$\mu\mu$	$0.30 < b < 0.50$	1.177 ± 0.013	1.16 ± 0.12
$\mu\mu$	$0.30 < b < 0.60$	1.184 ± 0.009	
$\mu\mu$	$0.30 < b < 0.70$	1.189 ± 0.007	
$\mu\mu$	$0.30 < b < 0.80$	1.177 ± 0.005	
$\mu\mu$	$0.60 < b < 1.00$	1.148 ± 0.005	
$\mu\mu$	$0.50 < b < 1.00$	1.153 ± 0.004	
$\mu\mu$	$0.40 < b < 1.00$	1.154 ± 0.004	
$\mu\mu$	$0.30 < b < 1.00$	1.155 ± 0.004	
$\mu\mu$	$40 < E_{\mathrm{T}}^{\mathrm{miss}} < 50$ GeV	1.194 ± 0.020	
$\mu\mu$	$50 < E_{\mathrm{T}}^{\mathrm{miss}} < 60$ GeV	1.243 ± 0.038	
$\mu\mu$	$60 < E_{\mathrm{T}}^{\mathrm{miss}} < 70$ GeV	1.105 ± 0.072	
$\mu\mu$	$50 < E_{\mathrm{T}}^{\mathrm{miss}} < 80$ GeV	1.220 ± 0.033	
$\mu\mu$	$40 < E_{\mathrm{T}}^{\mathrm{miss}} < 60$ GeV	1.205 ± 0.018	
$\mu\mu$	$60 < E_{\mathrm{T}}^{\mathrm{miss}} < 80$ GeV	1.153 ± 0.068	
$\mu\mu$	$40 < E_{\mathrm{T}}^{\mathrm{miss}} < 80$ GeV	1.201 ± 0.017	

Table 7.7: Scale factors for Drell-Yan background prediction based on the binned control regions in $E_{\mathrm{T}}^{\mathrm{miss}}$ and b for the signal region. The nominal scale factor is applied to the final selection of Drell-Yan background [232].

7.4.1 Drell-Yan Process

The Drell-Yan process ($Z \to \ell\ell$) plays a crucial role in the region with $E_{\mathrm{T}}^{\mathrm{miss}} < 100$ GeV, whereby the signal region is defined by $E_{\mathrm{T}}^{\mathrm{miss}} > 80$ GeV. This process does not produce undetectable particles and can therefore only contribute to the $E_{\mathrm{T}}^{\mathrm{miss}}$ spectrum due to the limited detector acceptance. Following this argumentation, an additional technique is employed in order to verify and improve the Drell-Yan background prediction in the signal region. The contribution of this process for the final selection is estimated by defining two control regions where the Monte Carlo prediction is normalized with high statistics relying on the study performed in [232]. Based on inversion of two selection requirements ($E_{\mathrm{T}}^{\mathrm{miss}}$ and balance b), scale factors are derived which are subsequently applied to the Drell-Yan spectrum in the signal region. Hereby, contributions from other background processes are deducted. For the two control regions which are binned in the corresponding variable, the full selection is applied whereby the $\Delta\phi_{\ell\ell,\vec{p}_{\mathrm{T}}^{\mathrm{miss}}}$ requirement is dropped along the $E_{\mathrm{T}}^{\mathrm{miss}}$ and b requirements. Table 7.7 shows the different scale factors which are derived in each bin of the control region. The corresponding distributions of $E_{\mathrm{T}}^{\mathrm{miss}}$ and b are shown in Fig. 7.10.The study concludes with an overall scaling factor of 1.16 which is then applied to the Monte Carlo estimated Drell-Yan prediction in the signal region. The corresponding uncertainty is discussed in Sec. 7.5. It has to be noted that the contribution of the Drell-Yan process for the signal region is expected to play a subleading role (cf. Fig. 7.9).

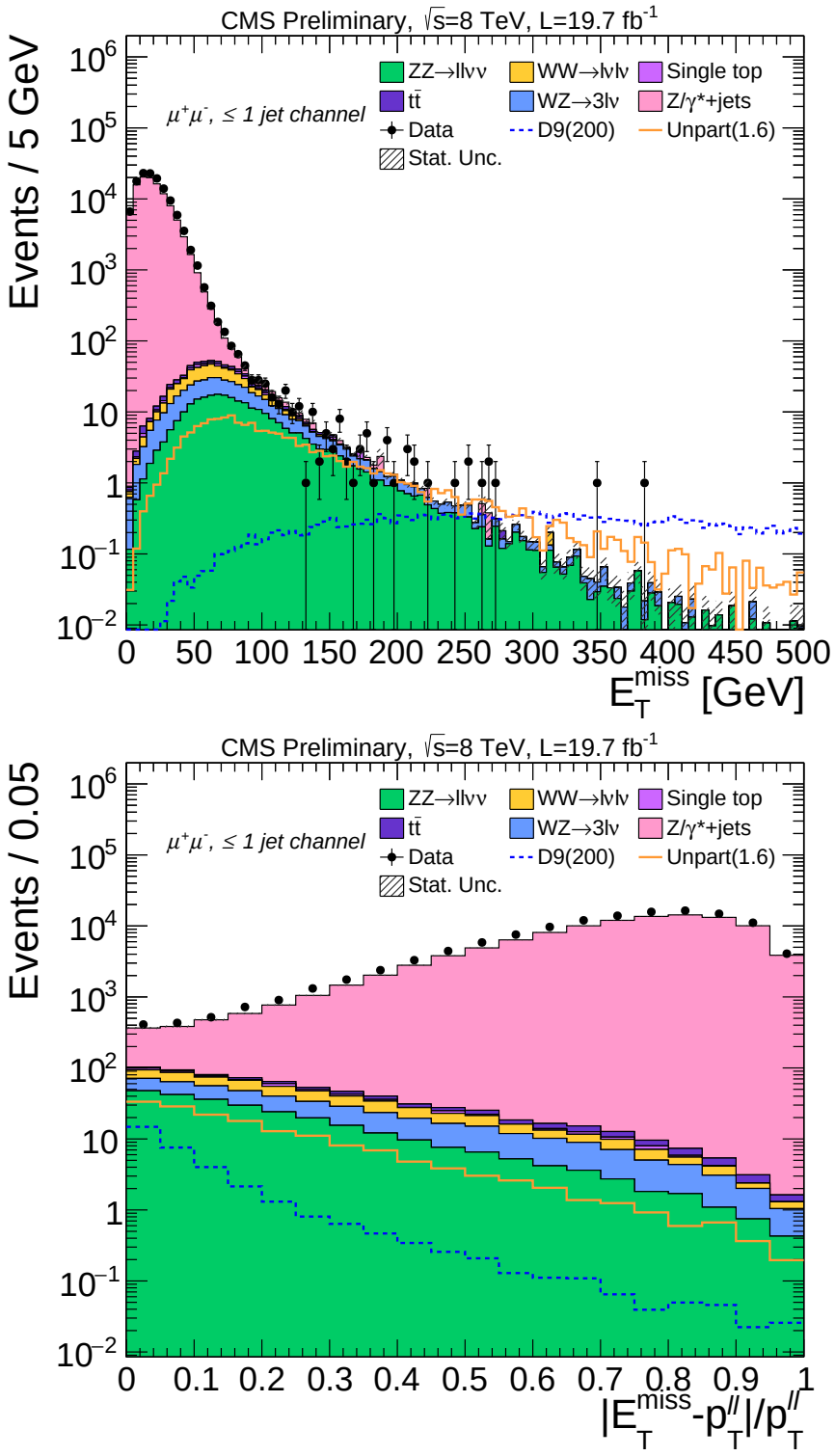

Figure 7.10: Distributions of $E_{\mathrm{T}}^{\mathrm{miss}}$ (top) and balance b (bottom) employed for the derivation of the Drell-Yan scale factors in the control regions (before the application of scale factors). The full selection except $E_{\mathrm{T}}^{\mathrm{miss}}$, balance b and $\Delta\phi$ requirements is applied [232].

α	$N_{e\mu}$	$N^{\text{est}}_{\text{data}}$	$N^{\text{est}}_{\text{mc}}$
0.57 ± 0.03	42.0 ± 6.5	$23.3 \pm 3.7 \pm 5.8$	14.2 ± 1.3

Table 7.8: Yields for the data driven non-resonant background estimation using α-method [232].

7.4.2 Non-resonant background processes

The background contribution through top quark (pair) production, W and WW decays is estimated using a control sample where the selection on one of either leptons is flipped from electron to muon or vice versa resulting in a $e^{\pm}\mu^{\mp}$ selection requirement. The shape of the contribution of those background processes is estimated from simulation whereas the total yield of events is normalized to the findings of this study [232]. Two methods are employed for the derivation of the total yield of events.

7.4.2.1 α-method

In this approach, one defines a scale factor α which is used for the prediction of the total event yield $N_{\mu\mu}$ following the relation

$$N_{\mu\mu} = \alpha_{\mu\mu} \cdot N_{e\mu}, \tag{7.4}$$

whereby $N_{e\mu}$ is the number of selected $e^{\pm}\mu^{\mp}$ events. The scale factor is computed in two sidebands aside from the Z boson mass peak requiring $40 < m_{\ell\ell} < 70$ GeV and $110 < m_{\ell\ell} < 200$ GeV using the link

$$\alpha_{\mu\mu} = \frac{N^{\text{SB}}_{\mu\mu}}{N^{\text{SB}}_{e\mu}}, \tag{7.5}$$

whereby $N^{\text{SB}}_{e\mu}$ is the number of $e^{\pm}\mu^{\mp}$ events selected in the sideband and $N^{\text{SB}}_{\mu\mu}$ denotes the number of $\mu\mu$ events, both measured in top-enriched samples. In order to increase the statistical richness of the sample and thus decrease the corresponding uncertainty, the selection requirements are loosened. It is demanded that $E^{\text{miss}}_{\text{T}} > 65$ GeV and $0.4 < \frac{E^{\text{miss}}_{\text{T}}}{p^{\ell\ell}_{\text{T}}}$. The systematic uncertainty of this method is estimated by inversion of the b tag veto and performing the procedure again – 25% are assigned due rather large deviations [232]. The value of $\alpha_{\mu\mu}$ and the corresponding event yields are shown in Tab. 7.8. The corresponding distributions of $m_{\ell\ell}$ are shown in Fig. 7.11.

7.4.2.2 k-method

Another approach uses the fact that the branching ratio of non-resonant backgrounds (e.g. WW) to $e\mu$ and electron and muon pairs is $2:1:1$ due to flavor symmetry of those decays. The mass window requirement for the lepton pair is loosened in order to gain more statistics and the background contribution can be estimated via

$$N^{\text{est}}_{\text{bkg},\mu\mu} = N^{\text{data,corr}}_{e\mu} \cdot k_{\mu\mu} \quad \text{with} \quad k_{\mu\mu} = \frac{1}{2}\sqrt{\frac{N^{\text{data}}_{\mu\mu}}{N^{\text{data}}_{ee}}}. \tag{7.6}$$

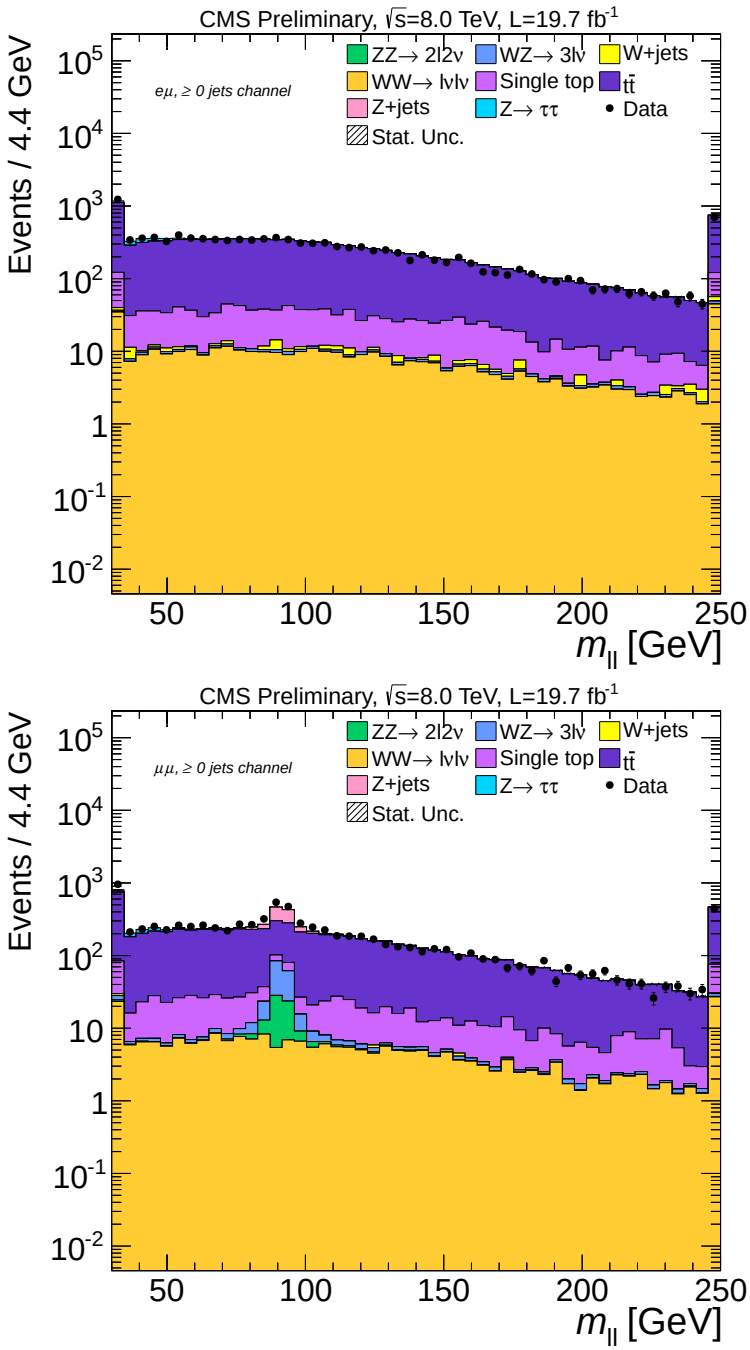

Figure 7.11: Distribution of dilepton invariant mass in $e\mu$ (top) and $\mu\mu$ (bottom) channel in the selected top-enriched sample. The region with $70 < m_{\ell\ell} < 110$ GeV is excluded from the calculation of α [232].

The factor $\frac{1}{2}$ originates from the branching ratio relations discussed above and the square root accounts for different detection efficiencies for muon and electron pairs. The estimated contribution is measured to be $N^{\text{est}}_{\text{bkg},\mu\mu} = 23.0 \pm 3.9$ whereby the uncertainty of 15% is derived from closure tests which employ simulated samples for deriving the scale factors [232](cf. Sec. 7.5). The distributions of $E_{\text{T}}^{\text{miss}}$ and $m_{\ell\ell}$ in the $e\mu$ sample are shown in Fig. 7.12.

7.4.3 *WZ* and *ZZ* background contributions

Since the top background is almost completely suppressed by the selection requirements, the *WZ* and *ZZ* backgrounds are expected to deliver leading contributions to the final signal region Fig. 7.4. The contributions of those samples are estimated using Monte Carlo simulation in leading order which is normalized to a next-to-leading order cross section using a flat k-factor. Furthermore, electroweak corrections have been derived in theoretical studies [240–242], which are applied to the final yields of *WZ* and *ZZ* backgrounds:

$$\text{ZZ: } 1 + \left(-\frac{1}{\text{GeV}} \cdot 0.071 \times p_{\text{T}} + 0.55 \right) / 100, \qquad \text{WZ: } 1 + \left(-\frac{1}{\text{GeV}} \cdot 0.037 \times p_{\text{T}} + 1.9 \right) / 100. \tag{7.7}$$

A typical correction value for the *ZZ* background in the signal region is determined to start around 8%, whereby the correction for the *WZ* is smaller with 2%. The corresponding function is shown in Fig. 7.13.

7.4.4 Pileup reweighting

During the simulation of bunch-bunch interactions inside the CMS detector, a scenario for multiple soft interactions has to be assumed and put into the simulation as a set of parameters. Since the simulation can only approximately account for various effects of pileup, a subsequent correction has to be applied in the analysis – the pileup reweighting. This procedure is performed as follows. The number of reconstructed vertices N_{vtx} is measured in both data (in a so called minimum bias sample – meaning that the number of requirements for data recording is kept to a minimum) and MC samples. The distribution of N_{vtx} in MC is then subsequently reweighted in order to match the distribution from data measurement. As a consequence, each MC event obtains an additional weight. The distribution of N_{vtx} for a basic muon pair selection before and after the reweighting procedure can be seen in Fig. 7.14.

7.4.5 *W*+jets background

Another source of background contribution in the dielectron final state arises from the misidentification of hadronic jets – these physics object can be mistakenly reconstructed as electrons (one often refers to those as "fake" electrons). As a consequence, the production of *W* boson along jets has to be considered for the dielectron side in order to estimate the contribution of the misidentified objects. Since the dielectron final state is not a central topic of the present thesis and the contribution of this background process is found to be small, the detailed estimation of these backgrounds is not discussed here and can be found in [232]. The contribution of *W*+jets background for the dimuon channel is found to be negligible.

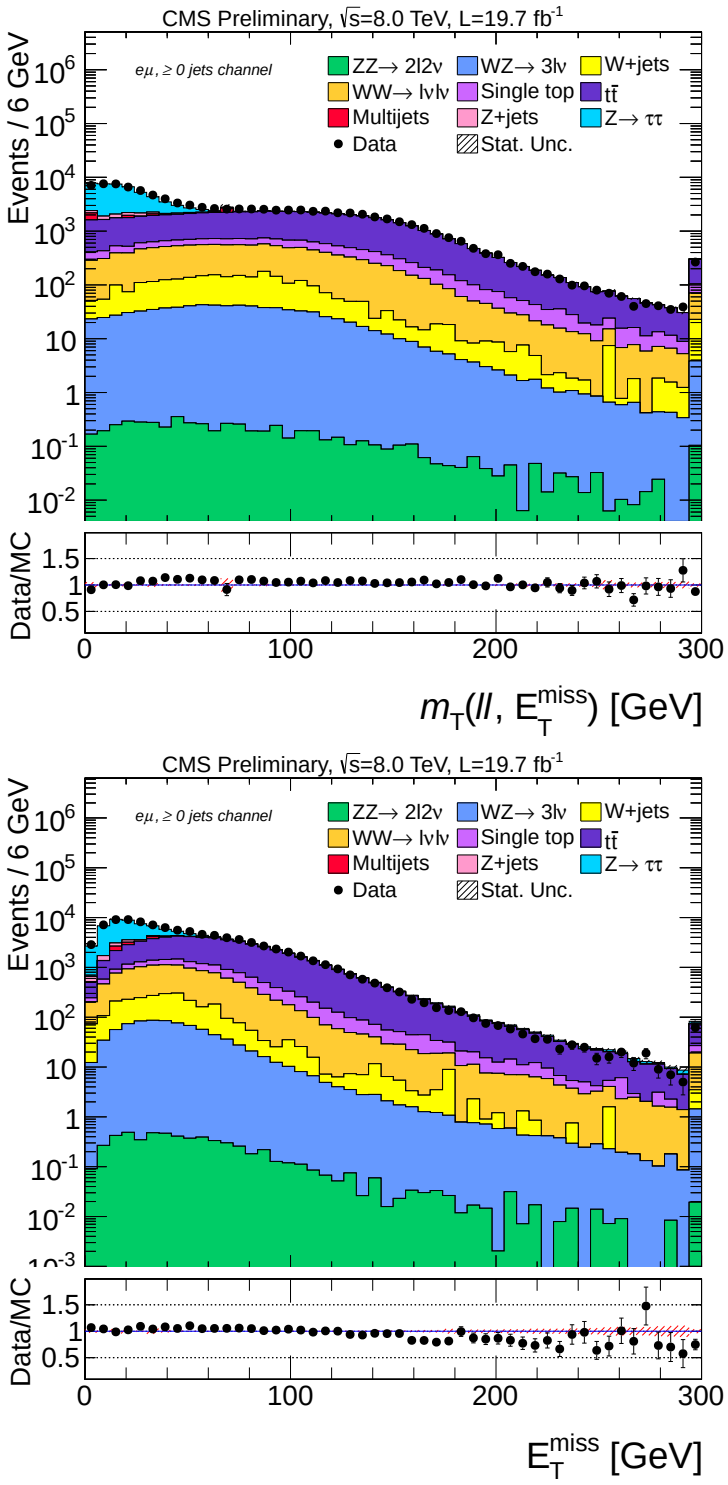

Figure 7.12: Distributions of $m_{\ell\ell}$ (top) and $E_{\mathrm{T}}^{\mathrm{miss}}$ (bottom) in the $e\mu$ control region. Agreement is observed between the Monte Carlo simulation and the data [232].

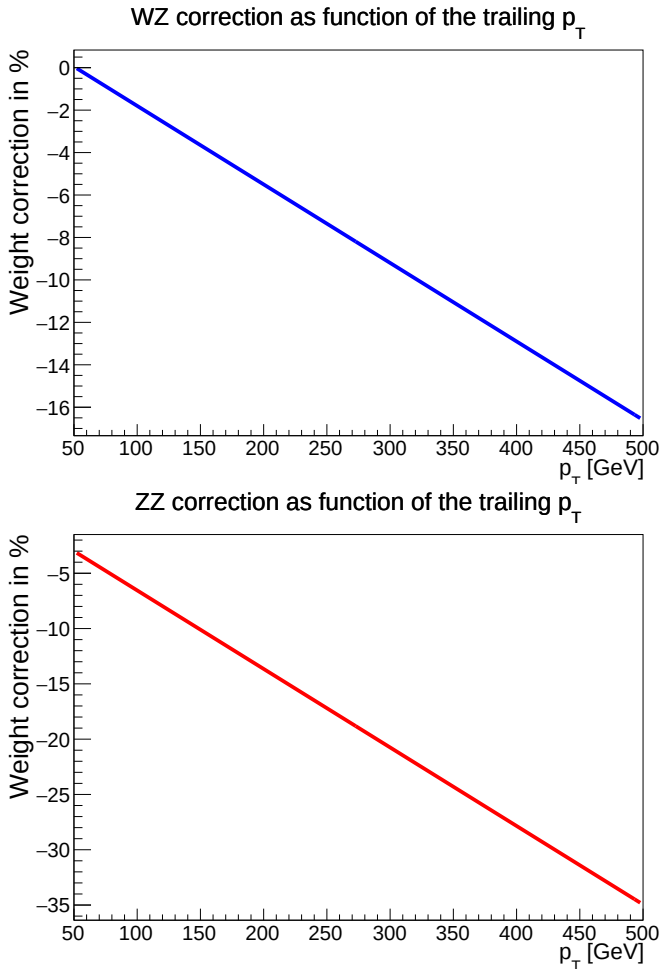

Figure 7.13: Electroweak corrections of the diboson background for WZ (top) and ZZ (bottom) as a function of the p_{T} of the trailing boson.

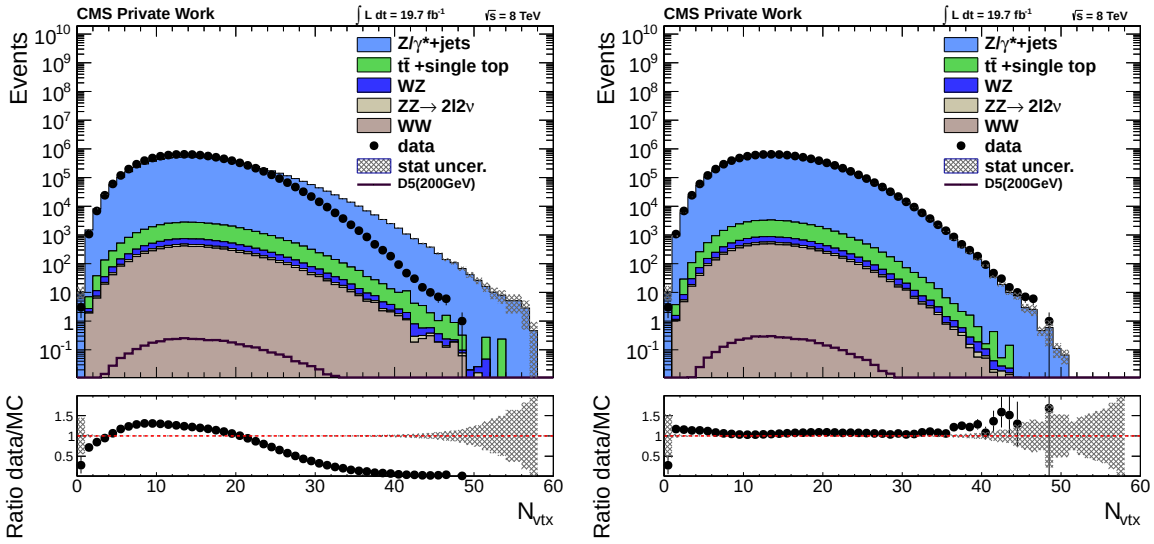

Figure 7.14: Distribution of the number of vertices N_{vtx} after a basic muon pair identification selection requirement before (left) and after (right) the pileup reweighting procedure. It is visible that the reweighting procedure leads to a much better agreement between the simulated and the measured distributions of N_{vtx}.

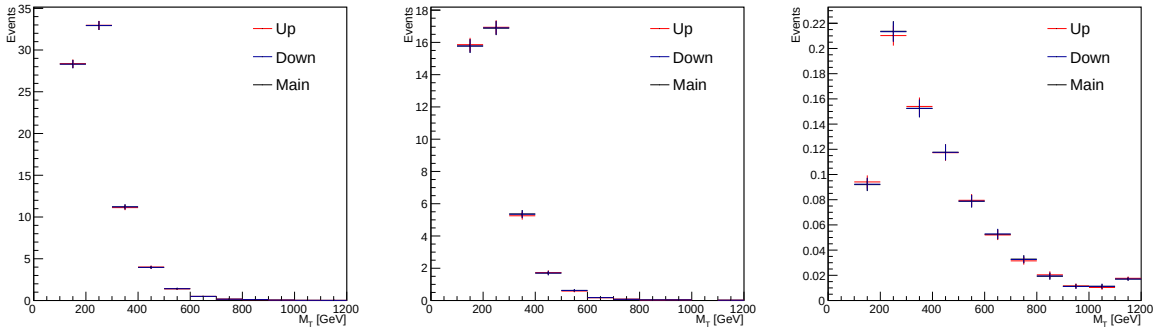

Figure 7.15: Shape uncertainties resulting from jet energy resolution variation for the *ZZ* (left), *WZ* (middle) and D8 with $m_\chi = 100$ GeV (right).

7.5 Systematic Uncertainties

The understanding of systematic uncertainties is crucial for any analysis. In the following, the systematic uncertainties are discussed based on their origin. If not stated otherwise, uncertainties are calculated for both the signal and the background prediction. Systematic uncertainties are considered in two approaches for the final selection. In the first approach, a source of systematic uncertainties acts as a normalization uncertainty for the complete spectrum of the corresponding prediction. In the second, the so called shape-based approach is used. In this approach, the source of the systematic (e.g. muon momentum scale) is varied by its uncertainty, which has been studied by the corresponding group, in each event and the resulting difference is propagated to the variable of interest. Thus, two new final distributions for each source of systematic uncertainties are created – for the variation up and down. These distributions are provided to the Higgs Combine Tool, which takes them into account when computing the exclusion limit.s It should be noted that in general the effect of these variations for the final distribution is not symmetrical. Studies have been performed both at the Northeastern University and in Aachen by the presenter of this thesis in order to optimize the final selection variable for the best expected exclusion limit. As a result, the final variable of interest is selected to be m_{T}.

7.5.1 Jet energy resolution

Studies have shown that the resolution of jet p_{T} in simulation is better than in recorded data. In order to take this effect into account, a jet smearing procedure is employed [243]. The smeared transverse momentum $\tilde{p}_{\mathrm{T}}$ of a reconstructed simulated jet which has been previously successfully matched to a jet on generation level is defined by

$$\tilde{p}_{\mathrm{T}} = \max(0, p_{\mathrm{T}}^{\mathrm{gen}} + c \cdot (p_{\mathrm{T}} - p_{\mathrm{T}}^{\mathrm{gen}})), \tag{7.8}$$

whereby $p_{\mathrm{T}}^{\mathrm{gen}}$ is the p_{T} of the generated jets and c denotes an η-dependent scaling factor. Reconstructed jets which could not be matched to a generated jet are smeared using a Gaussian with a width of 20% of jet's p_{T}. The uncertainty is propagated into the final selection as a shape uncertainty. The effect is found to be about $5-7\%$ for different background processes and $3-5\%$ for signal processes. The corresponding uncertainty is shown in Fig. 7.15.

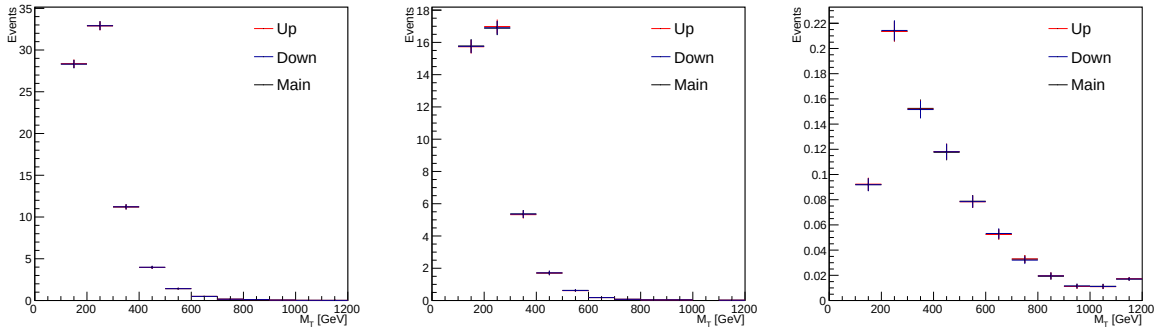

Figure 7.16: Shape uncertainties resulting from jet energy scale variation for the *ZZ* (left), *WZ* (middle) and D8 with $m_\chi = 100$ GeV (right).

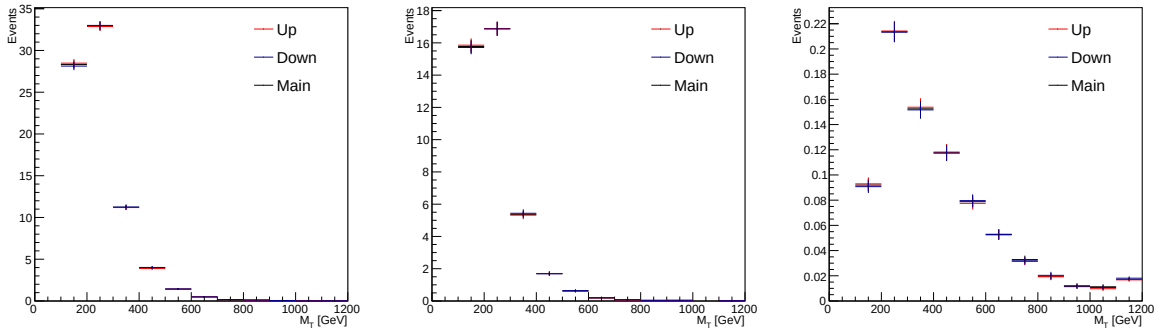

Figure 7.17: Shape uncertainties resulting from muon momentum scale variation for the *ZZ* (left), *WZ* (middle) and D8 with $m_\chi = 100$ GeV (right).

7.5.2 Jet energy scale

The scale of the jet p_T measurement also has to be taken into account. The energy of the reconstructed jets is shifted by a factor $1 + s$ up and down, whereby the scale s is a factor dependent on the p_T and η of the jet. The result of the shift is propagated into the final selection as a shape uncertainty. The effect is found to be about $5-7\%$ for different background processes and $3-5\%$ for signal processes.The corresponding uncertainty is shown in Fig. 7.16.

7.5.3 Muon scale and resolution

Muons originating from *Z* boson decays are well studied in CMS [244]. The impact of resolution is taken into account by smearing the reconstructed p_T of the muon with a Gaussian function and propagating the impact to the final selection. In a similar matter, the muon scale it shifted up and down, whereas the impact is propagated to the final selection. Both uncertainties are considered as shape uncertainties. The corresponding impact on the final selection is about 1%. The muon momentum scale uncertainty in shown in Fig. 7.17, the muon resolution uncertainty can be viewed in Fig. 7.18.

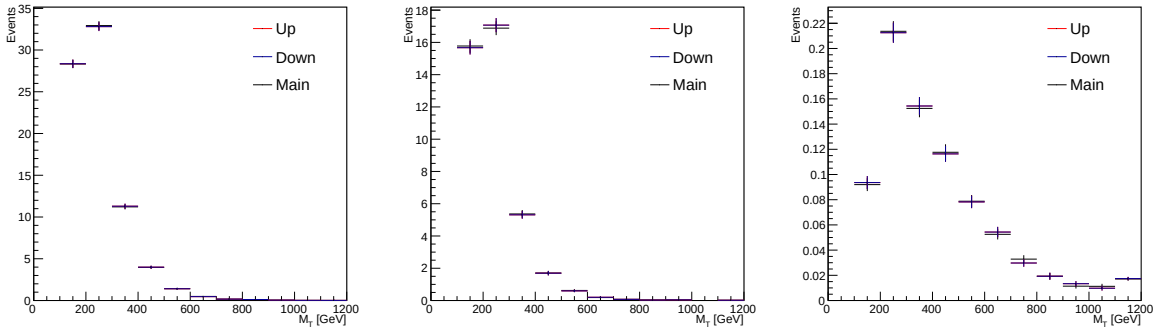

Figure 7.18: Shape uncertainties resulting from muon resolution variation for the *ZZ* (left), *WZ* (middle) and D8 with $m_\chi = 100$ GeV (right).

7.5.4 Unclustered $E_{\mathrm{T}}^{\mathrm{miss}}$

Unclustered $E_{\mathrm{T}}^{\mathrm{miss}}$ is estimated using the following technique. The transverse momentum of all reconstructed objects is subtracted from the $E_{\mathrm{T}}^{\mathrm{miss}}$ estimator resulting in the $E_{\mathrm{T}}^{\mathrm{miss}}$ calculated from contributions which are not included in considered physics object. The estimator is then varied by 10% up (down) and the subtracted momenta are added back. The resulting uncertainty is employed as shape based in the final selection.

7.5.5 Lepton trigger, reconstruction and efficiency

The efficiencies for triggering, reconstructing and identifying isolated leptons are determined from simulation and subsequently corrected with scale factors using the "tag-and-probe" technique [245]. The muon trigger efficiency is found to be above 90%, whereby the identification efficiency is found to be 94%. The corresponding data-to-MC scale factors are found to be around $0.98-1.02$. The overall corresponding uncertainty is determined to be 3% in each event and is employed as a normalization uncertainty. The overall signal reconstruction efficiency is found to be about 40%.

7.5.6 Parton distribution function uncertainties

During the generation of a Monte Carlo sample, certain assumptions have to be made about the content of the protons which are brought to a simulated collision – the parton distribution functions (PDF). Several approaches exist which are employed as a set of PDF which are plugged into the physics generator as external parameters [234, 246–248]. Following the interim recommendation issued by the PDF4LHC group [249–251], the expression for MSTW2008 is calculated via:

$$\sigma(+) = \sqrt{\sum_{i=1}^{\frac{N}{2}} \left(\max\{\mathcal{O}[\{q^{(2i-1)}\}] - \mathcal{O}[\{q^{(0)}\}], \mathcal{O}[\{q^{(2i)}\}] - \mathcal{O}[\{q^{(0)}\}], 0\}\right)^2} \tag{7.9}$$

$$\sigma(-) = \sqrt{\sum_{i=1}^{\frac{N}{2}} \left(\max\{\mathcal{O}[\{q^{(0)}\}] - \mathcal{O}[\{q^{(2i-1)}\}], \mathcal{O}[\{q^{(0)}\}] - \mathcal{O}[\{q^{(2i)}\}], 0\}\right)^2}. \tag{7.10}$$

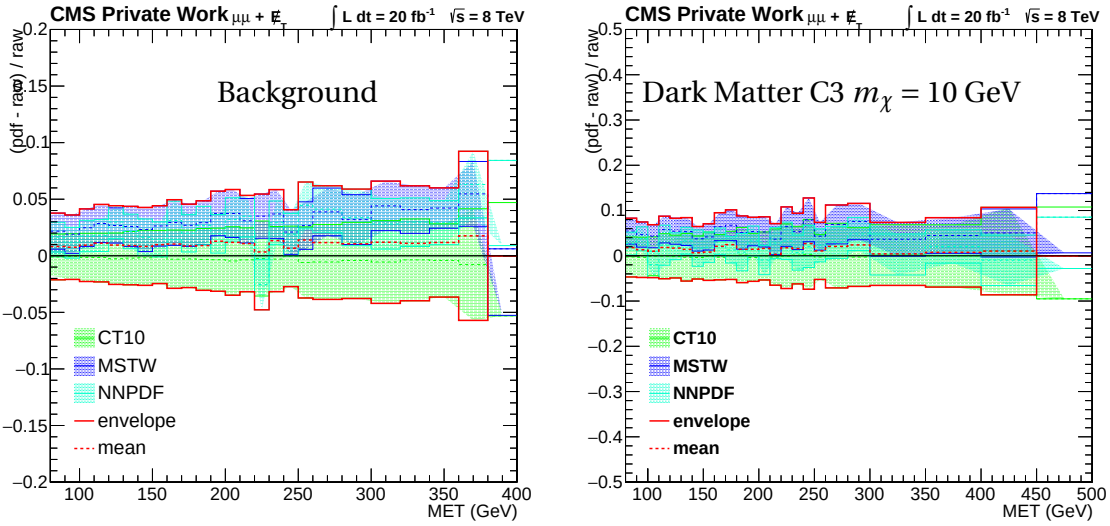

Figure 7.19: Relative uncertainty on the background prediction (left) and for C3 coupling with $m_\chi = 10$ GeV (right) for the final selection as a function of $E_{\mathrm{T}}^{\mathrm{miss}}$ due PDF. The uncertainty tends to grow with increasing $E_{\mathrm{T}}^{\mathrm{miss}}$.

MWST fits α_s together with PDF providing the best-fit value and four sets of PDFs which correspond to the variation of α_s by its standard deviation. The corresponding expression for NNPDF reads:

$$\sigma^{\mathrm{NNPDF}}(\alpha_S + \mathrm{PDF}) = \left[\frac{1}{N_{\mathrm{rep}}-1} \sum_{j=1}^{N_\alpha} \sum_{k_j=1}^{N_{\mathrm{rep}}^{\alpha_s^{(j)}}} \left(\mathcal{O}\left(PDF^{(k,j)}, \alpha_s^{(j)}\right) - \mathcal{O}_0 \right)^2 \right]^{\frac{1}{2}}. \tag{7.11}$$

Hereby, the standard deviation is computed by iterating over PDF sets (with values of the strong coupling $\alpha_s(m_Z)$ between 0.114 and 0.124 in steps of 0.001. The MC prediction is then shifted and propagated to the variable of interest. Only events passing the final selection are considered. The resulting variations and uncertainty are shown in Fig. 7.19 and Fig. 7.20. The PDF uncertainty on the background is estimated to be 5%. The PDF uncertainty for the signal is higher, starting at 8% and increasing to 20% with growing values of m_χ due to the diminishing phase space available for the production of the dark matter particles with high masses. The PDF uncertainty is the leading uncertainty for the signal prediction in the present analysis.

7.5.7 Pileup

The fact that the number of primary vertices in a collision event is not well modeled in MC is taken into account by the pileup reweighting and the uncertainty is estimated by shifting the corresponding weights. The impact of this uncertainty is propagated into the final selection as a shape uncertainty. The uncertainty is shown in Fig. 7.21.

7.5.8 Luminosity

The integrated luminosity for the CMS dataset from 2012 adds up to $\int \mathcal{L} = 19.7\ \mathrm{fb}^{-1}$. The corresponding uncertainty is a normalization uncertainty with 2.6% [235].

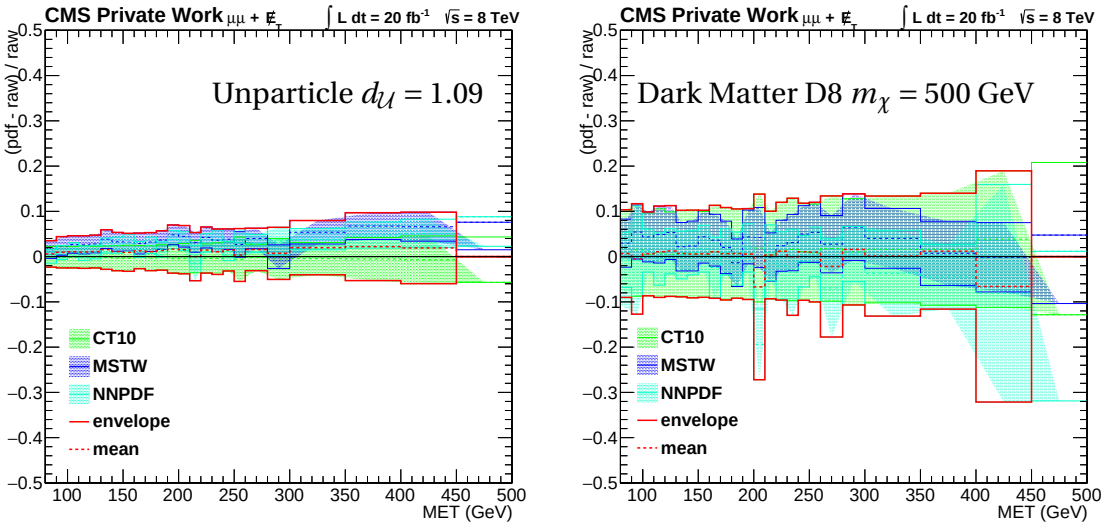

Figure 7.20: Relative uncertainty on the unparticle signal prediction with $d_{\mathcal{U}} = 1.09$ (left) and for D8 coupling with $m_\chi = 500$ GeV (right) for the final selection as a function of $E_{\mathrm{T}}^{\mathrm{miss}}$. The uncertainty increases rapidly for growing values of m_χ.

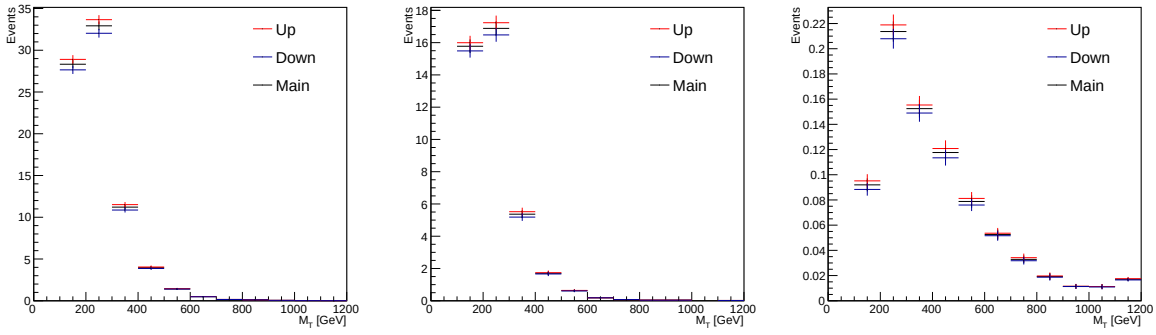

Figure 7.21: Shape uncertainties resulting from pileup for the *ZZ* (left), *WZ* (middle) and D8 with $m_\chi = 100$ GeV (right).

7.5.9 Drell-Yan and non-resonant backgrounds

The estimation of the Drell-Yan contribution employs a scaling technique in a control region. Variations of the resulting estimates in the corresponding binned control regions are used for building an envelope. The central value of the envelope is the resulting scale factor whereby the upper and lower bounds of the envelope provide an estimate of the systematic uncertainty. The final normalization uncertainty on the Drell-Yan prediction is found to be 11%. It should be noted that while the overall uncertainty is large, the impact of this particular background is not exceptionally high due to a small final yield.

The estimation of non-resonant backgrounds employs a data-driven technique as described in Sec. 7.4.2. Closure tests have been performed in [232] concluding with a final uncertainty of 15% on this background estimation technique.

7.5.10 *ZZ* background

Joint studies have been performed in collaboration with [232], in order to determine the uncertainty of the leading background. The *ZZ* background is estimated from simulation using `MadGraph` and different generators (MCFM, Powheg and Sherpa) have been employed in order to estimate the contribution of the *ZZ* background in the signal region. MCFM can not produce simulated events and is therefore not considered in the final evaluation. Fig. 7.22 and 7.23 show the distributions which have been considered during the *ZZ* studies. Based on the observed deviations, an overall normalization uncertainty of 14% is assigned to the *ZZ* contribution to the final selection. This uncertainty is the leading uncertainty for the background prediction in the signal region. More details can be found in Tab. 9.1 in the Appendix.

7.5.11 QCD scale uncertainty

The choice of the QCD scale (factorization and normalization scale) enters the simulation of the MC samples as a parameter. In order to estimate the impact on the final selection, the scale Q^2 is varied by factors $\frac{1}{2}$ and 2 and the resulting shift is propagated into the final selection (study performed by [232]). The uncertainty is found to be about 8% for background processes and about 5% for the signals. The uncertainty serves as a normalization uncertainty. Detailed values can be found in Tab. 9.2,9.3,9.4,9.5,9.6 of the Appendix.

7.5.12 Summary

The uncertainties contributing to the final selection have been discussed above. They overall uncertainties for both dielectron and dimuon channels are summarized in Tab. 7.9. Detailed discussions of the dielectron channel specific uncertainties can be found in [232].

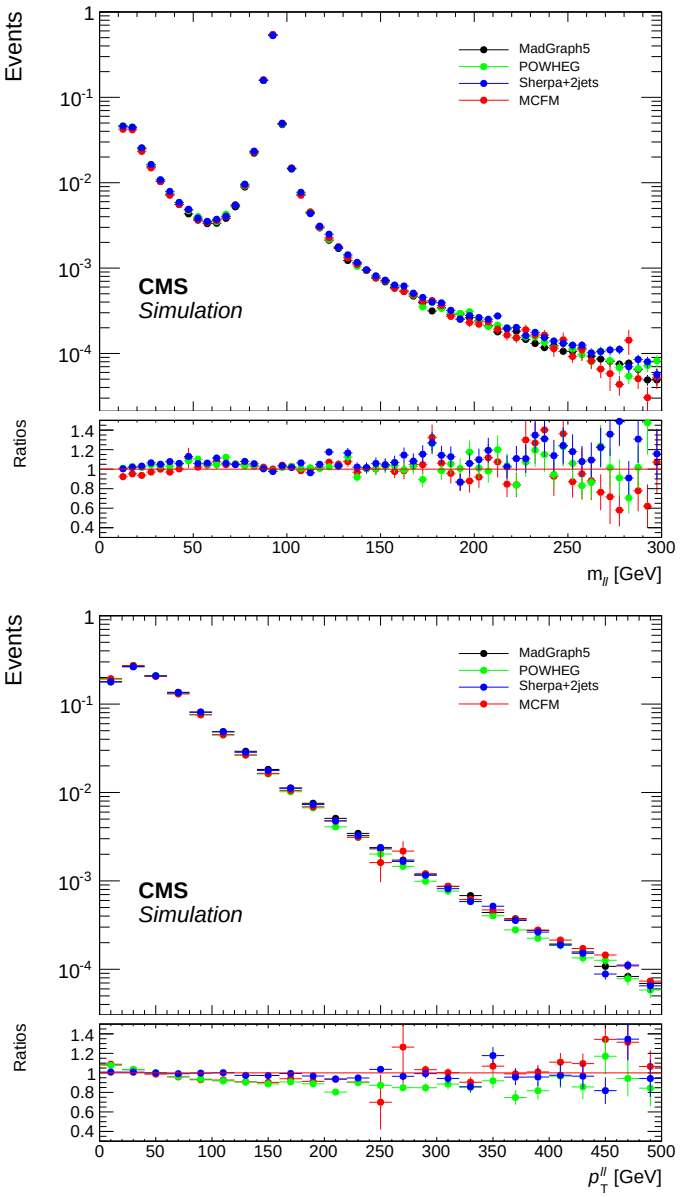

Figure 7.22: Distributions of dilepton mass (top) and dilepton p_{T} (bottom) at generator level for different generators employed for the estimation of the ZZ background uncertainty [232]. A deviation is visible which is interpreted as an uncertainty for the final ZZ background prediction.

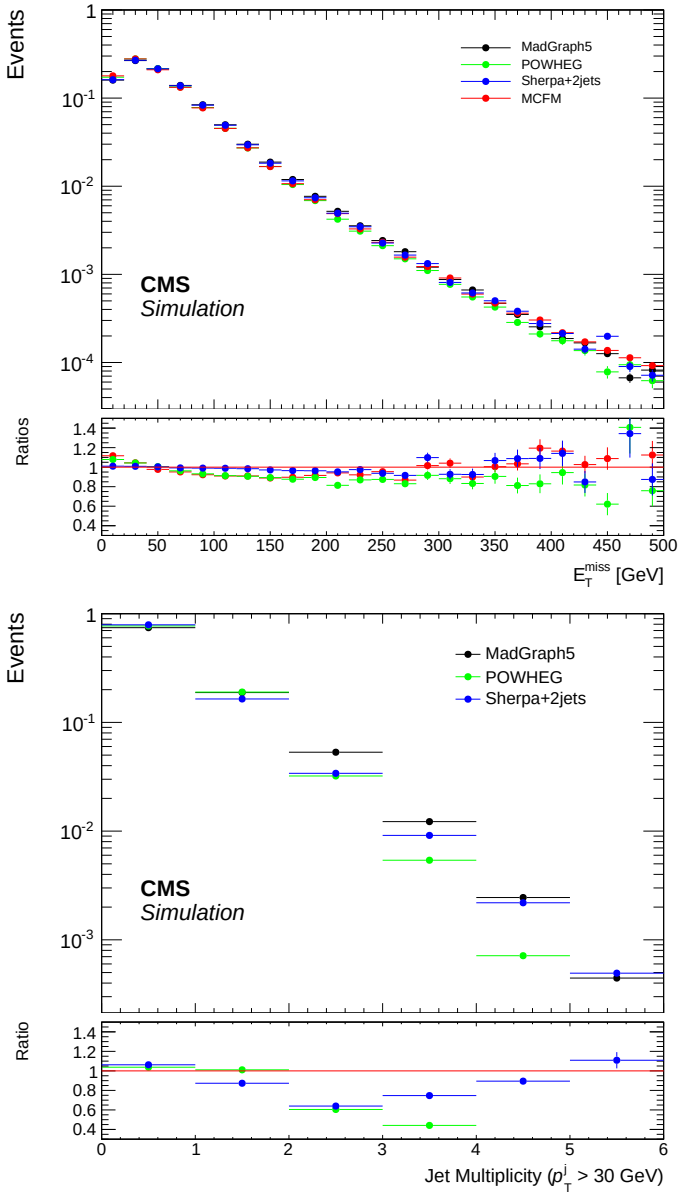

Figure 7.23: Distributions of $E_{\mathrm{T}}^{\mathrm{miss}}$ (top) and jet multiplicity (bottom) at generator level for different generators employed for the estimation of the *ZZ* background uncertainty [232]. A deviation is visible which is interpreted as an uncertainty for the final *ZZ* background prediction.

Source	Background uncertainty (%)	Signal uncertainty (%)
PDF+α_S	5–6	8–20
Factorization and renormalization scale	7–8	5
Acceptance (ZZ)	14	—
Integrated luminosity	2.6	2.6
Lepton trigger, reconstruction & identification, isolation	3	3
DY normalization	10–11	—
$t\bar{t}$, tW, WW normalization	15–17	—
W + jets normalization (ee only)	15–23	—
MC statistics (signal, ZZ, WZ)	1–2	1–2
Control region statistics (DY)	25	—
Control region statistics ($t\bar{t}$, tW, WW)	18	—
Control region statistics (W + jets, ee only)	36	—
Pileup	0.5–1	0.1–0.7
b-jet tagging efficiency	0.4–1.4	0.6–1
Lepton momentum scale	0.4–0.5	0.1–1
Jet energy scale and resolution	5–7	3–5
Unclustered $E_{\mathrm{T}}^{\mathrm{miss}}$ scale	1–2	1

Table 7.9: Summary of systematic uncertainties for the present analysis. Each background uncertainty represents the variation of the yields of the considered background contribution. For shape uncertainties, the values correspond to the overall effect of the shape variation on yield or acceptance. For signals, a region is indicated if the systematic uncertainty differs for samples with different parameters. Lepton trigger, reconstruction, isolation and identification uncertainties are assumed to be uncorrelated between the dielectron and the dimuon channel. The luminosity uncertainty is assumed to be fully correlated between the two channels and for signals. The symbol — indicates that the systematic uncertainty is not applicable ([1], based on input from the present analysis).

CHAPTER 8

Results and Limits

Based on the strategy discussed in the chapters above, the full selection for both the electron channel and the muon channel is applied. Fig. 8.2 shows the distribution of m_{T} for the two channels. The corresponding yield of contributing background processes, the observed data and exemplary dark matter and unparticle signal contributions are summarized in Tab. 8.1. Agreement is observed between the CMS measurement and the standard model prediction within the discussed uncertainties. Event views for a high energetic dielectron+$E_{\mathrm{T}}^{\mathrm{miss}}$ and a high energetic dimuon+$E_{\mathrm{T}}^{\mathrm{miss}}$ event are shown in Fig. 8.1. No signs of new physics could be found in the present analysis. The absence of new physics signatures is interpreted in terms of exclusion limits. The modified frequentist approach CL$_s$ employing asymptotic formulas is used in order to calculate those [198, 199, 201, 202]. Results from both the electron and the muon channel are combined in the limit setting procedure.

8.1 Dark Matter interpretation

Exclusion limits can be set on the parameter Λ which also translate into cross section exclusion limits. In contrary to the common practice, 90% confidence level (CL) exclusion limits are set – this allows for a better comparison to exclusion limits from dark matter direct detection experiments. Fig. 8.3 shows exclusion limits on the cutoff parameter Λ for the different coupling scenarios. These exclusion limits can be obtained using the relation

$$\Lambda_{\mathrm{obs}}^4 = \frac{\sigma_{\mathrm{calc}} \cdot \Lambda_{\mathrm{calc}}^4}{\sigma_{\mathrm{obs}}}, \tag{8.1}$$

where $\Lambda_{\mathrm{calc}} = 1000$ GeV as stated in Sec. 7.1,σ_{calc} is the cross section of the considered dark matter signal sample and σ_{obs} is the observed exclusion limit for the dark matter production. Several truncation scenarios are indicated in order to give the reader an estimate of the impact of the truncation procedure. In the next step, these exclusion limits can be translated into exclusion limits on the DM-nucleon scattering cross section – the common way results are presented direct searches for dark matter [9, 254, 255].The following relations are used [134, 256]:

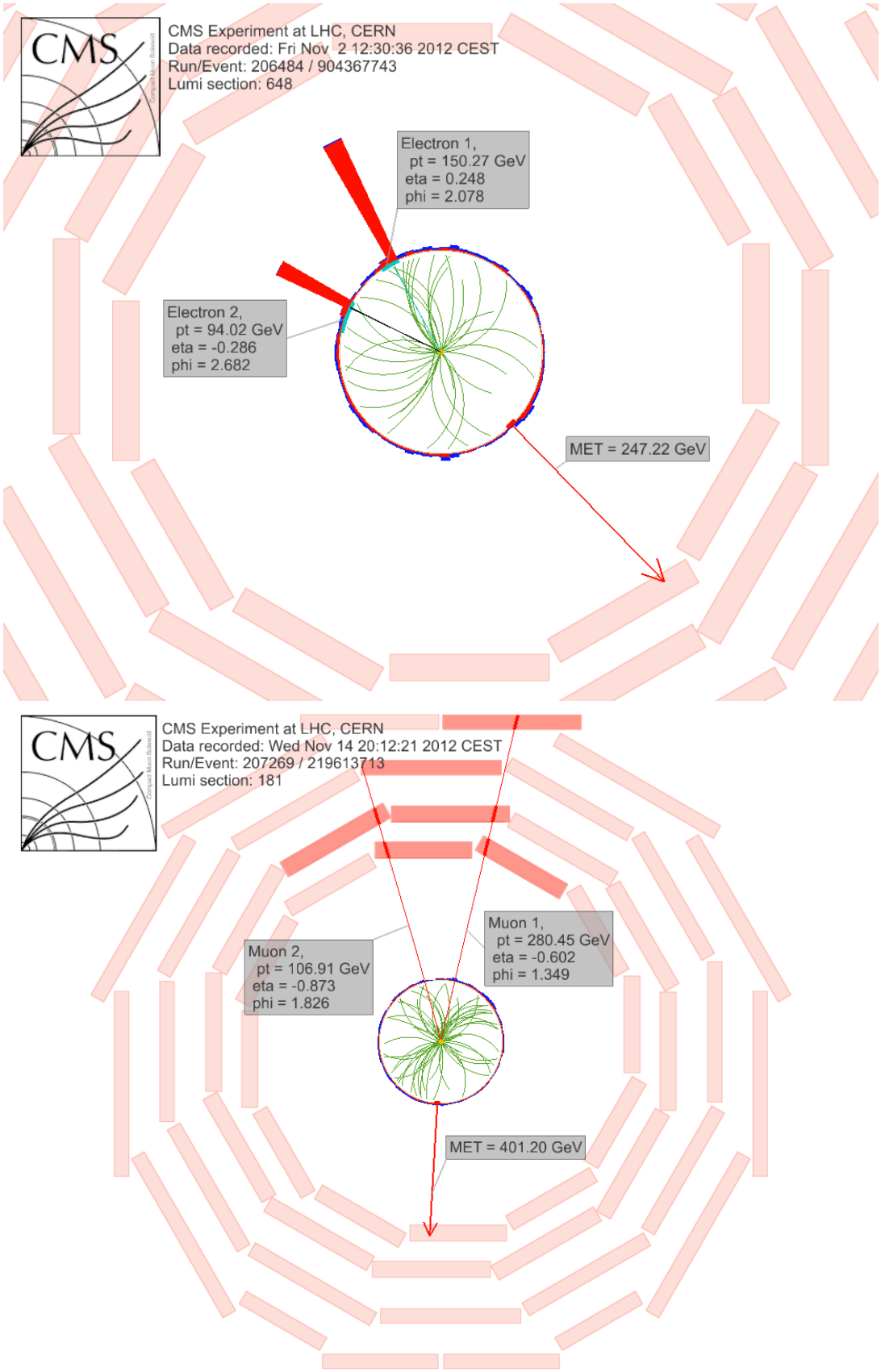

Figure 8.1: Event view for a high energetic dielectron+$E_{\mathrm{T}}^{\mathrm{miss}}$ (top) and a high energetic dimuon+$E_{\mathrm{T}}^{\mathrm{miss}}$ (bottom) events.

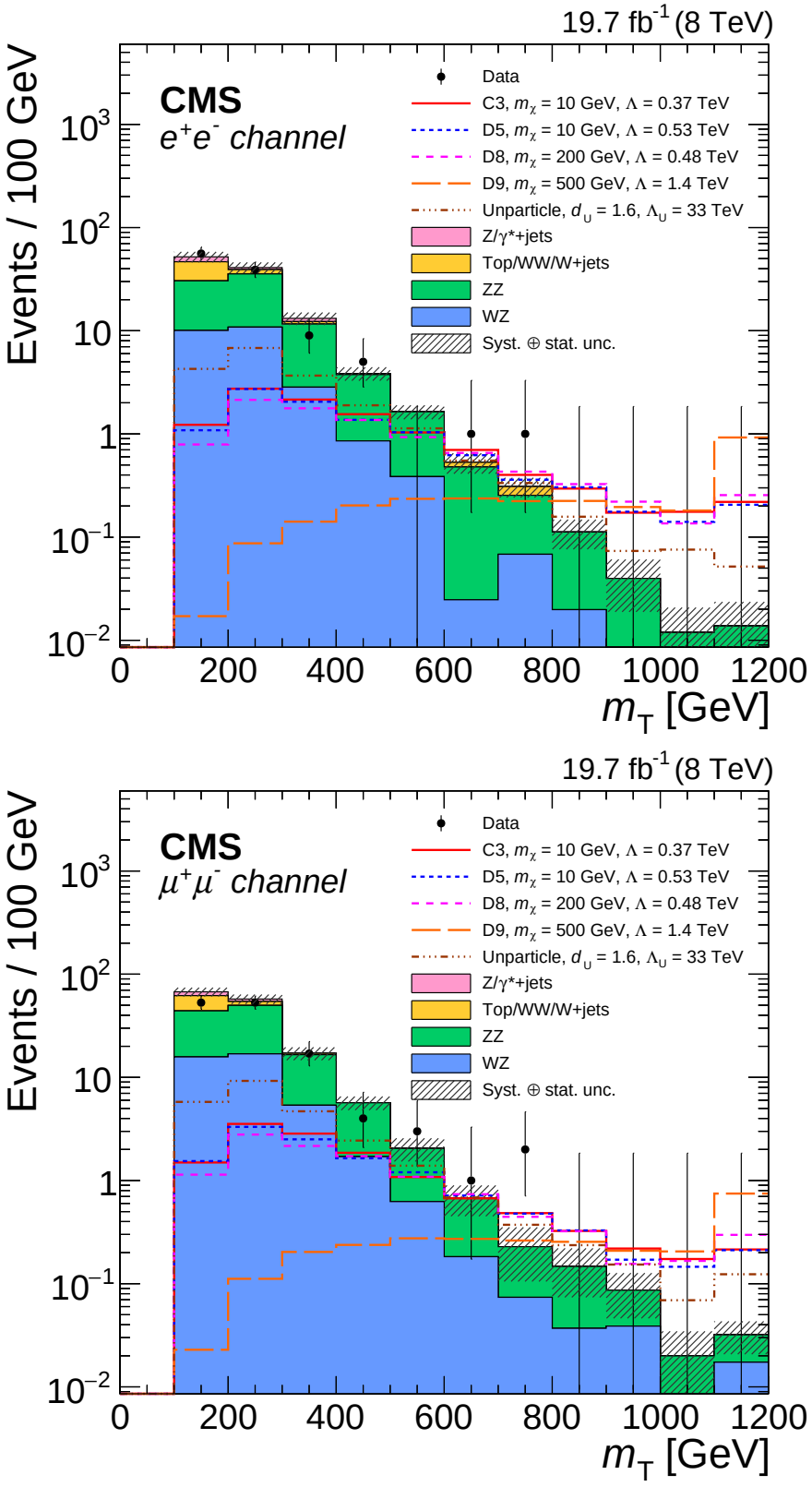

Figure 8.2: Distributions of the transverse mass m_T for the final selection in the electron (top, Northeastern) and muon (bottom, this thesis) channels. Sample distributions of m_T for several dark matter and unparticle signal hypotheses are shown. Examples of expected signal distributions are shown for DM production and unparticle production. The total statistical and systematic uncertainty in the overall background is shown as a hatched region. Overflow events are integrated in the last bin. Agreement is observed between the standard model prediction and the data measurement ([1], based on input from the present analysis).

Process	ee	$\mu\mu$
C3, $m_\chi = 10$GeV, $\Lambda = 0.37$TeV	$10.7 \pm 0.2 \pm 1.1$	$12.8 \pm 0.3 \pm 1.1$
D5, $m_\chi = 10$GeV, $\Lambda = 0.53$TeV	$10.0 \pm 0.3 \pm 1.1$	$12.3 \pm 0.3 \pm 1.1$
D8, $m_\chi = 200$GeV, $\Lambda = 0.48$TeV	$9.0 \pm 0.2 \pm 1.1$	$11.1 \pm 0.2 \pm 0.9$
D9, $m_\chi = 500$GeV, $\Lambda = 1.4$TeV	$2.67 \pm 0.03 \pm 0.41$	$2.81 \pm 0.03 \pm 0.26$
Unparticle, $d_\mathcal{U} = 1.6$, $\Lambda_\mathcal{U} = 33$TeV	$19.0 \pm 0.3 \pm 1.3$	$25.6 \pm 0.4 \pm 1.7$
$Z/\gamma^* \to \ell^+\ell^-$	$8.2 \pm 1.9 \pm 0.8$	$8.6 \pm 3.0 \pm 1.0$
$WZ \to 3\ell\nu$	$25.1 \pm 0.5 \pm 2.8$	$40.7 \pm 0.7 \pm 4.5$
$ZZ \to 2\ell 2\nu$	$59 \pm 1 \pm 10$	$79 \pm 1 \pm 14$
$t\bar{t}/tW/WW/Z \to \tau\tau$	$18.7 \pm 3.4 \pm 3.3$	$22.9 \pm 2.3 \pm 3.4$
W + jets	$1.8 \pm 0.6 \pm 0.3$	—
Total background	$113 \pm 4 \pm 13$	$151 \pm 4 \pm 18$
Data	111	133

Table 8.1: Background estimation yields, signal prediction yields and observed number of events for the final selection for the dielectron (Northeastern) and the dimuon (this thesis) channel. The scenarios of dark matter with $m_\chi = 10$, 200, and 500GeV and cutoff scales $\Lambda = 0.37$, 0.53, 0.48, and 1.4TeV are presented as benchmark points. Unparticle signal prediction is shown for a scaling dimension $d_\mathcal{U} = 1.6$ and a renormalization scale $\Lambda_\mathcal{U} = 33$TeV. Statistical and systematic uncertainties are shown for all yields in the order yield ± stat. ± sys. The data is found to be in agreement with the standard model prediction within the uncertainties ([1], based on input from the present analysis).

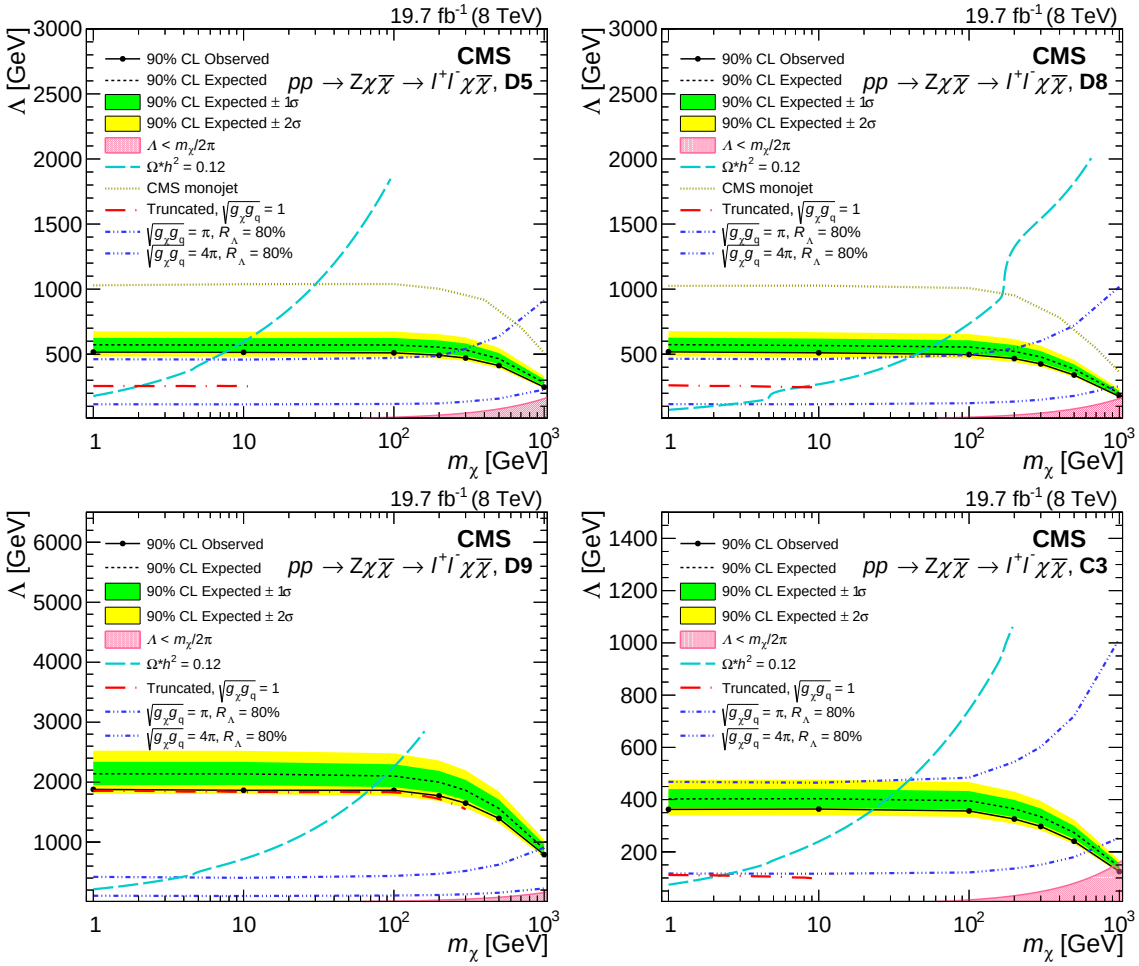

Figure 8.3: Expected and observed 90% CL lower exclusion limits on the EFT parameter Λ as a function of dark matter particle mass m_χ. Couplings D5 (top left), D8 (top right), D9 (bottom left), and C3 (bottom left) are shown. The cyan long-dashed line is calculated by MadDM 1.0 [252] and indicates the relic density of cold non-baryonic dark matter: $\Omega h^2 = 0.1198 \pm 0.0026$ as measured by the Planck telescope [253]. The pink shaded area shows the lower bound with $\Lambda > m_\chi/2\pi$ where the effective field theory approach is no longer valid. Results from CMS monojet search [16] is shown for D5 and D8 scenarios. Truncated limits with the requirement $\sqrt{g_q g_\chi} = 1$ are presented with red dot long-dashed lines. The blue triple-dot and double-dot dashed lines show the contours of truncated exclusion limits with $R_\Lambda = 80\%$ for all considered operators. Hereby, the couplings are set to $\sqrt{g_q g_\chi} = \pi$ and 4π ([1], based on input from the present analysis).

$$\sigma_0^{\mathrm{D8,D9}} = \sum_{\mathrm{q}} \frac{3\mu_{\chi N}^2}{\pi\Lambda^4}\left(\Delta_{\mathrm{q}}^N\right)^2 = 9.18\times10^{-40}\mathrm{cm}^2\left(\frac{\mu_{\chi N}}{1\mathrm{GeV}}\right)^2\left(\frac{300\mathrm{GeV}}{\Lambda}\right)^4,$$
$$\sigma_0^{\mathrm{D5}} = \sum_{\mathrm{q}} \frac{\mu_{\chi N}^2}{\pi\Lambda^4}\left(f_{\mathrm{q}}^N\right)^2 = 1.38\times10^{-37}\mathrm{cm}^2\left(\frac{\mu_{\chi N}}{1\mathrm{GeV}}\right)^2\left(\frac{300\mathrm{GeV}}{\Lambda}\right)^4, \tag{8.2}$$
$$\sigma_0^{\mathrm{C3}} = \sum_{\mathrm{q}} \frac{4\mu_{\chi N}^2}{\pi\Lambda^4}\left(f_{\mathrm{q}}^N\right)^2 = 5.52\times10^{-37}\mathrm{cm}^2\left(\frac{\mu_{\chi N}}{1\mathrm{GeV}}\right)^2\left(\frac{300\mathrm{GeV}}{\Lambda}\right)^4.$$

Hereby, $\mu_{\chi N}$ denotes the reduced mass of the DM-nucleon system, the parameter f_{q}^N characterizes the nucleon structure ($f_{\mathrm{u}}^p = f_{\mathrm{d}}^n = 2$ and $f_{\mathrm{d}}^p = f_{\mathrm{u}}^n = 1; f = 0$ otherwise), and Δ_{q}^N is a spin-dependent form factor ($\Delta_{\mathrm{u}}^p = \Delta_{\mathrm{d}}^n = 0.842\pm0.012$, $\Delta_{\mathrm{d}}^p = \Delta_{\mathrm{u}}^n = -0.427\pm0.013$, $\Delta_{\mathrm{s}}^p = \Delta_{\mathrm{s}}^n = -0.085\pm0.018$) as specified in [257]. The corresponding exclusion limits are shown in Fig. 8.4. It should be noted that the presentation of DM-nucleon scattering cross section exclusion limits is subdivided in two coupling types – spin dependent and spin independent. In the EFT approach, D8 and D9 operators represent the spin dependent dark matter coupling whilst D5 and C3 are spin independent. It is observed that results obtained in the present analysis along other collider searches provide stronger exclusion limits in regions with $m_\chi < 10$ GeV, and non-collider searches provide stronger exclusion limits above this threshold. Furthermore, it is visible that collider searches provide better exclusion limits for spin dependent coupling types. Summary tables 9.7, 9.8, 9.9 and 9.10 of observed and expected exclusion limits on various parameters can also be found in the Appendix.

Exclusion limits for D5 and D8 are furthermore translated into 95% CL exclusion limits on the dark matter annihilation rate $\langle\sigma v\rangle$ (cf. Fig. 8.5). Hereby, σ denotes the annihilation cross section of dark matter and v the relative velocity of annihilating dark matter particles. Here, $\langle\sigma v\rangle$ is averaged over the distribution dark matter velocity. In the present analysis, the assumption about the astrophysical environment of $\langle v^2\rangle = 0.24$ is made corresponding to the assumption of the early universe at the time when dark matter froze out resulting in the thermal relic abundance. The label "Thermal relic value" denotes the value at which dark matter can make up the relic abundance of dark matter. A further assumption of a 100% branching ratio of dark matter which annihilates into quarks is made. Employing these constraints, it can be concluded that a Dirac fermion dark matter with vector coupling is ruled out for $m_\chi < 6$ GeV at 95% CL whereas for an axial-vector coupling the scenario with $m_\chi < 30$ GeV is excluded at 95% CL. In order to draw a comparison to indirect astrophysical searches, results of γ ray observations by H.E.S.S. [259] and Fermi-LAT [260] are shown. These results are multiplied by a factor of 2, since there Majorana dark matter is assumed instead of Dirac fermions.

8.2 Unparticle interpretation and model-independent limits

The same approach in terms of exclusion limits is applied in order to interpret the observed spectra for the unparticle signal scenario – here 95% CL exclusion limits are computed. The exclusion limit on the coupling of unparticles to standard model particles λ as a function of the unparticle dimension $d_{\mathcal{U}}$ assuming two scenarios for the effective cutoff scale with $\Lambda_{\mathcal{U}} = 10, 100$ TeV are set. Furthermore, exclusion limits on the cutoff scale $\Lambda_{\mathcal{U}}$ are set assuming $\lambda = 1$ for the coupling to

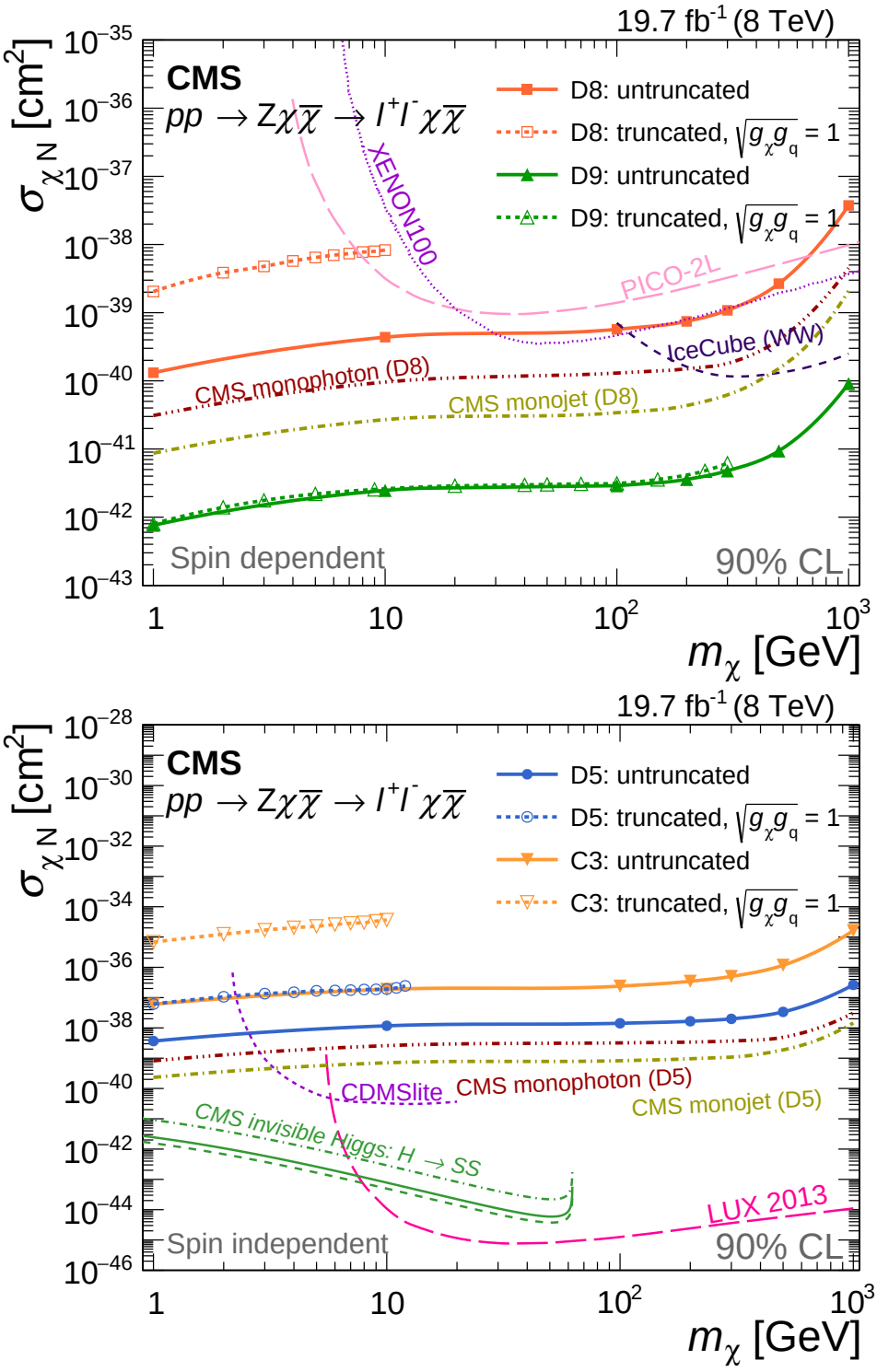

Figure 8.4: The 90% CL upper exclusion limits on the DM-nucleon cross section as a function of the dark matter particle mass m_χ. Spin dependent exclusion limits for axial-vector D8 and tensor D9 couplings are shown on the top. For comparison, results from the PICO [254], XENON100 [255], and IceCube [9] collaborations are also shown. Spin independent exclusion limits for vector coupling operators C3 and D5 are shown on the bottom of the figure along results from CDMSlite [10], LUX [12], as well as Higgs-portal scalar DM results from CMS [258] with central (solid), minimum (dashed) and maximum (dot dashed) values of Higgs-nucleon couplings. Collider search results from CMS monojet [16] and monophoton [18] searches are included for comparison. Truncated exclusion limits with parameters $\sqrt{g_q g_\chi} = 1$ are denoted by dashed lines ([1], based on input from the present analysis).

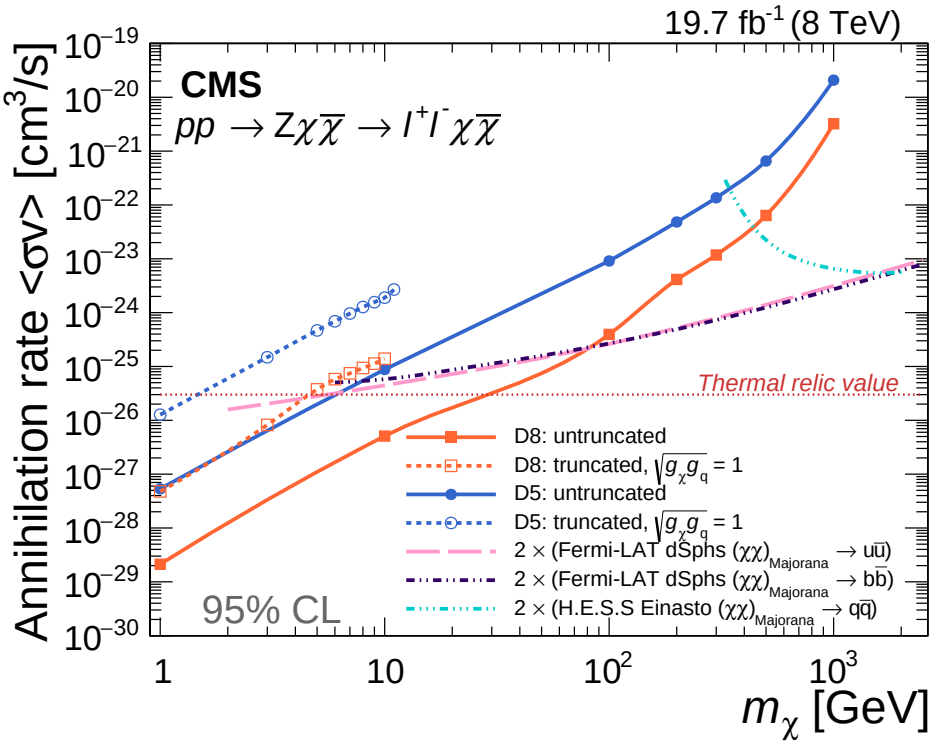

Figure 8.5: 95% CL upper exclusion limits on the dark matter annihilation rate $\langle\sigma v\rangle$ for $\chi\overline{\chi} \rightarrow q\bar{q}$ as a function of the DM particle mass m_χ for vector coupling (D5) and axial-vector (D8) coupling. It is assumed that dark matter annihilates to quark with a 100% branching fraction. Experimental results from H.E.S.S [259] and Fermi-LAT [260] are also shown. Thermal relic value (the value which is required for dark matter in order to account for the relic abundance of dark matter) is shown as a red dotted line. Truncated limits with couplings set to $\sqrt{g_q g_\chi} = 1$ are denoted by dashed lines ([1], based on input from the present analysis).

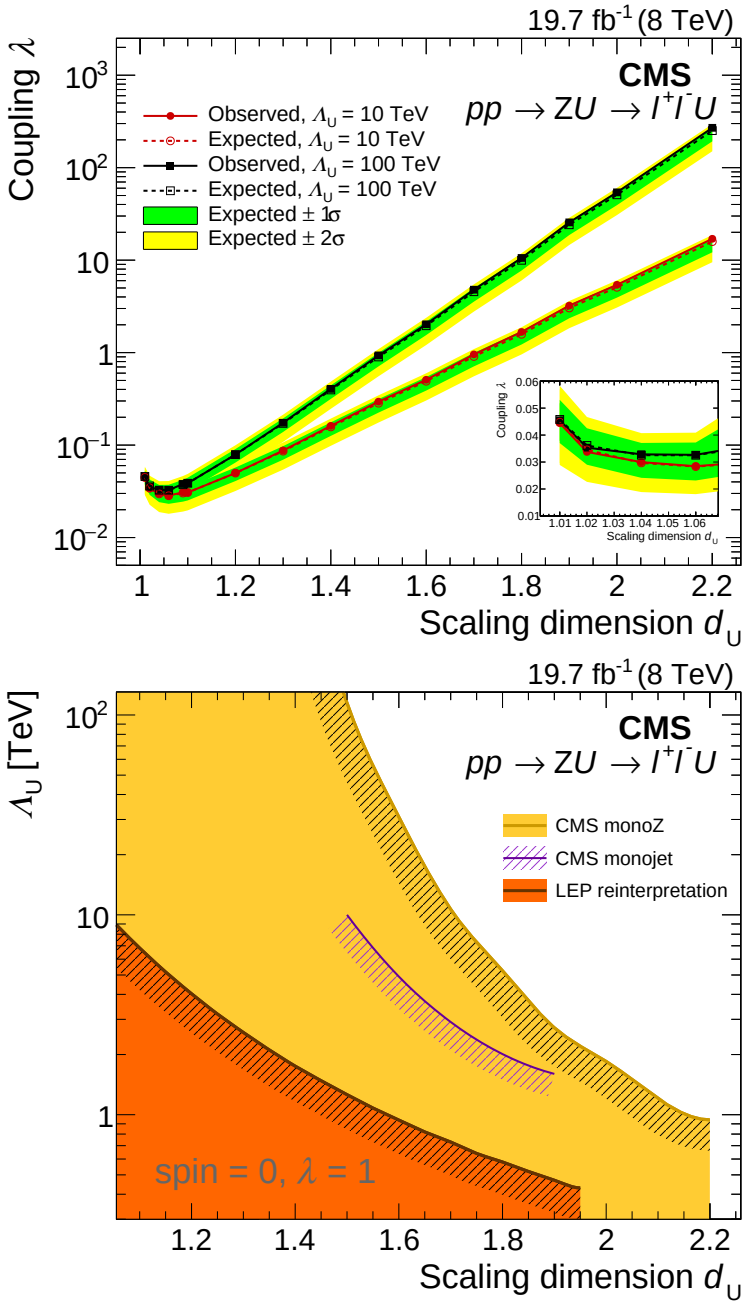

Figure 8.6: Top: 95% CL upper exclusion limits on the coupling λ of the unparticle to the standard model particles for two effective cutoff scale scenarios $\Lambda_{\mathcal{U}} = 10$ and 100TeV (left). An additional enhanced presentation is plotted for clarity. Bottom: 95% CL lower exclusion limits on unparticle effective cutoff scale $\Lambda_{\mathcal{U}}$. Hereby, the coupling strength is fixed to $\lambda = 1$. The results from CMS monojet search [16] along the reinterpretation of LEP searches [102] are shown for comparison. The shading indicates the excluded region of the parameter space ([1], based on input from the present analysis).

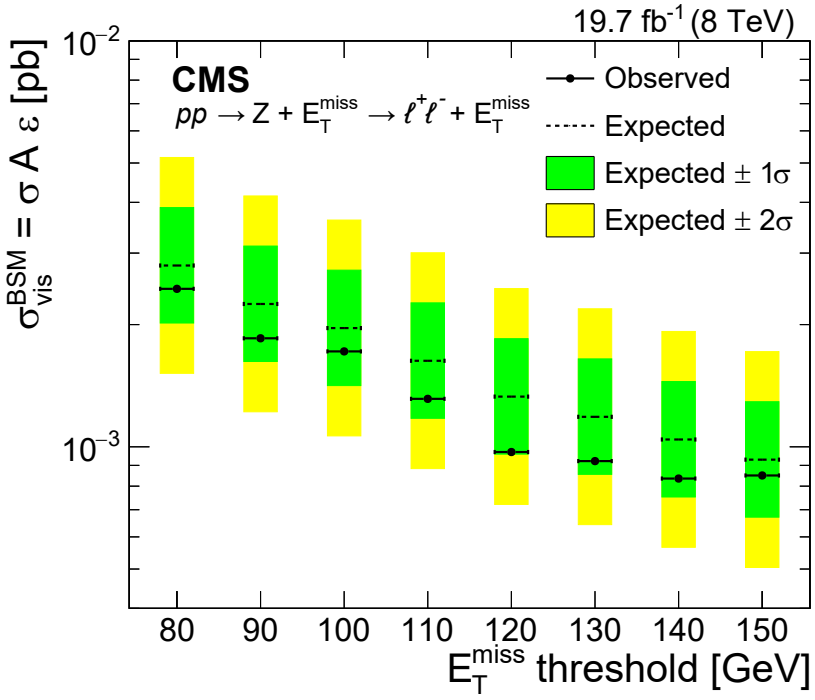

Figure 8.7: 95% CL model-independent upper limits on the visible cross section ($\sigma A\epsilon$) for production of events beyond the standard model as a function of $E_{\mathrm{T}}^{\mathrm{miss}}$ cutoff threshold ([1], based on input from the present analysis).

standard model particles. Both results are shown in Fig. 8.6. It is observed that the result of the present thesis (labeled "monoZ" in the figure) delivers the most stringent exclusion limits observed to date. The corresponding tables can be found in Tab. 9.11, 9.12 and 9.13 of the Appendix.

Finally, a single-bin counting experiment performed in the $E_{\mathrm{T}}^{\mathrm{miss}}$ spectrum is employed for setting model-independent upper exclusion limits at 95% CL on the possible signatures of physics beyond the standard model. Starting at the lower threshold of $E_{\mathrm{T}}^{\mathrm{miss}} > 80$ GeV and increasing it in steps of 10 GeV to $E_{\mathrm{T}}^{\mathrm{miss}} > 150$ GeV, possible signal cross sections between $\sigma_{\mathrm{BSM}} > 2.5$ fb and $\sigma_{\mathrm{BSM}} > 0.8$ fb are excluded at 95% CL (cf. Fig. 8.7 and Tab. 9.14). Hereby, A denotes the acceptance and ϵ denotes the final signal efficiency in the corresponding $E_{\mathrm{T}}^{\mathrm{miss}}$ region.

8.3 Updated preliminary result from CMS

A subsequent study[1] of the $Z \to \ell\ell$ along $E_{\mathrm{T}}^{\mathrm{miss}}$ channel has been performed using the recent data collected by CMS at the world record center of mass energy $\sqrt{s} = 13$ TeV with an integrated luminosity of $\mathcal{L} = 2.3$ fb^{-1}. The preliminary results are available in [128].

The new analysis employs a simplified model approach as well as an effective field theory approach for the dark matter signal estimation. The event selection criteria have been slightly adjusted and $E_{\mathrm{T}}^{\mathrm{miss}}$ is now considered as the final variable of interest. For both the dielectron and the dimuon channels, agreement between CMS data and standard model background estimation is observed which is interpreted in terms of exclusion limits (cf. Fig. 8.8). For the new simplified model approach,

[1] Studies for the new analysis have been performed by the presenter of this thesis

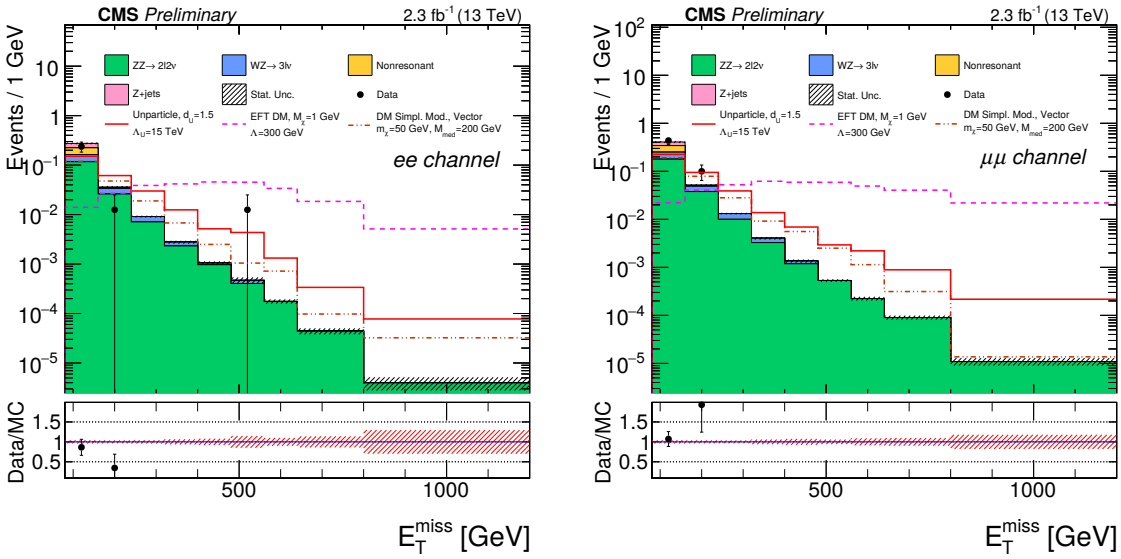

Figure 8.8: The distribution of $E_{\mathrm{T}}^{\mathrm{miss}}$ after for the final selection for the $Z \to ee$ (left) and $Z \to$ (right) channels of the 13 TeV analysis. Expected signal distributions are shown for the simplified model of DM production with vector couplings, the EFT scenario of DM production, and unparticles. Agreement is observed between the measurement and background prediction [128].

the preliminary result presents exclusion limits in the two-dimensional m_χ vs. m_{Med} space for different coupling type (vector, axial-vector) and coupling strength ($g_\chi = g_q = 0.25$ and $g_\chi = g_q = 1$) scenarios (the latter case is shown in Fig. 8.9). One should be careful when comparing the exclusion limits observed by the analysis at $\sqrt{s} = 13$ TeV to the results of the present thesis. This is due to the fact that the effective field theory considered for the dataset of 2012 is known to not deliver precise predictions for all points of the parameter space (cf. Sec. 3.4.4.4).

However, here an approximate "rule of thumb" comparison shall be discussed here briefly. It is visible in Fig. 8.9 that, once one assumes the case of light dark matter mass with $m_\chi \approx$ 1GeV, the observed exclusion limit for the dark matter mediator in the 13 TeV analysis is ≈ 400 GeV for both coupling cases. Recalling the relation from Eq. 3.28 and substituting $g_q = g_\chi = 1$ yields

$$\Lambda = \frac{m_{\mathrm{med}}}{\sqrt{g_q g_\chi}} = m_{\mathrm{med}}. \tag{8.3}$$

In this case, one can directly translate Λ into m_{med}. For the 8 TeV analysis, one can see on the top of Fig. 8.3 that for both the D5 and the D8 coupling cases the *non*truncated exclusion limit for $m_\chi = 1$ GeV is approximately 500 GeV. Since it is known that in this region the cross section is overestimated by the effective field theory approach, one shall compare the exclusion limits for different truncation scenarios. It is also to be kept in mind that the exclusion limits in 13 TeV are given with 95% CL while the 8 TeV limits have been calculated with 90% CL and therefore the 13 TeV exclusion limits are somewhat more conservative. One observes, that, depending on the truncation scenario, the exclusion limit for dark matter mass $m_\chi = 1$ in this scenario is either comparable or even better for the 13 TeV analysis.

For the unparticle interpretation, the exclusion limit of the $\Lambda_{\mathcal{U}}$ as a function of $d_{\mathcal{U}}$ is calculated analogously to the approach of the present thesis (cf. Fig. 8.10). Despite the cross section gain for

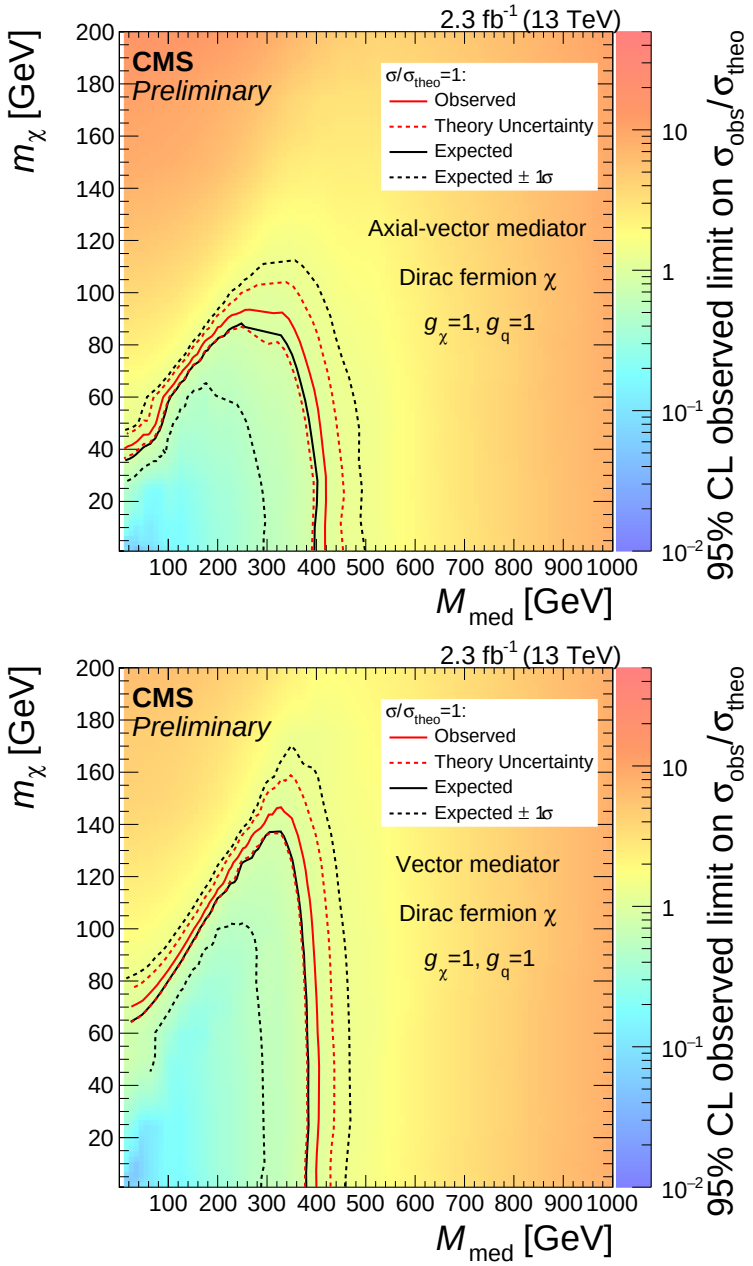

Figure 8.9: 95% CL exclusion limits in terms of the mediator mass M_{med} and the dark matter particle mass m_χ obtained by the 13 TeV $Z+E_{\text{T}}^{\text{miss}}$ analysis for vector mediator (top) and axial-vector mediator (bottom). Hereby, the coupling of the mediator particle to quarks and to dark matter is assumed to be equal $g_q = g_\chi = 1$ [128].

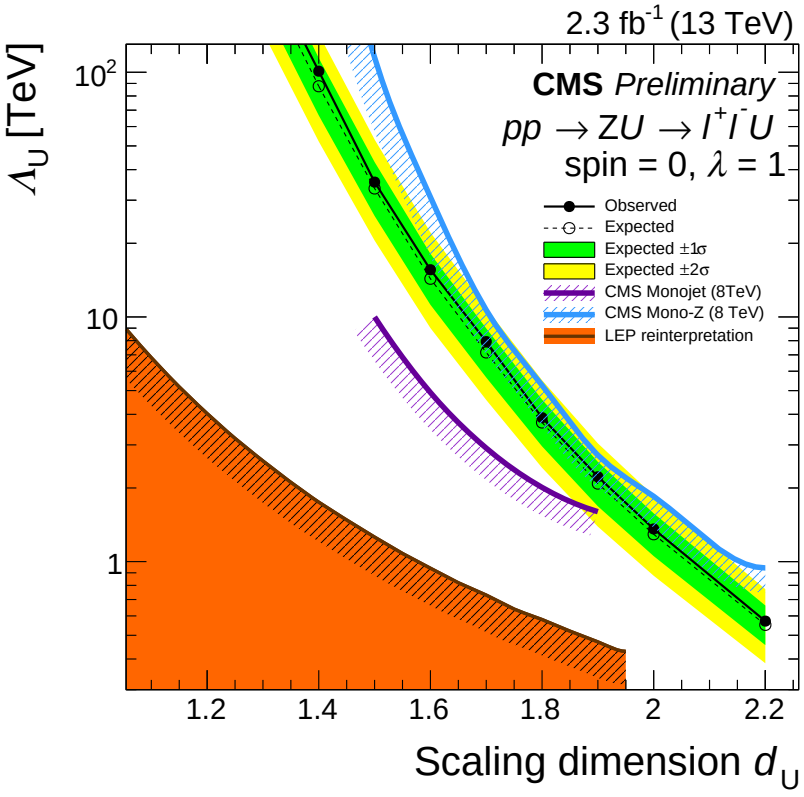

Figure 8.10: 95% CL lower exclusion limits on unparticle effective cutoff scale $\Lambda_{\mathcal{U}}$ assuming a fixed coupling $\lambda = 1$ obtained at $\sqrt{s} = 13$ TeV with an integrated luminosity of 2.3 fb^{-1}. Results from the 8 TeV monojet search [16], the reinterpretation of LEP searches [102] as well as the result of the present dissertation (cf. Fig.8.6) are shown for comparison. The observed sensitivity is comparable to the one observed in the 8 TeV case albeit the much smaller dataset size [128].

unparticle production arising from the larger $\sqrt{s}$, the new analysis can not yet reach the sensitivity of the present thesis due to a rather small size of the dataset collected in 2015. Given the much larger dataset already collected by CMS in 2016 at $\sqrt{s} = 13$ TeV, one can expect that the unparticle search in data of 2016 will be able to access unparticle parameter space which was not accessible to previous analyses, either finding a hint for unparticle production or increasing the exclusion limits set so far.

CHAPTER 9

Conclusion and Outlook

A search for dark matter, unparticles and physics beyond the standard model in events with a Z boson decaying into lepton pairs and large missing transverse energy has been presented within the scope of this thesis – the first search for dark matter to be performed with the CMS detector in this final state. The dataset was recorded by CMS in 2012 corresponding to an integrated luminosity of 19.7 fb^{-1} in proton-proton collisions at the center of mass energy $\sqrt{s} = 8$ TeV.

The background processes for both the dielectron and the dimuon channels have been studied and different data-driven techniques were employed along the Monte Carlo simulation for the estimate of the background contributions to the final event selection. Theoretical and experimental systematic uncertainties have been considered and included into the final interpretation of the observed spectra. The measurement is found to be in agreement with the standard model prediction. No evidence for the existence of dark matter, unparticles or other processes beyond the standard model can be found. The absence of possible signals is interpreted in terms of exclusion limits at 90% and 95% CL depending on the considered scenario – hereby, the most stringent exclusion limits for unparticle production are set up-to-date. Model-independent exclusion limits are calculated whereby a cross section of 2.5 fb for the signal region above 80 GeV is excluded at 95% CL. The newest preliminary CMS results in the considered channel have been briefly summarized and compared to the results of the present thesis.

Collider searches and direct (indirect) dark matter searches are complementary to each other, being sensitive to different dark matter scenarios and providing independent measurements. While non-collider searches feature high sensitivity for dark matter candidates with masses typically above 1 GeV, collider searches are also sensitive to dark matter masses below this threshold, being able to probe many different coupling scenarios. It is to be expected that the direct and indirect dark matter detection experiments, as well as the collider searches will progress quickly, given the future updates of various dark matter detection experiments and the upcoming studies performed at the LHC with the data of 2015 and 2016.

The searches for dark matter and unparticles in particular, as well as searches for physics beyond the standard model in general will continue – the publication of new (CMS) results will bring more insight into the challenging task of finding New Physics.

Appendix

Cut	MadGraph	POWHEG	Sherpa
Lepton	0.5403	0.5423 (0.37%)	0.5413 (0.18%)
$\lvert M_{\ell\ell} - M_Z \rvert < 10$ GeV	0.7723	0.7657 (-0.86%)	0.7630 (-1.20%)
$p_T^{\ell\ell} > 50$ GeV	0.4437	0.4193 (-5.52%)	0.4397 (-0.91%)
$E_{\mathrm{T}}^{\mathrm{miss}} > 80$ GeV	0.2196	0.1998 (-9.01%)	0.2160 (-1.62%)
$E_{\mathrm{T}}^{\mathrm{miss}} > 260$ GeV	0.0063	0.0054 (-13.71%)	0.0063 (0.38%)
$N_{\mathrm{jets}} \leq 1$	0.9317	0.9616 (3.21%)	0.9542 (2.41%)
$\Delta\phi(Z, E_{\mathrm{T}}^{\mathrm{miss}}) > 2.7$	0.6509	0.6510 (0.02%)	0.7007 (7.64%)
$\lvert p_T^{\ell\ell} - E_{\mathrm{T}}^{\mathrm{miss}} \rvert / p_T^{\ell\ell} < 0.2$	0.5324	0.5247 (-1.44%)	0.5807 (9.08%)
Total with $E_{\mathrm{T}}^{\mathrm{miss}} > 80$ GeV	0.0612	0.0586 (-4.20%)	0.0699 (14.24%)
Total with $E_{\mathrm{T}}^{\mathrm{miss}} > 90$ GeV	0.0483	0.0460 (-4.78%)	0.0553 (14.37%)
Total with $E_{\mathrm{T}}^{\mathrm{miss}} > 100$ GeV	0.0386	0.0368 (-4.56%)	0.0444 (15.07%)
Total with $E_{\mathrm{T}}^{\mathrm{miss}} > 110$ GeV	0.0309	0.0295 (-4.56%)	0.0359 (16.44%)
Total with $E_{\mathrm{T}}^{\mathrm{miss}} > 120$ GeV	0.0250	0.0239 (-4.53%)	0.0291 (16.36%)
Total with $E_{\mathrm{T}}^{\mathrm{miss}} > 130$ GeV	0.0201	0.0194 (-3.75%)	0.0238 (18.09%)
Total with $E_{\mathrm{T}}^{\mathrm{miss}} > 140$ GeV	0.0164	0.0157 (-4.48%)	0.0195 (18.66%)
Total with $E_{\mathrm{T}}^{\mathrm{miss}} > 150$ GeV	0.0134	0.0130 (-3.58%)	0.0161 (19.44%)
Total with $E_{\mathrm{T}}^{\mathrm{miss}} > 170$ GeV	0.0091	0.0089 (-2.41%)	0.0112 (23.31%)
Total with $E_{\mathrm{T}}^{\mathrm{miss}} > 190$ GeV	0.0063	0.0062 (-1.18%)	0.0078 (24.49%)
Total with $E_{\mathrm{T}}^{\mathrm{miss}} > 210$ GeV	0.0044	0.0044 (0.47%)	0.0055 (25.73%)
Total with $E_{\mathrm{T}}^{\mathrm{miss}} > 230$ GeV	0.0031	0.0032 (4.84%)	0.0040 (31.49%)
Total with $E_{\mathrm{T}}^{\mathrm{miss}} > 250$ GeV	0.0022	0.0023 (5.16%)	0.0030 (35.96%)
Total with $E_{\mathrm{T}}^{\mathrm{miss}} > 260$ GeV	0.0019	0.0020 (6.63%)	0.0026 (37.97%)

Table 9.1: MC $ZZ \to 2\ell 2\nu$ Acceptance comparison with different generators – `MadGraph` (which is used as the main prediction), `POWHEG` and `SHERPA`. The percentage uncertainties arise from the difference with respect to MadGraph. Especially the `SHERPA` prediction deviates from other estimates [232].

Operator	Mass(GeV)	+QCD Scale %	-QCD Scale %	QCD Scale %
D5	1	5.90	4.51	5.20
D5	10	5.86	4.64	5.25
D5	100	5.90	4.75	5.32
D5	200	6.01	4.72	5.37
D5	300	6.08	4.77	5.43
D5	500	6.12	4.92	5.52
D5	1000	6.43	4.96	5.70

Table 9.2: Theoretical uncertainties for D5 dark matter signal samples [232].

Operator	Mass(GeV)	+QCD Scale %	-QCD Scale %	QCD Scale %
D8	1	5.99	4.51	5.25
D8	10	5.82	4.72	5.27
D8	100	5.88	4.69	5.28
D8	200	6.10	4.76	5.43
D8	300	6.08	4.85	5.46
D8	500	6.23	4.91	5.57
D8	1000	6.31	4.97	5.64

Table 9.3: Theoretical uncertainties for D8 dark matter signal samples [232].

Operator	Mass(GeV)	+QCD Scale %	-QCD Scale %	QCD Scale %
D9	1	6.11	4.91	5.51
D9	10	6.23	4.87	5.55
D9	100	6.28	4.89	5.58
D9	200	6.24	4.95	5.59
D9	300	6.37	4.96	5.67
D9	500	6.40	5.07	5.73
D9	1000	6.39	5.05	5.72

Table 9.4: Theoretical uncertainties for D9 dark matter signal samples [232].

Operator	Mass(GeV)	+QCD Scale %	-QCD Scale %	QCD Scale %
C3	1	5.76	4.55	5.16
C3	10	5.89	4.63	5.26
C3	100	6.02	4.69	5.35
C3	200	6.07	4.77	5.42
C3	300	6.26	4.79	5.52
C3	500	6.26	4.96	5.61
C3	1000	6.30	4.92	5.61

Table 9.5: Theoretical uncertainties for C3 dark matter signal samples [232].

$d_{\mathcal{U}}$	+QCD Scale %	-QCD Scale %	QCD Scale %
1.01	2.92	2.59	2.76
1.02	2.93	2.58	2.76
1.04	2.84	2.58	2.71
1.06	2.82	2.52	2.67
1.09	2.76	2.44	2.60
1.10	2.71	2.44	2.57
1.20	2.46	2.22	2.34
1.30	2.15	1.83	1.99
1.40	1.82	1.51	1.66
1.50	1.34	1.21	1.28
1.60	0.96	0.88	0.92
1.70	0.47	0.48	0.47
1.80	0.09	0.27	0.18
1.90	0.54	0.66	0.60
2.00	1.41	0.34	0.88
2.20	2.55	0.85	1.70

Table 9.6: Theoretical uncertainties for unparticle signal samples produced with `Pythia` [232].

m_χ	Expected		Expected−1σ		Expected+1σ		Observed	
	Λ	$\sigma_{\chi N}$	Λ	$\sigma_{\chi N}$	Λ	$\sigma_{\chi N}$	Λ	$\sigma_{\chi N}$
(GeV)	(GeV)	(cm^2)	(GeV)	(cm^2)	(GeV)	(cm^2)	(GeV)	(cm^2)
1	572	2.4×10^{-39}	626	1.7×10^{-39}	522	3.5×10^{-39}	516	3.7×10^{-39}
10	570	7.8×10^{-39}	624	5.4×10^{-39}	520	1.1×10^{-38}	514	1.2×10^{-38}
100	571	9.1×10^{-39}	625	6.3×10^{-39}	521	1.3×10^{-38}	510	1.4×10^{-38}
200	554	1.0×10^{-38}	606	7.2×10^{-39}	505	1.5×10^{-38}	492	1.7×10^{-38}
300	533	1.2×10^{-38}	583	8.5×10^{-39}	486	1.7×10^{-38}	471	2.0×10^{-38}
500	465	2.1×10^{-38}	509	1.5×10^{-38}	425	3.0×10^{-38}	413	3.4×10^{-38}
1000	281	1.6×10^{-37}	308	1.1×10^{-37}	257	2.3×10^{-37}	247	2.6×10^{-37}

Table 9.7: Expected and observed 90% CL upper exclusion limits on the DM-nucleon cross section $\sigma_{\chi N}$ and effective cutoff scale Λ for the D5 coupling ([1], based on input from the present analysis).

m_χ	Expected		Expected−1σ		Expected+1σ		Observed	
	Λ	$\sigma_{\chi N}$	Λ	$\sigma_{\chi N}$	Λ	$\sigma_{\chi N}$	Λ	$\sigma_{\chi N}$
(GeV)	(GeV)	(cm^2)	(GeV)	(cm^2)	(GeV)	(cm^2)	(GeV)	(cm^2)
1	574	8.8×10^{-41}	627	6.1×10^{-41}	523	1.3×10^{-40}	518	1.3×10^{-40}
10	567	2.9×10^{-40}	620	2.0×10^{-40}	517	4.2×10^{-40}	511	4.4×10^{-40}
100	555	3.7×10^{-40}	607	2.6×10^{-40}	507	5.3×10^{-40}	498	5.7×10^{-40}
200	522	4.8×10^{-40}	570	3.3×10^{-40}	476	6.9×10^{-40}	467	7.5×10^{-40}
300	479	6.7×10^{-40}	524	4.7×10^{-40}	437	9.7×10^{-40}	425	1.1×10^{-39}
500	386	1.6×10^{-39}	422	1.1×10^{-39}	352	2.3×10^{-39}	340	2.7×10^{-39}
1000	199	2.3×10^{-38}	218	1.6×10^{-38}	182	3.3×10^{-38}	176	3.7×10^{-38}

Table 9.8: Expected and observed 90% CL upper exclusion limits on the DM-nucleon cross section $\sigma_{\chi N}$ and effective cutoff scale Λ for the D9 coupling ([1], based on input from the present analysis).

m_χ	Expected		Expected−1σ		Expected+1σ		Observed	
	Λ	$\sigma_{\chi N}$	Λ	$\sigma_{\chi N}$	Λ	$\sigma_{\chi N}$	Λ	$\sigma_{\chi N}$
(GeV)	(GeV)	(cm^2)	(GeV)	(cm^2)	(GeV)	(cm^2)	(GeV)	(cm^2)
1	2139	4.5×10^{-43}	2339	3.2×10^{-43}	1951	6.5×10^{-43}	1879	7.6×10^{-43}
10	2137	1.4×10^{-42}	2337	1.0×10^{-42}	1950	2.1×10^{-42}	1864	2.5×10^{-42}
100	2102	1.8×10^{-42}	2299	1.3×10^{-42}	1918	2.6×10^{-42}	1865	2.9×10^{-42}
200	2000	2.2×10^{-42}	2187	1.5×10^{-42}	1825	3.2×10^{-42}	1772	3.6×10^{-42}
300	1863	2.9×10^{-42}	2038	2.1×10^{-42}	1700	4.2×10^{-42}	1650	4.8×10^{-42}
500	1562	6.0×10^{-42}	1708	4.2×10^{-42}	1425	8.6×10^{-42}	1395	9.4×10^{-42}
1000	886	5.8×10^{-41}	969	4.0×10^{-41}	809	8.3×10^{-41}	790	9.1×10^{-41}

Table 9.9: Expected and observed 90% CL upper exclusion limits on the DM-nucleon cross section $\sigma_{\chi N}$ and effective cutoff scale Λ for the D9 coupling ([1], based on input from the present analysis).

m_χ	Expected		Expected−1σ		Expected+1σ		Observed	
	Λ	$\sigma_{\chi N}$	Λ	$\sigma_{\chi N}$	Λ	$\sigma_{\chi N}$	Λ	$\sigma_{\chi N}$
(GeV)	(GeV)	(cm^2)	(GeV)	(cm^2)	(GeV)	(cm^2)	(GeV)	(cm^2)
1	403	4.0×10^{-38}	440	2.8×10^{-38}	367	5.7×10^{-38}	363	6.1×10^{-38}
10	403	1.2×10^{-37}	441	8.7×10^{-38}	368	1.8×10^{-37}	364	1.9×10^{-37}
100	396	1.6×10^{-37}	433	1.1×10^{-37}	361	2.3×10^{-37}	356	2.4×10^{-37}
200	365	2.2×10^{-37}	399	1.5×10^{-37}	333	3.2×10^{-37}	326	3.5×10^{-37}
300	335	3.1×10^{-37}	366	2.2×10^{-37}	305	4.5×10^{-37}	297	5.0×10^{-37}
500	273	7.0×10^{-37}	299	4.9×10^{-37}	250	1.0×10^{-36}	241	1.2×10^{-36}
1000	143	9.5×10^{-36}	156	6.6×10^{-36}	130	1.4×10^{-35}	125	1.6×10^{-35}

Table 9.10: Expected and observed 90% CL upper exclusion limits on the DM-nucleon cross section $\sigma_{\chi N}$ and effective cutoff scale Λ for the C3 coupling ([1], based on input from the present analysis).

$d_{\mathcal{U}}$	λ			
	Expected	Expected−1σ	Expected+1σ	Observed
1.01	0.045	0.038	0.053	0.044
1.02	0.035	0.030	0.042	0.034
1.04	0.029	0.025	0.035	0.030
1.06	0.028	0.024	0.033	0.028
1.09	0.030	0.025	0.035	0.031
1.10	0.031	0.026	0.036	0.031
1.30	0.085	0.072	0.100	0.087
1.50	0.273	0.232	0.322	0.295
1.70	0.864	0.734	1.018	0.956
1.90	2.86	2.43	3.37	3.22
2.20	14.8	12.6	17.4	17.0

Table 9.11: Expected and observed 95% CL upper exclusion limits on the coupling λ between unparticles and the SM fields. The assumption $\Lambda_{\mathcal{U}} = 10$TeV is made ([1], based on input from the present analysis).

$d_{\mathcal{U}}$	λ			
	Expected	Expected-1σ	Expected$+1\sigma$	Observed
1.01	0.046	0.039	0.054	0.045
1.02	0.037	0.031	0.044	0.035
1.04	0.032	0.027	0.038	0.033
1.06	0.032	0.027	0.038	0.033
1.09	0.037	0.031	0.043	0.038
1.10	0.039	0.033	0.046	0.039
1.30	0.169	0.143	0.199	0.174
1.50	0.864	0.734	1.018	0.933
1.60	1.88	1.60	2.22	2.02
1.70	4.33	3.68	5.10	4.79
1.90	22.7	19.3	26.8	25.6
2.20	235	199	276	270

Table 9.12: Expected and observed 95% CL upper exclusion limits on the coupling λ between unparticles and the SM fields. The assumption $\Lambda_{\mathcal{U}} = 100$TeV is made ([1], based on input from the present analysis).

$d_{\mathcal{U}}$	$\Lambda_{\mathcal{U}}$ (TeV)			
	Expected	Expected-1σ	Expected$+1\sigma$	Observed
1.50	134	186	96.4	115
1.60	34.8	45.7	26.5	30.9
1.70	12.3	15.6	9.75	10.7
1.80	6.08	7.45	4.95	5.25
1.90	3.11	3.72	2.59	2.72
2.00	2.09	2.46	1.77	1.85
2.20	1.06	1.21	0.92	0.94

Table 9.13: Expected and observed 95% CL lower exclusion limits on the effective cutoff scale $\Lambda_{\mathcal{U}}$ for values $d_{\mathcal{U}} = 1.6, \ldots, 2.2$ in the range from 1.60 to 2.20. The coupling strength λ is fixed to 1 ([1], based on input from the present analysis).

$E_{\mathrm{T}}^{\mathrm{miss}}$ (GeV) threshold	80	90	100	110	120	130	140	150
Total SM	263	193	150	117	90.5	72.5	59.2	45.1
Total uncertainty	±30	±24	±20	±16	±13	±12	±9.6	±7.6
Data	244	172	141	104	74	61	50	43
Obs. upper limit	48.3	36.5	33.8	25.9	19.1	18.2	16.5	16.7
Exp. upper limit +2σ	102	81.7	71.3	59.2	48.3	43.1	37.9	33.8
Exp. upper limit +1σ	76.5	61.5	53.7	44.6	36.4	32.4	28.5	25.4
Exp. upper limit	55.1	44.3	38.6	32.1	26.2	23.4	20.5	18.3
Exp. upper limit -1σ	39.7	32.0	27.9	23.2	18.9	16.9	14.8	13.2
Exp. upper limit -2σ	29.9	24.0	21.0	17.4	14.2	12.7	11.1	9.90

Table 9.14: Total cumulative background prediction for both the electron and muon channel along the 95% CL upper exclusion limits on signatures from physics beyond the standard model. The listed uncertainties include both statistical and systematic contributions ([1], based on input from the present analysis).

Appendix 2

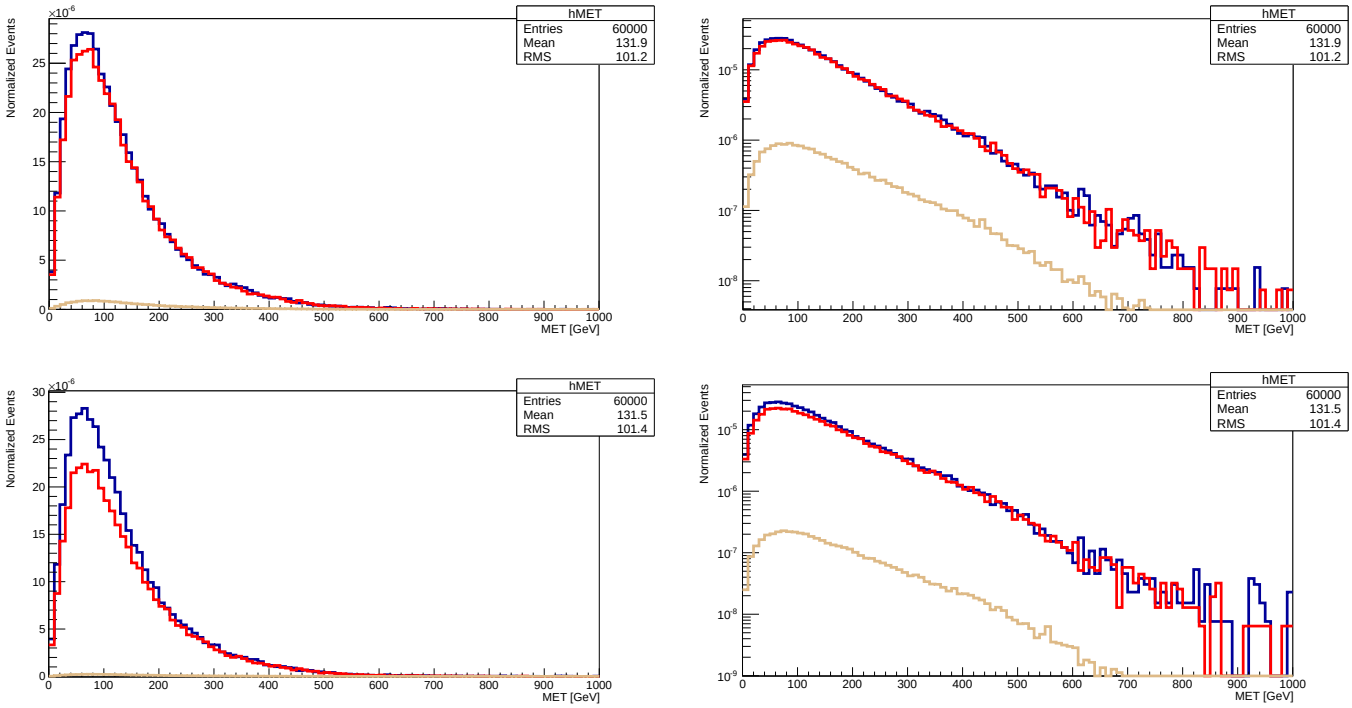

Figure 9.1: $E_{\mathrm{T}}^{\mathrm{miss}}$ distributions for m_{χ} = 10, 100, 1000GeV (blue, red and light-brown) for the vector D5 coupling (upper row) and axial-vector D8 (bottom row) in linear and logarithmic scale.

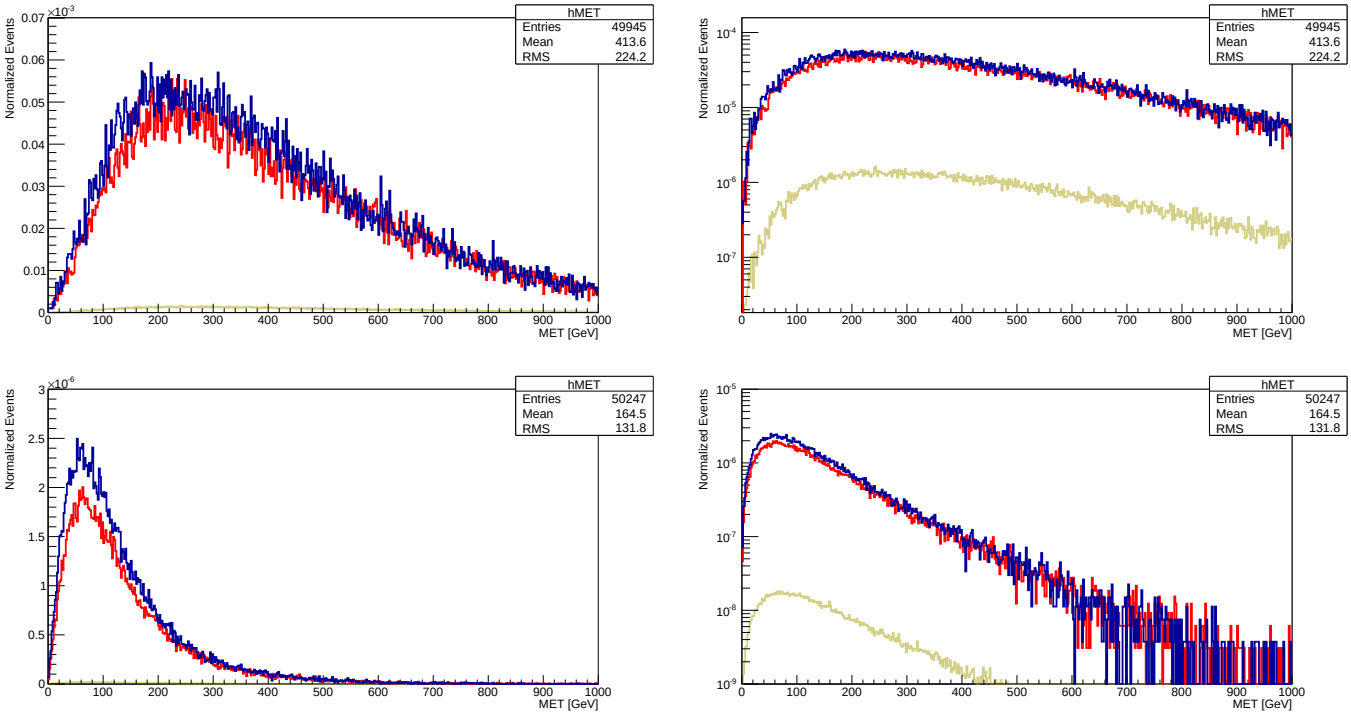

Figure 9.2: $E_{\mathrm{T}}^{\mathrm{miss}}$ distributions for $m_{\chi} = 10, 100, 1000$GeV (blue, red and light-brown) for the tensor D9 coupling (upper row) and axial-vector C3 (bottom row) in linear and logarithmic scale. It is visible that the shape of D9 signal is significantly different from other three coupling operators. This also results in a harder p_{T} spectrum of the dilepton pair.

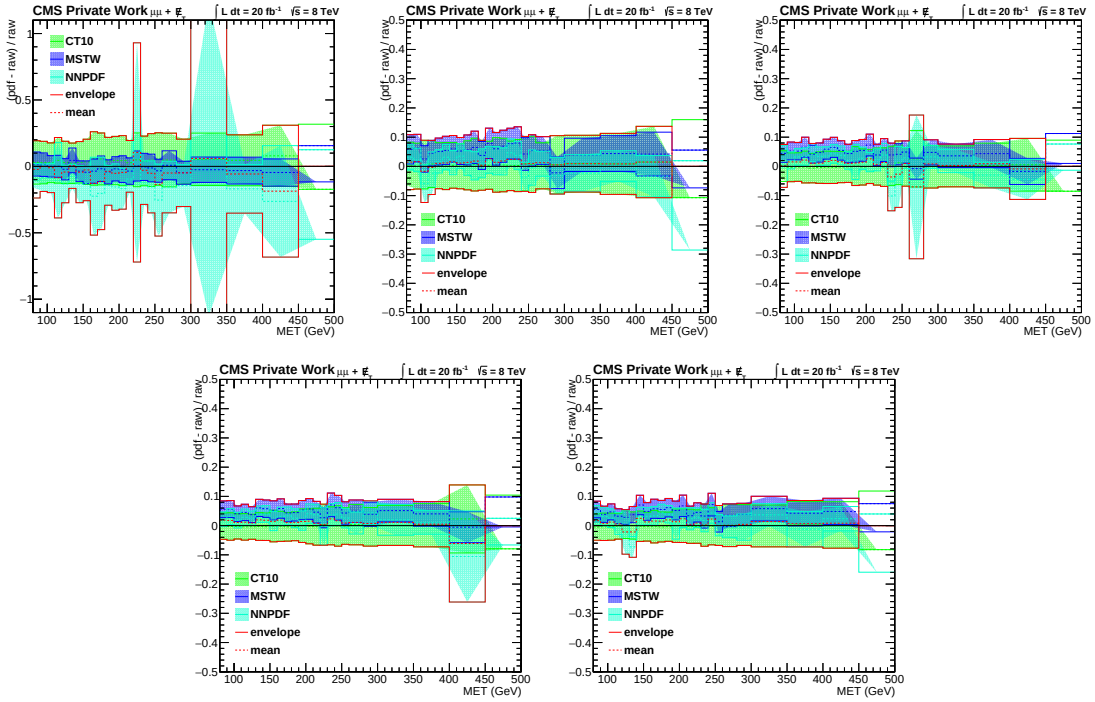

Figure 9.3: Signal PDF uncertainty for $m_\chi = 1000, 500, 200, 10, 1$GeV with D5 coupling as function of $E_{\mathrm{T}}^{\mathrm{miss}}$ (left to right, top to bottom)

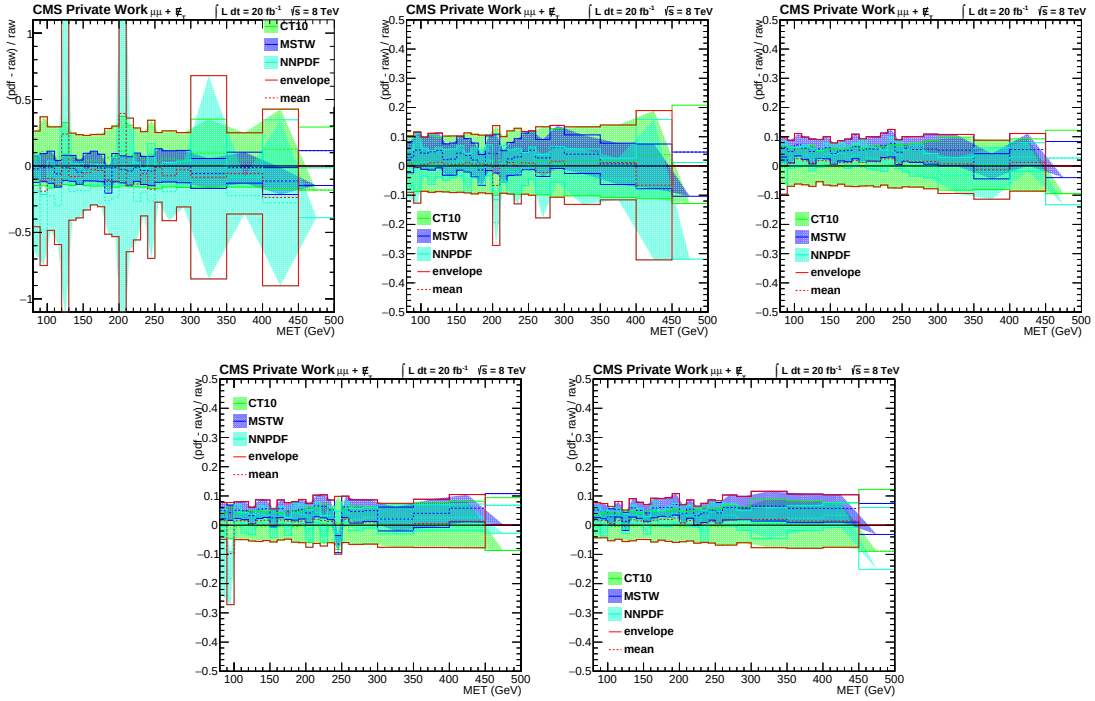

Figure 9.4: Signal PDF uncertainty for $m_\chi = 1000, 500, 200, 10, 1$GeV with D8 coupling as function of $E_{\mathrm{T}}^{\mathrm{miss}}$ (left to right, top to bottom)

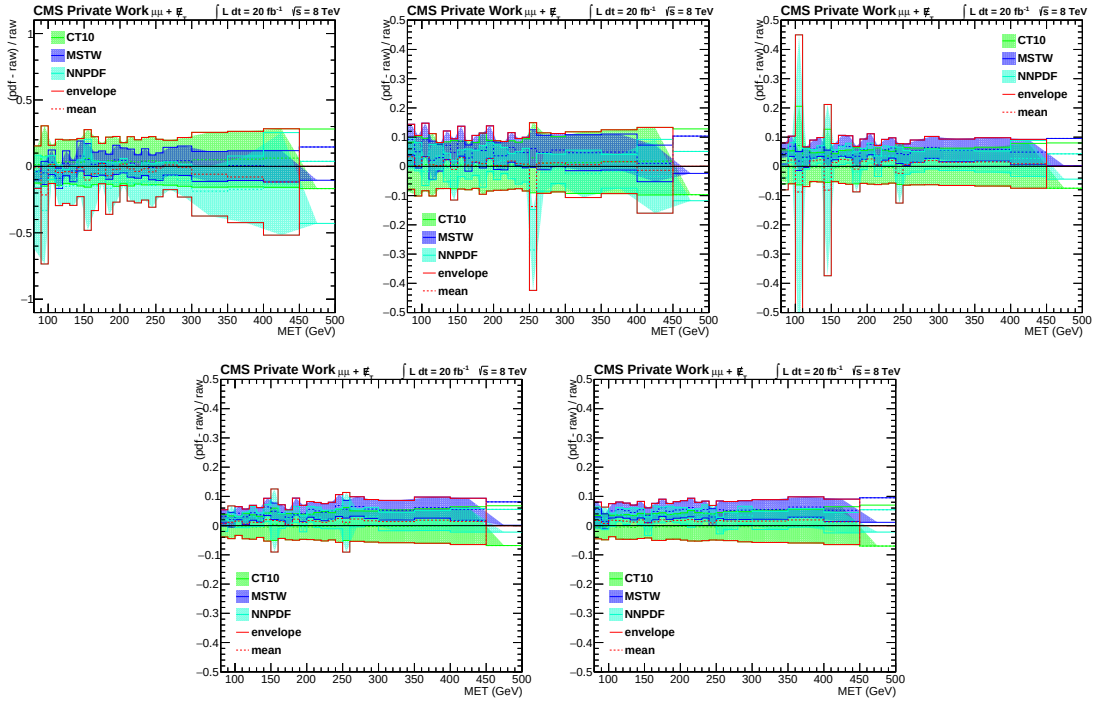

Figure 9.5: Signal PDF uncertainty for $m_\chi = 1000, 500, 200, 10, 1$GeV with D9 coupling as function of $E_{\mathrm{T}}^{\mathrm{miss}}$ (left to right, top to bottom)

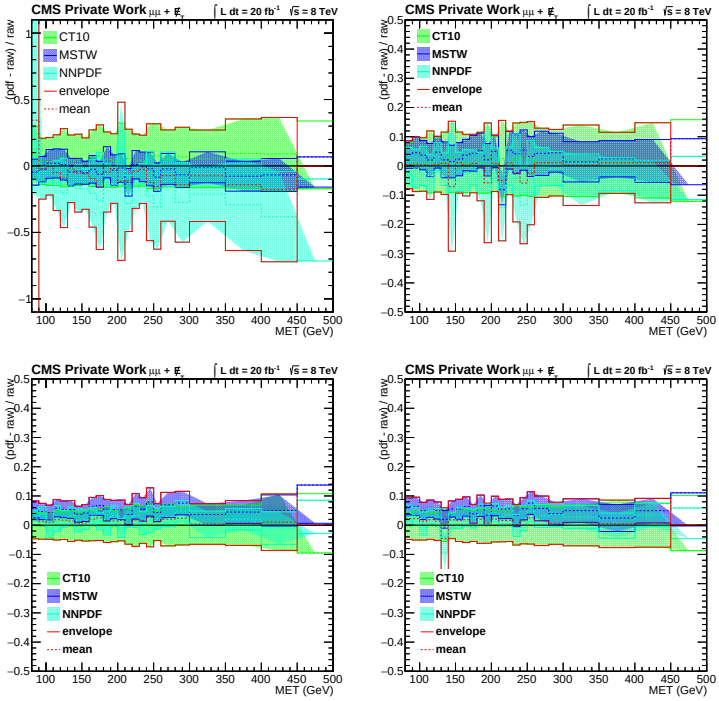

Figure 9.6: Signal PDF uncertainty for $m_\chi = 1000, 500, 10, 1$GeV with C3 coupling as function of $E_{\mathrm{T}}^{\mathrm{miss}}$ (left to right, top to bottom)

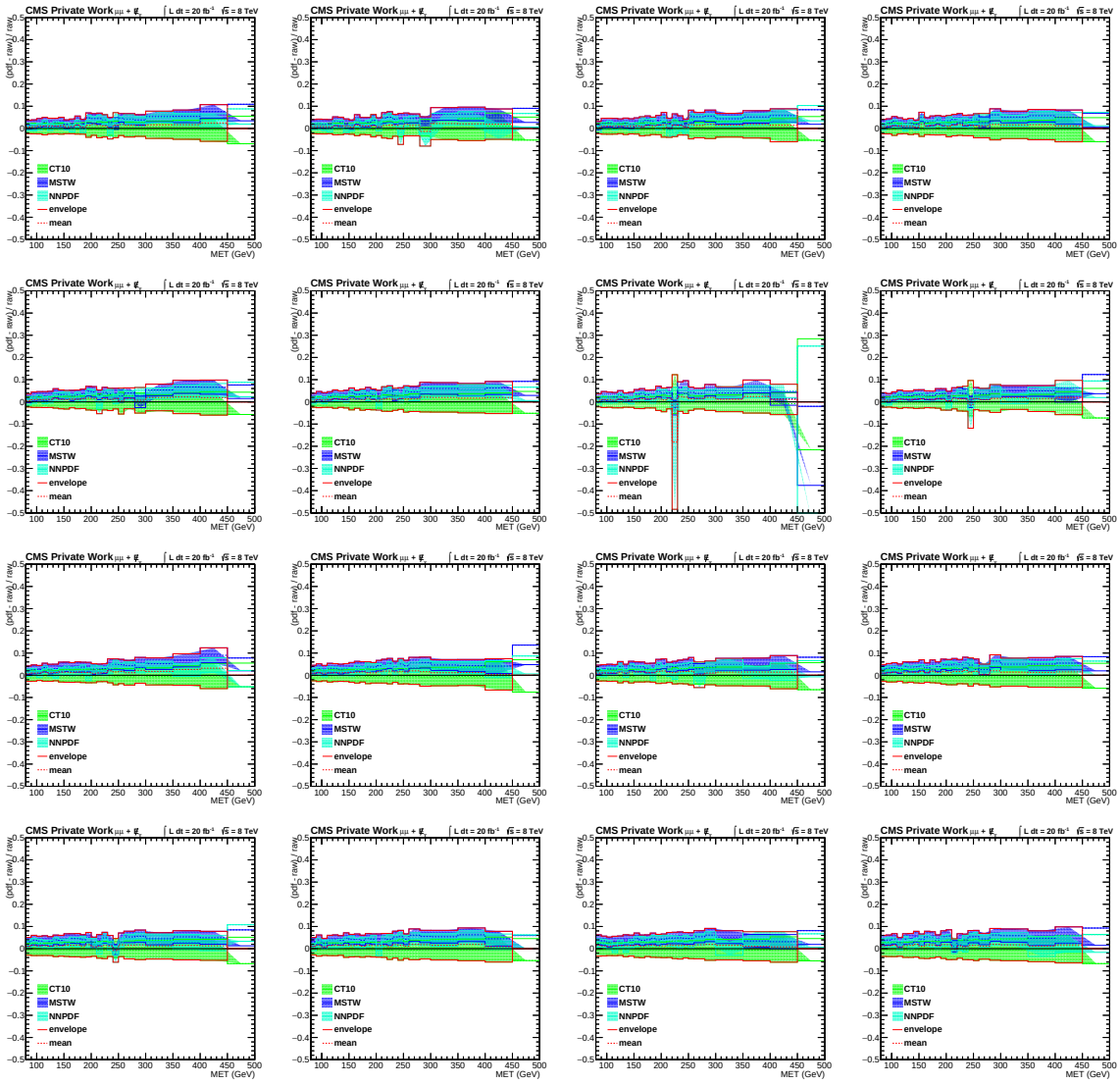

Figure 9.7: Signal PDF uncertainty for $d_{\mathcal{U}} = 1.01, 1.02, 1.04, 1.06, 1.09, 1.1, 1.2, 1.3, 1.4, 1.5, 1.6, 1.7, 1.8, 1.9, 2.0, 2.2$ as function of $E_{\mathrm{T}}^{\mathrm{miss}}$ (left to right, top to bottom)

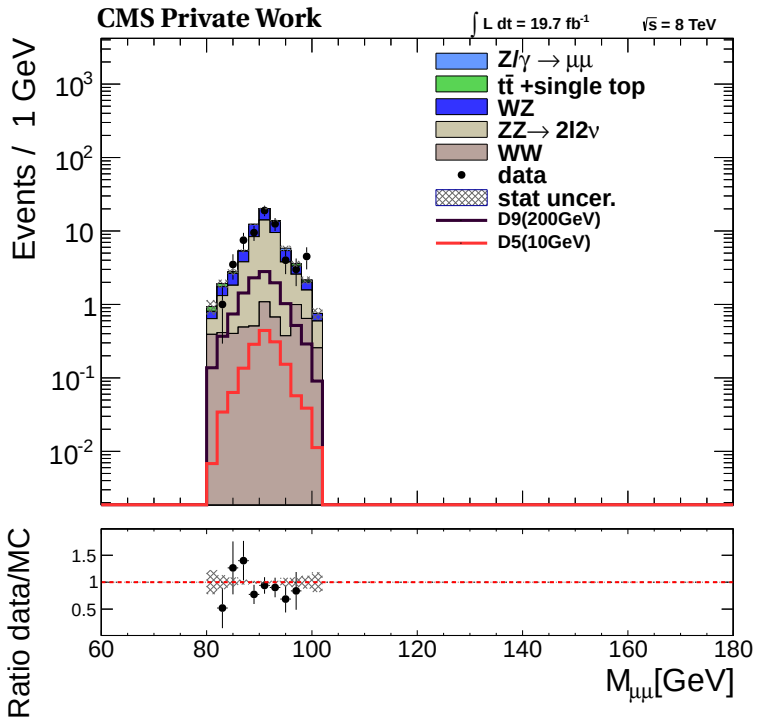

Figure 9.8: Mass of the dimuon system after all selection cuts.

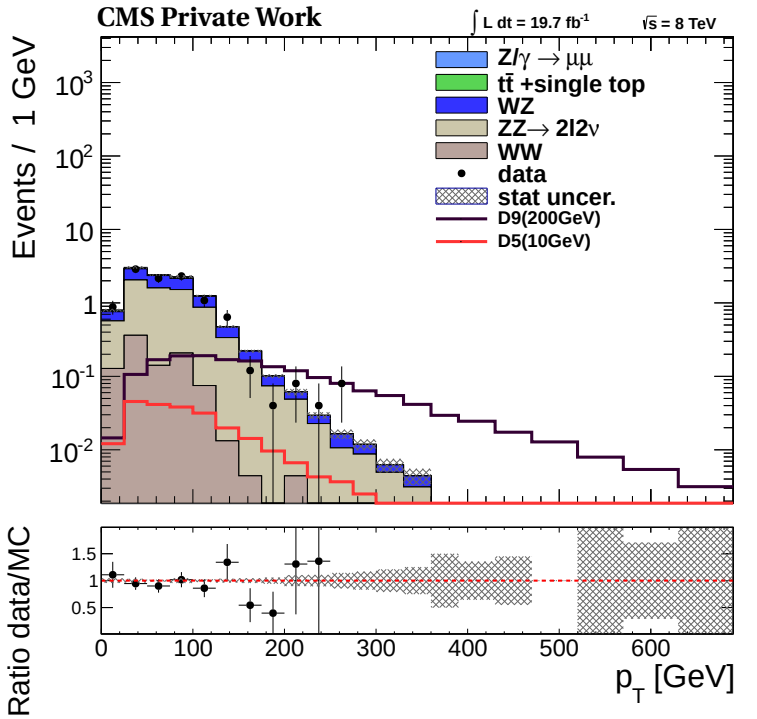

Figure 9.9: Muon p_T after all selection cuts.

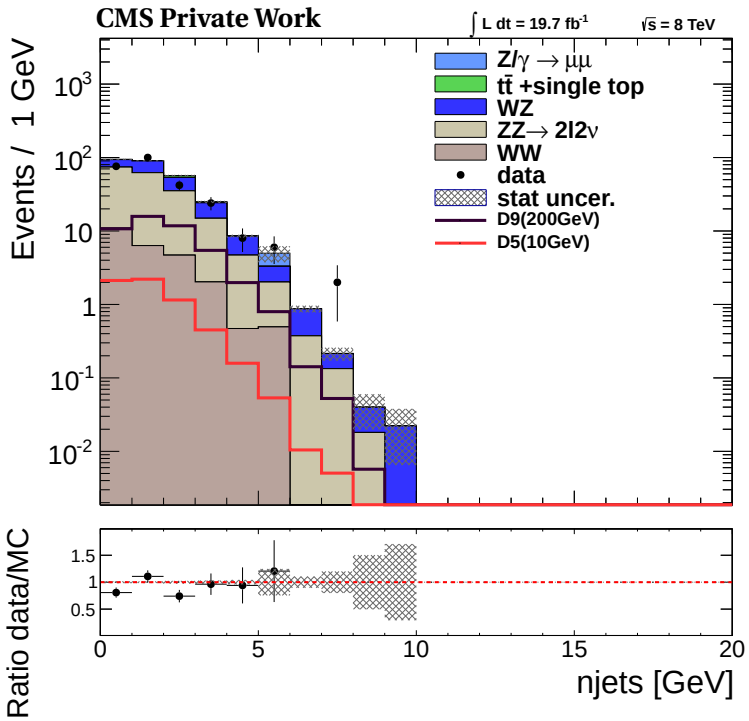

Figure 9.10: Number of jets in the final event selection excluding the jet veto in the dimuon channel.

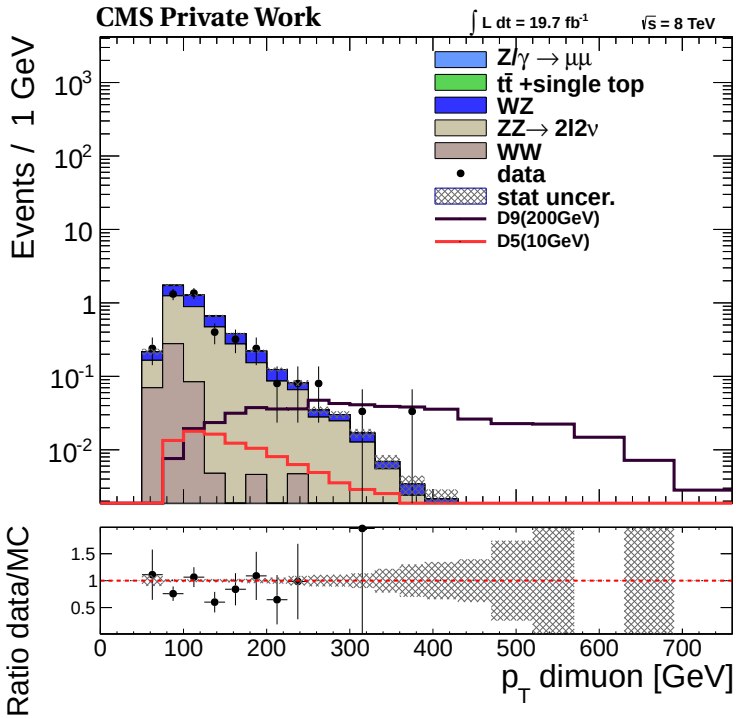

Figure 9.11: Vector sum of the dimuon p_T in the final event selection with no additional jets.

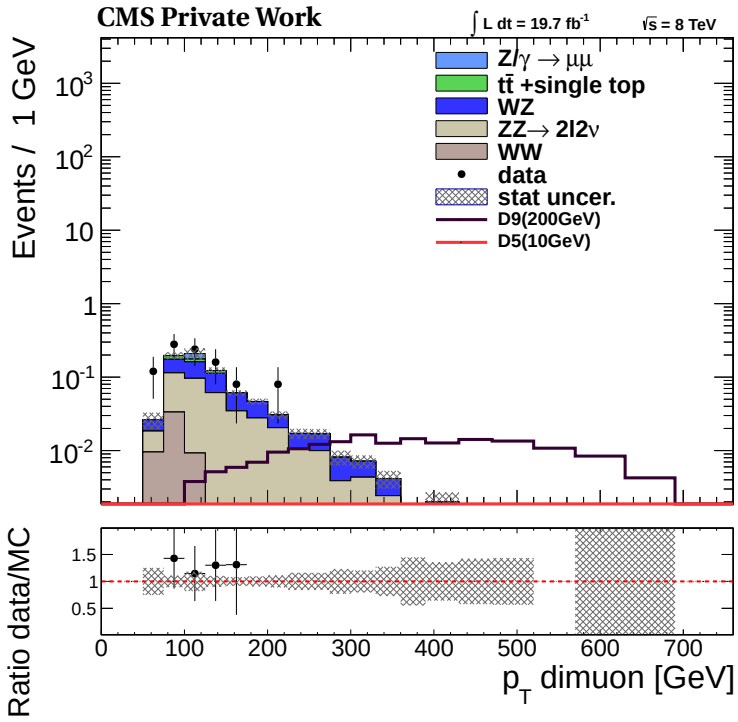

Figure 9.12: Vector sum of the dimuon p_T in the final event selection with one additional jet.

CHAPTER 10

Acknowledgements

Ich möchte Herrn Professor Hebbeker herzlich für die Betreuung während dieser Doktorarbeit danken. Die Zusammenarbeit mit Herrn Hebbeker empfand ich immer als sehr konstruktiv und ertragreich. Bei der Arbeit in solch einer großen Kollaboration wie CMS, in der man viele Diskussionen führen muss, hatte ich stets das Gefühl, dass mein Rücken im Heimatinstitut gedeckt ist. Einen besonderen Dank möchte ich Herrn Professor Hebbeker aussprechen für die Möglichkeit, einen verlängerten Aufenthalt am Forschungszentrum CERN während meiner Doktorandenzeit zu absolvieren und für die Unterstützung während dieser Zeit. Mein großer Dank gilt dem Zweitberichter Prof. Christopher Wiebusch.

Dr. Arnd Meyer betreute mich während dieser Zeit mit großer Sachkunde. Bei vielen wichtigen und richtungsweisenden Entscheidungen hat er mir Unterstützung gegeben, ohne die ich nicht weiter gewußt hätte. Dr. Arnd Meyer hat bei unzähligen Vortragkorrekturen, die immer in letzter Minute passieren, genug Zeit gefunden, um wichtige und umsetzbare Vorschläge zu machen. Danke, lieber Arnd – ich bin froh und stolz, mit Dir zusammen gearbeitet zu haben.

Einen ganz besonderen Platz in dieser Danksagung hat die Sekretärin und zugleich Institutsmutter von allen MitarbeiterInnen und StudentInnen – Frau Adriana del Piero. Adriana hat mich mit großer Wärme empfangen und in unseren vielen Gesprächen lernte ich sie als eine sehr weise und herzliche Person kennen. Liebe Adriana, ohne Dich wäre diese Arbeit nicht denkbar gewesen – danke für Deine kompromisslose Unterstützung in den letzten fünf Jahren.

Dr. Markus Merscheyer sorgte als Verwaltungschef stets für eine gute Laune und eine Bezahlung. Die Betreuung der Kaffeemaschine, die zum gemeinsamen Baby von Dr. Markus Merschmeyer und mir wurde, hat mir viel Freude bereitet, besonders in den Momenten, wo Datenauswertung drohte, lebensgefährlich zu werden.

Dr. Kerstin Hoepfner möchte ich herzlich für die gemeinsame Betreuung des Studentenpraktikums danken. Dank Dr. Hoepfner habe ich viel über Experimentenbau und -betreuung gelernt. Dr. Hoepfner hat mich als Betreuer sehr herzlich im Betreuerteam aufgenommen. Dr. Kirill Grigoryev gilt mein großer Dank für unzähligen Tipps zu Vakuumsystemen und viele interessante Diskussionen. Oleg Tsigenov möchte ich für eine großartige Wartung unsere dCache Speichers und die vielen erheiternden und ausgelassenen Kommentare zu allen möglichen Themen danken.

Ich hatte großes Glück, mit vielen hervorragend ausgebildeten Kollegen zusammen zu promovieren. Klaas Ole "Lo" Padeken, von dem ich das Thema übernahm, hat mich mit viel Ausdauer unterstützt. Bei politischen Diskussionen mit Klaas habe ich mich auch als Person weiterentwickelt. Auch der Ehefrau von Klaas, Regina Padeken, die während unserer arbeitsfreien Treffen wichtige organisatorische Tätigkeiten übernahm, möchte ich für die gemeinsame Zeit "Danke" sagen. Andreas Albert, der meine Analyse im Run II des LHC mit großer Kompetenz übernimmt, danke ich für die tollen Diskussionen. Matthias Klaus Endres, Debbie Duchardt, Simon Knutzen, Sören Erdweg, Mark Olschewski, Sebastian Thüer, Henning Keller und Markus Radziej möchte ich für die unvergessliche Zeit in Aachen danken. Meinen "Klassische-Musik-Buddies" Andreas Güth und Leila Ali Cavasonza danke ich für die tollen Diskussionen über Brahms, Elgar, Rachmaninov und weitere Komponisten. Sophie Kretzschmar danke ich für ihren tollen Beitrag zur Suche nach Dark Matter bei 13 TeV. Ein Dank geht an Erik Dietz-Laursonn für die gemeinsame Betreuung des Stern-Gerlach Versuches.

Meinen Mitbewohnern am CERN – Thomas "Johnny Tesch" Esch, Philipp Millet, Tobias "Tobe" Pook und Andreas Albert möchte ich für eine unbeschreibliche Atmosphäre in der gemeinsamen Wohnung danken. Die vier Gänge Menüs und zahlreiche Diskussionen hier in St. Genis werden mir wie ein unlöschbares Licht im Badezimmer des Aparments A232 noch lange in Erinnerung bleiben. Für Korrekturlesen danke ich Tobias und Philipp ebenfalls, wobei ein besonderer Dank an Philipp für Hardware Support geht.

I want to express my sincere gratitude to my colleagues at CERN Point 5 near Cessy where I had the pleasure to study, monitor and control the CMS experiment. I would like to thank Niels Dupont, Wolfram Zeuner, Austin Ball, William Esposito, Laetitia Bardo, Christoph Schäfer, Zoltan Szilassi, Noemi Beni and Greg Rakness for our successfull collaborations which, I hope, will continue. I thank Dawn Hudson, Ioanna Koutava, Jim Cook, Sergei Lusin, Gerd Fetchenhauer, Antonio Cuenca Perez, Davide Pagnani, Alejandra Lorenzo Gomez, Sasha Nikitenko and Pavel Bunin for their support and cooperation. I thank Sandeep Bhowmik with whom I have shared an uncountable number of night shifts. I thank Serguei Ganjour for our many conversations about physics, photography, sports and music in the past months. I thank Ren-Jie Wang, Darien Wood and Daniele Trocino for our fruitful discussions during the preparation of our joint paper.

Meiner Schwester Renata danke ich für unsere gemeinsamen Auftritte, die ich immer sehr genoß. Meinem Bruder Boris möchte für seine Betreuung meiner Programmierversuche danken und für seine unterstützenden Worte, die er immer für mich findet. Meinem Zwillingsbruder Alexander möchte ich danken für alles, was wir teilen. Das Glück, mit einem Zwillingsbruder zusammen aufzuwachsen und mit ihm zusammen über die Jahre eine feste Freundschaft aufzubauen, ist etwas, was mich dominierend prägte. Ohne Alexander kann ich mir mein Leben nicht vorstellen. Michael Novoselsky danke ich für unsere nun über 15 Jahre alte Freundschaft – das soll uns jemand erstmal nachmachen. Ich danke Lüda Slepova und Valeriy Terskikh dafür, dass sie immer für mich da sind.

Meinen Eltern Rosa und Vladimir danke ich für ihren unzerstörbaren Glauben an meine Fähigkeiten, der mir besonders während der Publikation meiner Ergebnisse sehr half. Meiner Freundin "Solnyschko" Clara danke ich für ihre großartige Unterstützung. Meinem Onkel Vladimir Weinberg danke ich für seine Exkurse und Privatberatungen in theoretischer Physik. Die Erinnerung an meine Großeltern Sofja Levit und Mark Weinberg, die meinen Abschluss nicht mehr erlebten, hat mir viel Kraft verliehen.

Bibliography

[1] CMS Collaboration, "Search for dark matter and unparticles produced in association with a Z boson in proton-proton collisions at $\sqrt{s} = 8$ TeV", *Phys. Rev. D* **93** (Mar, 2016) 052011, arXiv:1511.09375. doi:10.1103/PhysRevD.93.052011.

[2] R. W. Tucker and C. Wang, "Dark matter gravitational interactions", *Class. Quant. Grav.* **15** (1998) 933–954, arXiv:gr-qc/9612019. doi:10.1088/0264-9381/15/4/015.

[3] M. Lopez-Corredoira, J. Beckman, and E. Casuso, "High-velocity clouds as dark matter in the local group", *Astron. Astrophys.* **351** (1999) 920, arXiv:astro-ph/9909389.

[4] D. Clowe, M. Bradac, A. H. Gonzalez et al., "A direct empirical proof of the existence of dark matter", *Astrophys. J.* **648** (2006) L109–L113, arXiv:astro-ph/0608407. doi:10.1086/508162.

[5] K. G. Begeman, A. H. Broeils, and R. H. Sanders, "Extended rotation curves of spiral galaxies: Dark haloes and modified dynamics", *Mon. Not. Roy. Astron. Soc.* **249** (1991) 523.

[6] PICASSO Collaboration, "Constraints on Low-Mass WIMP Interactions on ^{19}F from PICASSO", *Phys. Lett. B* **711** (2012) 153–161, arXiv:1202.1240. doi:10.1016/j.physletb.2012.03.078.

[7] M. Felizardo, T. Girard, T. Morlat et al., "Final Analysis and Results of the Phase II SIMPLE Dark Matter Search", *Phys. Rev. Lett.* **108** (2012) 201302, arXiv:1106.3014. doi:10.1103/PhysRevLett.108.201302.

[8] COUPP Collaboration, "First Dark Matter Search Results from a 4-kg CF_3I Bubble Chamber Operated in a Deep Underground Site", *Phys. Rev. D* **86** (2012) 052001, arXiv:1204.3094. doi:10.1103/PhysRevD.86.052001.

[9] IceCube Collaboration, "Multi-year search for dark matter annihilations in the Sun with the AMANDA-II and IceCube detectors", *Phys. Rev. D* **85** (2012) 042002, arXiv:1112.1840. doi:10.1103/PhysRevD.85.042002.

[10] SuperCDMS Collaboration, "Search for Low-Mass Weakly Interacting Massive Particles Using Voltage-Assisted Calorimetric Ionization Detection in the SuperCDMS Experiment", *Phys. Rev. Lett.* **112** (2014) 041302, arXiv:1309.3259. doi:10.1103/PhysRevLett.112.041302.

[11] SuperCDMS Collaboration, "Search for Low-Mass WIMPs with SuperCDMS", *Phys. Rev. Lett.* **112** (2014) 241302, arXiv:1402.7137. doi:10.1103/PhysRevLett.112.241302.

[12] LUX Collaboration, "First results from the LUX dark matter experiment at the Sanford Underground Research Facility", *Phys. Rev. Lett.* **112** (2014) 091303, arXiv:1310.8214. doi:10.1103/PhysRevLett.112.091303.

[13] P. Cushman, C. Galbiati, D. McKinsey et al., "Working Group Report: WIMP Dark Matter Direct Detection", arXiv:1310.8327.

[14] Fermi-LAT Collaboration, "Constraining Dark Matter Models from a Combined Analysis of Milky Way Satellites with the Fermi Large Area Telescope", *Phys. Rev. Lett.* **107** (2011) 241302, arXiv:1108.3546. doi:10.1103/PhysRevLett.107.241302.

[15] J. Buckley, D. Cowen, S. Profumo et al., "Working Group Report: WIMP Dark Matter Indirect Detection", arXiv:1310.7040.

[16] CMS Collaboration, "Search for dark matter, extra dimensions, and unparticles in monojet events in protonñproton collisions at $\sqrt{s} = 8$ TeV", *Eur. Phys. J. C* **75** (2015) 235, arXiv:1408.3583. doi:10.1140/epjc/s10052-015-3451-4.

[17] ATLAS Collaboration, "Search for new phenomena in final states with an energetic jet and large missing transverse momentum in pp collisions at $\sqrt{s} = 8$ TeV with the ATLAS detector", *Eur. Phys. J.* **C75** (2015), no. 7, 299, arXiv:1502.01518. doi:10.1140/epjc/s10052-015-3517-3.

[18] CMS Collaboration, "Search for new phenomena in monophoton final states in proton-proton collisions at $\sqrt{s} = 8$ TeV", *Phys. Lett.* **B755** (2016) 102–124, arXiv:1410.8812. doi:10.1016/j.physletb.2016.01.057.

[19] ATLAS Collaboration, "Search for new phenomena in events with a photon and missing transverse momentum in pp collisions at $\sqrt{s} = 8$ TeV with the ATLAS detector", *Phys. Rev.* **D91** (2015), no. 1, 012008, arXiv:1411.1559. doi:10.1103/PhysRevD.91.012008.

[20] CMS Collaboration, "Search for physics beyond the standard model in final states with a lepton and missing transverse energy in proton-proton collisions at sqrt(s) = 8 TeV", *Phys. Rev. D* **91** (2015) 092005, arXiv:1408.2745. doi:10.1103/PhysRevD.91.092005.

[21] ATLAS Collaboration, "Search for dark matter in events with heavy quarks and missing transverse momentum in pp collisions with the ATLAS detector", *Eur. Phys. J. C* **75** (2015) 92, arXiv:1410.4031. doi:10.1140/epjc/s10052-015-3306-z.

[22] ATLAS Collaboration, "Search for dark matter in events with a hadronically decaying W or Z boson and missing transverse momentum in pp collisions at $\sqrt{s} = 8$ TeV with the ATLAS detector", *Phys. Rev. Lett.* **112** (2014) 041802, arXiv:1309.4017. doi:10.1103/PhysRevLett.112.041802.

[23] ATLAS Collaboration, "Search for new particles in events with one lepton and missing transverse momentum in pp collisions at $\sqrt{s} = 8$ TeV with the ATLAS detector", *JHEP* **09** (2014) 037, arXiv:1407.7494. doi:10.1007/JHEP09(2014)037.

[24] ATLAS Collaboration, "Search for invisible particles produced in association with single-top-quarks in proton-proton collisions at $\sqrt{s} = 8$ TeV with the ATLAS detector", *Eur. Phys. J.* **C75** (2015), no. 2, 79, arXiv:1410.5404. doi:10.1140/epjc/s10052-014-3233-4.

[25] ATLAS Collaboration, "Search for Dark Matter in Events with Missing Transverse Momentum and a Higgs Boson Decaying to Two Photons in pp Collisions at $\sqrt{s} = 8$ TeV with the ATLAS Detector", arXiv:1506.01081.

[26] CMS Collaboration, "Search for Monotop Signatures in Proton-Proton Collisions at $\sqrt{s} = 8$ TeV", *Phys. Rev. Lett.* **114** (2015), no. 10, 101801, arXiv:1410.1149. doi:10.1103/PhysRevLett.114.101801.

[27] CMS Collaboration, "Search for the production of dark matter in association with top-quark pairs in the single-lepton final state in proton-proton collisions at sqrt(s) = 8 TeV", *JHEP* **06** (2015) 121, arXiv:1504.03198. doi:10.1007/JHEP06(2015)121.

[28] ATLAS Collaboration, "Search for dark matter in events with a Z boson and missing transverse momentum in pp collisions at $\sqrt{s}$=8 TeV with the ATLAS detector", *Phys. Rev. D* **90** (2014) 012004, arXiv:1404.0051. doi:10.1103/PhysRevD.90.012004.

[29] J. Goodman, M. Ibe, A. Rajaraman et al., "Constraints on Dark Matter from Colliders", *Phys. Rev. D* **82** (2010) 116010, arXiv:1008.1783. doi:10.1103/PhysRevD.82.116010.

[30] Y. Bai and T. M. Tait, "Searches with Mono-Leptons", *Phys. Lett. B* **723** (2013) 384–387, arXiv:1208.4361. doi:10.1016/j.physletb.2013.05.057.

[31] N. Metropolis and S. Ulam, "The Monte Carlo Method", *Journal of the American Statistical Association* **44** (1949), no. 247, 335–341.

[32] Particle Data Group Collaboration, "Review of Particle Physics", *Chin. Phys.* **C38** (2014) 090001. doi:10.1088/1674-1137/38/9/090001.

[33] T. Hebbeker, "Skript zur Vorlesung Elementarteilchenphysik". RWTH Aachen, 2010.

[34] A. Stahl, "Skript zur Vorlesung Elementarteilchenphysik I". 2010.

[35] A. Stahl, "Skript zur Vorlesung Elementarteilchenphysik II". 2011.

[36] M. E. Peskin and D. V. Schroeder, "An introduction to quantum field theory". Advanced book program. Westview Press Reading (Mass.), Boulder (Colo.), 1995. Autre tirage : 1997.

[37] Wikipedia Collaboration, "Standard Model From Fermi Lab", July, 2012. http://en.wikipedia.org/wiki/File:Standard_Model_From_Fermi_Lab.jpg.

[38] S. Knutzen, "Study of the $W' \to \tau\nu_\tau$", Master's thesis, RWTH, 2013.

[39] M. Brodski, "Model Unspecific Search in CMS with τ Leptons", Master's thesis, RWTH, 2012.

[40] C. L. Cowan, F. Reines, F. B. Harrison et al., "Detection of the Free Neutrino: a Confirmation", *Science* **124** (1956), no. 3212, 103–104, arXiv:http://www.sciencemag.org/content/124/3212/103.full.pdf. doi:10.1126/science.124.3212.103.

[41] S. Hossenfelder, "A possibility to solve the problems with quantizing gravity", *Phys. Lett.* **B725** (2013) 473–476, arXiv:1208.5874. doi:10.1016/j.physletb.2013.07.037.

[42] K. Eppley and E. Hannah, "The necessity of quantizing the gravitational field", *Foundations of Physics* **7** (1977), no. 1, 51–68. doi:10.1007/BF00715241.

[43] J. F. Donoghue, "Introduction to the effective field theory description of gravity", in *Advanced School on Effective Theories Almunecar, Spain, June 25-July 1, 1995*. 1995. arXiv:gr-qc/9512024.

[44] B. S. DeWitt, "Quantum Theory of Gravity. I. The Canonical Theory", *Phys. Rev.* **160** (Aug, 1967) 1113–1148. doi:10.1103/PhysRev.160.1113.

[45] R. P. Feynman, "Quantum theory of gravitation", *Acta Phys. Polon.* **24** (1963) 697–722.

[46] J. E. Kim, "Towards unification of GUT families", *PoS* **PLANCK2015** (2015) 067, arXiv:1510.01824.

[47] G. Altarelli, P. A. N. Machado, and D. Meloni, "On Bimaximal Neutrino Mixing and GUT's", *PoS* **CORFU2014** (2015) 012, arXiv:1504.05514.

[48] Z. Berezhiani, M. Chianese, G. Miele et al., "Chances for SUSY-GUT in the LHC Epoch", *JHEP* **08** (2015) 083, arXiv:1505.04950. doi:10.1007/JHEP08(2015)083.

[49] S. Carlip, "Quantum gravity: a progress report", *Reports on Progress in Physics* **64** (2001), no. 8, 885.

[50] A. D. Sakharov, "Cosmological Models of the Universe With Rotation of Time's Arrow", *Sov. Phys. JETP* **52** (1980) 349–351. [Sov. Phys. Usp.34,401(1991)].

[51] C. S. Wu, E. Ambler, R. W. Hayward et al., "Experimental Test of Parity Conservation in Beta Decay", *Physical Review* **105** (February, 1957) 1413–1415. doi:10.1103/PhysRev.105.1413.

[52] M. Goldhaber, L. Grodzins, and A. W. Sunyar, "Helicity of Neutrinos", *Phys. Rev.* **109** (Feb, 1958) 1015–1017. doi:10.1103/PhysRev.109.1015.

[53] J. H. Christenson, J. W. Cronin, V. L. Fitch et al., "Evidence for the 2π Decay of the K_2^0 Meson", *Phys. Rev. Lett.* **13** (Jul, 1964) 138–140. doi:10.1103/PhysRevLett.13.138.

[54] A. Kobakhidze, "Solving the Strong CP Problem with High-Colour Quarks and Composite Axion", arXiv:1602.06363.

[55] P. G. Harris, C. A. Baker, K. Green et al., "New Experimental Limit on the Electric Dipole Moment of the Neutron", *Phys. Rev. Lett.* **82** (Feb, 1999) 904–907. doi:10.1103/PhysRevLett.82.904.

[56] J. E. Kim and G. Carosi, "Axions and the Strong CP Problem", *Rev. Mod. Phys.* **82** (2010) 557–602, arXiv:0807.3125. doi:10.1103/RevModPhys.82.557.

[57] Particle Data Group Collaboration, "Review of particle physics", *J. Phys. G* **37** (2010). doi:10.1088/0954-3899/37/7A/075021.

[58] T2K Collaboration, "Upper bound on neutrino mass based on T2K neutrino timing measurements", *Phys. Rev.* **D93** (2016), no. 1, 012006, arXiv:1502.06605. doi:10.1103/PhysRevD.93.012006.

[59] R. G. H. Robertson, "Direct probes of neutrino mass", in *Neutrino Oscillation Workshop (NOW 2014) Conca Specchiulla, Otranto, Lecce, Italy, September 7-14, 2014*. 2015. arXiv:1502.00144.

[60] J. C. Helo, M. Hirsch, T. Ota et al., "Double beta decay and neutrino mass models", *JHEP* **05** (2015) 092, arXiv:1502.05188. doi:10.1007/JHEP05(2015)092.

[61] S. P. Martin, "A Supersymmetry primer", arXiv:hep-ph/9709356. [Adv. Ser. Direct. High Energy Phys.18,1(1998)]. doi:10.1142/9789812839657_0001, 10.1142/9789814307505_0001.

[62] H. Murayama, "Supersymmetry phenomenology", in *Particle physics. Proceedings, Summer School, Trieste, Italy, June 21-July 9, 1999*, pp. 296–335. 2000. arXiv:hep-ph/0002232.

[63] A. B. Lahanas, "LSP as a Candidate for Dark Matter", *Lect. Notes Phys.* **720** (2007) 35–68, arXiv:hep-ph/0607301. doi:10.1007/978-3-540-71013-4_2.

[64] H. Baer, V. Barger, P. Huang et al., "Natural SUSY with a bino- or wino-like LSP", *Phys. Rev.* **D91** (2015), no. 7, 075005, arXiv:1501.06357. doi:10.1103/PhysRevD.91.075005.

[65] J. Ellis and K. A. Olive, "Supersymmetric Dark Matter Candidates", arXiv:1001.3651.

[66] G. R. Farrar and P. Fayet, "Phenomenology of the production, decay, and detection of new hadronic states associated with supersymmetry", *Physics Letters B* **76** (1978), no. 5, 575 – 579. doi:http://dx.doi.org/10.1016/0370-2693(78)90858-4.

[67] V. D. Barger and E. Ma, "Natural conservation of R-parity in supersymmetry", *Phys. Rev.* **D51** (1995) 1332–1336, arXiv:hep-ph/9312232. doi:10.1103/PhysRevD.51.1332.

[68] S. P. Martin, "Implications of supersymmetric models with natural R-parity conservation", *Phys. Rev. D* **54** (Aug, 1996) 2340–2348. doi:10.1103/PhysRevD.54.2340.

[69] T. Han, Z. Liu, and S. Su, "Light Neutralino Dark Matter: Direct/Indirect Detection and Collider Searches", *JHEP* **08** (2014) 093, arXiv:1406.1181. doi:10.1007/JHEP08(2014)093.

[70] C. Arina, M. E. C. Catalan, S. Kraml et al., "Constraints on sneutrino dark matter from LHC Run 1", *JHEP* **05** (2015) 142, arXiv:1503.02960. doi:10.1007/JHEP05(2015)142.

[71] D. Feldman, Z. Liu, and P. Nath, "Light Higgses at the Tevatron and at the LHC and Observable Dark Matter in SUGRA and D Branes", *Phys. Lett.* **B662** (2008) 190–198, arXiv:0711.4591. doi:10.1016/j.physletb.2008.02.063.

[72] R. Hempfling, "Gauge coupling unification in general supersymmetric models", in *Perspectives for electroweak interactions in e+ e- collisions. Proceedings, Ringberg Workshop, Tegernsee, Germany, February 5-8, 1995*. 1995. arXiv:hep-ph/9506296.

[73] G.-C. Cho, N. Maru, and K. Yotsutani, "Perturbative unification of gauge couplings in supersymmetric E_6 models", arXiv:1602.04271.

[74] CMS Collaboration, "Search for supersymmetry in events with photons and missing transverse energy", Technical Report CMS-PAS-SUS-15-012, CERN, Geneva, 2016.

[75] CMS Collaboration, "Search for direct production of top squark pairs decaying to all-hadronic final states in pp collisions at sqrt(s) = 13 TeV", Technical Report CMS-PAS-SUS-16-007, CERN, Geneva, 2016.

[76] ATLAS Collaboration, "Search for gluinos in events with an isolated lepton, jets and missing transverse momentum at $\sqrt{s}$ = 13 TeV with the ATLAS detector", arXiv:1605.04285.

[77] CMS Collaboration, "Searches for electroweak neutralino and chargino production in channels with Higgs, Z, and W bosons in pp collisions at 8 TeV", *Phys. Rev.* **D90** (2014), no. 9, 092007, arXiv:1409.3168. doi:10.1103/PhysRevD.90.092007.

[78] R. Catena and L. Covi, "SUSY dark matter(s)", *Eur. Phys. J.* **C74** (2014) 2703, arXiv:1310.4776. doi:10.1140/epjc/s10052-013-2703-4.

[79] CMS Collaboration, "Phenomenological MSSM interpretation of CMS searches in pp collisions at sqrt(s) = 7 and 8 TeV", *Submitted to: JHEP* (2016) arXiv:1606.03577.

[80] L. Mitzka and W. Porod, "Reinterpretation of ATLAS 8 TeV searches for Natural SUSY with a R-Sneutrino LSP", arXiv:1603.06130.

[81] N. Arkani-Hamed, S. Dimopoulos, and G. R. Dvali, "The Hierarchy problem and new dimensions at a millimeter", *Phys. Lett.* **B429** (1998) 263–272, arXiv:hep-ph/9803315. doi:10.1016/S0370-2693(98)00466-3.

[82] T. Pook, "Search for large extra dimensions in dimuon events with the CMS experiment at $\sqrt{s} = 8$ TeV", Master's thesis, RWTH, May, 2014.

[83] S. A. Schmitz, "Search for Large Spatial Extra Dimensions with Dimuon Events from 7 TeV pp collisions at CMS", July, 2013. Doctoral Thesis, http://web.physik.rwth-aachen.de/~hebbeker/theses/schmitz_phd.pdf.

[84] CMS Collaboration, "Search for large extra dimensions in dimuon and dielectron events in pp collisions at $\sqrt{s} = 7$ TeV", *Phys. Lett. B* **711** (2012) 15–34, arXiv:1202.3827. doi:http://dx.doi.org/10.1016/j.physletb.2012.03.029.

[85] CMS Collaboration, "Search for physics beyond the standard model in dilepton mass spectra in proton-proton collisions at $\sqrt{s} = 8$ TeV", *JHEP* **04** (2015) 025, arXiv:1412.6302. doi:10.1007/JHEP04(2015)025.

[86] T. Kaluza, "Zum Unitätsproblem der Physik", *Sitzungsber. Preuss. Akad. Wiss., Phys.-Math. Kl.* **1921** (1921) 966–972.

[87] O. Klein, "Quanten-Theorie und 5-dimensionale Relativitätstheorie", *Z. Phys.* **37** (1926) 895–906.

[88] O. Klein, "The Atomicity of Electricity as a Quantum Law", *Nature* **118** (1926) 516. doi:10.1038/118516a0.

[89] CMS Collaboration, "Search for Large Extra Spatial Dimensions in Dielectron Production with the CMS Detector", Technical Report CMS-PAS-EXO-12-031, CERN, Geneva, 2013.

[90] CMS Collaboration, "Search for Extra Dimensions in Dimuon Events in pp Collisions at sqrt(s) = 8 TeV", Technical Report CMS-PAS-EXO-12-027, CERN, Geneva, 2013.

[91] ATLAS Collaboration, "Search for dark matter candidates and large extra dimensions in events with a jet and missing transverse momentum with the ATLAS detector", *JHEP* **04** (2013) 075, arXiv:1210.4491. doi:10.1007/JHEP04(2013)075.

[92] H. Georgi, "Unparticle physics", *Phys. Rev. Lett.* **98** (2007) 221601, arXiv:hep-ph/0703260. doi:10.1103/PhysRevLett.98.221601.

[93] H. Georgi, "Another odd thing about unparticle physics", *Phys. Lett.* **B650** (2007) 275–278, arXiv:0704.2457. doi:10.1016/j.physletb.2007.05.037.

[94] K. Cheung, W.-Y. Keung, and T.-C. Yuan, "Collider signals of unparticle physics", *Phys. Rev. Lett.* **99** (2007) 051803, arXiv:0704.2588. doi:10.1103/PhysRevLett.99.051803.

[95] K. Cheung, W.-Y. Keung, and T.-C. Yuan, "Collider Phenomenology of Unparticle Physics", *Phys. Rev.* **D76** (2007) 055003, arXiv:0706.3155. doi:10.1103/PhysRevD.76.055003.

[96] Z. Kang, "Upgrading sterile neutrino dark matter to FImP using scale invariance", *Eur. Phys. J.* **C75** (2015), no. 10, 471, arXiv:1411.2773. doi:10.1140/epjc/s10052-015-3702-4.

[97] M. Rinaldi, G. Cognola, L. Vanzo et al., "Inflation in scale-invariant theories of gravity", *Phys. Rev.* **D91** (2015), no. 12, 123527, arXiv:1410.0631. doi:10.1103/PhysRevD.91.123527.

[98] H. Cheng, "Possible Existence of Weyl's Vector Meson", *Phys. Rev. Lett.* **61** (Nov, 1988) 2182–2184. doi:10.1103/PhysRevLett.61.2182.

[99] L. D. Reusch, "Search for Unparticles in the Z + MET channel with the CMS Experiment at $\sqrt{s} = 8$ TeV", October, 2013. Diplomarbeit, https://web.physik.rwth-aachen.de/~hebbeker/theses/reusch_diploma.pdf.

[100] T. Pook, "Search for Unparticles in Dielectron Final States with the CMS Experiment", February, 2012. Bachelor thesis, https://web.physik.rwth-aachen.de/~hebbeker/theses/pook_bachelor.pdf.

[101] K. O. Padeken, "Search for Unparticles in Z and Missing Transverse Energy with the CMS Detector", September, 2012. Master's thesis, https://web.physik.rwth-aachen.de/~hebbeker/theses/padeken_master.pdf.

[102] S. Kathrein, S. Knapen, and M. J. Strassler, "Bounds from LEP on unparticle interactions with electroweak bosons", *Phys. Rev. D* **84** (2011) 015010, arXiv:1012.3737. doi:10.1103/PhysRevD.84.015010.

[103] M. Dahiya, S. Dutta, and R. Islam, "Constraining Unparticles from Top Physics at TeVatron", *Phys. Rev.* **D86** (2012) 115022, arXiv:1206.5447. doi:10.1103/PhysRevD.86.115022.

[104] S. Ask, "Simulation of Z plus Graviton/Unparticle Production at the LHC", *Eur. Phys. J. C* **60** (2009) 509–516, arXiv:0809.4750. doi:10.1140/epjc/s10052-009-0949-7.

[105] S. Ask, I. Akin, L. Benucci et al., "Real Emission and Virtual Exchange of Gravitons and Unparticles in Pythia8", *Comput. Phys. Commun.* **181** (2010) 1593–1604, arXiv:0912.4233. doi:10.1016/j.cpc.2010.05.013.

[106] B. Grinstein, K. A. Intriligator, and I. Z. Rothstein, "Comments on Unparticles", *Phys. Lett.* **B662** (2008) 367–374, arXiv:0801.1140. doi:10.1016/j.physletb.2008.03.020.

[107] M. C. Kumar, P. Mathews, V. Ravindran et al., "Unparticle physics in diphoton production at the CERN LHC", *Phys. Rev.* **D77** (2008) 055013, arXiv:0709.2478. doi:10.1103/PhysRevD.77.055013.

[108] G. Cacciapaglia, G. Marandella, and J. Terning, "The AdS/CFT/Unparticle Correspondence", *JHEP* **02** (2009) 049, arXiv:0804.0424. doi:10.1088/1126-6708/2009/02/049.

[109] J. R. Primack, "Whatever happened to hot dark matter?", *SLAC Beam Line* **31N3** (2001) 50–57, arXiv:astro-ph/0112336.

[110] R. D. Peccei and H. R. Quinn, "CP Conservation in the Presence of Pseudoparticles", *Phys. Rev. Lett.* **38** (Jun, 1977) 1440–1443. doi:10.1103/PhysRevLett.38.1440.

[111] L. D. Duffy and K. van Bibber, "Axions as Dark Matter Particles", *New J. Phys.* **11** (2009) 105008, arXiv:0904.3346. doi:10.1088/1367-2630/11/10/105008.

[112] P. Sikivie, "Dark matter axions", *Int. J. Mod. Phys.* **A25** (2010) 554–563, arXiv:0909.0949. doi:10.1142/S0217751X10048846.

[113] Q. Yang, "Axions and Dark Matter", arXiv:1509.00673.

[114] Y. B. Zel'dovich, L. B. Okun', and S. B. Pikel'ner, "QUARKS: ASTROPHYSICAL AND PHYSICOCHEMICAL ASPECTS", *Soviet Physics Uspekhi* **8** (1966), no. 5, 702.

[115] J. R. Primack, "Dark matter and structure formation", in *Midrasha Mathematicae in Jerusalem: Winter School in Dynamical Systems Jerusalem, Israel, January 12-17, 1997*. 1997. arXiv:astro-ph/9707285.

[116] J. R. Primack and M. A. K. Gross, "Hot dark matter in cosmology", arXiv:astro-ph/0007165.

[117] J. Abdallah et al., "Simplified Models for Dark Matter Searches at the LHC", *Phys. Dark Univ.* **9-10** (2015) 8–23, arXiv:1506.03116. doi:10.1016/j.dark.2015.08.001.

[118] H. Georgi, "Effective Field Theory", 1993. http://www.people.fas.harvard.edu/ hgeorgi/review.pdf.

[119] L. M. Carpenter, A. Nelson, C. Shimmin et al., "Collider searches for dark matter in events with a Z boson and missing energy", *Phys. Rev. D* **87** (2013) 074005, arXiv:1212.3352. doi:10.1103/PhysRevD.87.074005.

[120] J. Goodman, M. Ibe, A. Rajaraman et al., "Constraints on light Majorana dark matter from colliders", *Physics Letters B* **695** (2011), no. 1ñ4, 185 – 188. doi:http://dx.doi.org/10.1016/j.physletb.2010.11.009.

[121] J. Goodman, M. Ibe, A. Rajaraman et al., "Constraints on dark matter from colliders", *Phys. Rev. D* **82** (Dec, 2010) 116010. doi:10.1103/PhysRevD.82.116010.

[122] M. Beltran, D. Hooper, E. W. Kolb et al., "Deducing the nature of dark matter from direct and indirect detection experiments in the absence of collider signatures of new physics", *Phys. Rev. D* **80** (Aug, 2009) 043509. doi:10.1103/PhysRevD.80.043509.

[123] E. Dudas, Y. Mambrini, S. Pokorski et al., "(In)visible Z-prime and dark matter", *JHEP* **08** (2009) 014, arXiv:0904.1745. doi:10.1088/1126-6708/2009/08/014.

[124] J. Goodman and W. Shepherd, "LHC Bounds on UV-Complete Models of Dark Matter", arXiv:1111.2359.

[125] H. An, X. Ji, and L.-T. Wang, "Light Dark Matter and Z' Dark Force at Colliders", *JHEP* **07** (2012) 182, arXiv:1202.2894. doi:10.1007/JHEP07(2012)182.

[126] M. T. Frandsen, F. Kahlhoefer, A. Preston et al., "LHC and Tevatron Bounds on the Dark Matter Direct Detection Cross-Section for Vector Mediators", *JHEP* **07** (2012) 123, arXiv:1204.3839. doi:10.1007/JHEP07(2012)123.

[127] R. C. Cotta, A. Rajaraman, T. M. P. Tait et al., "Particle Physics Implications and Constraints on Dark Matter Interpretations of the CDMS Signal", *Phys. Rev.* **D90** (2014), no. 1, 013020, arXiv:1305.6609. doi:10.1103/PhysRevD.90.013020.

[128] CMS Collaboration, "Search for dark matter and unparticles in events with a Z boson and missing transverse momentum in proton-proton collisions at sqrt(s) = 13 TeV", Technical Report CMS-PAS-EXO-16-010, CERN, Geneva, 2016.

[129] G. Busoni, A. D. Simone, E. Morgante et al., "On the validity of the effective field theory for dark matter searches at the {LHC}", *Physics Letters B* **728** (2014) 412 – 421. doi:http://dx.doi.org/10.1016/j.physletb.2013.11.069.

[130] J. Abdallah et al., "Simplified Models for Dark Matter and Missing Energy Searches at the LHC", arXiv:1409.2893.

[131] O. Buchmueller, M. J. Dolan, and C. McCabe, "Beyond effective field theory for dark matter searches at the LHC", *Journal of High Energy Physics* **2014** (2014), no. 1, 1–24. doi:10.1007/JHEP01(2014)025.

[132] B. Holdom, "Two U(1)'s and ϵ charge shifts", *Physics Letters B* **166** (1986), no. 2, 196 – 198. doi:http://dx.doi.org/10.1016/0370-2693(86)91377-8.

[133] K. S. Babu, C. Kolda, and J. March-Russell, "Implications of generalized $Z-Z^{'}$ mixing", *Phys. Rev. D* **57** (Jun, 1998) 6788–6792. doi:10.1103/PhysRevD.57.6788.

[134] Y. Bai, P. J. Fox, and R. Harnik, "The Tevatron at the Frontier of Dark Matter Direct Detection", *JHEP* **12** (2010) 048, arXiv:1005.3797. doi:10.1007/JHEP12(2010)048.

[135] A. Friedland, M. L. Graesser, I. M. Shoemaker et al., "Probing Nonstandard Standard Model Backgrounds with LHC Monojets", *Phys. Lett. B* **714** (2012) 267–275, arXiv:1111.5331. doi:10.1016/j.physletb.2012.06.078.

[136] O. Buchmueller, M. J. Dolan, and C. McCabe, "Beyond Effective Field Theory for Dark Matter Searches at the LHC", *JHEP* **01** (2014) 025, arXiv:1308.6799. doi:10.1007/JHEP01(2014)025.

[137] P. J. Fox, R. Harnik, J. Kopp et al., "Missing Energy Signatures of Dark Matter at the LHC", *Phys. Rev. D* **85** (2012) 056011, arXiv:1109.4398. doi:10.1103/PhysRevD.85.056011.

[138] I. M. Shoemaker and L. Vecchi, "Unitarity and Monojet Bounds on Models for DAMA, CoGeNT, and CRESST-II", *Phys. Rev.* **D86** (2012) 015023, arXiv:1112.5457. doi:10.1103/PhysRevD.86.015023.

[139] G. Busoni, A. De Simone, J. Gramling et al., "On the Validity of the Effective Field Theory for Dark Matter Searches at the LHC, Part II: Complete Analysis for the *s*-channel", *JCAP* **1406** (2014) 060, arXiv:1402.1275. doi:10.1088/1475-7516/2014/06/060.

[140] IceCube Collaboration, "Preliminary Design Document", Technical Report https://icecube.wisc.edu/icecube/static/reports/IceCubeDesignDoc.pdf, 2001.

[141] IceCube Collaboration, "Icecube - the next generation neutrino telescope at the south pole", *Nucl. Phys. Proc. Suppl.* **118** (2003) 388–395, arXiv:astro-ph/0209556. [,388(2002)]. doi:10.1016/S0920-5632(03)01337-9.

[142] IceCube Collaboration, "First Year Performance of The IceCube Neutrino Telescope", *Astropart. Phys.* **26** (2006) 155–173, arXiv:astro-ph/0604450. doi:10.1016/j.astropartphys.2006.06.007.

[143] T. K. Gaisser, G. Steigman, and S. Tilav, "Limits on Cold Dark Matter Candidates from Deep Underground Detectors", *Phys. Rev.* **D34** (1986) 2206. doi:10.1103/PhysRevD.34.2206.

[144] IceCube Collaboration, "Search for dark matter annihilations in the Sun with the 79-string IceCube detector", *Phys. Rev. Lett.* **110** (2013), no. 13, 131302, arXiv:1212.4097. doi:10.1103/PhysRevLett.110.131302.

[145] IceCube Collaboration, "Improved limits on dark matter annihilation in the Sun with the 79-string IceCube detector and implications for supersymmetry", *JCAP* **1604** (2016), no. 04, 022, arXiv:1601.00653. doi:10.1088/1475-7516/2016/04/022.

[146] J. Blumenthal, P. Gretskov, M. Kr‰mer et al., "Effective field theory interpretation of searches for dark matter annihilation in the Sun with the IceCube Neutrino Observatory", *Phys. Rev.* **D91** (2015), no. 3, 035002, arXiv:1411.5917. doi:10.1103/PhysRevD.91.035002.

[147] J. Heisig, M. Kr‰mer, M. Pellen et al., "Constraints on Majorana Dark Matter from the LHC and IceCube", *Phys. Rev.* **D93** (2016), no. 5, 055029, arXiv:1509.07867. doi:10.1103/PhysRevD.93.055029.

[148] LUX Collaboration, "The Large Underground Xenon (LUX) Experiment", *Nucl. Instrum. Meth.* **A704** (2013) 111–126, arXiv:1211.3788. doi:10.1016/j.nima.2012.11.135.

[149] LUX Collaboration, "Improved Limits on Scattering of Weakly Interacting Massive Particles from Reanalysis of 2013 LUX Data", *Phys. Rev. Lett.* **116** (2016), no. 16, 161301, arXiv:1512.03506. doi:10.1103/PhysRevLett.116.161301.

[150] E. Aprile, K. Arisaka, F. Arneodo et al., "The {XENON100} dark matter experiment", *Astroparticle Physics* **35** (2012), no. 9, 573 – 590. doi:http://dx.doi.org/10.1016/j.astropartphys.2012.01.003.

[151] E. Aprile, J. Angle, F. Arneodo et al., "Design and performance of the {XENON10} dark matter experiment", *Astroparticle Physics* **34** (2011), no. 9, 679 – 698. doi:http://dx.doi.org/10.1016/j.astropartphys.2011.01.006.

[152] XENON100 Collaboration, "Search for Event Rate Modulation in XENON100 Electronic Recoil Data", *Phys. Rev. Lett.* **115** (2015), no. 9, 091302, arXiv:1507.07748. doi:10.1103/PhysRevLett.115.091302.

[153] XENON1T Collaboration, "The XENON1T Dark Matter Search Experiment", *Springer Proc. Phys.* **148** (2013) 93–96, arXiv:1206.6288. doi:10.1007/978-94-007-7241-0_14.

[154] XENON1T Collaboration, "XENON1T at LNGS", Technical Report www.bo.infn.it/xenon/docs/tdr2010.pdf, 2010.

[155] J. Sander, Z. Ahmed, A. J. Anderson et al., "SuperCDMS status from Soudan and plans for SNOLab", *AIP Conference Proceedings* **1534** (2013), no. 1, 129–135. doi:http://dx.doi.org/10.1063/1.4807350.

[156] R. Calkins and S. collaboration, "The SuperCDMS Soudan high threshold WIMP search and the planned SuperCDMS SNOLAB experiment", *Journal of Physics: Conference Series* **718** (2016), no. 4, 042009.

[157] SuperCDMS Collaboration, "New Results from the Search for Low-Mass Weakly Interacting Massive Particles with the CDMS Low Ionization Threshold Experiment", *Phys. Rev. Lett.* **116** (Feb, 2016) 071301. doi:10.1103/PhysRevLett.116.071301.

[158] A. Kounine, "The Alpha Magnetic Spectrometer on the International Space Station", *Int. J. Mod. Phys.* **E21** (2012), no. 08, 1230005. doi:10.1142/S0218301312300056.

[159] B. Beischer, P. von Doetinchem, H. Gast et al., "Perspectives for indirect dark matter search with AMS-2 using cosmic-ray electrons and positrons", *New J. Phys.* **11** (2009) 105021. doi:10.1088/1367-2630/11/10/105021.

[160] PAMELA Collaboration, "An anomalous positron abundance in cosmic rays with energies 1.5-100 GeV", *Nature* **458** (2009) 607–609, arXiv:0810.4995. doi:10.1038/nature07942.

[161] HEAT Collaboration, "Measurements of the cosmic ray positron fraction from 1-GeV to 50-GeV", *Astrophys. J.* **482** (1997) L191–L194, arXiv:astro-ph/9703192. doi:10.1086/310706.

[162] A. De Simone, A. Riotto, and W. Xue, "Interpretation of AMS-02 Results: Correlations among Dark Matter Signals", *JCAP* **1305** (2013) 003, arXiv:1304.1336. doi:10.1088/1475-7516/2013/05/003.

[163] A. Arbey and F. Mahmoudi, "LHC and ILC Data and the Early Universe Properties", *Nuovo Cim.* **C33N2** (2010) 151–157, arXiv:1002.4096. doi:10.1393/ncc/i2010-10593-1.

[164] D. Feldman, Z. Liu, and P. Nath, "Decoding the Mechanism for the Origin of Dark Matter in the Early Universe Using LHC Data", *Phys. Rev.* **D78** (2008) 083523, arXiv:0808.1595. doi:10.1103/PhysRevD.78.083523.

[165] L. Evans and P. Bryant, "LHC Machine", *Journal of Instrumentation* **3** (2008), no. 08, S08001. http://stacks.iop.org/1748-0221/3/i=08/a=S08001.

[166] CMS Collaboration, "The CMS experiment at the CERN LHC", *JINST* **3** (August, 2008) S08004. doi:10.1088/1748-0221/3/08/S08004.

[167] "Overview schematic shows the four main experiments and the two ring structure of the LHC, CERN". http://lhc-machine-outreach.web.cern.ch/lhc-machine-outreach/images/lhc-schematic.jpg accessed on 2016.03.16.

[168] ATLAS Collaboration, "The ATLAS Experiment at the CERN Large Hadron Collider", *JINST* **3** (2008) S08003. doi:10.1088/1748-0221/3/08/S08003.

[169] ALICE Collaboration, "The ALICE experiment at the CERN LHC", *JINST* **3** (2008) S08002. doi:10.1088/1748-0221/3/08/S08002.

[170] LHCb Collaboration, "The LHCb Detector at the LHC", *JINST* **3** (2008) S08005. doi:10.1088/1748-0221/3/08/S08005.

[171] "LEP design report". CERN, Geneva, 1984. Copies shelved as reports in LEP, PS and SPS libraries.

[172] CMS Collaboration, "Total Integrated Luminosity in 2012". https://twiki.cern.ch/twiki/bin/view/CMSPublic/LumiPublicResults#2012_Proton_Proton_Collisions accessed on 2016.03.17.

[173] "The HL-LHC Project – High Luminosity Large Hadron Collider, CERN", technical report. http://hilumilhc.web.cern.ch/ accessed on 2016.03.17.

[174] R. Placakyte, "Parton Distribution Functions", in *Proceedings, 31st International Conference on Physics in collisions (PIC 2011): Vancouver, Canada, August 28-September 1, 2011.* 2011. arXiv:1111.5452.

[175] J. Hauptman, "Particle physics experiments at high energy colliders". Wiley, Weinheim, 2011.

[176] D. Green, S. Kunori, K. Maeshima et al., "Dijet Mass Resolution of the CMS Calorimeter", Technical Report CMS-NOTE-1998-026, CERN, Geneva, May, 1998.

[177] CMS Collaboration, "Jet Energy Resolution in CMS at sqrt(s)=7 TeV", Technical Report CMS-PAS-JME-10-014, CERN, Geneva, 2011.

[178] M. Schröder and the CMS collaboration, "Performance of jets at CMS", *Journal of Physics: Conference Series* **587** (2015), no. 1, 012004.

[179] D0 Collaboration, "High-p_T jets in $\bar{p}p$ collisions at $\sqrt{s}$ = 630 GeV and 1800 GeV", *Phys. Rev.* **D64** (2001) 032003, arXiv:hep-ex/0012046. doi:10.1103/PhysRevD.64.032003.

[180] A. Tricomi, "Upgrade of the CMS tracker", *Journal of Instrumentation* **9** (2014), no. 03, C03041.

[181] V. Gori, "The CMS High Level Trigger", *Int. J. Mod. Phys. Conf. Ser.* **31** (2014) 1460297, arXiv:1403.1500. doi:10.1142/S201019451460297X.

[182] WLCG Collaboration, "Worldwide LHC Grid Website". http://wlcg.web.cern.ch/.

[183] CMS Collaboration, "CMSSW Application Framework", September, 2011. https://twiki.cern.ch/twiki/bin/view/CMSPublic/WorkBookCMSSWFramework.

[184] P. Elmer, B. Hegner, and L. Sexton-Kennedy, "Experience with the CMS event data model", *Journal of Physics: Conference Series* **219** (2010), no. 3, 032022.

[185] R. Brun and F. Rademakers, "{ROOT} ó An object oriented data analysis framework", *Nuclear Instruments and Methods in Physics Research Section A: Accelerators, Spectrometers, Detectors and Associated Equipment* **389** (1997), no. 1-2, 81 – 86. New Computing Techniques in Physics Research V. doi:http://dx.doi.org/10.1016/S0168-9002(97)00048-X.

[186] Aachen 3A Analysis Group Collaboration, "TAPAS – Three A Physics Analysis Software, Github repository", 2015. https://github.com/Aachen-3A/TAPAS.

[187] J. M. Campbell and R. K. Ellis, "MCFM for the Tevatron and the LHC", *Nucl. Phys. roc. Suppl.* **205-206** (2010) 10–15. doi:10.1016/j.nuclphysbps.2010.08.011.

[188] R. Gavin, Y. Li, F. Petriello et al., "W Physics at the LHC with FEWZ 2.1", *Comput. Phys. Commun.* **184** (2013) 208–214, arXiv:1201.5896. doi:10.1016/j.cpc.2012.09.005.

[189] J. Alwall et al., "MadGraph 5 : going beyond", *JHEP* **06** (2011) 128. doi:10.1007/JHEP06(2011)128.

[190] T. Sjöstrand, S. Mrenna, and P. Skands, "PYTHIA 6.4 physics and manual", *JHEP* **05** (2006) 026, arXiv:hep-ph/0603175. doi:10.1088/1126-6708/2006/05/026.

[191] T. Sjöstrand, S. Mrenna, and P. Skands, "A Brief Introduction to PYTHIA 8.1", *Comput. Phys. Commun.* **178** (2008) 852. doi:10.1016/j.cpc.2008.01.036.

[192] S. Alioli, P. Nason, C. Oleari et al., "A general framework for implementing NLO calculations in shower Monte Carlo programs: the POWHEG BOX", *JHEP* **1006** (2010) 043, arXiv:1002.2581. doi:10.1007/JHEP06(2010)043.

[193] T. Gleisberg, S. Hoeche, F. Krauss et al., "Event generation with SHERPA 1.1", *JHEP* **02** (2009) 007, arXiv:0811.4622. doi:10.1088/1126-6708/2009/02/007.

[194] J. Alwall et al., "A Standard format for Les Houches event files", *Comput. Phys. Commun.* **176** (2007) 300–304, arXiv:hep-ph/0609017. doi:10.1016/j.cpc.2006.11.010.

[195] GEANT4 Collaboration, "GEANT4: A Simulation toolkit", *Nucl. Instrum. Meth. A* **506** (2003) 250–303. doi:10.1016/S0168-9002(03)01368-8.

[196] CMS Collaboration, "Documentation of the RooStats-based statistics tools for Higgs PAG". https://twiki.cern.ch/twiki/bin/viewauth/CMS/SWGuideHiggsAnalysisCombinedLimit restricted access.

[197] CMS Collaboration, "RooStats Wiki". https://twiki.cern.ch/twiki/bin/view/RooStats/WebHome.

[198] G. Cowan, K. Cranmer, E. Gross et al., "Asymptotic formulae for likelihood-based tests of new physics", *Eur. Phys. J. C* **71** (2011) 1554, arXiv:1007.1727. [Erratum: Eur. Phys. J.C73,2501(2013)]. doi:10.1140/epjc/s10052-011-1554-0.

[199] A. L. Read, "Presentation of search results: the CL s technique", *Journal of Physics G: Nuclear and Particle Physics* **28** (2002), no. 10, 2693.

[200] "1st Workshop on Confidence Limits, pp 1st Workshop on Confidence Limits, Geneva", 2000. https://cds.cern.ch/record/411537.

[201] T. Junk, "Confidence level computation for combining searches with small statistics", *Nucl. Instrum. Meth.* **A434** (1999) 435–443, arXiv:hep-ex/9902006. doi:10.1016/S0168-9002(99)00498-2.

[202] The ATLAS Collaboration, The CMS Collaboration, The LHC Higgs Combination Group Collaboration, "Procedure for the LHC Higgs boson search combination in Summer 2011", Technical Report CMS-NOTE-2011-005. ATL-PHYS-PUB-2011-11, CERN, Geneva, Aug, 2011.

[203] R. Fisher, "Statistical Methods for Research Workers". Oliver and Boyd, 1925.

[204] CMS Collaboration, "Performance of electron reconstruction and selection with the CMS detector in proton-proton collisions at vs = 8 TeV", *JINST* **10** (2015) P06005, arXiv:1502.02701. doi:10.1088/1748-0221/10/06/P06005.

[205] S. Baffioni, C. Charlot, F. Ferri et al., "Electron reconstruction in CMS", *The European Physical Journal C* **49** (2007), no. 4, 1099–1116. doi:10.1140/epjc/s10052-006-0175-5.

[206] CMS Collaboration, "Description and performance of track and primary-vertex reconstruction with the CMS tracker", *JINST* **9** (2014), no. 10, P10009, arXiv:1405.6569. doi:10.1088/1748-0221/9/10/P10009.

[207] W. Adam, R. Frühwirth, A. Strandlie et al., "Reconstruction of electrons with the Gaussian-sum filter in the CMS tracker at the LHC", *Journal of Physics G: Nuclear and Particle Physics* **31** (2005), no. 9, N9.

[208] CMS Collaboration, "EgammaCutBasedIdentification". https://twiki.cern.ch/twiki/bin/view/CMS/EgammaCutBasedIdentification, restricted access.

[209] R.-J. Wang, D. Wood, D. Trocino et al., "Search for dark matter in events with a Z boson and missing transverse momentum in pp collisions at $\sqrt{s} = 8$ TeV", Technical Report CMS AN-2014/147, 2014. Restricted access.

[210] CMS Collaboration, "Performance of CMS muon reconstruction in pp collision events at $\sqrt{s} = 7$ TeV", *JINST* **7** (2012) P10002, arXiv:1206.4071. doi:10.1088/1748-0221/7/10/P10002.

[211] CMS Collaboration, "Performance of muon identification in pp collisions at $\sqrt{s} = 7$ TeV", CMS Physics Analysis Summary CMS-PAS-MUO-10-002, 2010.

[212] G. Abbiendi, N. Adam, J. Alcaraz et al., "Muon Reconstruction in the CMS Detector", Technical Report CMS AN-2008/097, 2008. Restricted access.

[213] R. Fruhwirth, "Application of Kalman filtering to track and vertex fitting", *Nucl. Instrum. Meth.* **A262** (1987) 444–450. doi:10.1016/0168-9002(87)90887-4.

[214] A. Strandlie and R. Frühwirth, "Track and vertex reconstruction: From classical to adaptive methods", *Rev. Mod. Phys.* **82** (May, 2010) 1419–1458. doi:10.1103/RevModPhys.82.1419.

[215] CMS Collaboration, "SWGuideMuonId". https://twiki.cern.ch/twiki/bin/view/CMSPublic/SWGuideMuonId.

[216] CMS Collaboration, "Reference muon id and isolation efficiencies". https://twiki.cern.ch/twiki/bin/view/CMS/MuonReferenceEffs, accessed on 29.08.2016, restricted access.

[217] CMS Collaboration, "SWGuideMuonId". https://twiki.cern.ch/twiki/bin/view/CMSPublic/SWGuideMuonId#Muon_Isolation.

[218] CMS Collaboration, "Determination of jet energy calibration and transverse momentum resolution in CMS", *Journal of Instrumentation* **6** (November, 2011) 11002, arXiv:1107.4277. doi:10.1088/1748-0221/6/11/P11002.

[219] S. D. Ellis and D. E. Soper, "Successive combination jet algorithm for hadron collisions", *Phys. Rev.* **D48** (1993) 3160–3166, arXiv:hep-ph/9305266. doi:10.1103/PhysRevD.48.3160.

[220] Y. L. Dokshitzer, G. D. Leder, S. Moretti et al., "Better jet clustering algorithms", *JHEP* **08** (1997) 001, arXiv:hep-ph/9707323. doi:10.1088/1126-6708/1997/08/001.

[221] M. Wobisch and T. Wengler, "Hadronization corrections to jet cross-sections in deep inelastic scattering", in *Monte Carlo generators for HERA physics. Proceedings, Workshop, Hamburg, Germany, 1998-1999*. 1998. arXiv:hep-ph/9907280.

[222] M. Cacciari, G. P. Salam, and G. Soyez, "The anti- k t jet clustering algorithm", *Journal of High Energy Physics* **2008** (2008), no. 04, 063. http://stacks.iop.org/1126-6708/2008/i=04/a=063.

[223] CMS Collaboration, "Jet Identification". https://twiki.cern.ch/twiki/bin/viewauth/CMS/JetID, restricted access.

[224] CMS Collaboration, "Performance of b tagging at sqrt(s)=8 TeV in multijet, ttbar and boosted topology events", Technical Report CMS-PAS-BTV-13-001, CERN, Geneva, 2013.

[225] CMS Collaboration, "Identification of b-quark jets with the CMS experiment", *JINST* **8** (2013) P04013, arXiv:1211.4462. doi:10.1088/1748-0221/8/04/P04013.

[226] W. Waltenberger, R. Fr¸hwirth, and P. Vanlaer, "Adaptive vertex fitting", *Journal of Physics G: Nuclear and Particle Physics* **34** (2007), no. 12, N343.

[227] CMS Collaboration, "CMS Data Analysis School Exercises - Beyond Two Generations Top-Antitop Resonances". https://twiki.cern.ch/twiki/bin/view/CMS/SWGuideCMSDataAnalysisSchool2015B2GTTbar, accessed on 29.08.2016, restricted access.

[228] CMS Collaboration, "Particle–Flow Event Reconstruction in CMS and Performance for Jets, Taus, and MET", CMS Physics Analysis Summary CMS-PAS-PFT-09-001, 2009.

[229] CMS Collaboration, "Commissioning of the particle-flow event reconstruction with the first LHC collisions recorded in the CMS detector", CMS Physics Analysis Summary CMS-PAS-PFT-10-001, 2010.

[230] CMS Collaboration, "Missing transverse energy performance of the CMS detector", *Journal of Instrumentation* **6** (September, 2011) 9001, arXiv:1106.5048. doi:10.1088/1748-0221/6/09/P09001.

[231] CMS Collaboration, "Performance of the CMS missing transverse momentum reconstruction in pp data at $\sqrt{s} = 8$ TeV", *JINST* **10** (2015), no. 02, P02006, arXiv:1411.0511. doi:10.1088/1748-0221/10/02/P02006.

[232] R.-J. Wang, "Search for physics beyond the Standard Model in pp collisions at the CMS experiment with a signature of a Z boson plus missing transverse energy, Doctoral dissertation", February, 2016. Northeastern University http://hdl.handle.net/2047/D20202765.

[233] M. Brodski, T. Hebbeker, and A. Meyer, "Search for Dark Matter in events with dimuons and MET", Technical Report CMS AN-2014/020, 2014. Restricted access.

[234] J. Pumplin, D. R. Stump, J. Huston et al., "New generation of parton distributions with uncertainties from global QCD analysis", *JHEP* **07** (2002) 012, arXiv:hep-ph/0201195. doi:10.1088/1126-6708/2002/07/012.

[235] CMS Collaboration, "CMS Luminosity Based on Pixel Cluster Counting – Summer 2013 Update", CMS Physics Analysis Summary CMS-PAS-LUM-13-001, 2013.

[236] CMS Collaboration, "Muon POG trigger discussion". https://indico.cern.ch/getFile.py/access?contribId=2&resId=0&materialId=slides&confId=289302, page 35, restricted access.

[237] S. Malhotra, M. Naimuddin, T. Hebbeker et al., "Model Unspecific Search in CMS", *EPJ Web Conf.* **28** (2012) 12004, arXiv:1201.4954. doi:10.1051/epjconf/20122812004.

[238] CMS Collaboration, "Model Unspecific Search for New Physics in $p\bar{p}$ Collisions at $\sqrt{s} = 7$TeV", *CMS PAS* **EXO-10-021** (2011). http://cms-physics.web.cern.ch/cms-physics/public/EXO-10-021-pas.pdf.

[239] S. A. Schmitz, "Model Unspecific Search for New Physics with High p_T Photons in CMS", October, 2009. Diplomarbeit, http://web.physik.rwth-aachen.de/~hebbeker/theses/schmitz_diploma.pdf.

[240] A. Bierweiler, T. Kasprzik, and J. H. K¸hn, "Vector-boson pair production at the LHC to $\mathcal{O}(\alpha^3)$ accuracy", *JHEP* **12** (2013) 071, arXiv:1305.5402. doi:10.1007/JHEP12(2013)071.

[241] J. Baglio, L. D. Ninh, and M. M. Weber, "Massive gauge boson pair production at the LHC: a next-to-leading order story", *Phys. Rev.* **D88** (2013) 113005, arXiv:1307.4331. doi:10.1103/PhysRevD.88.113005.

[242] S. Gieseke, T. Kasprzik, and J. H. K¸hn, "Vector-boson pair production and electroweak corrections in HERWIG++", *Eur. Phys. J.* **C74** (2014), no. 8, 2988, arXiv:1401.3964. doi:10.1140/epjc/s10052-014-2988-y.

[243] CMS Collaboration, "Jet Energy Resolution Measurement Twiki". https://twiki.cern.ch/twiki/bin/viewauth/CMS/JetResolution, restricted access.

[244] CMS Collaboration, "Muon Resolution Twiki". https://twiki.cern.ch/twiki/bin/viewauth/CMS/MuonReferenceResolution, restricted access.

[245] CMS Collaboration, "Measurement of the Inclusive W and Z Production Cross Sections in pp Collisions at $\sqrt{s} = 7$ TeV", *JHEP* **10** (2011) 132, arXiv:1107.4789. doi:10.1007/JHEP10(2011)132.

[246] R. D. Ball et al., "Parton distributions with LHC data", *Nucl. Phys.* **B867** (2013) 244–289, arXiv:1207.1303. doi:10.1016/j.nuclphysb.2012.10.003.

[247] M. Guzzi, P. Nadolsky, E. Berger et al., "CT10 parton distributions and other developments in the global QCD analysis", arXiv:1101.0561.

[248] A. Martin, W. Stirling, R. Thorne et al., "Parton distributions for the LHC", *Eur. Phys. J. C* **63** (2009) 189–285, arXiv:0901.0002. doi:10.1140/epjc/s10052-009-1072-5.

[249] S. Alekhin et al., "The PDF4LHC Working Group Interim Report". 2011. arXiv:1101.0536.

[250] M. Botje, J. Butterworth, A. Cooper-Sarkar et al., "The PDF4LHC Working Group Interim Recommendations", arXiv:1101.0538.

[251] P. M. Nadolsky et al., "Implications of CTEQ global analysis for collider observables", *Phys. Rev. D* **78** (2008) 013004. doi:10.1103/PhysRevD.78.013004.

[252] M. Backovic, K. Kong, and M. McCaskey, "MadDM v.1.0: Computation of Dark Matter Relic Abundance Using MadGraph5", *Physics of the Dark Universe* **5-6** (2014) 18–28, arXiv:1308.4955. doi:10.1016/j.dark.2014.04.001.

[253] Planck Collaboration, "Planck 2013 results. XVI. Cosmological parameters", *Astron. Astrophys.* **571** (2014) A16, arXiv:1303.5076. doi:10.1051/0004-6361/201321591.

[254] PICO Collaboration, "Dark Matter Search Results from the PICO-2L C_3F_8 Bubble Chamber", *Phys. Rev. Lett.* **114** (2015), no. 23, 231302, arXiv:1503.00008. doi:10.1103/PhysRevLett.114.231302.

[255] XENON100 Collaboration, "Limits on spin-dependent WIMP-nucleon cross sections from 225 live days of XENON100 data", *Phys. Rev. Lett.* **111** (2013), no. 2, 021301, arXiv:1301.6620. doi:10.1103/PhysRevLett.111.021301.

[256] G. Belanger, F. Boudjema, A. Pukhov et al., "Dark matter direct detection rate in a generic model with micrOMEGAs 2.2", *Comput. Phys. Commun.* **180** (2009) 747–767, arXiv:0803.2360. doi:10.1016/j.cpc.2008.11.019.

[257] G. Belanger, F. Boudjema, A. Pukhov et al., "Dark matter direct detection rate in a generic model with micrOMEGAs 2.2", *Comput. Phys. Commun.* **180** (2009) 747–767, arXiv:0803.2360. doi:10.1016/j.cpc.2008.11.019.

[258] CMS Collaboration, "Search for invisible decays of Higgs bosons in the vector boson fusion and associated ZH production modes", *Eur. Phys. J. C* **74** (2014) 2980, arXiv:1404.1344. doi:10.1140/epjc/s10052-014-2980-6.

[259] HESS Collaboration, "Constraints on an Annihilation Signal from a Core of Constant Dark Matter Density around the Milky Way Center with H.E.S.S.", *Phys. Rev. Lett.* **114** (2015), no. 8, 081301, arXiv:1502.03244. doi:10.1103/PhysRevLett.114.081301.

[260] Fermi-LAT Collaboration, "Dark matter constraints from observations of 25 Milky Way satellite galaxies with the Fermi Large Area Telescope", *Phys. Rev.* **D89** (2014) 042001, arXiv:1310.0828. doi:10.1103/PhysRevD.89.042001.